

ADDRESS OF PUBLISHER
& EDITOR'S OFFICE:

GDAŃSK UNIVERSITY
OF TECHNOLOGY

Faculty of Ocean Engineering
& Ship Technology
G. Narutowicza 11/12
80-233 Gdańsk, POLAND

tel.: +48 58 347 13 66
fax: +48 58 341 13 66

EDITORIAL STAFF:

Jacek Rudnicki
| Editor in Chief
Rafał Szłapczyński
| Associate Editor
Jerzy Świrzydźczuk
| Associate Editor
Przemysław Wierzchowski
| Associate Editor
Aleksander Kniat
| Editor for international
relations

Price:
single issue: 25 PLN

Prices for abroad
single issue:
- in Europe EURO 15
- overseas USD 20

WEB:
pg.edu.pl/pmr

e-mail: pmr@post.pl

ISSN 1233-2585

CONTENS

4	Marcin Życzkowski, Przemysław Krata, Rafał Szłapczyński <i>MULTI-OBJECTIVE WEATHER ROUTING OF SAILBOATS CONSIDERING WAVE RESISTANCE</i>
13	Tomasz Praczyk <i>CORRECTION OF NAVIGATIONAL INFORMATION SUPPLIED TO BIOMIMETIC AUTONOMOUS UNDERWATER VEHICLE</i>
24	Parviz Ghadimi, Nasrin Javanmardi <i>ANALYSIS OF VENTILATION REGIMES OF THE OBLIQUE WEDGE-SHAPED SURFACE PIERCING HYDROFOIL DURING INITIAL WATER ENTRY PROCESS</i>
35	Przemysław Król, Tomasz Bugalski <i>APPLICATION OF VORTEX FLOW MODEL IN PROPELLER-STATOR SYSTEM DESIGN AND ANALYSIS</i>
44	Kumars Mahmoodi, Hassan Ghassemi <i>OUTLIER DETECTION IN OCEAN WAVE MEASUREMENTS BY USING UNSUPERVISED DATA MINING METHODS</i>
51	Jeronimo Esteve-Perez, Antonio Garcia-Sanchez <i>DYNAMISM PATTERNS OF WESTERN MEDITERRANEAN CRUISE PORTS AND THE COOPETITION RELATIONSHIPS BETWEEN MAJOR CRUISE PORTS</i>
61	Qianli Ma, Wenyan Wang, Yun Peng, Xiangqun Song <i>AN OPTIMIZATION APPROACH TO THE INTERMODAL TRANSPORTATION NETWORK IN FRUIT COLD CHAIN, CONSIDERING COST, QUALITY DEGRADATION AND CARBON DIOXIDE FOOTPRINT</i>
70	Damian Bocheński <i>SELECTION OF MAIN ENGINES FOR HOPPER SUCTION DREDGERS WITH THE USE OF PROBABILITY MODELS</i>
77	Bogdan Rozmarynowski, Tomasz Mikulski <i>SELECTED PROBLEMS OF SENSITIVITY AND RELIABILITY OF A JACK-UP PLATFORM</i>
85	Danuta Warnke <i>CONCEPT OF DEVICE TO INSPECT INTERNAL TECHNICAL CONDITION OF MARINE PIPELINE</i>
93	Agnieszka Maczyszyn <i>INVESTIGATION METHOD AND MATHEMATICAL MODEL OF PRESSURE LOSSES IN HYDRAULIC ROTARY MOTOR</i>

**ADDRESS OF PUBLISHER
& EDITOR'S OFFICE:**

**GDAŃSK UNIVERSITY
OF TECHNOLOGY**

**Faculty of Ocean Engineering
& Ship Technology
G. Narutowicza 11/12
80-233 Gdańsk, POLAND**

tel.: +48 58 347 13 66

fax: +48 58 341 13 66

- 99 Tomasz Hajduk**
*RESEARCH OF DEPOSIT ACCUMULATED ON HEAT EXCHANGE SURFACES IN
THE LIGHT OF THERMAL DEGRADATION OF HEAT EXCHANGE APARATUS
OF STEAM POWER PLANTS. PART I: STUDY OF REAL SEDIMENTS*
- 108 Gvidonas Labeckas, Stasys Slavinskas, Jacek Rudnicki, Ryszard Zadrąg**
*THE EFFECT OF OXYGENATED DIESEL-N-BUTANOL FUEL BLENDS
ON COMBUSTION, PERFORMANCE, AND EXHAUST EMISSIONS
OF A TURBOCHARGED CRDI DIESEL ENGINE*
- 121 Karol Niklas, Janusz Kozak**
*THE EFFECT OF NUMERICAL 2D AND 3D FEM ELEMENT MODELLING ON
STRAIN AND STRESS DISTRIBUTIONS AT LASER WELD NOTCHES IN STEEL
SANDWICH TYPE PANELS*
- 128 Grzegorz Robak, Daniel Krzyżak, Artur Cichański**
*DETERMINING EFFECTIVE LENGTH FOR 40 HM-T STEEL BY USE OF NON-
LOCAL LINE METHOD CONCEPT*

Editorial

POLISH MARITIME RESEARCH is a scientific journal of worldwide circulation. The journal appears as a quarterly four times a year. The first issue of it was published in September 1994. Its main aim is to present original, innovative scientific ideas and Research & Development achievements in the field of :

Engineering, Computing & Technology, Mechanical Engineering,

which could find applications in the broad domain of maritime economy. Hence there are published papers which concern methods of the designing, manufacturing and operating processes of such technical objects and devices as : ships, port equipment, ocean engineering units, underwater vehicles and equipment as well as harbour facilities, with accounting for marine environment protection.

The Editors of POLISH MARITIME RESEARCH make also efforts to present problems dealing with education of engineers and scientific and teaching personnel. As a rule, the basic papers are supplemented by information on conferences , important scientific events as well as cooperation in carrying out international scientific research projects.

Scientific Board

Chairman : Prof. JERZY GIRTLEK - Gdańsk University of Technology, Poland

Vice-chairman : Prof. MIROSLAW L. WYSZYŃSKI - University of Birmingham, United Kingdom

Dr POUL ANDERSEN
Technical University of Denmark
Denmark

Dr MEHMET ATLAR
University of Newcastle United
Kingdom

Prof. GÖRAN BARK
Chalmers University of Technology
Sweden

Prof. SERGEY BARSUKOV
Army Institute of Odessa Ukraine

Prof. MUSTAFA BAYHAN
Süleyman Demirel University
Turkey

Prof. VINCENZO CRUPI
University of Messina, Italy

Prof. MAREK DZIDA
Gdańsk University of Technology
Poland

Prof. ODD M. FALTINSEN
Norwegian University of Science
and Technology
Norway

Prof. PATRICK V. FARRELL
University of Wisconsin Madison,
WI
USA

Prof. HASSAN GHASSEMI
Amirkabir University of Technology
Iran

Prof. STANISŁAW GUCMA
Maritime University of Szczecin
Poland

Prof. ANTONI ISKRA
Poznań University of Technology
Poland

Prof. JAN KICIŃSKI
Institute of Fluid-Flow Machinery
of PASci
Poland

Prof. ZBIGNIEW KORCZEWSKI
Gdańsk University of Technology
Poland

Prof. JANUSZ KOZAK
Gdańsk University of Technology
Poland

Prof. JAN KULCZYK
Wrocław University of Technology
Poland

Prof. NICOS LADOMMATOS
University College London United
Kingdom

Prof. JÓZEF LISOWSKI
Gdynia Maritime University Poland

Prof. JERZY MATUSIAK
Helsinki University of Technology
Finland

Prof. JERZY MERKISZ
Poznań University of Technology
Poland

Prof. EUGEN NEGRUS
University of Bucharest Romania

Prof. YASUHIKO OHTA
Nagoya Institute of Technology
Japan

Dr YOSHIO SATO
National Traffic Safety and
Environment Laboratory
Japan

Prof. KLAUS SCHIER
University of Applied Sciences
Germany

Prof. FREDERICK STERN
University of Iowa, IA, USA

Prof. ILCEV DIMOV STOJCE
Durban University of Technology
South Africa

Prof. JÓZEF SZALA
Bydgoszcz University
of Technology and Agriculture
Poland

Prof. WITALIJ SZCZAGIN
State Technical University of
Kaliningrad, Russia

Prof. BORIS TIKHOMIROV
State Marine University of St.
Petersburg, Russia

Prof. DRACOS VASSALOS
University of Glasgow and
Strathclyde United Kingdom

MULTI-OBJECTIVE WEATHER ROUTING OF SAILBOATS CONSIDERING WAVE RESISTANCE

Marcin Życzkowski¹

Przemysław Krata²

Rafał Szłapczyński¹

¹ Gdańsk University of Technology, Poland

² Gdynia Maritime University, Poland

ABSTRACT

The article presents a method to determine the route of a sailing vessel with the aid of deterministic algorithms. The method assumes that the area in which the route is to be determined is limited and the basic input data comprise the wind vector and the speed characteristic of the vessel. Compared to previous works of the authors, the present article additionally takes into account the effect of sea waves with the resultant resistance increase on the vessel speed. This approach brings the proposed model closer to real behaviour of a sailing vessel. The result returned by the method is the sailing route, optimised based on the multi-criteria objective function. Along with the time criterion, this function also takes into account comfort of voyage and the number of performed turns. The developed method has been implemented as simulation application SaillingAssistance and experimentally verified.

Keywords: sailing vessels, weather routing, waves, navigation, resistance

INTRODUCTION

Although practised from very beginning of navigation, only in recent decades planning the vessel's route has been dynamically developed in terms of both applied methods, and implemented algorithms. This has led to the evolution from single criterion optimisation, which usually aimed at determining the fastest route, to modern multi-criteria approach with a set of constraints, also of dynamic nature.

The analysed problem of vessel's route planning belongs to good seamanship standards and is executed, using available methods, on all vessels, regardless of their size or propulsion type. In sea navigation, the International Convention for the Safety of Life at Sea (SOLAS) imposes a formal requirement of route planning for a conventional ship before the start of its voyage. For obvious practical reasons, the route plan refers not only to conventional ships, but to all watercraft: power-driven ships, sailing vessels, small tourist and sport yachts, and other watercraft units, including unmanned vessels. According to International Regulations for Preventing Collisions at Sea

(COLREGS), the term "ship" means floating equipment of any type. Depending on the type of voyage and requirements of the ship user, various initial assumptions and tasks to be performed can be formulated, which results in different sequence of items in the voyage plan. For instance, the ship user can be a merchant ship owner, or the captain of a sailing vessel, the team of a sailing yacht taking part in a great ocean race, or the person controlling an unmanned vessel. That is why the shortest possible route is not always the only required result of the use of an optimisation method.

Criteria taken into account when vessel's route planning can also include feeling of comfort (for passenger ships, or recreation yachts), minimal stock consumption (for merchant ships), feeling of safety (for novice sailors), or finding the longest route without repetitions (for devices monitoring a given water region). What should also be taken into consideration is a very important group of criteria referring to various aspects of safety of sailing. In the optimisation task, those criteria can play a role of either objective function

or constraint, and cover the issues of avoiding excessive ship rolling and accelerations [7] and other elements specific for a given navigation zone (for instance avoiding excessive rolling of a sailing yacht during recreation navigation). Due to a great variety of requirements expected by people involved in given ship navigation, its priority is selecting a vessel's route which will be optimal from the subjective point of view of its user [23].

Along with subjective requirements of the user, the route also depends on objective factors, such as the type of watercraft and navigation, and the navigation zone. These factors impose some constraints affecting the final shape of the sailing trajectory. For instance, when planning the route in ocean navigation, special attention is paid to limited visibility areas, ice-covered areas, and iceberg occurrence areas, as a result of which so-called meteorological navigation is conducted [1]. It is noteworthy that a key issue in those cases is the assistance of e-navigation systems [21, 27]. During great sailing races, in which of major importance is competition between the racing teams, the abovementioned meteorological aspects are complemented by strategic planning during the race [19] in which different weather scenarios are assumed [18]. For unmanned sailing vessels, the properly selected route may be crucial for correct execution of voyage tasks (such as monitoring, or hydrographic work), avoiding damages and, above all, reaching the assumed reception point by the vessel. For this type of vessels of high importance is to maintain sailing abilities along the entire voyage trajectory [22].

Overall, the vessel's route depends on: voyage priorities and tasks formulated by the user, type of watercraft unit, and water region. The contemporary literature on the subject does not offer solutions to all abovementioned aspects of the problem. Such a solution was only proposed by the authors in [24, 29], where the problem of planning the route for a sailing vessel from starting point to target point in discrete space is solved. In these works, a discrete model of vessel motion and the discrete model of navigation environment are proposed. Also, a method is described to determine the route for a given sailing vessel with given speed parameters. The method takes into account various route optimisation criteria, such as minimal voyage time, maximal feeling of comfort, or minimal number of course changes. Moreover, certain constraints are introduced, such as, for instance, navigable and unnavigable zones, or the maximal course change value. In the proposed model, the navigable zone is represented by a grid of points covering a limited area. At each point of this area, for current hydrometeorological data a temporary, local speed characteristic of the sailing vessel is determined. The present article is continuation of that research, taking into consideration the effect of waves on the vessel speed, omitted in earlier works. For this purpose, the authors propose a method which takes into account the action of waves when determining the vessel speed and, indirectly, its route. The effect of waves has the form of changes introduced to the polar speed characteristic of sailing vessel at each point of the discrete grid representing the navigable zone for given hydrometeorological conditions. All this finally results in

significant modification of the shape of the navigable zone as a whole, due to changes of the dead angle of sailing vessel navigation in situation when the vessel experiences additional resistance generated on the hull by sea waves.

RESEARCH METHODS

This Section presents an overview of basic methods used in vessel's route planning (Subsection "*Route planning methods available in literature*"), and then discusses two versions of the method proposed by the authors (Subsections "*Method variant without sea wave effect*" and "*Extended method variant taking into account sea wave effect*").

ROUTE PLANNING METHODS AVAILABLE IN LITERATURE

The applicable route planning methods can be basically divided into deterministic and nondeterministic (Fig. 1.).

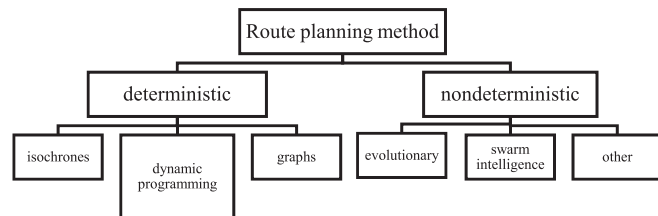


Fig. 1 Division of route planning methods

The deterministic isochrone based method was firstly presented in [5] as the manual graphic method of meteorological navigation. It was then modified and implemented in [1] and [28]. Provided that the isochrones are constant, this method can be considered deterministic. Other methods in this group, which can be found in [2, 10, 12, 13, 25], are based on dynamic programming, in which the route finding process is executed in a recursive manner. The literature also provides descriptions of deterministic graph methods, for instance those based on the modified Dijkstra algorithm [14, 16] or the A* algorithm [15].

The other group comprises nondeterministic methods, which do not guarantee repeatability of the same results for the same input data, nor obtaining the optimal solution in the strict sense. Here, evolutionary methods can be named, including evolutionary and genetic algorithms, in which the solution is iteratively improved in successive generations [23], and methods based on so-called Swarm intelligence (SI), including Ant Colony Optimisation (ACO) [11] or Particle Swarm Optimisation (PSO). Another family in the group of nondeterministic methods comprises evolutionary-probabilistic methods, discussed in [3] for instance.

Inspired by the above methods available in scientific literature, the authors propose a novel method to determine the optimal route for a sailing vessel. The proposed method can

be classified as a deterministic multi-criteria graph method. In this sense it is comparable with the method presented in [10], but with a number of substantial differences, including larger number of directions of motion and the effect of sea

wave action. These two aspects contribute to obtaining more realistic routes as the solution of the optimisation task executed by the algorithm of the proposed method.

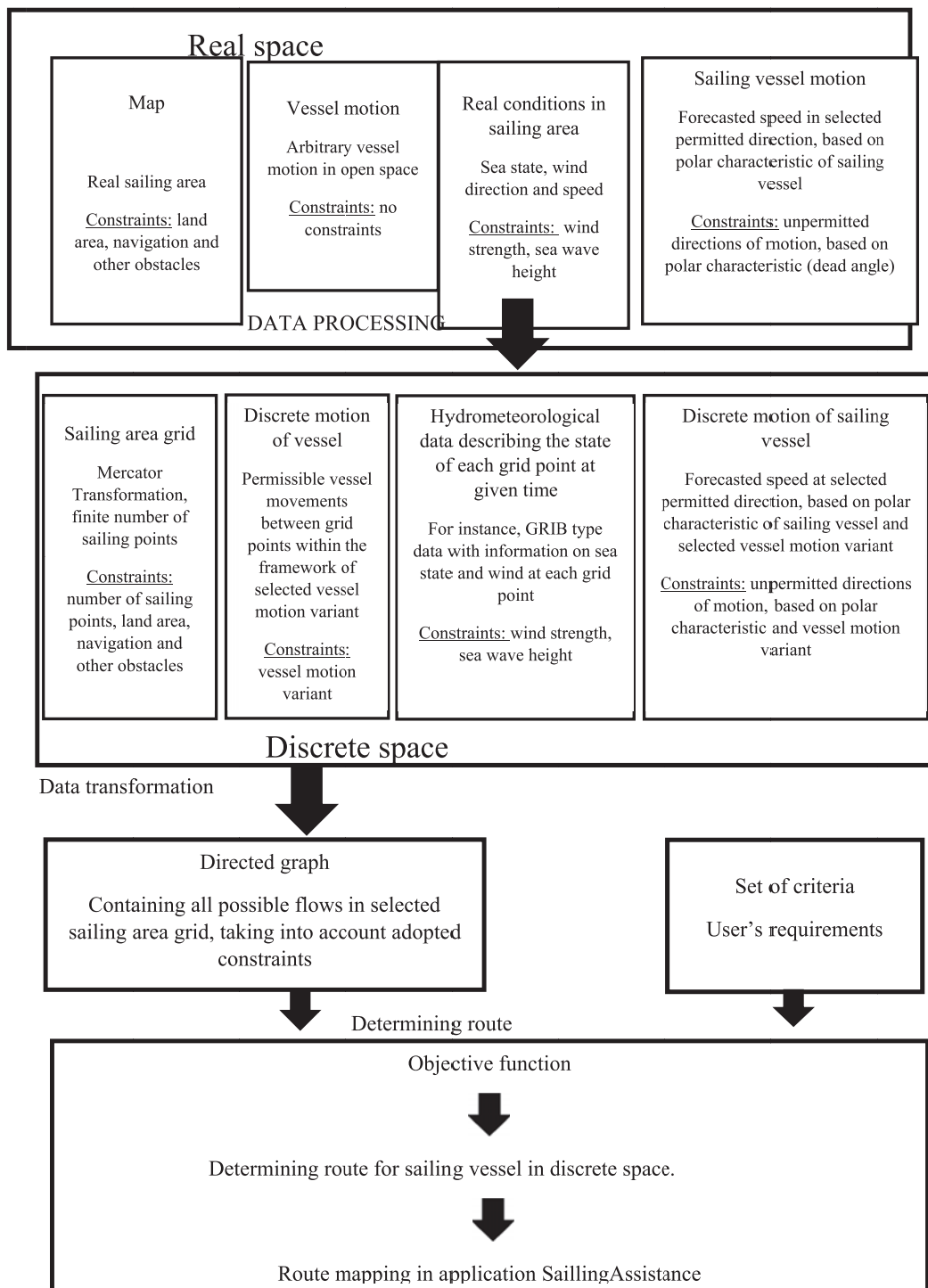


Fig. 2 Scheme of applied methodology

METHOD VARIANT WITHOUT SEA WAVE EFFECT

This method is executed in accordance with the scheme of methodology applied at subsequent research stages (Fig. 2.) The proposed discrete model of sailing vessel motion is an approximate representation of vessel motion in real space. Consequently, the real space is replaced by discrete space – a grid of points of certain resolution. This discrete space is described by the graph $G(V,E)$, where V represents a set of graph vertices – grid points P_{ij} , i.e.

$$V = \{ P_{i,j}; i = 1,2, \dots, m. j = 1,2, \dots, n \} \quad (1)$$

The set of edges E determines possibilities of passing between all vertices in the graph (points P_{ij}). The graph $G(V, E)$ defined in the above way represents all possible routes from distinctive point A to distinctive point B .

Taking into account sailing conditions and parameters of the vessel (including its speed characteristic), the graph $G(V, E)$ is transformed into the weighted graph $+G(V, E, S)$ which is then used for determining the optimal route with the aid of the modified Dijkstra algorithm for the assumed optimisation criteria.

In earlier studies conducted by the authors, the optimisation problem was described with the aid of a multi-criteria objective function which should be minimised.

$$f_g = \sum_{i=1}^m [t_i \cdot c(\beta_i)] + \sum_{i=1}^{m-1} [t(|\alpha_{i+1} - \alpha_i|) + p(|\alpha_{i+1} - \alpha_i|)] \quad (2)$$

where:

- m – number of all route segments (flows),
- i – current route segment (flow)
- t_i – time of flowing past i -th route segment
- $c(\beta_i)$ – discomfort coefficient for i -th route segment, depending on ship rolling (value 1 means no feeling of discomfort)
- (α_i) – course on i -th route segment,
- $t(|\alpha_{i+1} - \alpha_i|)$ – time of course change between route segments,
- $p(|\alpha_{i+1} - \alpha_i|)$ – additional coefficient of temporary discomfort, depending on course change magnitude.

EXTENDED METHOD VARIANT TAKING INTO ACCOUNT SEA WAVE EFFECT

In this variant, sailing conditions are described by the wind vector and, optionally, by wave parameters. The action of these waves can be neglected or taken into account to assess their effect on final result of vessel's route optimisation. Taking into account the sea wave effect as a component of sailing conditions leads to the appearance of new constraints concerning the sailing area. These constraints result from the wave spectrum which affects the vessel motion vector, especially when the vessel course is opposite to the wave approach direction (windward course). It is noteworthy that the polar speed characteristic VPP which is only available

on a sailing vessel is determined for calm water, using, for instance, the typical application MaxSurf VPP 30.

In the article, the speed characteristic of the sailing vessel is assessed for a given wave spectrum. To obtain the polar speed characteristic taking into account waves, a model was developed which is executed by the procedure named VppCorr for the purpose of the performed research.

The procedure VppCorr is implementation of the model adopted to determine speed changes of the sailing vessel caused by the presence of waves. When the vessel sails on rough sea, an additional force bearing the name of added resistance is generated on its hull. This added resistance can be determined. In the reported experiments, it was calculated using the code MaxSurf Motion 30. However, a key input variable to this code is the vessel speed, which also depends on the added resistance (i.e. on the final result of modelling with the aid of MaxSurf Motion). That is why an iterative approach was applied to determine the magnitude of total resistance of the vessel sailing on rough sea, which is described further in the article.

Introducing certain technical data of a sailing vessel to the application Bentley MaxSurf VPP we get the following output data: (1) vessel speed diagram, which depends on wind speed (in knots) and wind attack angle (in degrees); (2) hull resistance R_{hull} at given vessel speed V_s . The calculations are performed for calm water and meet the conditions of IMS VPP standards of ORC 31. The hull resistance R_{hull} is determined using the method Delft II [4, 17]. Moreover, an assumption is made that the sail propeller generating the effective thrust $Thrust_{calm}$ on calm water is equivalent to hull resistance R_{hull} . Here, the effective propeller thrust is understood as the thrust deducted by losses resulting from propeller/hull cooperation. In the analysis, the term of effective thrust can be replaced by total efficiency, used in screw propeller analyses and defined by the ratio of effective towing power to power delivered by the engine. This way, total efficiency takes into account hull efficiency, including thrust deduction factor and wake coefficient, efficiency of isolated propeller, rotating efficiency, and shafting efficiency. However, for sail propulsion the term of total efficiency is not well grounded in the literature, that is why the approach based on balance of forces (term: "effective propeller thrust") is applied instead of energy related approach which makes use of efficiency terms. The effective propeller thrust takes into account factors which affect total efficiency on a sailing vessel.

Based on the grid of results obtained using the application Maxsurf VPP, the diagram of vessel speed V_s is approximated by the fifth-order polynomial taking into account wind speed V_w and wind direction angle β_{TW} with respect to the vessel.

$$V_s = \sum_{i=1}^5 p_i V_w^i \beta_{TW}^{5-i} \quad (3)$$

where:

p_i – coefficients of polynomial

The above diagram-to-polynomial transformation, being in fact construction of a meta-model, is shown in Fig. 3. Here,

the surface on the diagram is described by the fifth-order polynomial, while black points represent data calculated by the application Maxsurf VPP.

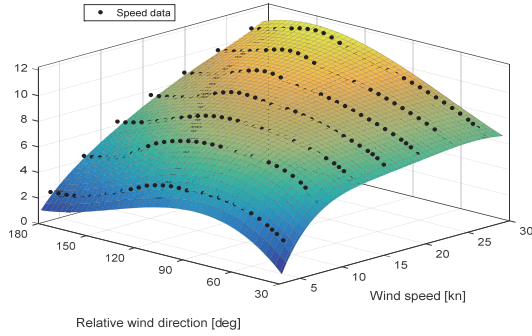


Fig. 3 Surface visualisation of VPP calm water speed meta-model using fifth-order polynomial. Points represent data from application Maxsurf VPP

The hull resistance on calm water is approximated by the fifth-order polynomial depending on the vessel speed V_s . As the forces are in balance during vessel motion with constant speed, at the present stage this resistance is equated with effective propeller thrust force $Thrust_{calm}$.

$$Thrust_{calm} = \sum_{i=1}^5 p_i V_s^i \quad (4)$$

where:

p_i – coefficients of polynomial

Then, making use of the method based on widely used strip theory, described in [20] and applied in the application MaxSurf Motion, the added hull resistance resulting from sea waves is calculated. Here, an assumption is made that the total hull resistance is given by the formula:

$$R_T = R_{hull} + \Delta R \quad (5)$$

The additional resistance ΔR obtained from MaxSurf Motion is approximated by the third-order polynomial, depending on wind speed V_w and wind direction angle β_{TW} with respect to the vessel.

$$\Delta R = \sum_{i=1}^3 p_i V_w^i \beta_{TW}^{3-i} \quad (6)$$

The quality of modelling can be assessed based on the visualisation in Fig. 4, which shows the convergence between the polynomial surface and points representing the results obtained from the application.

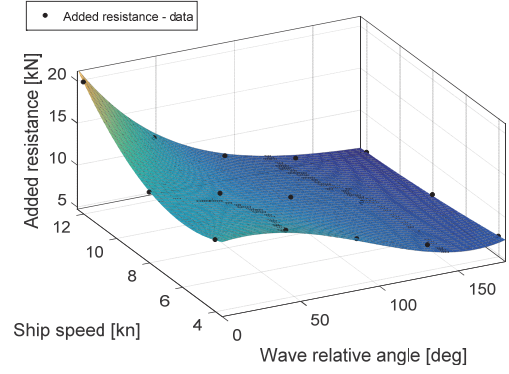


Fig. 4 Visualisation of added resistance meta-model (third-order polynomial)

In the next step, the balance of forces is calculated, from which the effective propeller thrust $Thrust_{corr}$ deduced by the added resistance ΔR is obtained according to the formula:

$$Thrust_{corr} = Thrust_{calm} - \Delta R \quad (7)$$

Then, for the corrected propeller thrust $Thrust_{corr}$ new vessel speed V_{scorr} is read from the initial VPP, i.e. for calm water. This relation is described in polynomial form:

$$V_{scorr} = \frac{\sum_{i=0}^3 p_{i+1} Thrust_{corr}^i}{\sum_{i=0}^3 q_{i+1} Thrust_{corr}^i} \quad (8)$$

As the final step, the added resistance ΔR_{corr} is recalculated using the corrected speed V_{scorr} . Then, the propeller thrust $Thrust_{calm}$ is deduced by new added resistance ΔR_{corr} and the corrected speed V_{scorr} is calculated. As a result of this iterative procedure, the speed V_s of the sailing vessel is determined for specific wave spectrum.

RESULTS

The developed method was implemented in the application SailingAssistance, which was used in numerical experiments comparing the method variants taking into account and neglecting the effect of sea waves. In both variants, the same starting and final positions were assumed. The algorithm searching for the optimal route minimises the objective function (Equation 2).

All these routes were determined for a sailing vessel characterised by technical parameters given in Table 1.

Tab. 1 Technical data of sailing vessel used in experiments

Name of parameter	Value	Unit
Displacement	6,531	t
Volume (displaced)	6,372	m ³
Draft Amidships	2,475	m
Immersed depth	3,054	m
WL Length	10,636	m
Beam max extents on WL	2,866	m

Wetted Area	29,911	m ²
Max sect. area	1,213	m ²
Waterplane Area	21,243	m ²
Foresails		
I	16.605	m
J	4.489	m
LP	7.602	m
SPL	4.871	m
SL	16.002	m
SMW	8.778	m
Mainsail		
P	14.783	m
E	4.203	m
MGU	1.554	m
MGM	2.743	m
BAS	2.102	m
Mast		
MDT1	0.116	m
MDL1	0.213	m
MDT2	0.116	m
MDL2	0.152	m
HBI	1.126	m
TL	2.262	m

where:

- I - height from the sheer line to the top of the foretriangle,
- J - distance from the headstay base to the front of the mast,
- LP - jib clew to the luff taken perpendicular to the luff,
- SPL - spinnaker pole length,
- SL - spinnaker luff length,
- SMW - spinnaker maximum width,
- P - mainsail luff length from lower to upper band on the mast,
- E - mainsail foot length from the mast to the boom band,
- MGU/MGM - upper and middle girth dimensions of the mainsail,
- BAS - height of the lower mainsail luff band above the sheer line,
- MDT 1/MDL 1 - athwartships measurement and fore and aft dimension of the mast near the deck (below any taper),
- MDT 2/MDL 2 - the same measurements as above taken at the upper mainsail band. If there is no mast taper, the upper and lower dimensions will match and the TL will be zero,
- HBI - freeboard at the base of the mast,
- TL - taper length of the mast.

During the tests, the same sailing conditions were assumed for all routes. The wind speed in the sailing area ranged from 9 m/s to 12 m/s, and its direction was: NE – E. The wave spectrum assumed for these conditions is given in Table 2

Tab. 2 Wave spectrum during performed tests

Spectrum Type	Char. height [m]	Modal period [s]	Average period [s]	Zero crossing period [s]
DNV	1,23	5,797	4,991	4,724

Routes 1 and 3, marked blue in Fig. 5 and Fig. 6, neglect the effect of sea waves, while routes 2 and 4, marked yellow, take it into account. They are characterised by numerical results given in Table 3.

Tab. 3 Comparison of method variants. Results obtained from simulation application SailingAssistance

Route	1	2	3	4
Takes into account sea waves	No	Yes	No	Yes
Initial position "S"	54.79° N 018. 84° E	54.79° N 018. 84° E	54.50° N 018.65° E	54.79° N 018. 84° E
Final position "F"	54.50° N 018.65° E	54.50° N 018.65° E	54.50° N 018.65° E	54.79° N 018.84° E
Total length of route [Nm]	23.5	24.1	21.7	26.7
Time of route passing [min]	128	124	142	223
No of course changes	7	8	5	10

The obtained results of the research allow us to assess the extent to which taking into account sea waves (routes 2 and 4 in Table 3), as compared to planning which neglects this effect (routes 1 and 3 in Table 3), affects the planned route when determining it with the aid of the developed method. In the light of Fig. 5 and Fig. 6 it should be concluded that this effect is significant. The tests were performed for a sailing vessel of about 10 m in total length. Simultaneously, relatively strong wind was assumed, of about 5B, and corresponding high wave. For such a small watercraft unit, especially when it sails by the wind in the assumed conditions, the observed time of voyage along the examined route is extended by more than half when taking into account sea waves – routes 3 and 4. On the other hand, when the ship sails downwind the additional required time is shorter when taking into account sea waves – routes 1 and 2. An attempt to explain this result may refer to the trochoidal theory of waves and circular motion of water particles described by it. A vessel with relatively shallow draught increases its speed over the seabed when sailing with local surface current generated by waves, and decreases when sailing against the waves. Of some importance is also the generation of a large local water uplift at vessel's bow when it crosses successive wave crests.

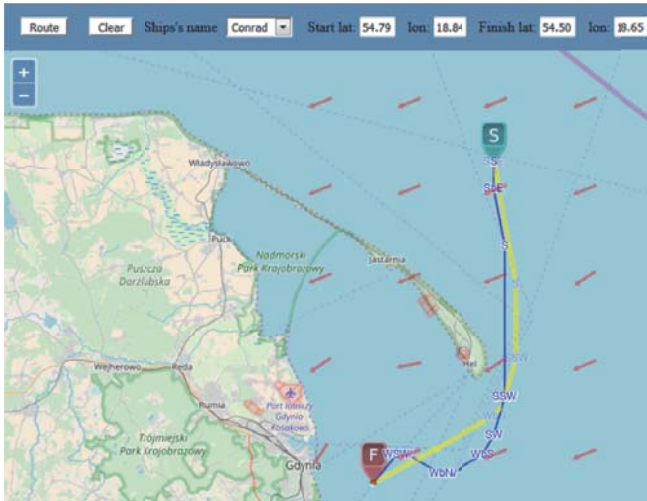


Fig. 5. Route 1 (marked blue) neglects sea waves, while route 2 (marked yellow) takes into account the sea state.

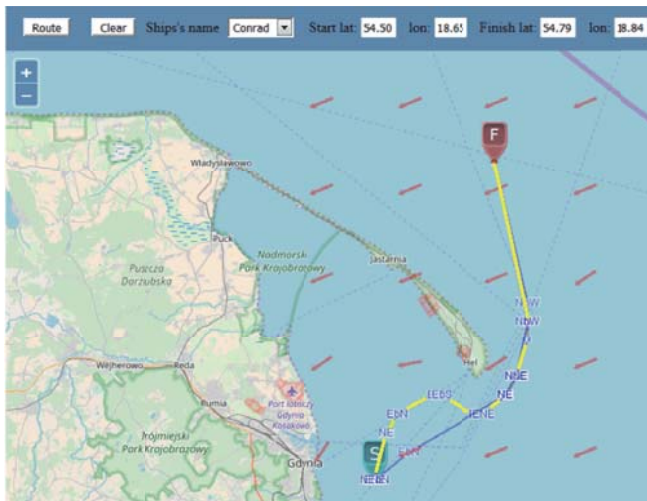


Fig. 6. Route 3 (marked blue) neglects sea waves, while route 4 (marked yellow) takes into account the sea state.

It is also noteworthy in Fig. 5 and Fig. 6 that the sailing vessel routes which take into account sea waves coincide with those neglecting this effect only at starting and final positions.

DISCUSSION

The presented method to determine the optimal route for a sailing vessel takes into account an important aspect, which is the change of polar speed characteristic generated by the wave field in the area of navigation. The performed research has revealed unmistakably that ignoring the effect of waves leads to determining routes which significantly differ from optimal, with respect to both time, and the aggregated cost criterion represented by the objective function. This conclusion is essential from the point of view of a typical method to determine and present to the user the speed

characteristic in the form of a diagram in which this speed depends only on the wind speed and the sailing vessel course with respect to the wind. This approach can be misleading, especially for inexperienced sailors who intuitively may think that the sea waves decelerate, to some extent, the sailing vessel, but the assumed target can still be successfully reached when sailing along a similar route as that for light wave field, with smaller speed being the only difference. The truth is, however, that neglecting sea waves may lead to determining the route which will be much more difficult or – in an extreme case – impossible for practical execution.

CONCLUSIONS

The results of the performed research have revealed that far-reaching modification of the speed characteristic in the rough water region not only extends the time of voyage but also, above all, may require another route planning, as the sailing vessel has much greater dead angle in heavy waves. This observation is of high importance from the practical point of view. In particular, the assumed target point, for instance the port of refuge, may be hardly available by the vessel after worsening of hydrometeorological conditions, especially when the vessel sails upwind. If the captain makes an attempt to sail in close hauled point of sail, the increased dead angle resulting from the modified polar speed characteristic can even make reaching the target impossible, which will lead to hazardous navigation situation. In those circumstances, the use of the method proposed in the article will allow the captain to plan a feasible route, which may be related, for instance, with choosing another port of refuge. Even if that port is situated farther than the initial option, real possibility to reach it is undoubtedly much safer for the vessel and its crew than failing to reach a closer target, but situated in the unfavourable sector from the point of view of upwind course.

In the presented method, one selected wave spectrum was considered which was specific for the adopted meteorological conditions. A planned direction of further method development assumes taking into account mixed wave structures comprising wave systems of different height and frequency. Another significant direction is including the stability related vessel motion dynamics on waves to the optimisation algorithm. The vessel motion on waves can provoke dangerous phenomena, such as resonance rolling, or so-called broaching. In particular, resonance amplification of ship rolling is the effect which significantly affects the safety of navigation [9]. Most recent works on vessel's route optimisation already take into account dynamic conditions of resonance avoidance [6]. However, those works do not refer to sailing vessels and do not analyse their specificity of rolling damping, which significantly differs from that of power-driven ships. Neglecting this phenomenon may lead to annihilation of optimisation results, as rapid increase of rolling amplitude is in contrast to objective function criteria concerning the comfort of navigation. Further method development will also include extending the range of phenomena which

are modelled and taken into account in optimisation, with particular attention focused on nonlinearities in the description of ship stability characteristics, as, according to recent literature on the subject, these nonlinearities are essential for determining the configuration of ship course and speed to avoid dangerous dynamic phenomena [26, 8]. The results of past research, along with observation of possibilities to introduce new objective functions and constraints to the developed method, indicate that the planned development directions will bring the route optimisation results closer to real conditions of sailing.

BIBLIOGRAPHY

1. Bijlsma, S.J.: Minimal Time Route Computation for Ships with Pre-Specified Voyage Fuel Consumption, *J. Navig.* 61 (2008) 723–733.
2. Dębski, R.: An adaptive multi-spline refinement algorithm in simulation based sailboat trajectory optimization using onboard multi-core computer systems, *Int. J. Appl. Math. Comput. Sci.* 26 (2016) 351–365.
3. Gao, M., G. Shi, W. Li, Y. Wang, D. Liu: ScienceDirect An improved genetic algorithm for island route planning, *Procedia Eng.* 174 (2017) 433–441.
4. Gerritsma, J., J.A. Keuning, R. Onnink: *The Delft Systematic Yacht Hull Series II Experiments*, 1990.
5. James, R.W.: *APPLICATION OF WAVE FORECASTS TO MARINE NAVIGATION*, (1957).
6. Krata, P., J. Szłapczyńska: Ship weather routing optimization with dynamic constraints based on reliable synchronous roll prediction, *Ocean Eng.* 150 (2018) 124–137.
7. Krata, P., J. Szłapczyńska: Weather Hazard Avoidance in Modeling Safety of Motor-Driven Ship for Multicriteria Weather Routing, *TransNav.* 6 (2012) 71–78.
8. Krata, P., W. Wawrzyński: On ship roll resonance frequency, *Ocean Eng.* 126 (2016) 92–114.
9. Krata, P., W. Wawrzyński: Prediction of Ship Resonant Rolling - Related Dangerous Zones with Regard to the Equivalent Metacentric Height Governing Natural Frequency of Roll, *TransNav, Int. J. Mar. Navig. Saf. Sea Transp.* 11 (2017).
10. Langbein, J., R. Stelzer, T. Frühwirth: A Rule-Based Approach to Long-Term Routing for Autonomous Sailboats, in: *Robot. Sail.*, Springer Berlin Heidelberg, Berlin, Heidelberg, 2011: pp. 195–204.
11. Lazarowska, A.: Multi-criteria ACO-based Algorithm for Ships Trajectory Planning, *TransNav, Int. J. Mar. Navig. Saf. Sea Transp.* 11 (2017) 31–36.
12. Lisowski, J.: ScienceDirect Computational intelligence methods of a safe ship control, *Procedia - Procedia Comput. Sci.* 35 (2014) 634–643.
13. Lisowski, J.: THE SENSITIVITY OF STATE DIFFERENTIAL GAME VESSEL TRAFFIC MODEL, *POLISH Marit. Res.* 2 (2016) 14–18.
14. Mannarini, G., G. Coppini, P. Oddo, N. Pinardi: A Prototype of Ship Routing Decision Support System for an Operational Oceanographic Service, *TransNav, Int. J. Mar. Navig. Saf. Sea Transp.* 7 (2013) 53–59.
15. Naus, K., M. Wąz: The idea of using the A* algorithm for route planning an unmanned vehicle “Edredon,” *Zesz. Nauk. / Akad. Morska W Szczecinie.* (2013) 143--147.
16. Neumann, T.: Method of Path Selection in the Graph - Case Study, *TransNav, Int. J. Mar. Navig. Saf. Sea Transp.* 8 (2014) 557–562.
17. Niklas, K., J. Kozak: Experimental investigation of Steel-Concrete-Polymer composite barrier for the ship internal tank construction, *Ocean Eng.* 111 (2016) 449–460.
18. Philpott, A., A. Mason: Optimising yacht routes under uncertainty, *Proc. 15th Chesap. Sail. Yacht Symp. Annapolis, MD.* (2001).
19. Philpott, a B., I.M. Viola, R.G.J. Flay: Optimal Yacht Routing Tactics, *Innovsail.* (2013) 231–237.
20. Salvesen, N., E. Tuck, O. Faltinsen: Vessel motions and sea loads, *Trans. SNAME.* 78 (1970) 250–287.
21. Specht, C., A. Weintrit, M. Specht, Y. Wo: A History of Maritime Radio- Navigation Positioning Systems used in Poland, (2017).
22. Stelzer, R., K. Jafarmadar: The robotic sailing boat asv roboat as a maritime research platform, *Proc. 22nd Int. HISWA Symp. Yacht Des. Yacht Constr.* (2012).
23. Szłapczyńska, J.: Multi-objective Weather Routing with Customised Criteria and Constraints, *J. Navig.* 68 (2015) 338–354.
24. Szłapczyński, R., M. Życzkowski: Multi-objective weather routing of sailing vessels, *Polish Marit. Res.* 24 (2017) 10–17.
25. Tagliaferri, F., I.M. Viola: A real-time strategy-decision program for sailing yacht races, (2017).
26. Wawrzyński, W., P. Krata: METHOD FOR SHIP’S

ROLLING PERIOD PREDICTION WITH REGARD TO
NON-LINEARITY OF GZ CURVE, J. Theor. Appl. Mech.
54 (2016) 1329–1343.

27. Weintrit, A., P. Kopacz: Computational Algorithms Implemented in Marine Navigation Electronic Systems, in: Springer, Berlin, Heidelberg, 2012: pp. 148–158.
28. Wiśniewski, B.: Programowanie tras statków na oceanach, Zesz. Nauk. / Akad. Morska W Szczecinie. 29 (2012) 164–173.
29. Życzkowski, M.: Sailing Vessel Routing Considering Safety Zone and Penalty Time for Altering Course, TransNav, Int. J. Mar. Navig. Saf. Sea Transp. 11 (2017) 49–54.
30. MAXSURF Design & Analysis Software - Home, (2017).
31. ORC - World Leader in Rating Technology, (2017).

CONTACT WITH THE AUTHOR

Marcin Życzkowski

e-mail: marzyczk@pg.edu.pl

Gdańsk University of Technology
11/12 Narutowicza St.
80 - 233 Gdańsk
POLAND

CORRECTION OF NAVIGATIONAL INFORMATION SUPPLIED TO BIOMIMETIC AUTONOMOUS UNDERWATER VEHICLE

Tomasz Praczyk

Polish Naval Academy, Gdynia, Poland

ABSTRACT

In order to autonomously transfer from one point of the environment to the other, Autonomous Underwater Vehicles (AUV) need a navigational system. While navigating underwater the vehicles usually use a dead reckoning method which calculates vehicle movement on the basis of the information about velocity (sometimes also acceleration) and course (heading) provided by on-board devices like Doppler Velocity Logs and Fibre Optical Gyroscopes. Due to inaccuracies of the devices and the influence of environmental forces, the position generated by the dead reckoning navigational system (DRNS) is not free from errors, moreover the errors grow exponentially in time. The problem becomes even more serious when we deal with small AUVs which do not have any speedometer on board and whose course measurement device is inaccurate. To improve indications of the DRNS the vehicle can emerge onto the surface from time to time, record its GPS position, and measure position error which can be further used to estimate environmental influence and inaccuracies caused by mechanisms of the vehicle. This paper reports simulation tests which were performed to determine the most effective method for correction of DRNS designed for a real Biomimetic AUV.

Keywords: underwater navigation, odometry, underwater vehicle

INTRODUCTION

To make Autonomous Underwater Vehicle (AUV) [15] capable of acting without an external support it has to be equipped with systems which ensure its operational independence. To decide about actions which has to be taken to achieve a desired goal, the vehicle has to be supplied with information describing the state of the vehicle and its surrounding. The fundamental information required for safe underwater navigation is that about vehicle position.

To acquire such information in a fully autonomous mode, a dead reckoning is usually used by AUV. Knowing a starting position of the vehicle, its orientation and velocity, the dead

reckoning navigation can estimate motion of the vehicle, and in consequence, its position. To measure orientation, compasses, Inertial Navigational Systems (INS), and Fibre Optical Gyroscopes (FOG) can be applied. In turn, velocity in the underwater environment is measured by using logs. There are different types of logs, namely, mechanical, electromagnetic, pressure, and Doppler logs which differ in accuracy and size. Electromagnetic ones seem to be the smallest in size, however, they are rather inapplicable to lower speeds of underwater vehicles. The same applies to mechanical logs. The Doppler logs are very precise, even for low speeds, moreover they measure velocity with respect to the seabed, which means that they take sea current into

account in their measurements. Their drawback is, however, large cost and size which make them impractical in use on board of small vehicles.

An alternative solution for logs, especially for small vehicles like those presented in Fig. 1, is odometry. It estimates momentary velocity of the vehicle on the basis of the information from its control system. When the vehicle has a limited number of motion modes (or motion patterns), e.g. fast sharp turn, slow sharp turn, slow gentle turn, slow move ahead, submerge vertically, average speed of the vehicle in each mode may be measured and then used for position calculation.

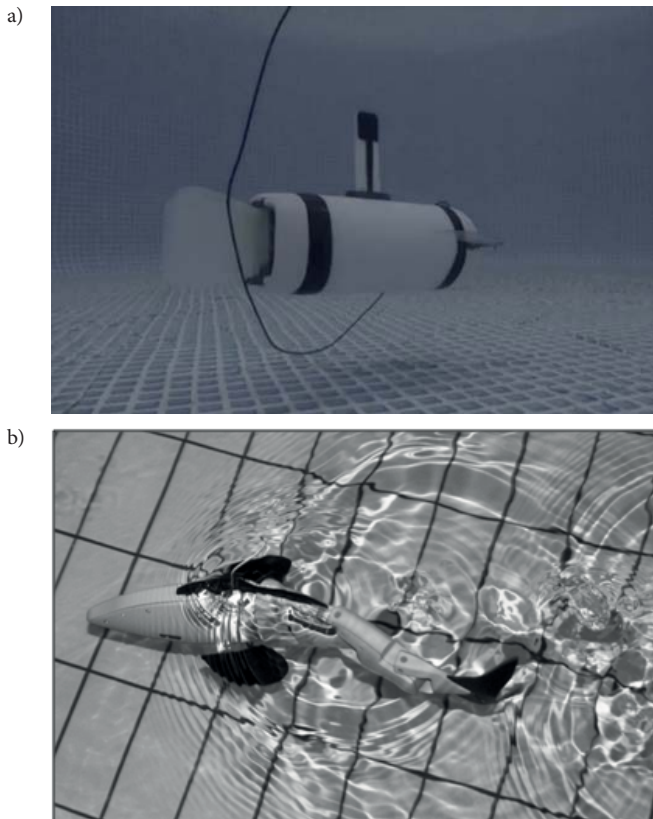


Fig. 1 Small biomimetic vehicles, (a) – AUV called CyberSeal, (b) – Remotely Operated Vehicle called CyberFish [11]

All the above mentioned solutions, regardless of the applied device technology, produce a position error which depends on three factors:

- the accuracy of the orientation and velocity (provided by the above mentioned navigational devices),
- vehicle controllers (velocity, depth and course controller) whose task is to maintain desired vehicle parameters, and
- environmental factors, of a random nature, e.g. the sea current. To improve the accuracy of position produced by a dead reckoning navigational system (DRNS), we can try to estimate all the above specified factors and take them into account while calculating vehicle position. To this end, the vehicle can emerge onto the surface from time to time, record its GPS position, determine position error, and finally use it to estimate all forces which affect the error.

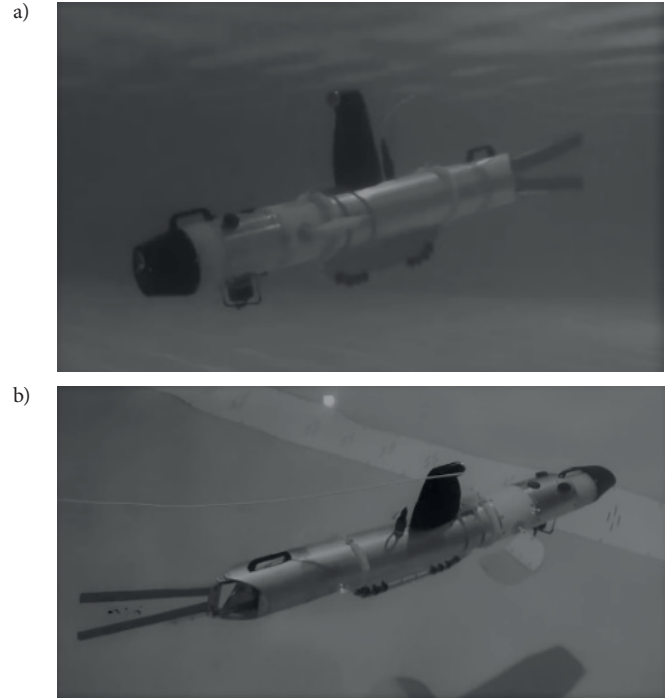


Fig. 2 BAUV used in experiments in the pool

To verify usefulness of this approach for the Biomimetic Autonomous Underwater Vehicle (BAUV) (see Fig. 2) being designed within the project titled “Autonomous underwater vehicles with silent undulating propulsion for underwater ISR”, and financed by Polish National Centre of Research and Development [13,14,16,17], simulation tests were carried out whose results are presented in this paper. Application of a correction system for BAUV DRNS appeared to be necessary during initial tests in a 25 m swimming pool. The vehicle is equipped with only two navigational devices, i.e. a digital compass to measure course and pressure sensor used to sense depth. There is no device to measure speed which is determined by means of odometry. The consequence is that accuracy of the DRNS is inadequate with respect to tasks imposed on the BAUV. Example wrong locations of the BAUV in the swimming pool, determined by DRNS are depicted in Fig. 3, the straight lines indicate simultaneously a desired path of the vehicle and left and upper edges of the pool. In spite of the fact that the vehicle is inside the pool, the DRNS indicates something else.

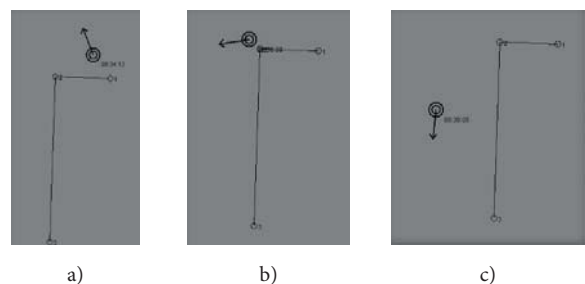


Fig. 3 Example location of BAUV during experiments in the pool

The rest of the paper is organized as follows: Section 2 is a short review of the presented work, Section 3 is a description of position correction method applied to the simulations, Section 4 is a report from the experiments, and the final section is a summary.

CONSIDERED WORK

According to [8,10] underwater navigation has generally two main approaches, namely: dead reckoning, and acoustic. In the dead reckoning navigation [1,3,12] we deal with three main components, i.e. sensors, kinematic model of underwater vehicle, and vehicle state estimation method. The estimation method, typically, family of Extended Kalman Filters (EKF) [5] or Unscented Kalman Filters (UKF) [7,18], but also Particle Filters [2,4], is supplied with the vehicle model and sensor outputs (observations) and produces estimations of vehicle state vector including at least position of the vehicle in a chosen coordinate system. The sensors provide information about orientation of the vehicle (INSSs, digital compasses, FOGs), depth (pressure sensors), velocities (logs) and sometimes also accelerations (INSSs). The more information from the sensors and the more accurate it is, the more accurate the estimations. Of course, the same applies to kinematic model of the vehicle.

When estimations are performed basing on reliable information about spatial orientation and velocity acquired e.g. from optical gyro and Doppler log, moreover, when the vehicle has classical torpedo-shape construction with one rear screw propeller which is equivalent to presence of reliable models of such vehicles, and the sea current is estimated, e.g. basing on historical data or satellite photos, then results of dead reckoning approach are usually satisfactory. However the application of the above discussed approach seems to be impossible in case when the vehicle cannot directly sense its velocity, information about accelerations is available but seriously disturbed (hence it is practically useless at least to accurately estimate velocity), information about the spatial orientation is less accurate than that produced by optical gyros, and moreover, the vehicle itself is highly complicated in terms of construction which results in lack of its reliable model. Unfortunately, this is exactly what we are dealing with in the case of the BAUV.

A separate approach in the dead reckoning navigation is application of visual information about surrounding environment as observations to estimation methods [6,19,20]. However, this approach known as Simultaneous Mapping and Localization (SLAM) requires the vehicle to move close the seabed, and moreover, to have special equipment like sonar or, rarely, a camera.

As mentioned above, the other approach in the underwater navigation is an acoustic stream (Long Baseline, Ultra-short Baseline, and Short Baseline systems - LBL, USBL and SBL) which is generally based on location in relation to sources of an acoustic signal of a known position. The main drawback of this approach is the need to have an additional

infrastructure (except of the vehicle itself) with the effect that it can be only used locally in areas which allow to deploy the system. Of course, the other issue is preparation of the area to work, which requires a time.

CORRECTION OF DRNS

FUNDAMENTALS

DRNS of the BAUV is a navigation system with a school kinematic model of the vehicle in the form of $S = Vt$, where: S – displacement in the horizontal plane, V – a velocity, and t – a time interval. The model is supplied with vehicle progressive speed provided by the odometry, course obtained from a digital compass, and additionally, a vehicle depth - from a pressure sensor. The speed and the course are used to calculate the horizontal displacement and the pressure sensor determines the depth. Simplicity of the vehicle model applied in DRNS results from difficulty in defining more accurate models of such vehicles as the BAUV. It has three independent propellers in the form of fins which, when course and depth controllers are activated, can work in different directions and with a different force, with the effect that e.g. trim (pitch) of the vehicle does not generally reflect change of depth.

The consequence of such very simple vehicle model and its poor equipment is that to apply the dead reckoning approach outlined in the previous section is impossible. Effective usage of the state estimation methods like EKF or UKF requires to confront outputs of the model and sensors. In the simplest case, vehicle orientation along with progressive speed is used in the model to calculate z – coordinate of the vehicle (coordinate towards Earth). At the same time, z – coordinate is also measured by a pressure sensor with the effect that both z – values can be confronted with each other and the whole vehicle state vector produced by the model can be recalculated and improved.

Unfortunately, in the case of the BAUV, we do not have such comfort. The cause is that, as mentioned above, the orientation of the BAUV does not reflect change of depth. In consequence, we cannot estimate z – coordinate based on the measured orientation and odometric speed, compare it with a measured value of z , and finally, improve vehicle position estimated by the model.

However, to improve accuracy of DRNS we can periodically resurface the BAUV to get precise GPS position, roughly estimate all internal and external forces having influence on the vehicle motion and use the estimates (along with other available vehicle state parameters) for position calculation. At the very start of a vehicle mission, DRNS relies only on odometric speed, orientation measured by compass and the depth fixed by a pressure sensor. Then, a correction procedure is performed to estimate the above mentioned forces and use them in calculations of vehicle coordinates xy . The depth

of the vehicle is still fixed by the pressure sensor only. Details of the correction procedure are given in the following section.

FORMULATION

The correction method proposed in this paper and described below is based on the assumption that the correction procedure (CP) is always carried out during BAUV mission. There is no separate CP performed in advance, the BAUV runs the mission and the CP is its integral part.

A perfect situation for the CP would be to perform it in two distinct stages, first, in the area without any influence of the environment or at most with a slight influence, and then in the vehicle operational area. In this case, the objective of the first stage would be to determine inaccuracies resulting from the vehicle itself, whereas the second stage would be dedicated exclusively to estimate influence of environmental factors like the sea current. Unfortunately, a number of tests performed by a project team showed that even lakes which at first glance should be filled with still water, are inadequate for the first stage of CP, as the environmental factors, e.g. the wind, may cause water to move, making the objective of the first stage unattainable.

Moreover, since the vehicle can be used in different regions of the world with different salinity of water, we cannot assume that to adjust its buoyancy to the future operational area would be possible in advance. Since each change in vehicle construction (also in its buoyancy) causes changes in vehicle behaviour, which affect in turn the navigation, a separate CP considering only the vehicle, even in a lake with slight environmental influence, is not a solution which can ensure DRNS adequate accuracy in various operational areas.

In consequence, as mentioned above, the assumption is that the CP is performed just during the mission. The vehicle should emerge from time to time onto the surface for recording GPS position, calculating position error, and then fixing the correction. At the very start of the mission, the influence of both factors on DRNS inaccuracies should be only once estimated, then only environmental factors should be periodically determined, and, as inaccuracies affected by the vehicle are assumed to be invariable, they can be fixed only once. Since estimation of only one factor affecting DRNS inaccuracies is a trivial problem, only CP carried out at the beginning of the mission is considered in this paper. To this end, two different solutions are presented, say: CP1 and CP2, the first one is when CP cannot be a separate part of the mission, hence it has to be performed in the meantime, whereas the second one is when the beginning of the mission is devoted especially to CP, then the main part of the mission starts immediately after realization of the procedure.

But let us start with the formulation of vehicle motion with velocity V_a in x - and y - direction in the time T :

$$S_x = \int_0^T (V_a^x(t) + V_s^x(t))dt + \int_0^T V_c^x(t)dt + \int_0^T V_r^x(t)dt \quad (1)$$

$$S_y = \int_0^T (V_a^y(t) + V_s^y(t))dt + \int_0^T V_c^y(t)dt + \int_0^T V_r^y(t)dt \quad (2)$$

where:

S_x, S_y – displacements of vehicle in x - and y - direction in the time T , or x - and y - coordinates of vehicle originating from the point $x = 0, y = 0$;

V_a^x, V_a^y – x - and y - components of the vehicle velocity V_a measured by vehicle devices (direction) and odometry (magnitude);

V_s^x, V_s^y – x - and y - components of the vehicle velocity error V_s ;

V_c^x, V_c^y – x - and y - components of the sea current velocity V_c ;

V_r^x, V_r^y – x - and y - components of the random velocity V_r .

In Eq. (1) and (2), V_r is assumed to be very small compared to the remaining velocities and, moreover, its direction is random which means that in the long term the influence of V_r on the vehicle can be neglected – as the momentary velocities V_r are assumed to be compensated in the long term. In effect, Eq. (1), (2) can be simplified to the following form:

$$S_x = \int_0^T (V_a^x(t) + V_s^x(t))dt + \int_0^T V_c^x(t)dt \quad (3)$$

$$S_y = \int_0^T (V_a^y(t) + V_s^y(t))dt + \int_0^T V_c^y(t)dt \quad (4)$$

Moreover, if we assume that the move of the vehicle along a desired trajectory takes place between successive way-points with application of course and depth controllers, and the sea current is invariable at a short distance, Eq. (3), (4) for the vehicle moving between two neighboring way-points with the course angle equal to α , can be rewritten as follows:

$$S_y = S_x = (V_a^x + V_s^x + V_c^x)T \quad (5)$$

$$(V_a^x \tan(\psi(\alpha)) + V_s^x \tan(\psi(\alpha + \beta)) + V_c^x)T \quad (6)$$

where:

β – deviation from the course α ;

$$\psi(\theta) = \begin{cases} 90 - \theta & \text{if } \theta \in \langle 0, 180 \rangle \\ 270 - \theta & \text{otherwise} \end{cases} \quad \theta \neq 90, \theta \neq 270$$

Since the BAUV is not equipped with velocity measurement devices, moreover, we cannot also measure other velocities, we assume that all the velocities are constant in all calculations. In this case, V_a is a velocity in direction indicated by the course α and maintained by BAUV course controller. As previously, $|V_a|$ is determined by odometry and it corresponds to some settings of vehicle drive. In this case vehicle compass is used by the controller to maintain the course. Other velocities are also assumed to be constant, V_c is the velocity which is caused mainly by the sea current, at a short distance between two neighboring way-points it has a constant direction and value,

whereas V_s is constant in terms of value and deviated from α by a constant angle β , and it corresponds to all the features of the vehicle (like asymmetry of propellers, compass errors etc) which can have impact on DRNS errors.

The function ψ used in Eq.(6) reduces θ to the range $(0,90)$ and simultaneously determines V_s^y and V_s^x with respect to V_a^x and V_a^y . For example, if $\theta = 60$, then V_s^x and V_a^x act in the same direction and $V_s^y = V_a^x \tan(30)$, whereas, if $\theta = 120$, then $V_s^y = -V_a^x \tan(30)$.

Before the CP, the only values known to the DRNS is V_a and α . In consequence, vehicle motion is described as follows: $S_{x,1} = V_a^x T, S_{y,1} = V_a^x \tan(\psi(\alpha))T$ ("1" means the first way-point). Once the BAUV emerges onto the surface, its GPS position can be recorded and DRNS position error can be calculated, that we denote as $\Delta S_{x,1} = S_{x,GPS} - S_{x,1}$ and $\Delta S_{y,1} = S_{y,GPS} - S_{y,1}$. Assuming that the only velocity which "pushes" the BAUV towards $(S_{x,1}, S_{y,1})$ position is V_a , the remaining velocities are responsible for the error. In consequence, it is sufficient to fix V_s, V_c and β and take them into account when calculating the BAUV position to improve its accuracy. To this end, we have to solve the following system of equations:

$$\Delta S_{x,1} = (V_{s,1}^x + V_{c,1}^x)T_1 \quad (7)$$

$$\Delta S_{y,1} = (V_{s,1}^x \tan(\psi(\alpha_1 + \beta)) + V_{c,1}^y)T_1 \quad (8)$$

$$\Delta S_{x,2} = (V_{s,2}^x + V_{c,2}^x)T_2 \quad (9)$$

$$\Delta S_{y,2} = (V_{s,2}^x \tan(\psi(\alpha_2 + \beta)) + V_{c,2}^y)T_2 \quad (10)$$

Moreover, as $|V_{s,1}| = |V_{s,2}|$ we can also write the following:

$$(V_{s,1}^x)^2 + (V_{s,1}^y)^2 \tan^2(\psi(\alpha_1 + \beta)) = (V_{s,2}^x)^2 + (V_{s,2}^y)^2 \tan^2(\psi(\alpha_2 + \beta)) \quad (11)$$

In both Eq. (7),(8) and Eq.(9),(10) which specify position error in two consecutive way-points, we deal with the velocity V_s which does not change its magnitude but changes direction, and with the velocity V_c which changes its magnitude and does not change direction.

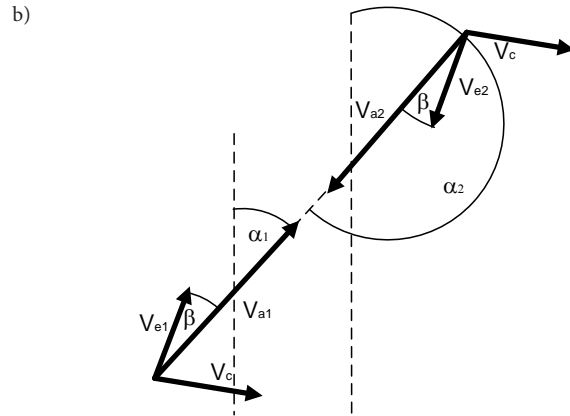
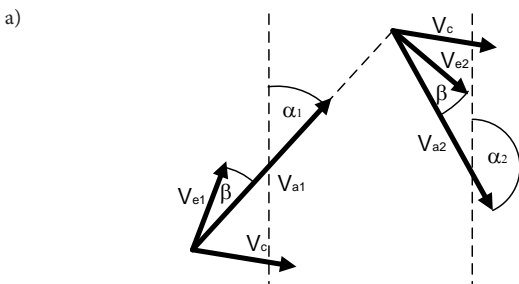


Fig. 4 Illustration of CP1 (a) and CP2 (b)

Direction of V_s is determined by the vehicle course α and deviation β . If the course is different while navigating to both way-points, direction of V_s is in effect also different, whereas the magnitude of V_s is the same in both cases because settings of drive are assumed to be the same during voyage both to way-point No. 1 and 2.

In turn, V_c is generally assumed to not change direction and magnitude, however, in order to take into account a different influence of the sea current on the vehicle hull depending on direction of vehicle course and direction of the current¹, the angle γ between vectors V_c and V_a , and magnitudes of V_c different for different courses α should be taken into consideration.

CORRECTION PROCEDURE NO. 1 - CPI

As mentioned above, the CP1 is based on the assumption that the procedure is performed simultaneously with other vehicle tasks, it does not have the vehicle at its disposal only. The consequence is lack of any limitations for the vehicle course when CP1 is performed in successive way-points (with one exception – see further). The other assumption made for CP1 is neglecting different sea current dynamic features for different courses of the vehicle. As a result, Eq.(7)-(10) are simplified to the form containing $V_{c,1}^x = V_{c,2}^x$ and $V_{c,1}^y = V_{c,2}^y$.

To determine V_s, V_c and β , the CP1 is performed in two phases. First, it calculates V_s and V_c with the assumption that $\beta = 0$. For that purpose, the system of linear equations (7)-(10) is solved. To make it solvable, the above mentioned assumption regarding the courses has to be somewhat relaxed, namely, the courses to way-points No. 1 and 2 cannot be the same and opposite. After the first phase, a simple gradient descent method is used for the following objective function to be minimized:

$$F(V_{s,1}^x, V_{s,2}^x, V_c^x, V_c^y, \beta) = \sum_{i=1}^5 Error_i \quad (12)$$

¹ The influence of the sea current on the vehicle hull is definitely more complex than the paper suggests. However, due to high complexity of the precise current model, for the CP purposes, it was reduced to the form described in the paper.

where

$$\begin{aligned} \text{Error}_1 &= (V_{s,1}^x + V_c^x - \Delta S_{x,1}/T_1)^2, \\ \text{Error}_2 &= (V_{s,1}^x \tan(\psi(\alpha_1 + \beta)) + V_c^y - \Delta S_{y,1}/T_1)^2, \\ \text{Error}_3 &= (V_{s,2}^x + V_c^x - \Delta S_{x,2}/T_2)^2, \\ \text{Error}_4 &= (V_{s,2}^x \tan(\psi(\alpha_2 + \beta)) + V_c^y - \Delta S_{y,2}/T_2)^2, \\ \text{Error}_5 &= (V_{s,1}^x)^2 + (V_{s,1}^x)^2 \tan^2(\psi(\alpha_1 + \beta)) - (V_{s,2}^x)^2 - (V_{s,2}^x)^2 \tan^2(\psi(\alpha_2 + \beta)) \end{aligned}$$

To increase the chance of finding a global optimum of the function (12), the optimization algorithm is repeated from many starting points which differ in value of β . Starting values for V_s and V_c do not change and they are solutions of the linear problem.

The result of the optimization procedure are values $|V_s|$, β , V_c^x and V_c^y which can be then used during vehicle navigation to improve DRNS indications.

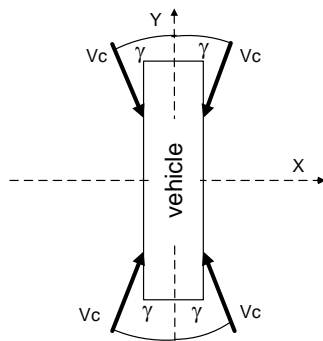


Fig. 5 The same influence of the sea current on vehicle hull for angles γ , $180 - \gamma$, $180 + \gamma$, and $360 - \gamma$

CORRECTION PROCEDURE NO. 2 - CP2

In the case of CP2, the beginning of BAUV mission is devoted exclusively to CP which means that we can adjust operation of the vehicle to the CP. In CP2, it is done by moving the vehicle first along the course $\alpha_1 = 45$ and then along the opposite course $\alpha_2 = 225$. Thanks to that, to determine V_s , V_c and β , it is enough to solve the following simple system of equations:

$$V_{s,1}^x + V_c^x = \frac{\Delta S_{x,1}}{T_1} = A \quad (13)$$

$$V_{s,1}^x \tan(\psi(\alpha_1 + \beta)) + V_c^y = \frac{\Delta S_{y,1}}{T_1} = B \quad (14)$$

$$-V_{s,1}^x + V_c^x = \frac{\Delta S_{x,2}}{T_2} = C \quad (15)$$

$$-V_{s,1}^x \tan(\psi(\alpha_1 + \beta)) + V_c^y = \frac{\Delta S_{y,2}}{T_2} = D \quad (16)$$

In CP2 the same magnitude of V_c in both directions of vehicle motion is also assumed. This assumption results from that the influence of the sea current on the vehicle hull is symmetrical with respect to X - and Y - axes of the vehicle, i.e., it is the same e.g. for the angles of 10, 170, 190 and 350 deg – see Fig. 5.

The solution of Eq. (13)-(16) looks as follows:

$$V_{s,1}^x = \frac{A-C}{2} \quad (17)$$

$$V_c^x = A - \frac{A-C}{2} \quad (18)$$

$$\beta = \arctan\left(\frac{B-D}{A-C}\right) - \alpha_1 \quad (19)$$

$$V_c^y = B - \left(\frac{A-C}{2}\right) \tan\left(\arctan\left(\frac{B-D}{A-C}\right)\right) \quad (20)$$

Of course, knowing $V_{s,1}^x$ and β we can calculate $V_{s,1}^y = V_{s,1}^x \tan(\alpha_1 + \beta)$ and then $|V_s| = \sqrt{(V_{s,1}^x)^2 + (V_{s,1}^y)^2}$ which, along with β , is necessary to determine the influence of V_s on motion of the vehicle in each point of the voyage.

Unfortunately, the velocities V_c^x and V_c^y calculated according to Eq. (13), (14) can be only used for the course α_1 and the opposite course, for other vehicle courses they have to be recalculated. To this end, a simplified model $\xi(V_{c,\alpha_1}^x, V_{c,\alpha_1}^y, \alpha_1, \alpha_2)$ of the sea current influence on the vehicle hull is used. It produces the magnitude $|V_{c,\alpha_2}|$ for any vehicle course α_2 . Since direction of the sea current is assumed to not change V_{c,α_2}^x and V_{c,α_2}^y , it can be then calculated basing on V_{c,α_1}^x , V_{c,α_1}^y and $|V_{c,\alpha_2}|$.

The model ξ is based on the function $\varrho(\gamma)$ which produces the current magnitude $|V_c|$ for any angle γ , i.e. the angle between vehicle course and direction of the sea current. The value generated by ϱ , according to the assumptions made for CP2, is symmetrical with respect to X - and Y - axes of the vehicle, and it corresponds to velocity of the vehicle “Gluptak” (see Fig. 6) equal to 1m/s and velocity of the sea current equal to 0.4 m/s. The vehicle “Gluptak” is a torpedo-shape ROV (Remotely Operated Vehicle) of the size and shape similar to the BAUV.

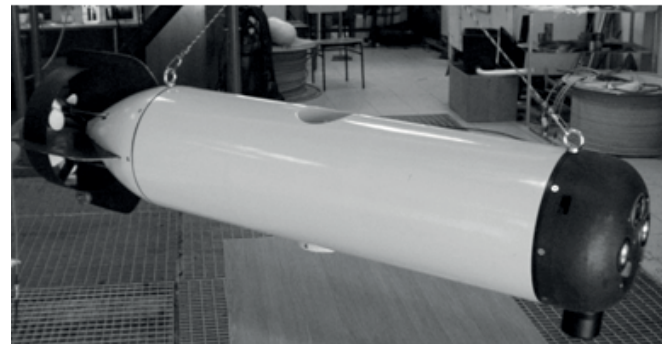


Fig. 6 ROV “Gluptak” [9,21]

To determine the value $|V_c|$ for other velocities, in the model ξ it is assumed that $\frac{\varrho(\gamma_2)}{\varrho(\gamma_1)}$ is constant regardless of vehicle and sea current velocities. The consequence of the above given assumption is possibility of calculating $|V_{c,\alpha_2}|$ for any vehicle course α_2 in the following way:

$$|V_{c,\alpha_2}| = \xi(V_{c,\alpha_1}^x, V_{c,\alpha_1}^y, \alpha_1, \alpha_2) = |V_{c,\alpha_1}| \frac{\varrho(\gamma_2)}{\varrho(\gamma_1)} \quad (21)$$

where :

$\gamma_i = \text{diffCourse}(\text{getCourse360}(V_{c,\alpha_i}^x, V_{c,\alpha_i}^y), \alpha_i)$, $i = 1, 2$, diffCourse is a function that gets difference between courses ranging $\langle 0, 180 \rangle$ deg, whereas function getCourse produces course based on V^x, V^y .

CONSIDERING PRESENCE OF ENVIRONMENTAL FORCES WHEN NAVIGATING TO WAY-POINT

When navigating to a way-point two different strategies can be used. The first one is simply to determine a direct course ν to the way-point and updating it periodically. This strategy is, however, impractical when the vehicle operates in the environment with a serious influence of the current and/or wind. In this case, the vehicle path to the way-point is very far from the optimum one, i.e. the path which leads the vehicle straight from the current vehicle position to the way-point.

The other strategy is to estimate all environmental forces which may have influence on the vehicle motion and to take them into account when determining the vehicle course α to the way-point. In the case of CP1, to calculate the course the following system of equations is solved²:

$$\frac{V_a^x + V_{c,CP}^x}{V_a^y + V_{c,CP}^y} = \tan(\vartheta(\nu)) \quad (22)$$

$$(V_a^x)^2 + (V_a^y)^2 = |V_{a,CP}|^2 \quad (23)$$

where ;

V_a^x, V_a^y - x - and y - velocities of vehicle which together with sea current velocities lead vehicle along desired course ν , in the velocities the deviation β is not considered,

$V_{c,CP}^x, V_{c,CP}^y$ - x - and y - components of the velocity V_c , estimated by CP,

ϑ - a function transforming course ν to the range $\langle 0, 90 \rangle$,

ν - direct course from a given position of vehicle to way-point, which does not correspond to the vehicle course α ,

$V_{a,CP}$ - vehicle velocity magnitude after CP, which is defined as follows:

$$V_{a,CP} = \left(\text{getVelocityX}(|V_{c,CP}|, \beta_{CP}) \right)^2 + \left(V_a + \text{getVelocityY}(|V_{c,CP}|, \beta_{CP}) \right)^2 \quad (24)$$

² The system of Eq.(22), (23) is used only for $\nu \in \{0, 90, 180, 270\}$, e.g. for $\nu = 0$: $V_a^x = -V_{c,CP}^x$ and $V_a^y = (V_a)^2 - (V_{c,CP}^y)^2$

where:

$\text{getVelocityX}(W, Z)$ and $\text{getVelocityY}(W, Z)$ are functions which produce x - and y - components of a vector determined by the length W and the direction $Z \in \langle -180, 180 \rangle$.

The system of Eq.(22), (23) has four different solutions of V_a^x, V_a^y , in total. The correct solution is the one which leads the vehicle along the course ν with the highest resulting velocity. After determining the correct values of V_a^x, V_a^y , the vehicle course is calculated according to Eq.(25), and then improved according to Eq. (26):

$$\alpha = \text{getCourse360}(V_a^x, V_a^y) \quad (25)$$

$$\alpha = \alpha - \text{getCourse180}(U_1, U_2) \quad (26)$$

where:

$$U_1 = \text{getVelocityX}(|V_{c,CP}|, \beta_{CP}),$$

$$U_2 = \text{getVelocityY}(|V_{c,CP}|, \beta_{CP}),$$

and $\text{getCourse180}(V_x, V_y)$ is a function which determines direction of the vector V expressed in the range $\langle -180, 180 \rangle$ deg, V_x and V_y are x - and y - components of V .

In the case of CP2, another approach is used. Since in case of Eq. (22), (23) it is necessary to know $V_{c,CP}^x, V_{c,CP}^y$ to determine α which, according to Eq.(21), cannot be estimated as long as α is unknown, CP2 is performed in three phases to fix course of the vehicle. First, Eq.(22), (23) are used to estimate $V_{c,CP}^x, V_{c,CP}^y$ for $\alpha=45$ deg, then Eq.(21) is applied to improve the estimations, and finally, procedure of solving Eq. (22), (23) is run again to fix final value of α .

EXPERIMENTS

CONDITIONS OF EXPERIMENTS

To test what improvement of position accuracy can be achieved when using CP, simulation experiments were carried out. In the experiments, motion of the vehicle was calculated in three different ways. The pattern motion to be used as a point of reference for DRNS was computed as follows:

$$S_{x,j,GPS} = \sum_{i=1}^N (V_{a,j}^x + V_{s,j}^x + V_{c,i}^x + V_{r,j,i}^x) t \quad (27)$$

$$S_{y,j,GPS} = \sum_{i=1}^N (V_{a,j}^y \tan(\psi(\alpha_j)) + V_{s,j}^y \tan(\psi(\alpha_j + \beta)) + V_{c,i}^y + V_{r,j,i}^y) t \quad (28)$$

where :

i - i -th time step during motion toward j -th way-point;

j - number of way-point;

t - time interval;

N - number of steps necessary to reach way-point;

V_r^x, V_r^y - random values such that $|V_r| \in \langle 0, r_{max} \rangle$, direction of V_r ranges $\langle 0, 359 \rangle$.

Eq. (27), (28), reflect determinism of the vehicle and randomness of the environment, the velocities V_a , V_e representing the vehicle are constant during each run of simulation, whereas, V_c , and V_r are random variables. It is assumed that the vehicle is a deterministic device with a known desired speed and course represented by V_a and with an unknown deterministic working inaccuracy represented by V_e . On the other hand, the environment is random and partly unpredictable which is reflected in V_c and V_r .

V_c represents mainly the sea current and wind, so, environmental forces whose characteristic is, on the one hand, of a random nature, but on the other hand, it determines a dominant direction α_c and magnitude $|V_c|$ which are parameters of simulation. Value of $V_{c,i}$ is fixed in two stages. First, magnitude of V_c is adjusted to the vehicle course α_j and the deviation from the course β ; and the following formula is used for this purpose:

$$|V_{c,i,\alpha_j+\beta}| = |V_c| \varrho_s(\text{diffCourse}(\alpha_j + \beta, \alpha_c)) / \varrho_s(\alpha_c) \quad (29)$$

where ϱ_s is variant of the function ϱ which is symmetrical only with respect to axis Y of the vehicle, which means that $V_{c,i}$ is the same, e.g. for 10 and -10 (or 350) deg, and different at the same time for 10 and 170 degrees. The consequence is that ϱ_s more exactly reflects the influence of the sea current on vehicle hull than ϱ .

In the second stage, both the direction and magnitude of $V_{c,i}$ are randomly deviated according to the normal distribution with parameters $N(|V_{c,i,\alpha_j+\beta}|, \sigma_v^2)$, and $N(\alpha_c, \sigma^2)$.

The same deviation is used for the number N_d of steps i , where N_d is a random variable uniformly distributed within $(1, N_{d,max})$ range.

In turn, V_r represents all other possible environmental random factors that can affect motion of the vehicle and for that reason it is completely chaotic. Direction of V_r is uniformly distributed within $(0, 359)$ range, whereas $|V_r|$ is a random uniform value in the range of $(0, r_{max})$, where r_{max} is a parameter of simulation which is a fraction of V_a .

The estimated motion without CP was determined in the following way:

$$S_{x,j,noCP} = \sum_{i=1}^N V_{a,j}^x t \quad (30)$$

$$S_{y,j,noCP} = \sum_{i=1}^N V_{a,j}^x \tan(\psi(\alpha_j)) t \quad (31)$$

which means that S_{noCP} is calculated on the basis of only a desired vehicle velocity $|V_a|$ and course α , which are provided to the vehicle course controller and the vehicle drive.

The estimated motion after CP looks, in turn, as follows:

$$S_{x,j,CP} = \sum_{i=1}^N (V_{a,j}^x + V_{e,j,CP}^x + V_{c,CP}^x) t \quad (32)$$

$$S_{y,j,CP} = \sum_{i=1}^N (V_{a,j}^x \tan(\psi(\alpha_j)) + V_{e,j,CP}^x \tan(\psi(\alpha_j + \beta_{CP})) + V_{c,CP}^y) t \quad (33)$$

where $|V_{e,CP}^x|$, β_{CP} , $V_{c,CP}^x$, and $V_{c,CP}^y$ are the result of applying CP for $\Delta S_{x,i} = S_{x,i,noCP} - S_{x,i,GPS}$, and $\Delta S_{y,j} = S_{y,j,noCP} - S_{y,j,GPS}$ $i = 1, 2$. In all the simulations, the assumption was made that $\beta \in (-90, 90)$. In consequence, to consider the fact that V_e can increase or decrease progressive speed of the vehicle, V_e must be able to change sign, i.e. to be positive or negative. To determine sign of $V_{e,CP}$, which together with $|V_{e,CP}|$ and β_{CP} is necessary to perform CP, the following simple formula was used:

$$\text{sign}(V_{e,CP}^x, V_{e,CP}^y, \alpha) = \begin{cases} (+) & \text{if } U_3 < 90 \\ (-) & \text{otherwise} \end{cases} \quad (34)$$

where :

$$U_3 = \text{diffCourse}(\text{getCours360}(V_{e,CP}^x, V_{e,CP}^y), \alpha).$$

After the CP simulations additional tests were also carried out to verify effectiveness of the method for determining vehicle course in conditions of presence of forces which can affect vehicle movement (Section 3.5). Conditions of the tests were the same as those described above. The only difference was that α was not the course to way-point but the course calculated according to Eq. (22)-(26).

In order to test CP1, CP2 and their influence on accuracy of the DRNS, a virtual vehicle with the motion model defined by Eq. (27), (28) performed thirty missions for each type of CP and each parameter setting. In each mission the vehicle was moved along a trajectory including 3 way-points. The distance between the way-points was always equal to 100 m, whereas the course between them was completely random for CP1 and partly random for CP2. In the former case, course to the first way-point was equal to 45 deg, whereas to the second one 225 deg. Regardless of the correction method being tested, the vehicle, when moving to the first of the two way-points, used DRNS which operated according to Eq. (30), (31). Once the vehicle approached the second way-point it performed the CP and changed DRNS operation to that based on Eq.(32), (33).

The characteristics of CP1 is two-phase determination of $|V_{e,CP}|$, β_{CP} , sign of $V_{e,CP}$, $V_{c,CP}^x$, and $V_{c,CP}^y$. In the first phase, β_{CP} was assumed to be zero and the remaining parameters were fixed according to Eq. (7)-(10). Afterwards, in the second phase, the gradient descent of the function (12) was applied to determine all the parameters. Initial values for gradient descent were the ones calculated in the first phase and, additionally, a value of $\beta_{CP} = -\beta_{CP}^{max}, -\beta_{CP}^{max} + 1, \dots, 0, \dots, \beta_{CP}^{max} - 1, \beta_{CP}^{max}$.

CP2 was also performed in two phases: first, Eq. (17)-(20) was used to determine vehicle inaccuracies – both in velocity direction and magnitude, and to estimate direction and magnitude of environmental forces, then Eq. (21) was applied to tune the before estimated magnitude.

In addition to the vehicle trajectory, individual missions differed also in parameter setting. The following parameter values were applied: $t = 0.001s$, $V_a = 1$

m/s, $V_a = \{-0.3, -0.1, 0.1, 0.3\}$ m/s, $\beta = \{-20, -5, 5, 20\}$ deg, $\alpha_c = 20$ deg, $|V_c| = \{0.1, 0.5\}$ m/s, $r_{max} = 0.3$ m/s, $\beta_{CP}^{max} = 20$ deg, $\sigma_V^2 = 0.02$, $\sigma_\alpha^2 = 10$, $N_{d,max} = 10000$.

In the experiments the assumption was made that vehicle inaccuracies cannot be very high due to application of course and depth controllers. For this reason, the tested values of β were not greater than ± 20 deg, whereas, the magnitude of V_g was at the most equal to ± 0.3 m/s. During all the tests the sea current was assumed to have the same direction, i.e. equal to 20° deg. The magnitude of the current velocity did not exceeded 0.5 m/s, i.e. only a half of the vehicle velocity. The remaining parameters of the simulation, i.e. parameters which determine their randomness were fixed so that they could not dominate results of the simulation.

RESULTS OF EXPERIMENTS

Results of all the tests are given in Tab. 1-3 which include only the ones for $r_{max} = 0.3$ and positive values of β and V_g . The reason is that simulations with $r_{max} = 0.1$ and negative values of β and V_g produced very similar outcomes.

Tab. 1. Average errors [m] occurred along 100 m distance

		$ V_g = 0.1$		$ V_g = 0.3$	
		$ V_c = 0.1$	$ V_c = 0.5$	$ V_c = 0.1$	$ V_c = 0.5$
without CP		12.84	47.96	31.1	43.19
$\beta = 5$	CP1	2.58	10.9	2.45	11.4
	CP2	1.17	4.68	0.93	4.42
$\beta = 20$	CP1	3.39	8.33	2.51	10.6
	CP2	1.21	4.57	1.01	5.4

Tab. 2. Maximum errors [m] occurred along 100 m distance

		$ V_g = 0.1$		$ V_g = 0.3$	
		$ V_c = 0.1$	$ V_c = 0.5$	$ V_c = 0.1$	$ V_c = 0.5$
without CP		18.83	58.7	38.61	74.92
$\beta = 5$	CP1	6.07	35.64	15.69	28.69
	CP2	2.74	11.57	1.87	10.92
$\beta = 20$	CP1	15.89	19.51	8.77	43.12
	CP2	2.24	11.04	2.49	9.46

Tab. 3. Average deviation from desired course, [deg], with and without applying the method specified in Section 3.5

		$ V_g = 0.1$		$ V_g = 0.3$	
		$ V_c = 0.1$	$ V_c = 0.5$	$ V_c = 0.1$	$ V_c = 0.5$
without CP		4.77	13.29	4.68	16.52
$\beta = 5$	CP1	0.73	2.92	0.65	3.45
	CP2	0.46	2.31	0.25	2.4
$\beta = 20$	CP1	0.99	2.7	0.63	4.04
	CP2	0.48	3.34	0.29	2.2

Generally, as expected, the simulations showed that CP added to the DRNS improves its accuracy, moreover, in some cases the improved accuracy was even thirty-fold greater (Tab. 1, the result for CP2, $\beta = 5$, $|V_g| = 0.3$, $|V_c| = 0.1$). Tab. 2 shows that in conditions with a stronger influence of the environment ($|V_c| = 0.5$) the neglecting of correction may

even result in the error of 70 m in value which is almost the whole distance covered by the vehicle between way-points. This means that CP embedded in DRNS is a necessary condition for applying BAUV at sea. When the vehicle is not equipped with such devices like log which can provide more precise navigational information mainly about velocity of the sea current, CP can be the only way to make the vehicle capable of operating at sea. Relying only on resetting position of the vehicle to GPS position, when only it is available, seems to be definitely insufficient, particularly when distance between way-points is large. In such case, safety of the vehicle would require it to appear very frequently on the surface to record GPS position. The CP enables the vehicle to cover longer distances beneath the surface, without necessity to frequently correct the position by means of GPS.

When comparing CP1 and CP2 it is clear that CP2 outperforms CP1 as in all cases positions corrected by CP2 are more accurate than those obtained with CP1. Of course, it is not a surprising result which is mainly due to the fact assumed in CP1 that the environmental forces are constant regardless of mutual arrangement of velocity vectors representing the vehicle and the environment. However, in spite of the fact that CP2 outperforms CP1, the influence of the latter on position accuracy is definitely positive compared to the case without CP. In this case (except of that with $V_c = 0.1$ and $V_g = 0.3$) the average improvement of the accuracy is approximately four-fold greater. Generally, the results of CP1 mean that at the position error not exceeding 100 m in the worst case, the vehicle can cover a bit greater distance than 200 m (the maximum error for CP1 = 43.12 m), however, in the average case, it is almost 1000 m distance covered without appearing on the surface on the assumption that the sea current is invariable on the distance.

The results of CP2 are the most promising. As mentioned above, in this case, the largest average improvement of position accuracy is even thirty-fold greater compared to situation without CP. In the remaining cases, it is more or less tenfold greater with the effect that when the position error not to exceed 100 m in the worst case, the vehicle can cover almost 1000 m distance, however, in the average case, it is as long as 2000 m voyage without emerging. As previously, such result is achievable provided that the sea current is invariable in vehicle operational area.

Tab. 3 shows results of the additional simulations whose goal was to test how information from the CP can improve quality of vehicle path to a way-point. Typically, the vehicle course corresponds to a direct course to the way-point, which under the conditions of the sea current, wind, and inaccuracies coming from the vehicle itself, may result in a path very far from the optimum one. However, when DRNS is supplied with additional information about possible sources of inaccuracies it can use this information to fix the course of the vehicle in a more optimum manner e.g. that presented in Section 3.5.

The simulation results given in Tab. 3 showed to what extend application of the information from CP can smooth out the vehicle path. At small influence of external factors,

the improvement of vehicle course compared to the optimum one, i.e. the course leading vehicle directly to a way-point, is almost invisible. However for $V_c = 0.5$ the improvement is even eight-fold greater.

SUMMARY

Underwater navigation of underwater vehicles without devices which provide precise navigational information about course and velocity with respect to Earth is a highly challenging problem which particularly affects small underwater units unable, because of their size, to carry large navigational instruments. One solution of the problem is the use of Simultaneous Localization and Mapping (SLAM), however, it requires moving the vehicle over a short distance from the sea bottom in order to refer position of the vehicle to position of visible landmarks.

When navigation close to the bottom is impossible the only method which can be applied to improve precision of underwater navigation is estimation of all unknown forces having influence on vehicle motion and taking them into account during calculations. This paper presented two solutions which can be applied for that purpose. In them it is assumed that two factors can affect all inaccuracies which can appear during underwater navigation, namely, external factors like wind and sea current which are jointly called environmental factors, and vehicle internal factors such as inaccuracies caused by lack of symmetry in vehicle drive, systematic compass errors etc. To estimate their influence on vehicle motion, GPS position has to be recorded from time to time and position error to be determined. The problem is, however, what position accuracy can be achieved by applying estimates fixed in this manner. Answer to this question is a very important issue because it may decide about distance which the vehicle can safely cover before it has to rise to the surface for taking GPS position.

The presented paper which is the report on simulation tests, offers the first step to answering that question. The tests revealed that estimation methods presented in the paper can significantly improve operation of underwater navigation. The results of the simulation showed that, under stable conditions of the sea current and wind, the vehicle can safely move beneath the surface over the distance as long as 1000 m and even 2000 m - in favorable conditions.

Of course, this result is based on the rather unrealistic assumption that the sea current and other environmental forces are invariable over greater areas of the sea. In the performed simulations the current could change both the direction and magnitude, however, the changes incorporated into the sea current model, introduced only slight random perturbation characteristics to the current with stable parameters. Unfortunately, lack of any device for measuring parameters of external forces affecting motion of the vehicle makes it impossible to effectively counteract the forces of variable nature. However, we always know where the vehicle has to operate and thereby we also know properties

of the future operational area with the effect that we can appropriately adjust its navigational system to the operational area in question. Variability of the sea current in a considered area results in necessity of more frequent emerging onto the surface, whereas, the opposite situation leads to a longer distance which the vehicle can cover underwater.

The other problem is reliability of course information acquired from different sorts of compasses as well as accessibility of reliable GPS signal for supporting the dead reckoning navigation. Contemporary digital compasses even the cheapest ones, if appropriately mounted far away from all sources of magnetic field, seem to be sufficiently accurate and thereby they should not have considerable negative influence on quality of navigational system. Unavailability of GPS signal is a more serious problem. When the vehicle operates in GPS-denied or GPS-inhibited environment, it is necessary to provide it with other source of pattern navigational information to reduce position error of the dead reckoning. One solution can be e.g. an optical system with the ability of identifying landmarks visible on the coast and to use them to estimate the vehicle position. Unfortunately, according to the knowledge of this author, such solution is still an undiscovered area in the marine technology, remaining therefore an attractive field for further research.

BIBLIOGRAPHY

1. B. Allotta, A. Caiti, L. Chisci, R. Costanzi, F. Di Corato, C. Fantacci, D. Fenucci, E. Meli, A. Ridolfi : Development of a Navigation Algorithm for Autonomous Underwater Vehicles. IFAC-PapersOnLine, Vol. 48, Is. 2, 2015, pp. 64-69
2. S. Arulampalam, S. Maskell, N. Gordon and T. Clapp: A tutorial on particle filters for on-line non-linear/non-Gaussian Bayesian tracking. IEEE Trans, Signal Processing, 50 (2), 2002, pp. 174-188
3. D. Li, D. Ji, J. Liu, Y. Lin : A Multi-Model EKF Integrated Navigation Algorithm for Deep Water AUV. International Journal of Advanced Robotic Systems, Vol. 13, Is. 1, 2016
4. A. Doucet, N. de Freitas, N. Gordon: Sequential Monte Carlo methods in practice. Statistics for Engineering and Information Science. Springer-Verlag, New York, 2001
5. G. Einicke, L. White: Robust Extended Kalman Filtering. IEEE Trans. Signal Processing. 47 (9), 1999, pp. 2596-2599
6. H. Johnnsson, M. Kaess, B. Englot, F. Hover, JJ. Leonard: Imaging Sonar-Aided Navigation for Autonomous Underwater Harbor Surveillance. 2010 IEEE/RSJ International Conference on Intelligent Robots and Systems, 2010, pp. 4396 - 4403
7. S. Julier, J. Uhlmann : Unscented filtering and nonlinear estimation. Proc. of the IEEE, 92, 2004, pp. 401-422.

8. J. Kinsey, R. Eustice, L. Whitcomb: A survey of underwater vehicle navigation: recent advances and new challenges. In Proc. Conf. Maneuvering Control Marine Craft. 2006, pp. 1-12
9. T. Leszczynski : The effect of interference parameters on the exploitation capabilities of an underwater vehicle . Scientific Journal of Polish Naval Academy, 3(26), 2016, pp. 85-106
10. L. Paull, S. Saeedi, M. Seto, H. Li : AUV Navigation and Localization: A Review. IEEE Journal of Oceanic Engineering, Volume: 39, Issue: 1, 2014, pp. 131 – 149
11. M. Malec, M. Morawski, and J. Zając: Fish-like swimming prototype of mobile underwater robot. Journal of Automation, Mobile Robotics and Intelligent Systems, Vol. 4, No. 3, 2010, pp. 25-30
12. A. Martinez, L. Hernandez, H. Sahli, Y. Valeriano-Medina, M. Orozco-Montegudo, D. Garcia-Garcia : Model-Aided Navigation with Sea Current Estimation for an Autonomous Underwater Vehicle. International Journal of Advanced Robotic Systems, Vol.12, Is. 7, DOI: <https://doi.org/10.5772/60415>
13. T. Praczyk : A quick algorithm for planning a path for biomimetic autonomous underwater vehicle. Scientific Journals of Maritime University of Szczecin, No. 45 (117), 2016, pp. 23-28
14. T. Praczyk : Using Genetic Algorithms for Optimizing Algorithmic Control System of Biomimetic Underwater Vehicle. Computational Methods in Science and Technology (CMST), Vol. 21 (4) 2015, pp. 251-260
15. R. Siegwart, I. R. Nourbakhsh : Introduction to Autonomous Mobile Robots. MIT Press, Cambridge 2004
16. P. Szymak, T. Praczyk, K. Naus, M. Malec, M. Morawski : Research on biomimetic underwater vehicles for underwater ISR. Ground/Air Multisensor Interoperability, Integration, and Networking for Persistent ISR VII, edited by Michael A. Kolodny, Tien Pham, Proc. of SPIE Vol. 9831, 98310K
17. P. Szymak, M. Malec, M. Morawski : Directions of development of underwater vehicle with undulating propulsion. Polish Journal of Environmental Studies, Hard Publishing Company, Vol.19, No. 3, Olsztyn 2010, pp. 107-110
18. E. Wan, R. Merwe : The Unscented Kalman Filter. T. Haykin Edition, New York, NY, USA, 2001
19. W. Zeng, L. Wan, T. Zhang : Simultaneous localization and mapping of autonomous underwater vehicle using looking forward sonar. Journal of Shanghai Jiaotong University (Science), Vol. 17, 2012 , Is. 1, pp 91-97,
20. T. Zhang, W. Zeng, and L. Wan : Underwater simultaneous localization and mapping based on forward-looking sonar. Journal of Marine Science and Application, (2011) pp.10:371. doi:10.1007/s11804-011-1082-1
21. <http://cmtm.pg.gda.pl/systemy-techniki-glebinowej>

CONTACT WITH THE AUTHOR

Tomasz Praczyk

e-mail: t.praczyk@amw.gdynia.pl
 Polish Naval Academy
 Institute of Naval Weapon
 Śmidowicza 69, 81-127 Gdynia
POLAND

ANALYSIS OF VENTILATION REGIMES OF THE OBLIQUE WEDGE-SHAPED SURFACE PIERCING HYDROFOIL DURING INITIAL WATER ENTRY PROCESS

Parviz Ghadimi

Nasrin Javanmardi

Amirkabir University of Technology, Tehran, Islamic Republic of Iran

ABSTRACT

The suction side of a surface piercing hydrofoil, as a section of a Surface Piercing Propeller (SPP), is usually exposed to three phases of flow consisting air, water, and vapour. Hence, ventilation and cavitation pattern of such section during the initial phase of water entry plays an essential role for the propeller's operational curves. Accordingly, in the current paper a numerical simulation of a simple surface piercing hydrofoil in the form of an oblique wedge is conducted in three-phase environment by using the coupled URANS and VOF equations. The obtained results are validated against water entry experiments and super-cavitation tunnel test data. The resulting pressure curves and free surface profiles of the wedge water entry are presented for different velocity ratios ranging from 0.12 to 0.64. Non-dimensional forces and efficiency relations are defined in order to present the wedge water entry characteristics. Congruent patterns are observed between the performance curves of the propeller and the wedge in different fully ventilated or partially cavitated operation modes. The transition trend from fully ventilated to partially cavitated operation of the surface piercing section of a SPP is studied and analyzed through wedge's performance during the transitional period.

Keywords: emi-submerged propeller; wedge water entry; ventilation pattern; free surface profile.

NOMENCLATURE

Independent Variables:	
D	Propeller diameter (m)
β	Wedge dead-rise angle
n	Shaft rotational speed(1/s)
U	Inlet flow velocity (m/s)
V	Wedge vertical velocity (m/s)
P	Pressure (Pa)
P_a	Ambient pressure (Pa)
P_v	Saturated vapour pressure (Pa)
ϵ	Velocity ratio (-)
J	Advance coefficient (-)
Fr	Froude number (-)
Re	Reynolds number (-)
σ_n	Cavitation number (-)

Dependent Variables:	
T	Thrust force (N)
Q	Torque (Nm)
K_q	Torque coefficient (-)
K_t	Thrust coefficient (-)
K_F	Force coefficient (-)
η_p	Propeller efficiency (-)
η_{wedge}	Wedge efficiency (-)
Physical parameters:	
ρ_s	Vapour density (kg/m ³)
ρ_w	Fluid density (kg/m ³)
ρ_a	Air density (kg/m ³)
μ_m	Mixture viscosity (kg/ms)
\dot{m}	Mass transfer rate (kg/s)

INTRODUCTION

Nowadays, surface piercing propellers (SPP) are well known for operating in semi-submersible condition at high advance speed (vessel speed greater than 50 knots). The conditions bring about complex ventilation and cavitation patterns to this type of propeller, which have necessitated wide range of research involving experiments and CFD modelling. However, numerical simulation of ventilation and cavitation patterns on this type of propeller still remains a CFD challenge, which can be accomplished through the analysis of a wedge-shape surface-piercing hydrofoil as its blade section.

During the past half-century, considerable number of hydrodynamic researches has been devoted to studying the SPP propeller. Two of the earlier and fundamental researches in this regard were conducted by Hadler (1968) and Hacker (1973). They introduced different partially cavitated and fully ventilated flow patterns for the SPP.

Their experiments indicated that in fully ventilated condition, the ventilated cavity may cover most of the blade's suction side and rotate with the blade. However, by increasing the advance ratio and exceeding a critical value, this regime changes to partially cavitated and as a result the cavity becomes smaller and unstable during blade's rotation. Kruppa (1972) also studied the scaling procedure for the SPP. His experiments revealed that Reynolds and Froude numbers greater than 5×10^5 and 3, respectively, have negligible influence on its scaling. Later, Brandt (1973) developed the primary performance curves of a SPP. Based on his experimental observations, the value of transition advance ratio can be affected by the Cavitation number as well as Froude number. Meanwhile, Olofsson (1993, 1996) conducted a wide range of experiments on the surface piercing propeller of 841-B model and recorded transient hydrodynamic forces and torques of a rotating blade. His findings revealed that small Cavitation number is likely to be an effective factor for the transient and average forces. In addition to the above mentioned observations, the value of critical or transition advance ratio of this propeller at different Cavitation numbers was determined.

High speed operation of the SPP requires to use expensive and accurate experimental equipment. To avoid such obstacles, analytical and numerical studies on wedge-shape surface-piercing hydrofoils water entry or in some cases a simplified wedge water entry can be considered suitable alternatives. Yim (1969, 1974) is considered a pioneer of the water entry theoretical analysis. He worked out a 2D potential flow approach for the water entry and exit of a thin infinite symmetric wedge to predict the characteristics of a SPP. His method was later extended by Wang (1977, 1979) to solve finite foil shape problems in fully ventilated condition. By using the conformal mapping method, Khabkhpasheva (2014) and Ghadimi (2011-2014) studied water entry problems of arbitrary objects. However, this method can be used only for the infinite object water entry and cannot take into consideration the nonlinearity and viscosity of fluid.

Through development and improvement of a numerical method based on lifting-line theory, Furuya (1985) was the first who presented a three-dimensional numerical model for the SPP in fully ventilated operation condition without considering the gravity and blade thickness effects. By using the negative image method, the linearized effect of the free surface was taken into consideration. On the other hand, Wang (1990) conducted a 3D numerical modelling to assess the performance of a fully ventilated SPP by applying an unsteady lifting surface method. Later, Kudo (1994, 1995) analyzed the SPP through a 3D lifting surface vortex lattice method (VLM) in submerged condition.

Kinnas and Young (2002, 2003) and Young *et al.* (2011) combined the surface panel method and potential flow based BEM ? to simulate the cavitation sheets on a SPP's blade in submerged and semi-submerged propeller operation. In this approach, cavity borders are assumed to be a boundary of fluid domain and, in order to predict the cavity shape, an iterative procedure is required. Consequently, the blade stable cavitation boundary and mean forces could be obtained from the simulation, but dynamic forces and ventilated free surface profile at entry stage could not be derived precisely. Faltinsen *et al.* (2008) considered the nonlinearity of the ventilating problem. They solved parametrically the ventilating entry of a semi-infinite flat plate through analytical expressions. Effects of gravity and fluid viscosity were neglected in this investigation. On the other hand, Vinayan (2010) worked out a 2D BEM code to consider the nonlinear nature of water entry process. He obtained the pressure curves and free surface patterns for vertical motion of a symmetric oblique wedge into the calm water and compared his findings with Cox's experiments (1971). Due to the initial usage of calm water condition, the influence of the horizontal water velocity could not be observed. To evaluate the effects of structural deformations on water entry process of a wedge, Maki *et al.* (2011), Piro and Maki (2011, 2013) and Dominic *et al.* (2013) used coupling elastic beam theory and URANS equations to simulate the flexible wedge water entry. Their studies revealed that for the small structural deformations and moderate dead-rise angle wedge, the effects of structural flexibility is negligible on the water entry process. However in surface piercing sections water entry study by using the coupled URANS and finite element method, Javanmardi and Ghadimi (2017a, 2017b) showed that the structural deformations of a SPP blade and its hydrofoil sections may have some influence on its water entry process.

Results obtained from the smoothed particle hydrodynamics methods and URANS based on the simulations conducted by Farsi and Ghadimi (2014a, 2014b, 2015), Feizi Chekab *et al.* (2015), and Shademani *et al.* (2016, 2017), in modelling the arbitrary object's water entry study, showed that considering the effects of fluid viscosity in the numerical simulations improve the accuracy of the flow simulation around the water entering wedge.

The artificial viscosity assumption and ideal fluid consideration in most of the presented numerical simulations have been the cause of some errors in the observed ventilation

patterns and dynamic forces. Furthermore, most of the numerical schemes have been developed for modelling the fully ventilated operation condition with constant ambient pressure in the ventilated zone. Therefore, the effect of air turbulence on the ventilated cavity has been ignored. In order to obtain more realistic ventilation regimes in different operating conditions such as different advance coefficients, consideration of the effects of some influential physical parameters is imperative. The parameters include fluid viscosity, surface tension, gas dynamics in the ventilated zone as well as growth and collapse of the vapour bubbles. Accordingly, in the current study, unsteady numerical simulations of the ventilating-cavitating turbulent flow around surface piercing hydrofoils in initial water entry phase, are conducted. Flow patterns in different conditions including low, transition, and high advance coefficients, are analyzed. Based on the obtained results, the influence of ventilation and cavitation phenomena on the performance of the SPP are analyzed. To this end, URANS (Unsteady Reynolds Averaged Navier-Stokes) is applied as the governing equations of the turbulent flow. Free surface shape and ventilation patterns are obtained by coupling the URANS and Volume - of - Fluid technique. Since cavitation phenomenon may occur in the initial water entry phase (Brandt (1973)), appropriate cavitation model is employed. In the presence of cavitation, vapour and injected air could coexist in the cavities which represent a multiphase mixture. Therefore, the basic two-phase cavitation model should be replaced by a multiphase model. In the current study, the validated cavitation model developed by Zwart (2004) is employed to capture and assess the cavitation effects on the wedge water entry hydrodynamics.

GOVERNING EQUATIONS

Since the present study deals with three different phases of water, vapour, and air, the mixture is assumed to be homogeneous. Accordingly, momentum URANS equations are used in terms of mixture's pressure, velocity, and viscosity. In general form, they are:

$$\begin{aligned} \partial(\rho_m \vec{v}) / \partial t + \nabla \cdot (\rho_m \vec{v} \vec{v}) = \\ \rho_m g - \nabla P + \nabla \cdot [\mu_m ((\nabla \vec{v} + \nabla \vec{v}^T) - 2 / 3 \nabla \cdot \vec{v} I)] \end{aligned} \quad (1)$$

where I is the unit tensor, \vec{v} and g are velocity and gravity force components, respectively. P , μ_m and ρ_m are also the mixture's pressure, viscosity and density, respectively. These parameters can be written in the fractional form of:

$$\rho_m = \sum \alpha_n \rho_n \quad (2)$$

$$\mu_m = \sum \alpha_n \mu_n \quad (3)$$

In this equation, α_n is the volume fraction of n -th fluid in a cell and it is known that:

$$\sum \alpha_n = 1 \quad (4)$$

Because of the presence of air in the vapour cavity bubbles, the basic two-phase cavitation model should be replaced by a multi-phase cavitation model. Equations proposed by Singhal (2002), Zwart (2004) and Schnerr (2001) are three available cavitation models which can be used for cavitating turbulence flow simulations. Continuity equation of the mixture can be extended to three modified equations based on the air, water, and vapour fractions. These equations are:

$$\partial(\alpha_a \rho_a) / \partial t + \nabla \cdot (\alpha_a \rho_a \vec{v}) = \quad (5)$$

$$\partial \alpha_w / \partial t + \nabla \cdot (\alpha_w \vec{v}) = -\dot{m} / \rho_w \quad (6)$$

$$\partial(\alpha_v \rho_v) / \partial t + \nabla \cdot (\alpha_v \rho_v \vec{v}) = \dot{m} \quad (7)$$

The subscripts a , v , and w refer to the air, vapour, and water components. In these equations, mass transfer occurs only between the water and vapour phase, which is denoted by \dot{m} . The value of the parameter depends on the pressure difference between the bubble boundaries and vapour saturation point. Based on this value, two different mass transformation directions, i.e. condensation or evaporation, may occur. Condensation and evaporation mass transfers in Zwart's model is identified by the following equations, respectively:

$$\dot{m} = \dot{m}_e - \dot{m}_c \quad (8)$$

$$\dot{m}_e = C_e \frac{3(1-\alpha_v)\alpha_{mc}\rho_v}{R_b} \times \sqrt{2(P_v - P_o) / 3\rho_w} \times \text{sign}(P_v - P_o) \quad (9)$$

$$\dot{m}_c = C_c \frac{3\alpha_v\rho_v}{R_b} \times \sqrt{2(P_o - P_v) / 3\rho_w} \times \text{sign}(P_o - P_v) \quad (10)$$

According to Zwart's investigation (2004), empirical constants C_e and C_c can be set equal to 50 and 0.01, respectively. Also, the non-condensable vapour fraction, α_{nc} , and mean radius of bubbles, R_b , are assumed to be 5×10^{-4} and 1×10^{-6} m, respectively. The constants are validated and presented by Mejri (2006) and Ji (2011). Moreover, to obtain the free surface pattern, the coupled volume - of - fraction equation is implemented. Since the flow is highly turbulent, the k - ω -SST turbulent model is applied.

DEFINITION OF PARAMETERS

To investigate the hydrodynamic behaviour of the initial water entry process of a SPP, the geometry of the wedge-shaped hydrofoil is taken from a section of 821-b surface piercing propeller. Since the sections with blade radius ranging from 0.5 to 0.7 have the most effective role in the propeller characteristics, the section at $0.55r$ is considered in this paper, because its shape is also similar to the wedge studied by Cox (1971). The combined principal parameters of the propeller and wedge water entry used in this paper are the advance coefficient J , velocity ratio ε , Froude (Fr) and Cavitation (σ_n) numbers, which are determined by using the following equations, respectively:

$$J=U/nD \quad (11)$$

$$V=0.55\pi nD=0.55\pi U/J \quad (12)$$

$$\varepsilon=U/V=J/0.55\pi \quad (13)$$

$$Fr=U/(g \cdot D)^{0.5} \quad (14)$$

$$\sigma_n=(P_{atm}-P_v) / 0.5 \rho_w U^2 \quad (15)$$

In the equations, D , n , U , V and P_{atm} denote the propeller diameter, shaft speed, water advance speed, foil rotational speed, and ambient pressure, respectively. The geometry of the considered SPP's wedge-shaped hydrofoil is illustrated in Fig. 1.

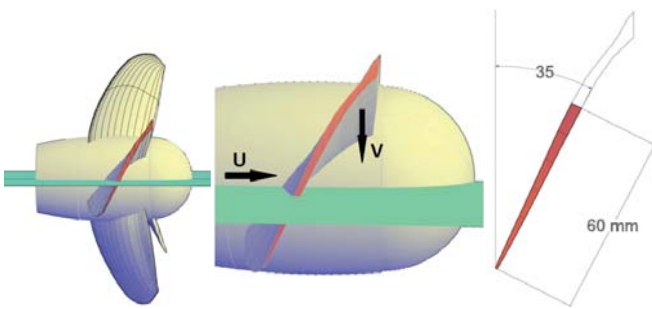


Fig. 1. The hydrofoil section of a SPP @0.55r

In addition to the principal parameters, there are also other dependent parameters which reflect the hydrodynamic performance of the wedge water entry. These parameters include the pressure coefficient, vertical and horizontal forces, and efficiency coefficient. The parameters are determined by using the following equations, respectively:

$$C_P=(P-P_{atm}) / 0.5 \rho_w V^2 \quad (16)$$

$$K_F=F / 0.5 \rho_w V^2 Vt \quad (17)$$

$$\eta_{wedge}=F_x U / F_y V \quad (18)$$

$$\eta_p = \frac{TU}{2\pi Qn} \quad (19)$$

$$Q = \int F_y r dr \quad (20)$$

In the equations, K_F indicates the dimensionless force in x or y direction. F_x indicates the wedge thrust force and F_y is the force produced by the propeller torque. The wedge efficiency is defined in a similar way as in the propeller efficiency expression (η_p). T and Q denote the propeller thrust force and shaft torque, respectively. The propeller performance is defined on the basis of the thrust and torque coefficients which are given as follows:

$$K_t = \frac{T}{\rho n^2 D^4} \quad (21)$$

$$K_q = \frac{Q}{\rho n^2 D^5} \quad (22)$$

The thrust and torque coefficients and efficiency of the above mentioned propeller have been determined in Olofsson's experiments (1993) for Froude number $Fr=6$ and Cavitation number $\sigma_n=2.3$.

VALIDATION OF THE SIMULATED MODEL

Various investigations have been conducted on the water entry and cavitation problems. Simultaneous presence of the two phenomena in this study requires two types of validations. First validation case is related to the water entry problem. For this case, the results of Cox's experiments (1971), and numerical simulations of Vinayan (2010) of the wedge water entry problem, are used. Second validation case is related to cavitation phenomenon. In this case, results of numerical simulation of a specific super-cavitating foil are compared against its corresponding tunnel test experimental outputs from Dinh's experiments (1968).

WEDGE WATER ENTRY

The experiment by Cox (1971) was conducted on the symmetric wedge with dimensions of 0.5" breadth and 6" height (c) in initial calm water condition. This wedge profile is the same as the wedge considered in the current paper. The wedge enters the initial calm water with the constant speed (V) of 2.45m/s. The free surface profile is investigated for two incident angles of 0 and 10 degrees. The wedge geometry and incident angle definition are illustrated in Fig.2a. The obtained free surface profiles are compared against the results of the experiment by Cox (1971) in Fig. 2 and 3. Also, the pressure distribution for the case $\alpha=10^\circ$ is compared with Vinayan's BEM results (1971).

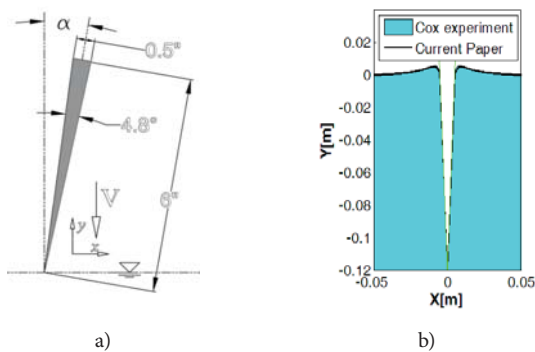


Fig. 2. a) Cox's wedge geometry and b) Comparison of the obtained free surface profile against the result of Cox's experiment (1971) @ $\alpha=0$, $V=2.45$ m/s.

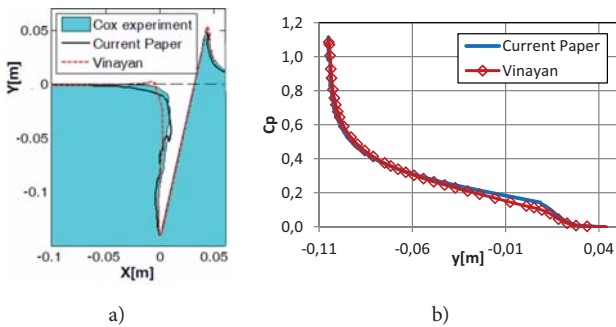


Fig. 3. a) Comparison of the computed free surface profile against the results of Cox's experiment (1971) @ $\alpha=10$, $V=2.45$ m/s, $Vt/c=0.75$ and b) Comparison of the computed C_p against that of BEM model by Vinayan (2010).

As evident in Fig.2b, in the case of symmetric vertical motion the numerical and experimental free surface profiles agree quite well to each other for the incident angle of 0 degree. In the case of 10 degrees incident angle, there is also a favourable agreement between the free surface profiles on the wedge's pressure side, while the profiles agreement on the suction side is relatively good. This is due to the fact that suction side separation profile is very sensitive to: a) edge's apex curvature radius which was not declared in Cox's results (1971) and b) fluid viscosity effects which was ignored in Vinayan's BEM results (2010). Comparison of the computed pressure coefficient C_p on the wedge's sides against the results of nonlinear BEM simulation by Vinayan (2010) indicates

favourable agreement and it is because of the ignorable effect of viscosity on this side, which has been predicted by Yim (1969).

FLOW AROUND A SUPER-CAVITATING HYDROFOIL

The super-cavitating flow is numerically simulated around a thin profile through coupled URANS and Zwart (2004) cavitation model equations. 300 000 cells are generated in the problem domain. The foil is exposed to the 20 fps fluid flow at the incident angle of 9° (Fig.4) and Cavitation number of $\sigma=(P-P_v)/0.5 \rho_w U^2=0.318$, where U represents the upstream velocity. The foil profile is originally tested by Dinh (1968) in the cavitation test tunnel of Laval University. The geometry of the super-cavitating profile is shown in Fig.4. Comparison of the obtained pressure coefficient ($C_p=(P-P_o)/0.5 \rho_w U^2$) around the foil against Dinh's experimental data (1968) and the results of Wu's analytical model (1956) are presented in Fig.5a. The cavity profile and measured length are also shown in Fig.5b.

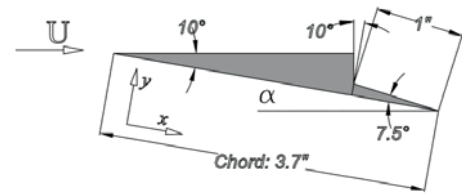


Fig. 4. Geometry of super-cavitating hydrofoil tested by Dinh (1968).

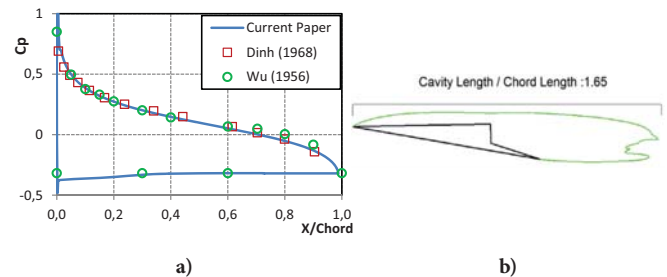


Fig. 5. (a) Comparison of the computed C_p against the results of Dinh's experiment (1968) and Wu's theoretical model (1956) @ $\alpha=9^\circ$, $V=6.15$ m/s and $\sigma_n=0.318$, and (b) Comparison of the obtained vapour cavity profile against Dinh's experimental result (1968).

As evident in Fig. 5, the stagnation point is at the leading edge of the foil and thus the local pressure coefficient at this point is equal to 1, which is synonymous to the presented numerical result. Furthermore, favourable agreement is observed between the numerically obtained pressure distribution and the results of Dinh's experiment (1968) and Wu's theoretical model (1956). Dinh (1968) recorded the cavity length of $1.8 \times$ chord for the implemented values of input speed, incident angle and ambient pressure. The cavity length obtained in the current study is equal to $1.65 \times$ chord length (as shown in Fig.5b), which indicates 8% error. It should be noted that radius of hydrofoil's leading edge has also important effects on the generated cavity length. Since this value is unknown it is set to be zero, which leads to some errors.

SETTING UP THE COMPUTATIONAL PROCEDURE

In the current study, the geometry of a wedge-shaped surface piercing (SP) hydrofoil with the left dead-rise angle of 120.2° and right dead-rise angle of 55° is considered to form a blade section, as shown in Fig.6. Based on the above mentioned dead-rise angles, the pitch angle is found to be 35° . The wedge is situated in a rectangular computational domain containing water and air separated by free surface at a specific height. The computational domain is illustrated in Fig. 6. Initially, the wedge's apex is located at an undisturbed free surface level.

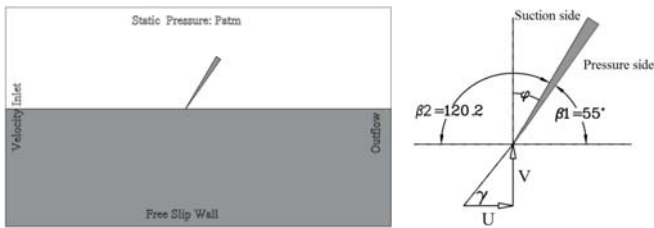


Fig. 6. The considered computational domain and wedge geometry

Similar to the propeller condition, the incoming flow with constant velocity (U) enters from an upstream boundary location. Similar to the Olofsson's experiments (1993), numerical simulation in the current paper is conducted in full-scale condition and the input velocity is set to be 9.39 m/s. Based on Olofsson's paper (1993), the characteristic curves of 821-b SPP have been presented for the advance coefficients in the range of [0.2 to 1.1]. Therefore, the hydrodynamic characteristics of the wedge water entry is investigated for this range, as well. Accordingly, by using Eq.12, the value of blade velocity V can be set for each simulation condition. Dimensions of the computational domain are selected based on the work of Shademani and Ghadimi (2016). By considering the gravity effects, distribution of initial hydrostatic pressure based on the water depth is implemented. Downstream location of the computational domain is defined to be an outflow patch, while "no-slip" condition is set for the wedge planes. By adjusting the Courant number below unity, the time step at each blade velocity is prescribed based on the vertical displacement step which is defined by $dy=h/k$. The parameter h is the oblique wedge height and k is the number of divisions assumed in wedge height. The effect of displacement step is assessed by subsequent assuming $k=40, 60, 120$, and 180. Based on the comparison of the obtained results against Olofsson's experimental data (1993) it is found that decreasing the displacement step slightly affects the computed forces, but strongly influences the free surface smoothness. Therefore, the case of $k=120$ ($dy \sim 0.5$ mm) (which shows an error less than 5%) is adopted for the targeted analyses in this paper.

A mesh of boundary layer type is used on the wedge sides to improve the accuracy of the predicted wall function, while a structured mesh parallel to the undisturbed free surface level is used for the remaining part of the considered domain. Three zones are formed in the problem domain in dealing with

the vertical translation of the wedge : two stationary zones and one moving zone (shown in Fig.7). Dynamic meshing technique is used in the stationary zones because of their moving boundaries (Vinayan, (2009)). The effects of mesh size on the solution are investigated by considering two different meshing options of 0.4 (Vinayan, (2009)) and 0.5 million cells. It is shown that increasing the cell number beyond 0.4 million has less than 5% effect on the forces. However the mesh option of 0.5 million cells yields a smoother free surface pattern. Accordingly, the mesh option of 0.5 million cells is adopted for the current study. A schematic diagram of the generated mesh is illustrated in Fig.7, where the upper and lower boundaries are kept at constant static pressure with free slip wall conditions. Upstream and downstream boundaries are considered as the inlet and outlet, respectively, as shown in Fig.6.

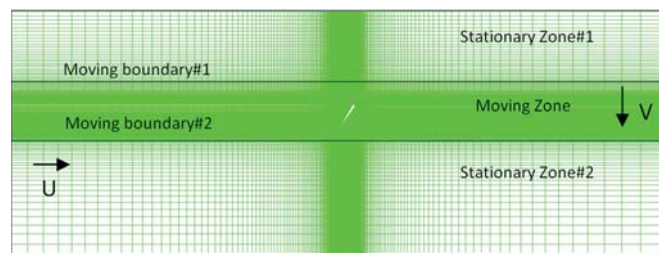


Fig. 7. Illustration of different zones in the domain and the generated mesh

RESULTS AND DISCUSSION

As previously pointed out in the introduction section, for a constant Froude and Cavitation numbers, the advance coefficient is the only influential parameter for the ventilation pattern. Variation of this parameter leads to the three types of operation conditions. The first subsection (6.1) deals with ventilation pattern and hydrodynamic forces in fully-ventilated operation condition, the second subsection (6.2) concentrates on the transition condition, and the third subsection (6.3) focuses on the partial cavitation condition. The fourth subsection (6.4) deals with combining the obtained results in a unified curve. To accomplish this, the required parameters for the targeted analyses are shown in Tab. 1.

Tab. 1. Parameter setting for the performed analyses

Parameter	Value
Advance ratio (J)	0.2 to 1.1
Velocity ratio (ϵ)	0.12 to 0.64
Cavitation number (σ_n)	2.3
Froude number (Fr)	6

FULLY VENTILATED OPERATION CONDITION

Fully ventilated operation condition deals with a situation in which a single cavity covers the entire wedge suction side (from the leading edge to the trailing edge) during the water entry process. The obtained pressure distributions and free surface patterns for $\epsilon=0.12-0.29$ are shown in Fig.8a and 8b by

using the dimensionless coordinates x/Vt and y/Vt . Also, the dimensionless exerted forces as well as the defined efficiency of the water entry movement are illustrated in Fig. 8d. The x-component of the cavity wall velocity in the ventilated zone is presented in Fig. 8c.

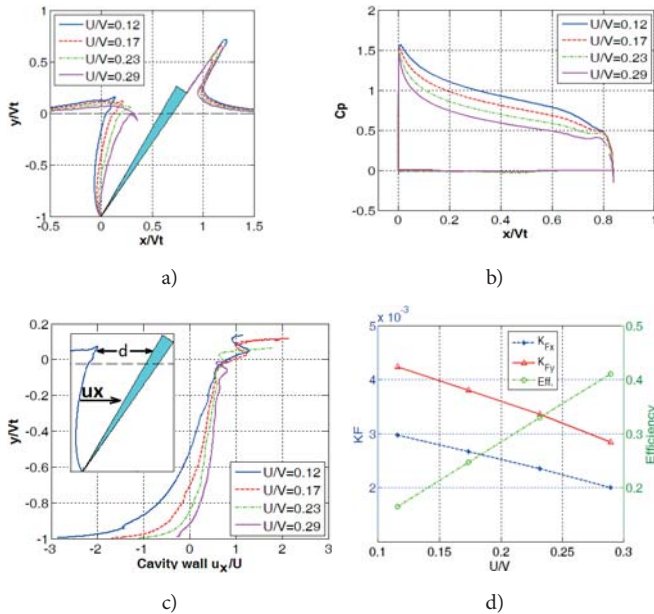


Fig. 8. (a) Free surface profiles, (b) Pressure distributions, (c) Cavity wall velocity x-component u_x , and (d) Dimensionless forces and water entry efficiency @ $Fr=6$, $\sigma_n=2.3$, $\epsilon=0.12-0.29$.

Based on the numerical results of the free surface profile at the initial stages of water entry (Fig.8a), it can be observed that the pressure drop at the wedge's apex causes an intake of air into the water zone and consequently separation of flow from the wedge apex may occur. The separated flow leads to cavity generation on the wedge's suction side. In this condition, only the pressure side of the wedge interacts with the water, and the resulting force on the wedge is similar to that of the water entry of a flat plate. As evident from the pressure distribution curves of Fig.8b, by increasing the incident angle (decreasing ϵ) at a constant input speed, the mean value of C_p increases and thus dimensionless forces increase, as well (Fig.8d). Contrary to this situation, the pressure on the ventilated side does not change significantly from the ambient pressure, and consequently C_p tends to zero on this side. Larger vertical blade velocity results in stronger water jet flow on the wedge's pressure side and causes an increase in the lost momentum which reduces the efficiency of water entry process (Fig.8d). Through vertical motion of the wedge, the volume of the ventilated zone gradually increases and, as a result, the atmosphere air is sucked into the cavity from "d" pathway. The width of the pathway depends on the cavity wall velocity in x- direction, (u_x), wedge velocity V and wedge pitch angle. Variation of the magnitude and direction of $u_x(\epsilon, y)$ on the cavity wall for $-1 < y/Vt < 0$ are shown in Fig.8c. It can be seen that as the wedge velocity V reduces the average value of u_x increases toward the wedge wall and consequently the volume of the ventilated zone decreases.

TRANSITION CONDITION

While the propeller rotating speed (wedge vertical speed) declines, the velocity ratio ϵ increases and the "full ventilation pattern" is transformed into "transition pattern". This is the unstable and fluctuating state in which its hydrodynamic behaviour highly depends on the wedge geometry, velocity ratio, and ambient pressure. Based on the observations made in the current paper, ϵ in the range from 0.36 to 0.42 corresponds to this operational condition. Isolation sequences of the leading edge cavity are shown in Fig. 9a and 9b. Pressure distribution curves are also shown in Fig.10a, while the dimensionless exerted forces and efficiency of the water entry process are illustrated in Fig.10b.

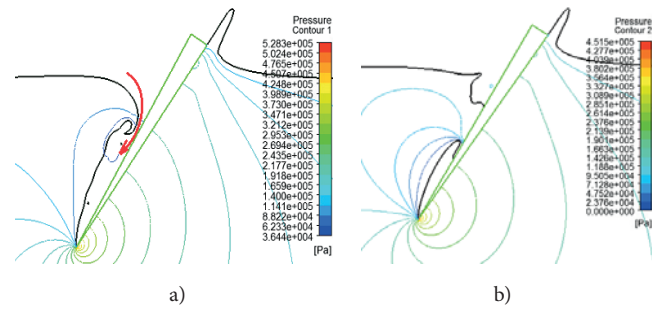


Fig. 9. Ventilated cavity collapse and apex vapour cavity replacement at different velocity ratios: a) $\epsilon=0.38$, b) $\epsilon=0.42$, @ $Fr=6$ and $\sigma_n=2.3$.

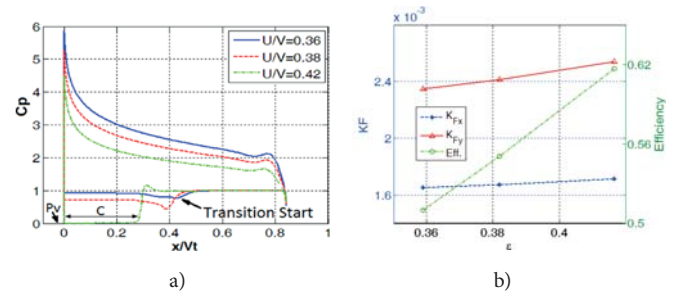


Fig. 10. (a) Pressure distributions, and (b) Dimensionless forces and water entry efficiency @ $Fr=6$, $\sigma_n=2.3$, $\epsilon=0.36-0.42$.

At a constant water advance velocity, a decrease in the wedge vertical speed would amplify the cavity wall velocity u_x toward the wedge ventilated side, which narrows the air pathway "d", as shown in Fig.8c. The narrowed air pathway causes a pressure drop in the ventilated cavity which can be observed on the pressure distribution curve of $\epsilon = 0.36$ in Fig.10a. The C_p variation on the pressure side has the same pattern as in the previous condition. It was pointed out before that the theoretical results can accurately predict the C_p pattern on this side (Fig.10a). While the vertical speed decreases further, top of the ventilated cavity wall ($y/Vt=0$) collapses through the wedge wall which traps the remaining air near the leading edge. As a result of the vertical displacement of the wedge throughout time and expansion of the cavity wall, the pressure inside the cavity drops. By decreasing the pressure value to that of vapour saturation point in the trapped isolated cavity, water vaporization

process on the cavity wall begins. The velocity ratio which corresponds to the largest non-ventilated cavity may be called critical velocity ratio. Increasing the forces exerted on the wedge sides in transition condition may be due to the fact that pressure on the wide area of the wedge suction side is less than the ambient pressure and even at critical advance ratio it is equal to vapour pressure (Fig.10b).

PARTIAL CAVITATION CONDITION

The last type of water entry pattern deals with high velocity ratio condition. The obtained results demonstrate that partially cavitated pattern may happen for the velocity ratio greater than 0.42. Free surface profile and pressure distribution along the wedge sides for $\varepsilon=0.46\div 0.64$ are illustrated in Fig.11a, and 11b. Dimensionless exerted forces and water entry efficiency are also shown in Fig.11c.

While the wedge vertical speed (or propeller rotating speed) is very low, the ventilated air cavity collapses in the very initial phase of water entry and only cavitation sheet is observed near the leading edge, whose volume decreases through an increase in ε value (Fig.11a). Accordingly, the pressure distribution on the wedge pressure side has the same patterns as previously (Figs.11b), while, depending on the cavity length, pressure on the part of the suction side would be equal to the vapour pressure.

Since the dimensionless values of F_x and F_y are the function of flow angle of attack (Fig. 8d and Fig.11c) through an increase of ε , the dimensionless values of F_x and F_y are reduced in both fully-ventilated and partially- cavitated operation conditions. This is while the efficiency of the blade section increases when ε rises. This may be attributed to the reduction of the spray height on the pressure side of the wedge and consequently the decrease in the wasted energy as the velocity ratio increases. As a result, the efficiency should increase in both the modes. However, there is an exception in the case of partial cavitation mode, where the impact velocity highly decreases and hence the wetted area increases considerably in such a way that the efficiency drops. Such phenomena can be seen for $\varepsilon=0.64$ (Fig.11c).

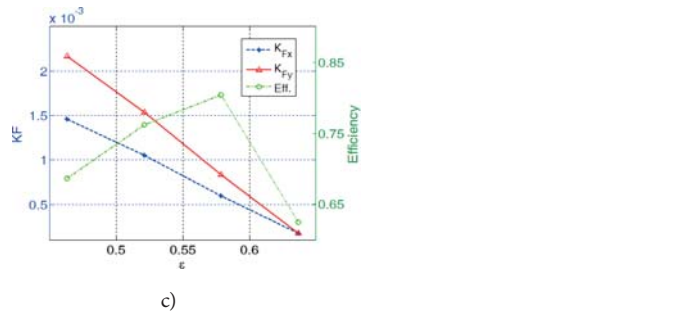
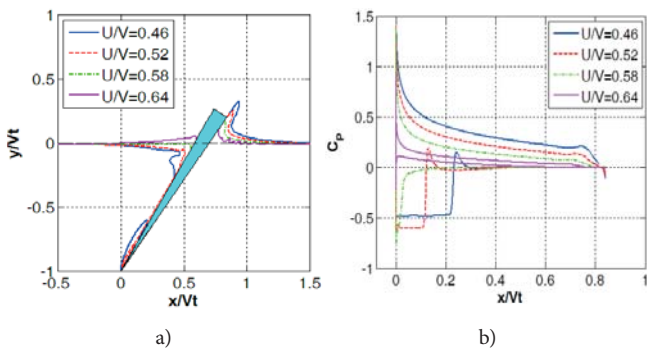


Fig. 11. a) Free surface profiles, b) Pressure distributions, c) Dimensionless forces and water entry efficiency @Fr=6, $\sigma_n=2.3, \varepsilon=0.46-0.64$.

INVESTIGATION OF THE PROPELLER AND ITS HYDROFOIL PERFORMANCE CURVES

The purpose of this subsection is to explore the possible similarity between the performance curve of the studied hydrofoil section and its original SPP. To this end, the results are presented based on the incorporation of wedge water entry and propeller characteristic parameters. For instance, the velocity ratio which is used to evaluate the wedge performance pattern has similar application in the propeller investigation. The experimental curves of 821-b propeller for Fr=6 have been obtained by Olofsson (1993). Irrespective of the magnitude of K_i and K_q , the overall trends of their corresponding curves are illustrated in Fig.12.

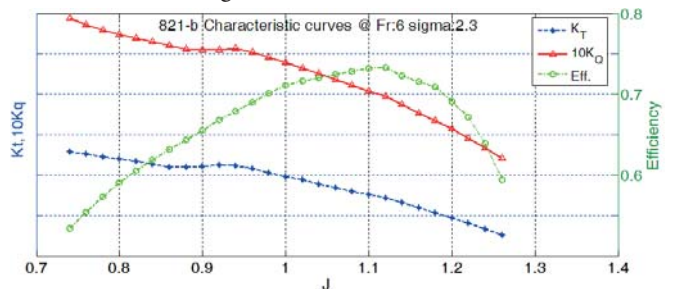


Fig. 12. The characteristic curves of 821-b propeller trend @ Fr=6, from Olofsson's (1993) experiments.

Through combining the results related to forces and efficiency at all three velocity ratios in the unified curves, comprehensive characteristic curves are worked out for the wedge water entry. The resulting curves are illustrated in Fig.13. It should be pointed out that in the curves equivalent value of the advance coefficient is used instead of the velocity ratio on the x-axis.

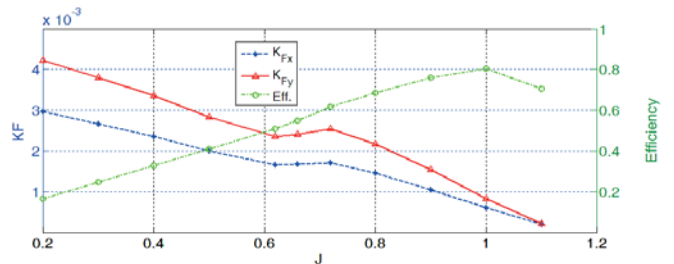


Fig. 13. The obtained characteristic curves for the SP hydrofoil water entry process @Fr=6, $\sigma_n=2.3$.

Comparison of the curves given in Fig.12 and 13 shows that the trends of dimensionless forces and efficiency for both SPP and simplified surface piercing hydrofoil are favourably similar. However, for the studied hydrofoil, the transition pattern occurs at the advance coefficient ($J=0.66$) lower than that of the SPP 821-b ($J=0.9$). This discrepancy reveals that transition point for a 3D blade may not be estimated by the simulation of its hydrofoil section. Consequently, estimation of accurate value of transition J for a SPP requires a 3D modelling of the blade water entry. However, this simulation shows that some challenging aspects of SPP's hydrodynamic performance can be recognized through the study of a simple thin wedge water entry.

CONCLUSIONS

In this paper, hydrodynamic behaviour of a surface piercing hydrofoil is numerically analyzed. The problem is investigated for a multiphase domain containing water, vapour, and air. Coupled URANS equation, VOF scheme, and Zwart's cavitation model (2004) are used to conduct the numerical simulation. The investigated wedge (SP hydrofoil) has the left dead-rise angle of 55° and right dead-rise angle of 120.2° , which is similar to the Cox's tested wedge (1971). Half a million cells and displacement-step of 0.5 mm are considered in this simulation. Cox's experimental free surface profiles (1971) are used to validate the water entry simulation part, while Dinh's experimental results (1968) are used for validation of the implemented cavitation model. Favourable accordance is observed in both validation cases between the obtained results and the published experimental data.

Afterwards, water entry process of the wedge is investigated for a particular range of advance coefficients at specific Cavitation and Froude numbers. Three ventilation patterns of fully ventilated, transition, and partially cavitated operation conditions are detected during the period of increasing advance coefficients. Free surface profile and pressure distributions on both sides of the wedge are achieved. The simulation reveals that for specific Froude and Cavitation numbers, the stability and collapse of the ventilated air cavity is highly dependent on the x -component of the cavity wall velocity. It is also found that the magnitude of this velocity is dependent on the wedge velocity ratio.

Similar to the propeller characteristic curves, the wedge's non-dimensional forces and efficiency curves are prepared. Comparison of the characteristics curves illustrates that similar patterns exist between the characteristic curves of the propeller and wedge water entry.

The future research may involve studying the effects of Cavitation number on the transition advance coefficient. This study may become instrumental in better understanding the transition condition regime of the surface piecing propellers.

BIBLIOGRAPHY

1. Brandt H.: *Modellversuche mit Schiffspropellern an der Wasseroberfläche*, Schiff und Hafen. 25(5), 1973, pp.415–422.
2. Cox B.D.: *Hydrofoil theory for vertical water entry*, PhD thesis, Massachusetts Institute of Technology, Cambridge, MA, USA, 1971.
3. Dinh N.N.: *Some Experiments on a Supercavitating Plane Hydrofoil with Jet-Flap*, J. Ship Research, SNAME,1968, pp. 207-219.
4. Faltinsen O.M., Semenov Y.A.: *Nonlinear problem of flat-plate entry into an incompressible liquid*. J. Fluid Mech. 611, 2008, pp. 151–173.
5. Farsi M., Ghadimi P.: *Finding the best combination of numerical schemes for 2D SPH simulation of wedge water entry for a wide range of dead-rise angles*. Int. J Naval Archit. Ocean Eng. 6, 2014, pp. 638-651.
6. Farsi M., Ghadimi P.: *Effect of flat deck on catamaran water entry through smoothed particle hydrodynamics*. Institution of Mechanical Engineering Part M, J. Engineering for the Maritime Environment, March, 2014, published online.
7. Farsi M., Ghadimi P.: *Simulation of 2D symmetry and asymmetry wedge water entry by smoothed particle hydrodynamics method*. J. Brazilian Society of Mech. Sci. Eng. 37(3), 2015, pp. 821-835.
8. Feizi Chekab M.A., Ghadimi P., Farsi M.: *Investigation of three-dimensionality effects on aspect ratio on water impact of 3D objects using smoothed particle hydrodynamics method*. J. Brazilian Soc. Mech. Sci. Eng, 2015, published online: June 2015. DOI: 10.1007/s40430-015-0367-8.
9. Furuya O.: *A performance-prediction theory for partially submerged ventilated propellers*. J. Fluid Mechanics, 151, 1985, pp. 311-335.
10. Ghadimi P., Saadatkah A., Dashtimanesh A.: *Analytical solution of wedge water entry by using Schwartz–Christoffel conformal mapping*. Int. J. Modeling, Simulation and Scientific Computing. 2(3), 2011, pp. 337-354.
11. Ghadimi P., Dashtimanesh A., Djeddi S.R.: *Study of water entry of circular cylinder by using analytical and numerical solutions*. J. Brazilian Society of Mech. Sci. Eng. 37(3), 2012, pp. 821-835
12. Ghadimi P., Feizi Chekab M.A., Dashtimanesh A.: *A numerical investigation of the water impact of an arbitrary bow section*. ISH J. Hydraul. Eng. 19(3), 2013, pp. 186-195.

13. 13. Ghadimi P., Feizi Chekab MA., Dashtimanesh A.: *Numerical simulation of water entry of different arbitrary bow sections*. J Naval Archit. Marine Eng. 11 (2), 2014, pp. 117-129.
14. 14. Hadler J.B., Hecker R.: *Performance of Partially Submerged Propellers*, Proc. 7th ONR Symposium on Naval Hydrodynamics, Rome, Italy. 1968.
15. 15. Hecker R.: *Experimental Performance of a Partially Submerged Propeller in Inclined Flow*, SNAME Spring Meeting, Lake Buena Vista, Florida, USA, 1973.
16. 16. Javanmardi N., Ghadimi P.: *Hydroelastic analysis of surface piercing hydrofoil during initial water entry phase*, J. Scientia Iranica, accepted to be published, 2017.
17. 17. Javanmardi N., Ghadimi P.: *Hydroelastic analysis of a semi submerged propeller using simultaneous solution of Reynolds averaged Navier–Stokes equations and linear elasticity equations*, Journal of Engineering for Maritime Environment,? 2017.
18. 18. Ji B., Luo X.W., Wang X., Peng X.X., Wu Y.L., Xu H.Y.: *Unsteady numerical simulation of cavitating turbulent flow around a highly skewed model marine propeller*. J. Fluids Eng.-Trans, ASME, 133 (1), 011102, 2011.
19. 19. Khabkhpasheva TI, Kim Y, Korobkin AA.: *Generalized Wagner Model of Water Impact by Numerical Conformal Mapping*. App. Ocean Res. 44, 2014, pp. 29-38.
20. 20. Kruppa CFL.: *Testing of Partially Submerged Propellers*, Proc. 13th ITTC Report on Cavitation. Berlin & Hamburg, Germany, 1972.
21. 21. Kudo T., Ukon Y.: *Calculation of super cavitating propeller performance using a vortex-lattice method*, in: Second International Symposium on Cavitation, Tokyo, Japan, 1994.
22. 22. Kudo T., Kinnas S.: *Application of vortex/source lattice method on supercavitating propellers*, in 24th American Towing Tank Conference, College Station, TX, USA, 1995.
23. 23. Maki K.J., Lee D., Troesch A.W., Vlahopoulos N.: *Hydroelastic impact of a wedge-shaped body*. Ocean Engineering 38, 2011, pp. 621–629.
24. 24. Mejri I., Bakir F., Rey R., Belamri T.: *Comparison of computational results obtained from a homogeneous cavitation model with experimental investigations of three inducers*, J. Fluids Eng.-Trans. ASME, 128, 2006, pp.1308–1323
25. 25. Olofsson N.: *A Contribution on the Performance of Partially Submerged Propellers*, Proc. FAST '93, 2nd Intl. Conf. on Fast Sea Transportation. Yokohama, Japan, 1, 1993, pp. 765-776.
26. 26. Olofsson N.: *Force and Flow Characteristics of a Partially Submerged Propeller*, PhD Thesis, Department of Naval Architecture and Ocean Engineering, Chalmers Univ., Gotenborg, Sweden,1996.
27. 27. Piro D.J., Maki K.J.: *Hydroelastic Wedge Entry and Exit* . 11th International Conference on Fast Sea Transportation FAST 2011, Honolulu, Hawaii, USA, September 2011.
28. 28. Piro D.J., Maki K.J.: *Hydroelastic analysis of bodies that enter and exit water*. Journal of Fluids and Structures 37, 2013, pp. 134–150.
29. 29. Panciroli, R.: *Water entry of flexible wedges: Some issues on the FSI phenomena*. App. Ocean Res. 39, 2013, pp.72-74.
30. 30. Schnerr G.H., Sauer J.: *Physical and numerical modeling of unsteady cavitation dynamics*, in: Proceeding of 4th International Conference on Multiphase Flow, New Orleans, USA, 2001.
31. 31. Shademani, R., Ghadimi P.: *Estimation of water entry forces, spray parameters and secondary impact of fixed width wedges at extreme angles using finite element based finite volume and volume of fluid methods*. J. Brodogradnja 67(2), 2016, pp. 101-124.
32. 32. Shademani, R., P. Ghadimi.: *Asymmetric Water Entry of Twin Wedges with Different Deadrisers, Heel Angles, and Wedge Separations using Finite Element Based Finite Volume Method and VOF*. Journal of Applied Fluid Mechanics, 10(1), 2017, pp. 353-368.
33. 33. Shademani R., Ghadimi P.: *Numerical assessment of turbulence effect on forces, spray parameters, and secondary impact in wedge water entry problem using k-ε method*, Scientia Iranica- B, 24(1), 2017, pp. 223-236.
34. 34. Singhal A.K., Athavale M.M., Li H., Jiang Y.: *Mathematical basis and validation of the full cavitation model*, J. Fluid Engineering, 124, 2002, pp. 617-624.
35. 35. Vinayan V., Kinnas S.A.: *A numerical nonlinear analysis of two-dimensional ventilating entry of surface-piercing hydrofoils with effects of gravity*, J. Fluid Mech. 658,2010, pp. 383–408 .
36. 36. Vinayan V. *A Boundary Element Method for the Strongly Nonlinear Analysis of Ventilating Water-entry and Wave-body Interaction Problems*. PhD thesis, Ocean Engineering Group, Architectural and Environmental Engineering, University of Texas at Austin, Austin, TX, USA, 2009.

37. 37. Wang D.P.: *Water entry and exit of a fully ventilated foil*, J. Ship Res. 21 (1), 1977, pp. 44–68.
38. 38. Wang D.P.: *Oblique water entry and exit of a fully ventilated foil*, J. Ship Res, 23, 1979, pp. 43–54.
39. 39. Wang G., Zhu X., Sheng Z.: *Hydrodynamic forces of a three-dimensional fully ventilated foil entering water*. J. Hydrodynamics, 5(2), 1990.
40. 40. Wu T.Y.: *A Free-Streamline Theory for Two-Dimensional Fully Cavitated Hydrofoils*, Mathematical Physics, 35, 1956, pp. 236–265.
41. 41. Yim B.: *An application of linearized theory to water entry and water exit problems. Part 2 with ventilation*, Rep. 3171. NSRDC, Washington, DC, USA. 1969.
42. 42. Yim B.: *Linear theory on water entry and exit problems of a ventilating thin wedge*, J. Ship Res. 18 (1), 1974, pp. 1–11.
43. 43. Young Y.L.: *Numerical modeling of supercavitating and surface-piercing propellers*, PhD thesis, Ocean Engineering Group, Department of Civil Engineering, University of Texas at Austin, Austin, TX, USA, 2002.
44. 44. Young Y.L., Kinnas S.A.: *Analysis of supercavitating and surface-piercing propeller flows via BEM*, J. Computational Mechanics, 32, 2003, pp. 269–280.
45. 45. Young Y.L., Savander B.R.: *Numerical analysis of large-scale surface-piercing propellers*. J. Ocean Engineering, 38, 2011, pp. 1368–1381.
46. 45. Zwart P., Gerber A.G., Belamri T.: *A Two-Phase Model for Predicting Cavitation Dynamics*, ICMF International Conference on Multiphase Flow, Yokohama, Japan, 2004.
47. Plik : PMR-2016-00084 : 43230 zn. norm. [24 str], stan 2018-01-16, kor. ang. epw

CONTACT WITH THE AUTHORS

Parviz Ghadimi

e-mail: pghadimi@aut.ac.ir
Amirkabir University of Technology
424 Hafez Ave., 3314 Tehran
ISLAMIC REPUBLIC OF IRAN

Nasrin Javanmardi

e-mail: n.javan@aut.ac.ir
Amirkabir University of Technology
424 Hafez Ave., 3314 Tehran
ISLAMIC REPUBLIC OF IRAN

APPLICATION OF VORTEX FLOW MODEL IN PROPELLER-STATOR SYSTEM DESIGN AND ANALYSIS

Przemysław Król

Ship Design and Research Centre, Gdańsk, Poland
Gdańsk University of Technology, Poland

Tomasz Bugalski

Ship Design and Research Centre, Gdańsk, Poland

ABSTRACT

The paper covers basics of the vortex model used for propeller-stator systems. The outline of the design algorithm is given and the results of its application are shown. The designed propeller-stator system was the subject of model tests run at the CTO model basin and cavitation tunnel. Stator's influence on the delivered power required by the propeller and its revolution rate has been examined by conducting self-propulsion tests with and without stator. The tests performed in the cavitation tunnel revealed only weak tip vortex cavitation on the propeller. No cavitation was observed on the stator at the design point. A wide range of the performed tests allowed the authors to identify details of the developed theory which will require further improvement.

Keywords: Propeller, Wake improving device, Upstream stator, Cavitation, Vortex lattice method

FLUID MOTION MODEL

The equations describing the motion of real fluid are almost impossible to solve – integrating them analytically is possible only for some simplified cases. Due to this, the ideal (incompressible, inviscid) fluid model is still in wide use. Within this model, the mass conservation equation is:

$$\operatorname{div} \vec{U} = 0 \quad (1)$$

and the momentum conservation equation (Euler equation) is:

$$\frac{D\vec{U}}{Dt} = \vec{F} - \operatorname{grad} p \quad (2)$$

Although significantly simplified, these equations are still hardly solvable. However, it is possible to introduce a scalar function of velocity potential:

$$\operatorname{grad} \varphi = \vec{U} \quad (3)$$

Applying this potential definition to the mass conservation equation leads to the Laplace equation:

$$\operatorname{div} \vec{U} \equiv \Delta \varphi = 0 \quad (4)$$

The above equation is linear, which means that the superposition of its individual solutions is still the equation's solution. A special class of individual, elementary solutions of the Laplace equation is known as hydrodynamic singularities.

Each type of hydrodynamic singularities induces a specific velocity field in the surrounding area. In general case, it may be expressed as:

$$\vec{U}_{ind}(\vec{r}) = A(\vec{r})\vec{e}(\vec{r}) \quad (5)$$

where A is the scalar value depending on the type of singularity, its strength, and the distance to the calculation point. The unit vector \vec{e} is dependent only on the type of singularity and its position with respect to the calculation point.

The use of hydrodynamic singularities is a convenient concept for solving flow problems with discrete panel approach. The surface of the body immersed in the flow is divided into small pieces, and at each of them the kinematic boundary condition for ideal fluid motion is demanded:

$$\vec{U}_{total}(\vec{r}) \bullet \vec{n}(\vec{r}) = 0 \quad (6)$$

Singularities of known type are distributed over the reference surface (which does not necessarily have to coincide with the surface of the body immersed in the flow). It is important to have a number of unknowns describing the singularity strength distribution, and the same number of panel control points at which the boundary condition is enforced. It allows to construct the system of linear equations and exactly determine the strengths of individual singularities.

It is noteworthy that the hydrodynamic singularities compose the solution for ideal fluid motion and, consequently, no viscous effects are taken into account. In most applications, viscous drag is calculated based on simplified formulas or the boundary layer analysis. Separation phenomena are omitted, or just signaled. Especially the latter may lead to unrealistic results, such as the well-known d'Alembert paradox.

Despite these limitations, the singularity method is quite useful – especially for slender bodies, such as hydrofoils for instance, where separation phenomena are in most cases of minor importance.

DESIGN VORTEX MODEL

ALGORITHM OUTLINE

The design algorithm is arranged as chain of subsequent logical steps. The starting point is the assumption on stator blade circulation distribution. It allows to determine the stator induced velocity field in propeller plane and the stator drag force, which are basic input data for further steps.

For the assumed stator circulation distribution, an optimum propeller is designed. Its initial design is prepared using the lifting line algorithm. Its only purpose is to evaluate the system efficiency that is expected to be achieved in the prescribed conditions. If it is satisfactory, the propeller design algorithm proceeds to a more detailed phase.

Once the propeller geometry is designed, it is possible to analyse it using the lifting surface model. One of its outputs is the propeller induced velocity field in stator plane. It serves as the input for subsequent stator design.

The block diagram presents the outline of the algorithm adopted for propeller–stator system design:

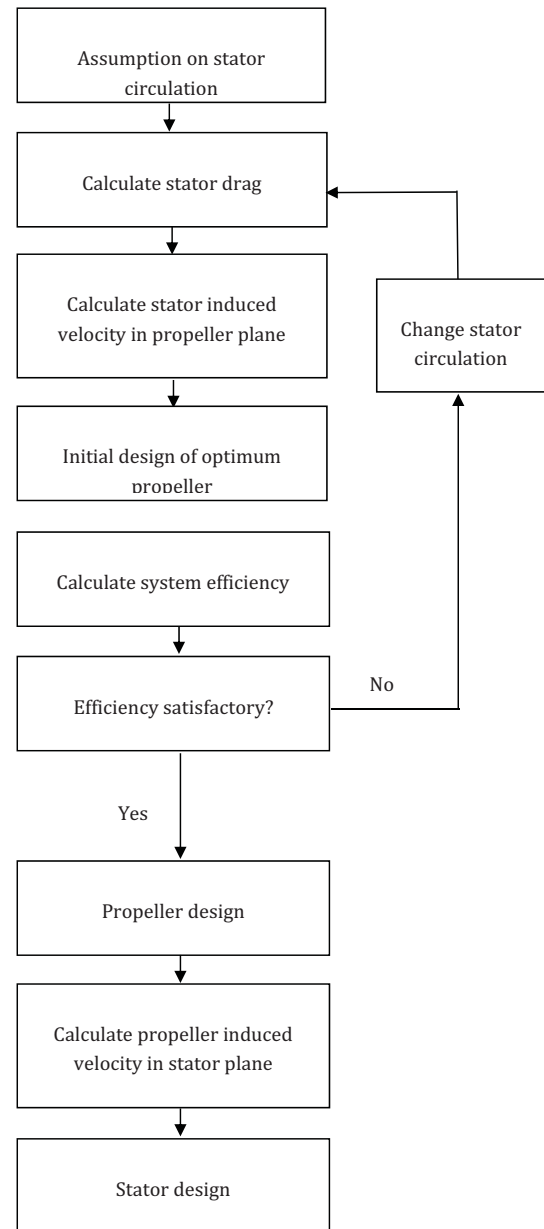


Fig. 1. Block diagram of the design algorithm

A detailed description of each step of the outlined algorithm is given further in the paper.

CIRCULATION DISTRIBUTION

Despite the fact that flow phenomena existing around the propeller-stator system are very complex, simple singularity models can still be successfully used [1]. From a wide family of singularity models, two were adopted in this work, which were: the lifting line model for the design task, and the lifting surface for the analysis task. In this section the former model is described.

The singularity model used for the design task is very simple. It replaces propeller and stator blades with lifting lines of variable radial circulation distribution. As it is the

initial theory, some additional simplifications have been introduced. First of all, the stator is assumed to be lightly loaded. Consequently, the deformation of its vortex wake is neglected and the wake is assumed to follow the external velocity field. This assumption turned out to be acceptable for low and moderate values of total bound circulations over the stator blade.

The circulation distribution along stator blades is a priori assumed to have an elliptical shape. This decision is based on the well-known conclusion from the Prandtl lifting line theory on the induced drag minimum for elliptical distribution of bound circulation.

The propeller itself is assumed to be moderately loaded, and the propeller induced velocities are taken into account while calculating the pitch of the propeller vortex wake. It is assumed to form a true helical surface, whose shape is determined upon the total velocity field, taking into account the external wakefield, and stator and propeller induced velocities. However, the propeller blades are replaced with lifting lines of radially variable bound circulation distribution. A general view of the actual vortex model is given in Fig. 2.

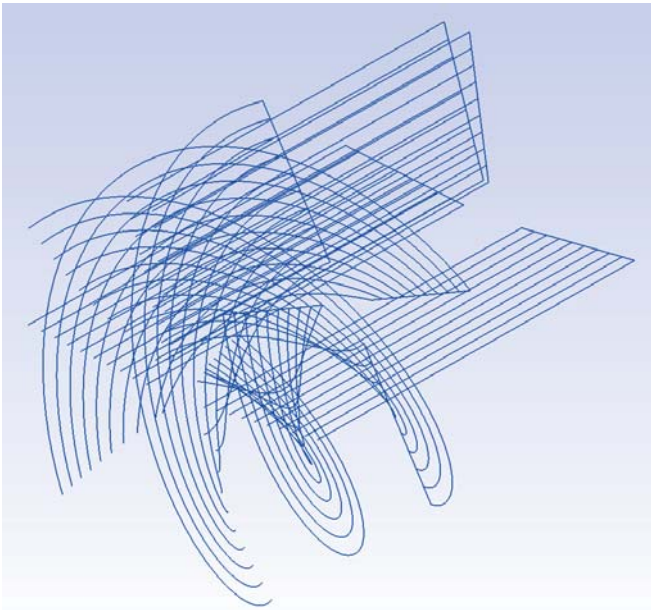


Fig. 2. Propeller and stator lifting line representation

The circulation distribution along the propeller blade does not follow any additional assumption – it is determined as in the classical lifting line algorithm for propeller design making use of Goldstein factors.

Since the deformations of the stator and propeller vortex wakes are neglected, there is no need for an iterative process of stator-propeller coupling. It must be underlined, however, that this assumption is rather crude and may lead to significant discrepancies between theoretical and experimental results – especially for higher propeller/stator loads.

STATOR INDUCED VELOCITIES

The very first step of the design task is to determine the velocity field induced by the stator in the propeller plane. As mentioned before, it is assumed that the bound circulation distribution over stator blades is elliptical. The free stator vortices are assumed to form flat surfaces, parallel to the external flow vector. Upon this assumption it is easy to determine the stator induced velocity field wherever around it. However, it is possible to make further simplification of calculations, as the mean velocities at each radius are the same for one lifting line with maximum bound circulation Γ and for the set of N lifting lines of the accumulated maximum bound circulation equal to Γ . This is true as long as all these lifting lines have the same shape of bound circulation distribution and the same blade length.

It is convenient to express stator induced velocities as coefficients:

$$c = u \cdot \frac{L}{\Gamma_{MAX}} \quad (7)$$

where u is the induced velocity, L is the length of the stator blade and Γ_{MAX} is the maximum value of bound circulation over the lifting line. When using the single lifting line approach, it shall be set equal to the accumulated value of maximum bound circulations values of all stator blades.

At the stage of propeller stator system design, the most important value to be known is the mean value of stator induced tangential velocity at each propeller radius. The induced velocities are in general complex functions of circulation distribution shape and position with respect to the lifting line. In the case of mean tangential components, they turned out to be very insensitive to the axial distance between propeller and stator planes; for a distance larger than $3L$ their changes are negligible. For further calculations, the values of c coefficients determined for the relative distance of $0.5L$ were used.

Since the viscous effects are neglected, the mean value of axial induced velocity is equal to zero for each radius. Due to the presence of the viscous wake behind a body in the real fluid, it shall have a small negative value. However, there is no simple and reliable method to determine it and that is why this effect has been neglected.

Within the flat wake assumption, the values of c coefficients are independent on Γ_{MAX} and once determined they can be used for seeking for the optimum value of stator bound vorticity. From the propeller point of view, the best approach is to apply as high stator circulation as possible. However, the stator itself generates a hydrodynamic drag. Its value is judged based on the simplified formula:

$$D = 1.5 \frac{L^2}{\frac{\pi\rho}{2} V^2 L^2} \quad (8)$$

where L is the lifting force determined using the lifting line model for stator blades, and V is the ship's advance speed. This formula is based on the induced drag experienced by a finite span hydrofoil with elliptical loading distribution operating in the ideal fluid.

After prescribing the arbitrarily chosen value of Γ_{MAX} for the whole stator, the initial propeller design is made. If the system efficiency, defined as:

$$\eta = \frac{(T_{PROP} - D_{STATOR})V}{2\pi nQ} \quad (9)$$

is satisfactory, then the stator circulation value is accepted as the design parameter.

PROPELLER DESIGN

The propeller design makes use of the very classic lifting line algorithm, supplemented with lifting surface correction factors [2]. The only difference, compared to conventional applications, is taking into account stator induced mean tangential velocities when calculating advance angles and coefficients.

At this stage, the propeller induced axial velocities in stator plane are calculated with the lifting surface software. Stator's presence is taken into account by applying stator induced tangential velocities in propeller plane. The propeller induced velocities are later used at the stator design stage.

STATOR DESIGN

The stator geometry was designed making use of an algorithm very similar to the classical propeller lifting line method [2]. Slight changes were necessary with respect to the local inflow angle definition, as the stator is not rotating.

The stator design starts with determining the value:

$$C_L b = 2 \frac{\Gamma}{V_w} \quad (10)$$

where C_L is the lift force coefficient, b is the blade width, Γ is the local bound circulation, and V_w is the local total velocity:

$$V_w = \sqrt{V_A^2 + V_T^2} \quad (11)$$

where V_T and V_A are the total tangential and axial velocities, respectively. They can be written as:

$$V_w = \sqrt{(V(1-w) + u_{A,B} + u_{A,S})^2 + u_{T,S}^2} \quad (12)$$

where V is the ship's advance speed, w is the wake fraction at the considered position, $u_{A,PS}$ is the axial velocity induced by the propeller in stator plane, and $u_{A,SS}$ and $u_{T,SS}$ are,

respectively, the axial and tangential velocity induced by the stator in its plane.

The stator induced velocities for formula (12) are determined with the discrete lifting line method, while the propeller induced axial velocity is determined with the discrete lifting surface analysis software, as mentioned before.

As the propeller rotates with respect to the stator, its induced velocity is taken as mean value at considered radius. However, the wake fraction w and the stator induced velocities $u_{A,PS}$ and $u_{T,SS}$ are functions of two coordinates: angle (defining the stator blade angular position with respect to the propeller shaft axis), and radius (being the stator blade radius).

Subsequently, the local cavitation number is calculated:

$$\sigma = \frac{p_A - p_v + \rho(h - l_z)g}{\frac{1}{2}\rho V_w^2} \quad (13)$$

The local blade thickness is initially assumed to be equal to:

$$t = 0.02 L \quad (14)$$

To determine the blade width-to-thickness ratio, cavitation diagrams are used. This allows us to determine the blade width b as:

$$b = t \left(\frac{b}{t} \right) \quad (15)$$

and to calculate directly the local lift force coefficient. The ideal attack angle is determined as:

$$\alpha_0 = 0.0245 C_L \quad (16)$$

Now, the local inclination angle of stator blade is given as:

$$\varphi = \arctan\left(\frac{V_T}{V_A}\right) + \alpha_0 \quad (17)$$

and the local camber value is:

$$f = 0.0679 f \cdot C_L \quad (18)$$

After determining the stator geometry, the stator drag is estimated from the formulas:

$$C_D = 0.008 + 1.7 \alpha_0^2 \quad (19)$$

$$\frac{dD}{dl} = \frac{1}{2} \rho V_w^2 b \quad (20)$$

where C_D is the local drag force coefficient and dD/dl is the drag force derivative along stator blade span. The overall stator drag is the sum of particular blade drag forces, obtained by integrating dD/dl over the span.

The abovementioned method for drag force determination is also applied to the propeller.

VORTEX MODEL ANALYSIS

The separate vortex model software was applied for the analysis task, upon the classical vortex lattice approach [2], [3], [4]. The first of them is used for analysing the propeller alone. It is meant for determining propeller open water loading characteristics. In this software, the propeller vortex wake is allowed to deform under its own induced velocities by convective manner. The propeller hub is also included, which allows the user to achieve reasonable results for high values of advance coefficient. The external wake field may be taken into account.

Sample results of propeller calculations with this software are given in Table 1:

Tab. 1. Representative results of lifting surface calculations

J	KT_{emp}	KT_{cal}	$10KQ_{emp}$	$10KQ_{cal}$	η_{emp}	η_{cal}
0.500	0.285	0.283	0.477	0.464	0.489	0.485
0.700	0.200	0.213	0.360	0.361	0.632	0.657
0.833	0.146	0.160	0.280	0.283	0.692	0.751
0.900	0.120	0.131	0.239	0.240	0.725	0.783
1.100	0.034	0.034	0.106	0.097	0.575	0.614

These results were obtained for a three-bladed symmetrical outline propeller [5]. The here presented lifting surface results are also representative for other propellers. However, better agreement for higher loads than for the design point is rather specific for this particular propeller. The overestimated efficiency values are likely to result from the underestimated value of viscous drag in the considered case.

This vortex lattice approach was considered capable of giving acceptable accuracy to be used for analysing propeller-stator systems. It is used for determining hydrodynamic characteristics of the propeller and the propeller induced velocity field.

Another piece of software was developed as the modification of the previous one. Initially, the vortex wakes were fixed to have certain rigid shape and no iterative relaxation was used. Some attempts were made to allow only the propeller vortex wake to deform, with the stator vortex fixed as flat surface. However, such a half-deformative approach turned out to lead to highly overestimated values of generated thrust force, so it was given up.

The first step of the VLM analysis comprises determining the stator blade circulation distribution. It is done based only on the external velocity field, while neglecting the presence

of the propeller. Once the stator circulation distribution is known, the mean value of the velocity vector (given in the cylindrical coordinate system) is calculated in the propeller plane for each radius (assuming that axial variation of stator induced velocities over propeller axial length is negligible). With this velocity field known, the propeller circulation distribution is determined and then the stator circulation distribution with propeller induced velocities is taken into account. This propeller-stator circulation coupling is an iterative process, but it converges very quickly – in 2–3 iterations.

4 APPLICATION

The ship Nawigator XXI was used as the test case for the above described algorithm. However, the newly designed system was not applied in full scale. The original propeller, which was the four-bladed CP469, served as the stock propeller during self-propulsion tests. Then, a decision was made that a new propeller expected to cooperate with the upstream stator shall be a five-bladed one. The input parameters for the design task were as following:

- design speed: $V = 12.9$ knots;
- propeller shaft rotation $n = 257.9$ rpm;
- required thrust $T = 124$ kN ;
- propeller diameter $D = 2260$ mm;
- stator blade length $L = 1130$ mm;
- number of propeller blades $Z = 5$;
- number of stator blades $N = 4$;
- propeller shaft immersion $h = 3500$ mm;
- average wake fraction coefficient $w = 0.362$;

Fig. 3. and Fig. 4 show 3D models of the designed propeller CP745 and stator ST001, respectively.

Main particulars of the propeller are:

- expanded area ratio $EAR = 0.7592$;
- mean pitch ratio $P/D = 0.7500$;
- skew angle $SKA = 15.85$ deg.

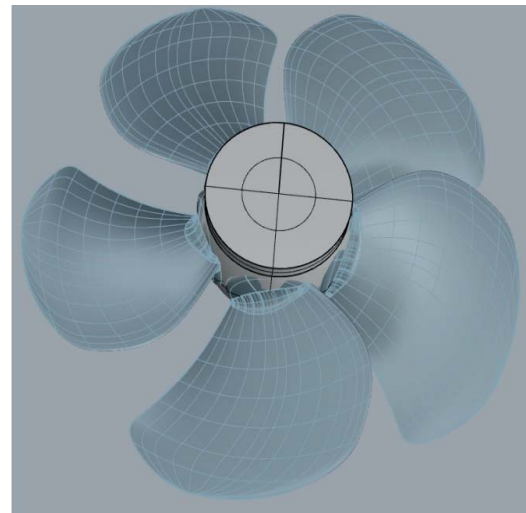


Fig. 3. Designed controllable pitch propeller CP745

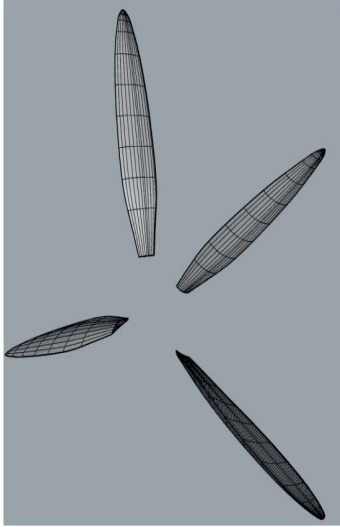


Fig. 4. Designed stator ST001

The presented propulsion system was manufactured in model scale and tested. The tests were performed for two arrangements - with and without stator:

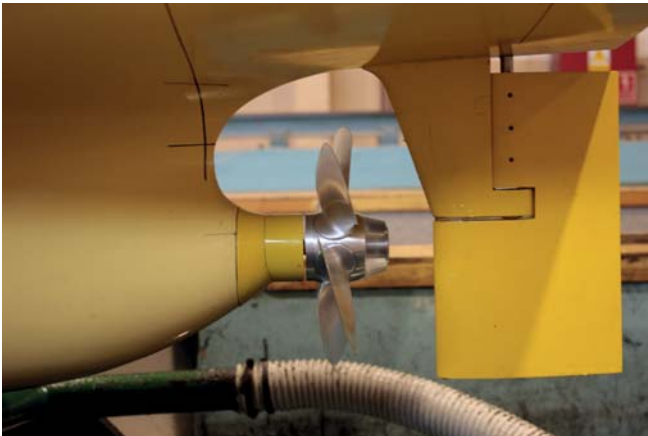


Fig. 5. Self-propulsion test arrangement without pre-swirl stator



Fig. 6. Self-propulsion test arrangement with pre-swirl stator

All models used in the tests were manufactured in the Ship Hydromechanics Division of CTO S.A. The aft bulb of the hull model was cut off and replaced with exchangeable ending. The latter was manufactured in two versions: one reproducing the original aft bulb geometry and the other – with stator blades mounted.

WAKEFIELD MEASUREMENT

The wakefield was measured behind the hull model without and with stator, Fig. 7 and Fig. 8, respectively.

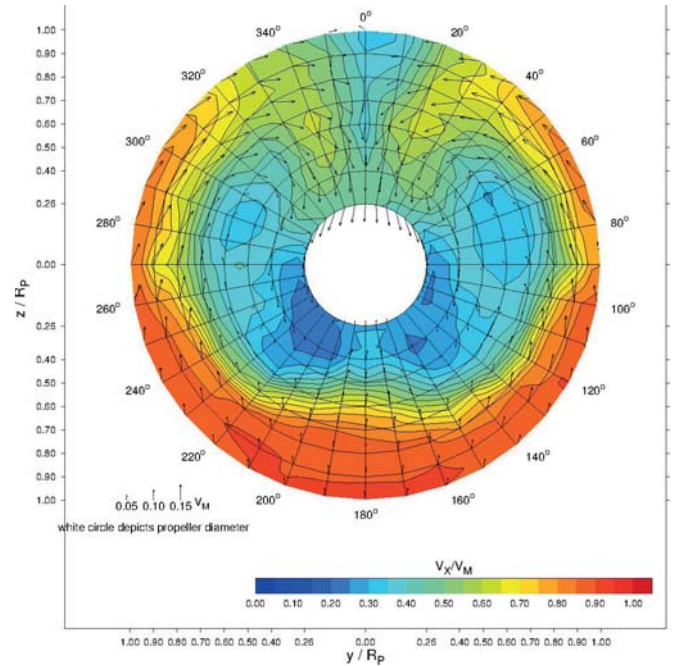


Fig. 7. Non-uniform velocity field behind hull model without stator

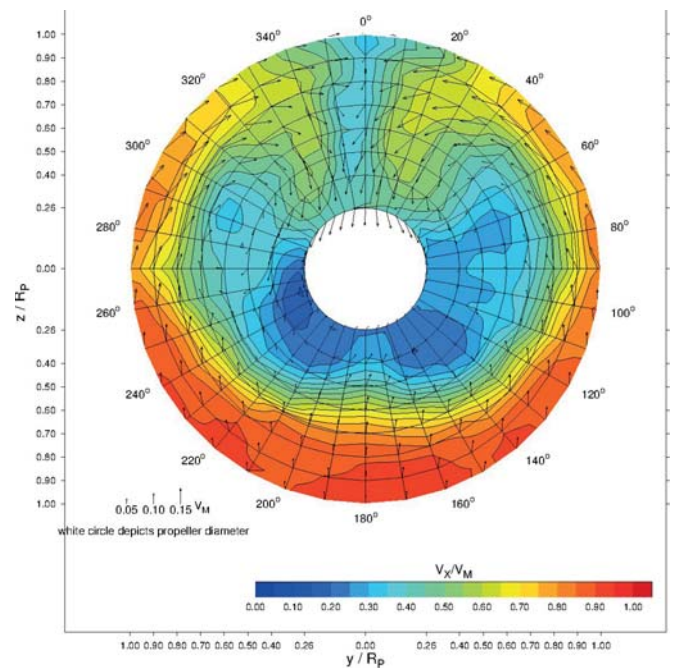


Fig. 8. Non-uniform velocity field behind hull model with stator

The differential wakefield is shown in Fig. 9. It presents the difference between velocity fields measured behind the hull with and without stator.

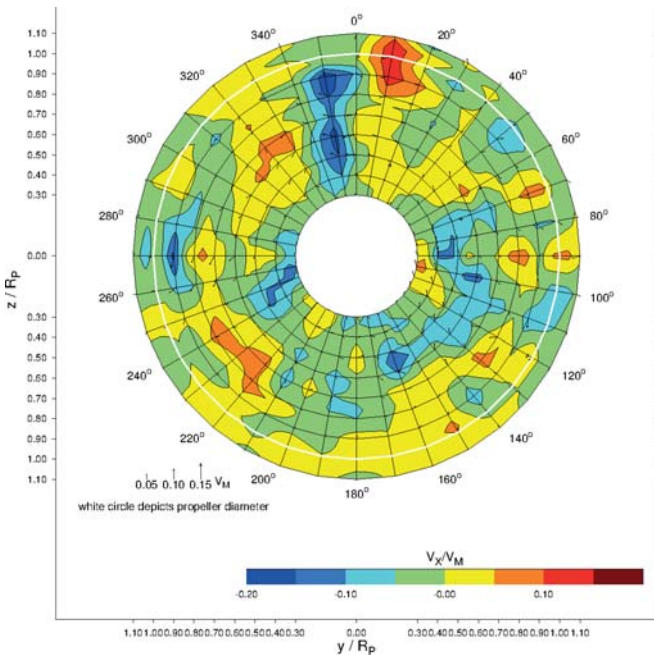


Fig. 9. Differential wakefield

The mean value of the differential wakefield is zero (within the measuring tolerance). It confirms the conclusion from the lifting line model that the stator, in general, does not influence the average axial velocity in the propeller disc.

However, there is no clear tendency in local axial velocity contribution with respect to particular stator blades (angular positions: 60, 120, 260 and 350 degrees). We believe that it results from the fact that the stator was designed to cooperate with the propeller. The inflow angles on the stand-alone stator are substantially different, and so is the stator's circulation distribution. This conclusion is not contradictory to the statement on average axial velocity, as it is independent of the lifting line load distribution.

The differential tangential component of the wakefield is given in Fig. 10.:

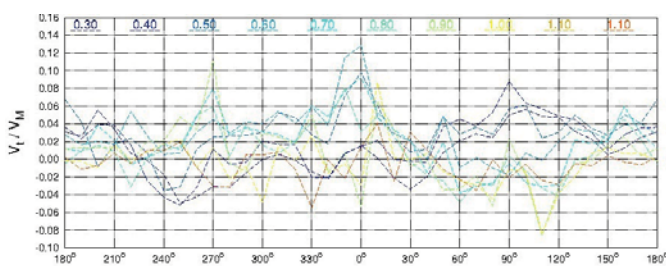


Fig. 10. Differential wakefield tangential component

It can be clearly seen that for most part of the measuring area, there is notable positive contribution from the stator to the tangential velocity component. However, since the stator

load without the cooperating propeller is much lower than the design one, the tangential induced velocities are also small. Nevertheless, the effect is as desired, and the stator introduces a non-zero tangential velocity component.

SELF-PROPULSION TEST

The self-propulsion test was performed in two configurations: with and without stator. The test results for these two configurations are compared in Table 2.

Tab. 2. Stator influence on propulsion prediction

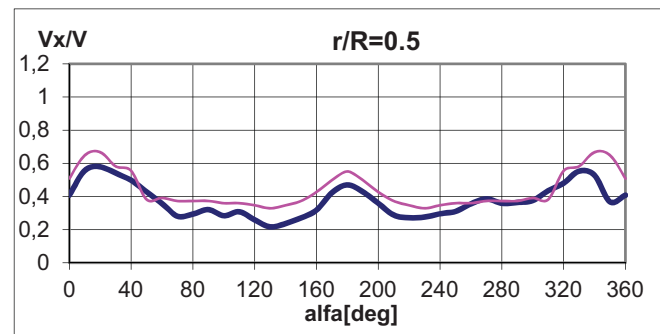
V[kn]	PD _o [kW]	n _{w/o} [rpm]	PD _w [kW]	n _w [rpm]
9.00	225	173.4	218	169.6
10.00	334	196.6	322	192.6
11.00	504	224.6	475	218.3
12.00	716	251.5	680	245.1
13.00	1123	289.3	1077	282.9

It can be clearly seen that the stator's presence significantly affected the propulsion system characteristics. The stator's presence allowed to reduce both the required power delivered to the propeller, and the revolution rate. This brings not only economical gains, thanks to the reduction in fuel consumption, but also decreases the risk of cavitation.

CAVITATION TEST

The designed system also underwent the cavitation test. The input parameters for this test were: $KT=0.253$ and $\sigma=2.622$. The nominal wakefield in propeller plane was reproduced with the use of a dummy model equipped with appropriate wire mesh.

The nominal wakefield applied for the cavitation test was that measured behind the hull without stator. As the stator was present in the testing arrangement, it was pointless to reproduce the wakefield measured behind the hull with the stator mounted. Fig. 11 compares the nominal wakefields measured in the towing tank and in the cavitation tunnel. The thick blue line refers to the towing tank wakefield, and the thin purple line refers to the cavitation tunnel.



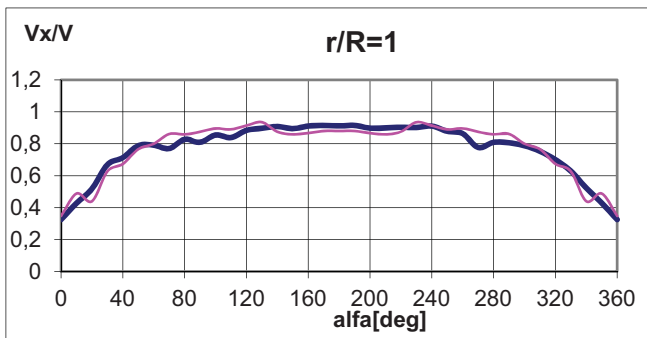
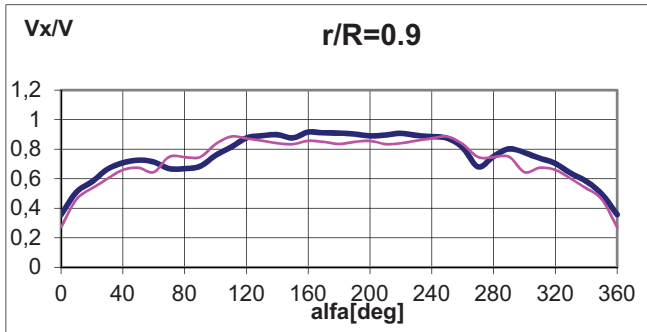
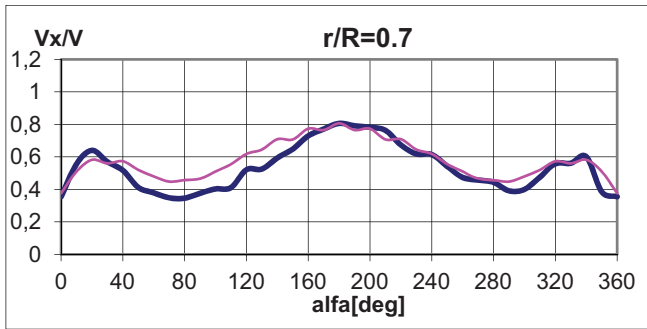


Fig. 11. Wakefield axial component

Cavitation observation revealed a weak, but stable cavitating tip vortex.

The presence of the tip vortex on the propeller is likely to result from an error made within the assumed designed condition saying that the stator blade should have the same length as the propeller radius. This error leads to the intersection of the stator tip vortex with the propeller tip, which may provoke increased cavitation in this region.

No cavitation was observed on the stator blades. An attempt to determine stator's cavitation limits failed, as the wire mesh applied for modelling the wakefield started to cavitate long before any form of cavitation became visible on the stator.

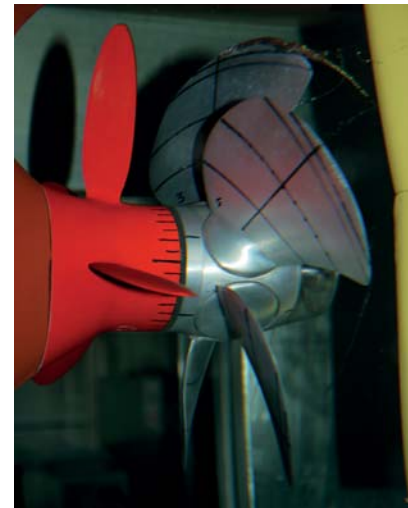


Fig. 12. Cavitation observation

TIP VORTICES

Additional cavitation test was performed to visualize propeller tip vortices. The rotational speed of the propeller was fixed and the advance speed of water in the cavitation tunnel was decreased to increase propeller load. The pressure in the test section was kept at such a level as to obtain stable cavitating tip vortices.

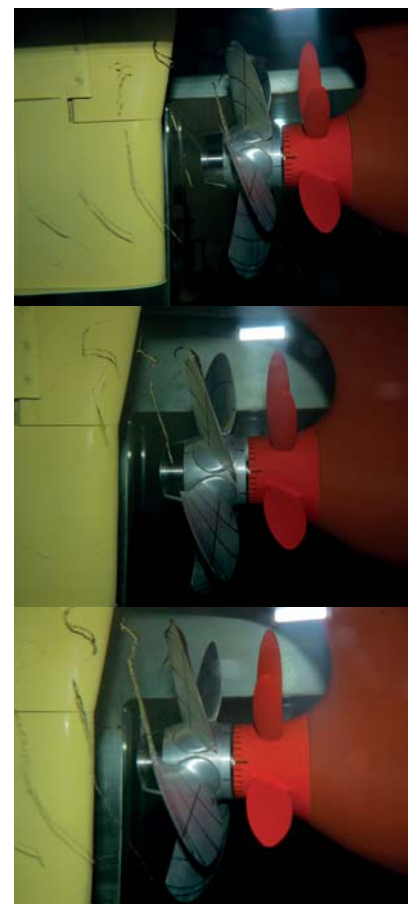


Fig. 13. Tip vortices for KT (from up to down): 0.191; 0.211; 0.243.



Fig. 14. Tip vortices for KT (from up to down): 0.243; 0.296; 0.361

This test was performed to collect the reference material for further validation of vortex wake relaxation procedures in the VLM-base propeller analysis software.

CONCLUSIONS AND FURTHER WORK

The actual vortex model is very robust. However, due to the applied simplifications it does not give very accurate results. The main reason for this was identified as neglecting the free vortex wake deformation. This effect is to be included in future development of the theory. Moreover, it is planned to replace the simple lifting line algorithm used for determining the pitch and camber of both propeller and stator with the lifting surface model. The presented method can be applied in designing propeller stator systems. However, the designed systems should be carefully tested in model scale, especially in cases of high propeller-stator loads, when the behaviour of vortex systems may significantly differ from that within the adopted model.

ACKNOWLEDGEMENT

Materials and concepts presented in this paper were elaborated within the INRETRO project realized as the European ERA-NET venture within the MARTEC II framework. The financial support by the national funding associations is gratefully acknowledged.

BIBLIOGRAPHY

1. Kerwin, J., Coney, W., Hsin, C.: *Hydrodynamic Aspects of Propeller/Stator Design*, The Society of Naval Architects and Marine Engineers, 1988.
2. Greeley, D., Kerwin, J.: *Numerical Methods for Propeller Design and Analysis in Steady Flow*, Transactions of Society of Naval Architects & Marine Engineers, 1982.
3. [3] Jarzyna, H., Koronowicz, T., Szantyr, J.: *Design of Marine Propellers - Selected Problems*, Wrocław: Ossolineum, 1996.
4. [4] Bugalski, T., Szantyr, J.: *Numerical Analysis of the Unsteady Propeller Performance in the Ship Wake Modified by Different Wake Improvement Devices*, Polish Maritime Research, 2014.
5. [5] Koyama, K.: *Comparative calculations of propellers by surface panel method - workshop organized by 20th ITTC Propulsor Committee*, Papers of Ship Research Institute, 1993.

CONTACT WITH THE AUTHORS

Przemysław Król

e-mail: przemyslaw.krol@cto.gda.pl

Ship Design and Research Centre

Szczecinska 65, 80-392 Gdańsk

POLAND

Faculty of Mechanical Engineering

Gdansk University of Technology

Narutowicza 11/12, 80-233 Gdańsk

POLAND

Tomasz Bugalski

e-mail: tomasz.bugalski@cto.gda.pl

Ship Design and Research Centre

Szczecinska 65, 80-392 Gdańsk

POLAND

OUTLIER DETECTION IN OCEAN WAVE MEASUREMENTS BY USING UNSUPERVISED DATA MINING METHODS

Kumars Mahmoodi, PhD student

Hassan Ghassemi, Prof.

Amirkabir University of Technology, Tehran, Iran

ABSTRACT

Outliers are considerably inconsistent and exceptional objects in the data set that do not adapt to expected normal condition. An outlier in wave measurements may be due to experimental and configuration errors, technical defects in equipment, variability in the measurement conditions, rare or unknown conditions such as tsunami, windstorm and etc. To improve the accuracy and reliability of an built ocean wave model, or to extract important and valuable information from collected wave data, detecting of outlying observations in wave measurements is very important. In this study, three typical outlier detection algorithms: Box-plot (BP), Local Distance-based Outlier Factor (LDOF), and Local Outlier Factor (LOF) methods are used to detect outliers in significant wave height (H_s) records. The historical wave data are taken from National Data Buoy Center (NDBC). Finally, those data points are considered as outlier identified by at least two methods which are presented and discussed. Then, H_s prediction has been modelled with and without the presence of outliers by using Regression trees (RTs).

Keywords: ocean wave data, data mining, outlier detection, data correction

INTRODUCTION

Appropriate data collection with the least uncertain instances is very important in the field and experimental researches. That is because such data are usually used for different objectives e.g. validation and calibration of numerical and mathematical models. Outliers affect the analysis and their results and also cause perturbation in process of concluding. Also they contain useful information underlying the abnormal behaviour. The data can arise from several different mechanisms or causes, such as human errors, errors in data recording or collection, environmental conditions, sampling errors, unusual phenomena in measurement conditions, faulty or non-calibrated equipment, Incorrect

assumptions about the distribution of the data [1], natural variations in the population and etc. So detecting of outlying observations in collected data is necessary. After detection of outliers, they can be removed or corrected.

There are different instruments for measuring sea data. These instruments are able to gather the metrological and oceanography data such as speed, direction and duration time of wind, air and water temperature, air pressure and humidity, density and salinity of sea water, and historical sea water level changes. Wave buoys are commonly used instruments to this end [2]. The devices can measure important wave data, such as height and period. Various factors may cause outliers in the buoys' measured values. It is necessary to detect outliers and remove or correct them before extracting any information from collected data.

Outlier detection in wave measurements can be used for automatic identification of hurricanes and typhoons [3, 4], identification of areas with the influence of storms, which should be further studied by using appropriate models with higher accuracy, detect potential height wave energy resources, awareness of ocean dynamics and climatic variability, definition of operable conditions in shipping routes, maintenance and repair strategies for offshore constructions, extreme wave analysis [5], eliminate data related to malfunctions of buoys, so the results will be accurate enough to make them suitable for ocean studies etc. [6].

The main aim of this study is to detect outliers in the historical data taken from buoys by using some unsupervised data mining approaches. Unsupervised outlier detection methods do not require training data, and assume that normal instances are far more frequent than outliers. So these techniques are most useful, when training data is not available. The discussed methods are: Box-plot, LDOF, and LOF. Here, outliers in measured significant wave heights (H_s) are selected as a case study. H_s is an average measurement of the largest one-third of wave heights, which is a useful way to describe the sea state. This parameter is the basis for many computations in the coastal and marine engineering. Therefore its correct measuring is very important.

OUTLIER DETECTION APPROACHES

Outlier detection, also known as anomaly detection or data cleansing [7], is an important research problem in data mining and a pre-processing step in any data analysis application that aims to discover useful abnormal and irregular patterns hidden in data sets [8, 9]. The discussed methods are presented below.

BOX-PLOT (BP)

Box-plot test [10] is the commonly used outlier test for normal distributions. It is a useful type of graph used to show the shape of distribution by using the five major attributes: smallest non-outlier observation (*Min*), lower quartile (Q1), median, upper quartile (Q3), and largest non-outlier observation (*Max*). The quantity $Q3 - Q1$ is called the Inter Quartile Range (*IQR*). A box-plot is constructed by drawing a box between the upper and lower quartiles with a solid line drawn across the box to locate the median. In this method a data point will be labelled as an outlier if it is located $1.5 \times IQR$ times lower than Q1 or $1.5 \times IQR$ times higher than Q3.

LOCAL DISTANCE-BASED OUTLIER FACTOR (LDOF)

LDOF [11] is a distance – based method which uses the relative location of an object to its neighbours to determine the degree to which the object deviates from its neighbourhood.

In this method only the objects with the highest LDOF values are regarded outliers. LDOF implementation includes the following steps:

- 1) Find k -nearest neighbours distance of object p : it equals the average distance from p to all objects in $N_k(p)$. The k -nearest neighbours distance of object p is defined as:

$$\bar{d}(p) = \frac{1}{k} \sum_{q \in N_k(p)} \text{dist}(p, q) \quad (1)$$

where p , and q are some data points in the data set D , $\text{dist}(p, q)$ denotes the distance between point p and q (in this research Euclidean distance), $N_k(p)$ is the set of the k -nearest neighbours of object p (excluding p), and k is a user-specified parameter which is selected according to the type of problem and nature of data set by trial-and-error method, but it is beneficial to use a large neighbourhood size k . kNN algorithm [12] is used to find nearest neighbours of object p . In data mining, the kNN algorithm is a very useful non-parametric method used to analyze a data object with respect to its nearest neighbours..

- 2) Find kNN inner distance of object p : given $N_k(p)$, the k -nearest neighbours inner distance of p is defined as the average distance among objects in $N_k(p)$:

$$\bar{D}(p) = \frac{1}{k(k-1)} \sum_{q, q' \in N_k(p)} \text{dist}(q, q') \quad (2)$$

- 3) Find LDOF of object p : the local distance-based outlier factor of p is defined as:

$$LDOF_k(p) = \frac{\bar{d}(p)}{\bar{D}(p)} \quad (3)$$

If $LDOF_k(p) > 1$, it means that p is outside its neighbourhoods and can be an outlier candidate.

LOCAL OUTLIER FACTOR (LOF)

LOF is the first major density-based outlier detection method proposed by Kriegel and Ng [13]. It is possible to detect local outliers by assigning an outlier score (LOF) to any given data point depending on its distance from its local neighbourhood. Assume that p, q and o are some data points in the data set D , LOF is computed in following procedure:

- 1) Find k -distance of object p : given a positive integer user-specified parameter k , $k_distance(p)$, is defined as the distance between object p and object o , denoted with $\text{dist}(p, o)$, such that:
 - i) for at least k objects $o' \in D \setminus \{p\}$ it holds that $\text{dist}(p, o') \leq \text{dist}(p, o)$, and
 - ii) for at most $k-1$ objects $o' \in D \setminus \{p\}$ it holds that $\text{dist}(p, o') < \text{dist}(p, o)$.
- 2) Find k -distance neighbourhood of object p : $k_distance_neighbourhood$ of p contains every object whose distance from p is not greater than the $k_distance$, i.e:

$$N_k(p) = \{q \in D \setminus \{p\} | \text{dist}(p, q) \leq k_distance\} \quad (4)$$

- 3) Find reachability distance of object p w.r.t. object o : The reachability distance of object p with respect to object o is defined as:

$$reach_{dist_k}(p, o) = \max \{k_distance(o), dist(p, o)\} \quad (5)$$

- 4) Find local reachability density of object p : the local reachability density of p is defined as:

$$lrd_k(p) = 1 / \left(\frac{\sum_{o \in N_k(p)} reach_{dist_k}(p, o)}{|N_k(p)|} \right) \quad (6)$$

- 5) Find local outlier factor of object p : the $LOF(p)$ is defined as:

$$LOF_k(p) = \frac{\sum_{o \in N_k(p)} \frac{lrd_k(o)}{|N_k(p)|}}{|N_k(p)|} \quad (7)$$

The LOF of an object reflects the density contrast between its density and those of its neighbourhood. So $LOF_k(p)$ captures the degree of a point being an outlier. If the LOF value becomes larger, then the degree of outlieriness will be risen. In general, if $LOF_k(p)$ were be close to 1, then object p is normal; and if $LOF_k(p)$ were be larger than 1, object p is outlier candidate.

DATA AND STUDY AREA

The historical wave data were taken from National Data Buoy Center (<http://www.ndbc.noaa.gov>). Tab. 1 shows the main characteristics of four buoys considered in this study at the Western coast of the USA. All historical data were collected in the year 2015. Missing records are removed from all the studied stations. The statistics and histogram bar plot with 20 bins of H_s data sets are presented in Tab. 2 and Fig. 1.

Tab. 1. Buoy's geographic coordinates and description

Characteristics	Station 46011 (34°57'22" N 121°1'7" W)	Station 46028 (35°42'42" N 121°51'30" W)	Station 46042 (36°47'29" N 122°27'6" W)	Station 46054 (34°15'53" N 120°28'37" W)
Site elevation	sea level	sea level	sea level	sea level
Air temperature height	4 m above site elevation	4 m above site elevation	4 m above site elevation	4 m above site elevation
Anemometer height	5 m above site elevation	5 m above site elevation	5 m above site elevation	5 m above site elevation
Barometer elevation	sea level	sea level	sea level	sea level
Sea temperature depth	0.6 m below water line	0.6 m below water line	0.6 m below water line	0.6 m below water line
Water depth	464.8 m	1036 m	2098 m	382.3 m

Tab. 2. Statistics of $H_s(m)$ data sets corresponding to all the studied stations

Station	Number of instances	Max	Min	Mean	Median	Std
46011	5355	7.08	0.66	1.9098	1.66	0.9308
46028	3593	5.14	0.56	2.0372	1.95	0.7468
46042	5714	8.92	0.63	2.0724	1.87	0.9865
46054	8700	7.08	0.69	1.8481	1.69	0.7610

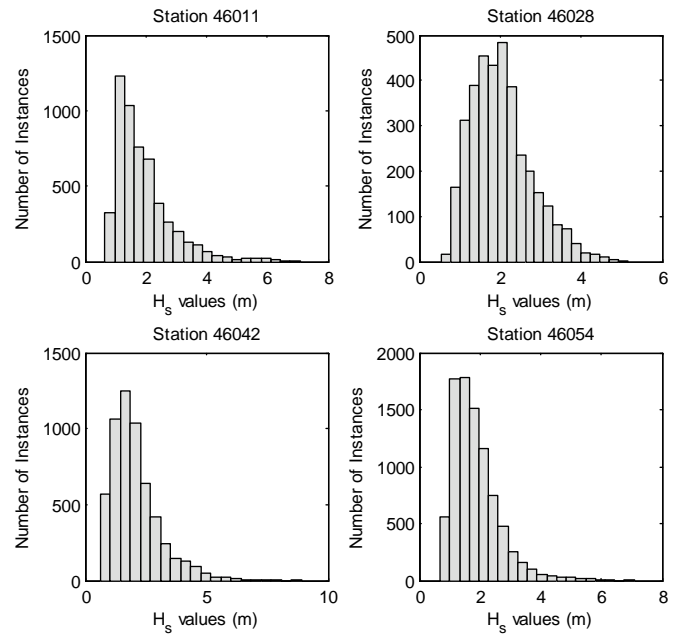


Fig. 1 Histogram bar plot of H_s with 20 bins of all the studied stations

EXPERIMENTAL RESULTS

In this section, the effectiveness of the three above mentioned outlier detection methods when applied on H_s data sets, is investigated. At first, outliers in all the data sets are detected individually by each method, then those data points are considered as outlier identified by at least two methods. All algorithms were implemented in Matlab software. The results of Box-plot method are shown in Tab. 3.

To implement LDOF to data sets it is necessary to determine the neighbourhood size k . Based on the rule for selecting k value, suggested by Zhang and *et al.*, $k = 150$ was assumed in all data sets. The data points with $LDOF > 1$ (Eq. 3) are considered outliers. Fig. 2 demonstrates the LDOF coefficient values in all the data sets along with the threshold limit value (horizontal line). The data points falling above the horizontal line have been considered the outlier candidates. The experimental results are listed in Tab. 3.

Similar LDOF method, to implement LOF for data sets requires to determine the neighbourhood size k to compute the density in the neighbourhood of data points. The value of this parameter is application-dependent and selected based on the nature of studied data sets. A heuristic method is proposed to pick the right k values for the LOF computation [13]. Its authors provided several guidelines for picking the range of k values. Following such guidelines, $k = 100$ is selected for lower bound and $k = 500$ for upper bound in the experiments. Fig. 3 shows the mean of data point LOF values of all data sets, with increasing k at the step of 20. It can be seen from this figure that for all the data sets the mean LOF values change a little and is almost stable when the k value is higher than 220. In fact, if k value is selected from the range of [150, 500], the mean LOF values and thus the results will not change much. For this reason and to reduce the amount of calculations and computation time, k is set to 220 for all data sets. In the LOF method, the data points with $LOF > 1$ (Eq. 7) are considered outliers. Here, the number 1.9 is considered a threshold for Stations 46011, 46028 and 46042, and number 2.15 - for Station 46054 by trial and error method. A data point is labelled an outlier if its LOF coefficient exceeds the thresholds. Tab. 3 provides the results of LOF method applied to the data sets. LOF coefficients of data sets are plotted in Fig. 4. The data points falling above the horizontal line have been considered the outlier candidates.

COMPRESSION OF RESULTS

As mentioned above, outliers are patterns which deviate from an expected normal behaviour. This definition looks simple but is highly challenging because it is difficult to define what is the normal behaviour or a normal region. Some of the difficulties are: the uncertainty in the exact boundary between normal and abnormal behaviour, the absence of a comprehensive definition of outliers, various definitions of outliers in the different science fields and applications, natural behaviours of the studied phenomenon in certain circumstances which tends to be similar to the actual outliers, availability of labelled data, and other additional factors. Due to the challenges, the outlier detection problem is not easy and is usually problematic. For this reason, most of the existing outlier detection techniques lead to different results, based on their formulation, definition of outliers and type of outliers to be detected. This matter is also observed in this study because different approaches produce different results, as seen in Tab. 3. Based on this table, Box-plot method detected more objects as being outlier; In fact, the sensitivity of this method was higher than other methods. However, depending on the parameters of each method, their sensitivity may also change. For example in LOF method, if threshold parameter is selected lower, more objects will be selected as being outlier. However, it is possible that some normal data are considered to be outliers by this method. Hence the right choice of each method parameters is always very important and may be changing the results. To detect potential outliers,

it is better to consider data points to be outlier candidates which are detected by most methods. In fact, such data are most likely to be considered outliers. In this research the voting method is used to better detect the outliers. Voting is not a new method and uses the results of other methods to detect outliers. In the voting method, outliers are data points which have been selected as the outlier by most methods. As a result, the voting method leads to more accurate and reliable results. To implement voting into results of the discussed outlier detection methods, those data points are considered as outlier which have been identified by at least two methods. The voting results are presented in Tab. 3. The final outlier candidates detected in all data sets, obtained by voting, are presented in Fig. 5. In this figure detected outliers are distinguished with circle marks.

After detecting outliers the reason of their occurrence should be carefully investigated because outliers in ocean wave measurements result from various reasons such as meteorological events like windstorm, or fail to function properly in sensor data streams, rare phenomena like tsunami, defects occurring in measurement devices and data transmission, etc. This way, valuable information can be achieved from the detection of outliers.

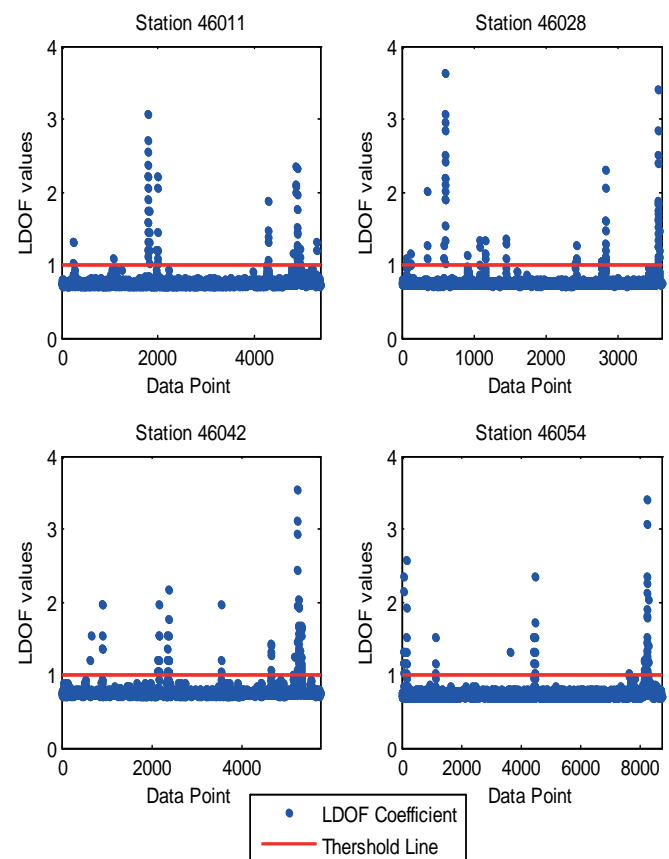


Fig. 2 LDOF coefficients for all the studied stations

SIGNIFICANT WAVE HEIGHT PREDICTION

Outlier detection is one of the major issues in preparing the data for data mining classification and prediction problems. In this study to show the importance of outlier detection in the ocean wave studies, significant wave height prediction using wave parameters is considered with and without the presence of outliers. Regression trees (RTs) [14] are used to model H_s . Tab. 4 shows details of the predictive variables for this problem. In all created models, the output variable is WVHT (H_s), and other variables are considered inputs. In this research two error criterion measurements are considered in order to evaluate the performance of the created models, namely, the Root Mean Square Error (RMSE) and the Pearson's correlation coefficient (R^2), according to the following equations:

$$RMSE = \sqrt{\frac{1}{n} \sum_{i=1}^n (T_i - O_i)^2} \quad (8)$$

$$R = \frac{\sum_{i=1}^n (T_i - \bar{T})(O_i - \bar{O})}{\sqrt{\sum_{i=1}^n (T_i - \bar{T})^2 \sum_{i=1}^n (O_i - \bar{O})^2}} \quad (9)$$

where n represents the total number of instances, while T_i and O_i represent the experimental and predicted values, respectively; \bar{T} and \bar{O} are the average values of these data.

Regression trees are the well-known predictive modelling approaches in data mining, which are built through a process known as binary recursive partitioning. It is necessary to set a series of parameters for the training of regression trees, such as tree depth etc. The optimal architecture of the developed RTs is presented in Tab. 5. The choice of the tuning parameters comes from preliminary tests carried out on the studied data sets. RTs results are presented in Tab. 6. Also in this case the experimental results demonstrated that after removing outliers the accuracy of the created models is increased.

Tab. 4. Variables used in the experiments

Acronym	Predictive variable	Unit
WDIR	Wind direction	[degree]
WSPD	Wind speed	[m/s]
GST	Gust speed	[m/s]
WVHT	Significant wave height	[m]
DPD	Dominant wave period	[sec]
APD	Average period	[sec]
PRES	Atmospheric pressure	[hPa]
ATMP	Air temperature	[°C]
WTMP	Water temperature	[°C]

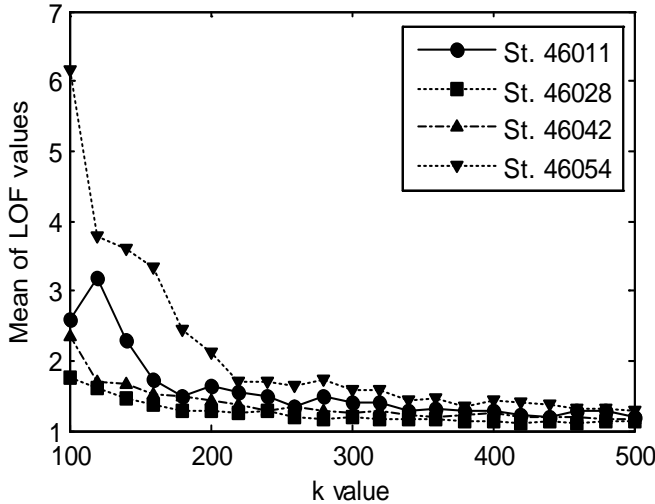


Fig. 3 Mean of data point LOF values with different k , for all the studied stations

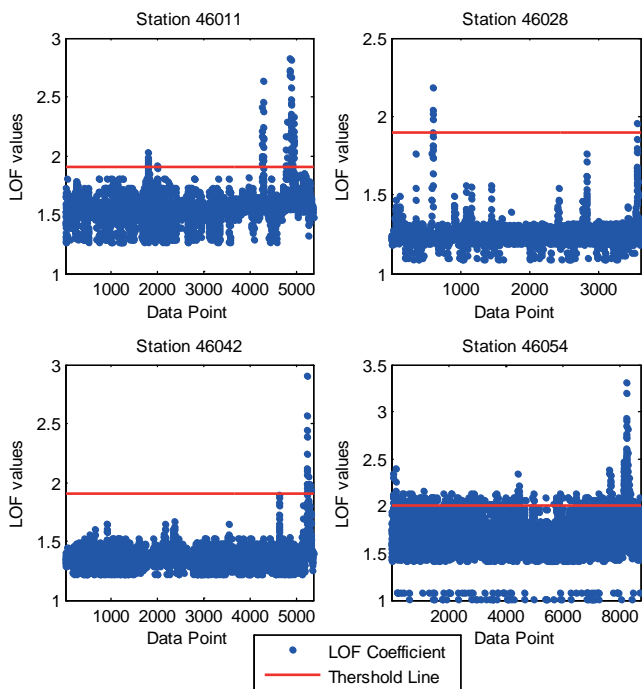


Fig. 4 LOF coefficients of all the studied stations

Tab. 3. Number of outliers in H_s data sets, detected by all methods

Station	BP	LDOF	LOF	Voting
46011	271	69	81	69
46028	69	78	6	1
46042	269	82	18	48
46054	299	67	83	71
Sum	908	296	188	189

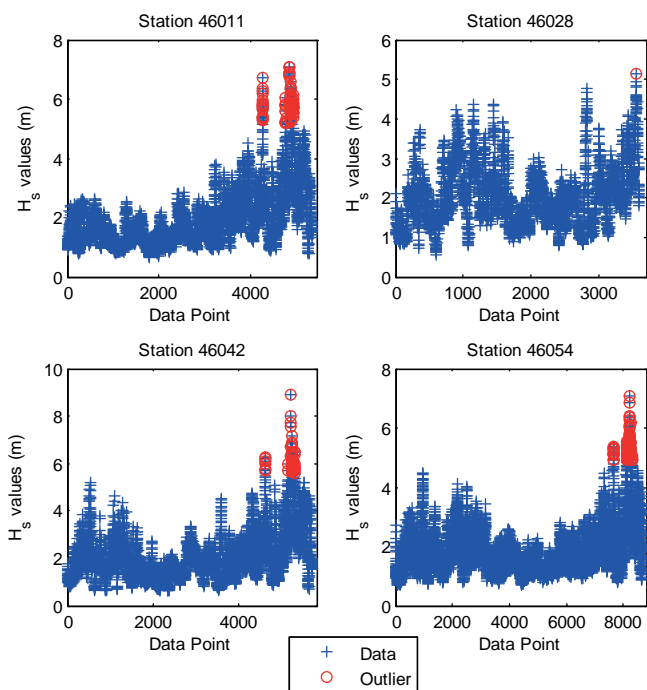


Fig. 5 Final outliers detected in all the studied stations by using voting method

Tab.5. RTs selected structure for all the studied stations

Parameter	Setup
Tree maximum depth	Automatic
Minimum leaf	1
Minimum parent	10
Split Criterion	Mean Squared Error

Tab. 6. Comparative performance of the H_s estimation by the RTs with and without the presence of outliers

Station	With outliers		Without outliers	
	RMSE (m)	R^2	RMSE (m)	R^2
46011	0.1530	0.9697	0.1410	0.9729
46028	0.1434	0.9629	0.1433	0.9630
46042	0.1709	0.9651	0.1697	0.9699
46054	0.1375	0.9640	0.1310	0.9673
Mean	0.1512	0.9654	0.1462	0.9683

CONCLUSIONS

In this paper, the outlier detection problem in data of the significant ocean wave height H_s was presented and discussed. Three outlier detection approaches, i.e. the Box-plot, LDOF, and LOF, were described and their performance were compared. Box plot can be used for one-dimensional data sets, while LDOF and LOF are methods for identifying outliers in multi-dimensional data sets, which utilize data density estimation concepts. Based on the experiments, the mentioned methods presented different results. Each method has several parameters which specify its performance. Input

parameters have great influence on the outlier detection performance and should be carefully selected based on the nature of studied data sets. Based on the obtained results it can be stated that the LOF and Box plot were of low and high sensitivity in outlier detection in studied data sets, respectively. In this research the voting method was used to achieve a better outlier identification. The experiment shows that the voting method can achieve a high performance in detecting outliers, compared to other methods. In general, outliers are caused due to an error or rare behaviour of studied phenomenon containing valuable information about some unexpected events. For example, it is possible to detect tsunami by recognizing the outliers. In H_s measurements the outlying observations are mostly related to the presence of typhoons and/or hurricanes, which must be removed to avoid wrong analysis of incorrect results and create accurate analytical and numerical models. To demonstrate the effect of outliers in wave measurement data collection, the significant wave height was modelled based on metrological and wave parameters. The results showed that the accuracy of the created models increased in case of absence of outliers. So far, many outlier detection methods which can be used to detect outliers in ocean wave measurements have been proposed by researchers. Experimental results demonstrated that the proposed approach is capable to better detect outliers. It is suggested that outliers should be identified before any analysis and deduction of data sets by using the presented procedure. A future direction of research is to apply this procedure to multi-dimensional data sets of sea variables with the use of different outlier detection methods.

REFERENCES

- Iglewicz, B., Hoaglin, D.C.: *How to detect and handle outliers*. Milwaukee, WI: ASQC Quality Press, 1993.
- Sun S. Z., LI, H., Sun, H. : *Measurement and analysis of coastal waves along the north sea area of China*. Polish Maritime Research, 3 (91) 2016, 23, pp. 72-78.
- Whan Lee, J., Park, S. C., Kee Lee, D., Ho Lee, J. : *Tsunami arrival time detection system applicable to discontinuous time-series data with outliers*. Journal of natural hazards and earth sciences, 2016, 16 (12), pp. 2603-2016.
- Mínguez, R., Reguero, B.G., Luceño, A., Méndez, F.J. : *Regression models for outlier identification (hurricanes and typhoons) in wave hindcast databases*. Journal of Atmospheric and Oceanic Technology, 2012, 29, pp. 267-285.
- Lucas, C., Muraleedharan, G., Soares, C. G. : *Outliers identification in a wave hindcast dataset used for regional frequency analysis*. Maritime Technology and Engineering, 2015, pp. 1317-1327.

6. Reguero, B.G., Menéndez, M., Méndez, F.J., Mínguez, R., Losada, I. J. : *A Global Ocean Wave (GOW) calibrated reanalysis from 1948 onwards*. Coastal Engineering, 2012, 65, pp. 38–55.
7. Chandola, V., Banerjee, A., Kumar, V. : *Anomaly detection – a survey*. ACM Comput Surv. 2009, 4 (3), pp. 1–58.
8. Barnett, V., Lewis, T. : *Outliers in Statistical Data*. John Wiley, 3rd edition 1994.
9. Zhang, Ji. : *Advancements of Outlier Detection: A Survey*. ICST Transactions on Scalable Information Systems, 2013, 13 (1), pp. 1-26.
10. Muraleedharan, G., Lucas, C., Guedes Soares, C.: *Regression quantile models for estimating trends in extreme significant wave heights*. J. Ocean Engineering, 2016, 118, pp. 204–215.
11. Zhang, K., Hutter, M., Jin, H. : *A new local distance-based outlier detection approach for scattered real-world data*. Proc. 13th Pacific-Asia Conf. on Knowledge Discovery and Data Mining, 2009, pp. 813-822.
12. Chen, Y., Miao, D., Zhang, H. : *Neighborhood outlier detection*. Expert Systems with Applications, 2010, 37 (12), pp. 8745-8749.
13. Breunig, M. M., Kriegel, H.-P., Ng, R. T., *et al.*: *LOF: Identifying density-based local outliers*. In W. Chen, J. F. Naughton, & P. A. Bernstein (Eds.), Proceedings of the ACM SIGMOD international conference on management of data, ACM Press , Dallas, Texas , 2000, pp. 93–104.
14. Troncoso, A., Salcedo-Sanz, Casanova-Mateo, S., Riquelme, J.C, C., Prieto, L. : *Local models-based regression trees for very short-term wind speed prediction*. Renewable Energy, 2015, 81, pp. 589-598.

CONTACT WITH THE AUTHORS

Hassan Ghassemi

e-mail: gasemi@aut.ac.ir

Department of Maritime Engineering
Amirkabir University of Technology
Hafez avenue, 14717 Tehran

IRAN

Kumars Mahmoodi

e-mail: kumarsmahmoodi@aut.ac.ir

Department of Maritime Engineering
Amirkabir University of Technology
Hafez avenue, 14717 Tehran

IRAN

DYNAMISM PATTERNS OF WESTERN MEDITERRANEAN CRUISE PORTS AND THE COOPETITION RELATIONSHIPS BETWEEN MAJOR CRUISE PORTS

Jeronimo Esteve-Perez

Universidad Politécnica de Cartagena, Department of Naval Technology, Spain

Antonio Garcia-Sanchez

Universidad Politécnica de Cartagena, Department of Economics, Spain

ABSTRACT

The Mediterranean Sea has seen an increase of ports hosting cruise ships during the first fifteen years of the 21st century. The increase in cruise ship presence in Mediterranean ports is associated with the dynamism of cruise traffic in recent years, with an average annual growth of 7.45% for cruise passengers worldwide during the period of 1990-2015. Cruise traffic is a maritime business that is primarily composed of two elements, maritime affairs and tourism. This article focuses on the maritime component. With the growth of the cruise industry, cruise lines have been forced to seek new ports to meet demand in an attempt to create differentiated products based on the ports that compose the itinerary. The itinerary system of cruise traffic makes the cruise ports depend on one another to design an itinerary. This feature results in both complex geographic relationships in the design of a cruise itinerary and complex competitive/cooperative relationships between ports. The aim of this article is to present the hierarchic picture of a sample of 29 cruise ports in the Western Mediterranean region during the period of 2000-2015. To achieve this goal, a port size classification is proposed and a shift-share analysis at the inter- and intra-group size level is applied. Moreover, concentration measures are used to determine the changes in the levels of market concentration. Furthermore, a dynamic model is proposed to determine the competitive or cooperative relationships between cruise ports. The proposed model is applied to the largest ports with data from the 2001-2015 period.

Keywords: cruise ports; Mediterranean ports; hierarchic patterns; coopetition; shift-share analysis

INTRODUCTION

Between the 1990s and 2015, the cruise industry exhibited extremely dynamic behaviour and high growth rates. In 2015, approximately 23 million people vacationed on cruise ships [4]. This figure is more than threefold higher than the number in 2000 (7.2 million passengers), and sixfold higher than in 1990 (3.8 million passengers). Moreover, the forecasts are positive — an average annual growth rate of 3.3% is expected for the period of 2016-2019 [5]. While the global financial crisis of 2008-09 had a major impact on maritime cargo shipping, for example, in 2009, the global containerised cargo rate fell by 9.0% compared to 2008, whereas worldwide cruise

passengers grew by 9.1% [26]. Cruise lines and cruise ports continued experiencing steadily rising numbers of passengers.

The cruise industry is composed of two overall components: maritime affairs and tourism. The maritime component is represented by cruise ships and cruise ports. Cruise ships have a dual function — the function of the vast majority of vessels, shipping, and as an accommodation and entertainment facility with a sophisticated design, which leads to their description as *floating hotels* and *marine resorts*. Cruise ports are a key element in drawing up an itinerary as they connect the ship and tourist destinations. With the growth of the cruise industry, cruise ports have been increasing in importance. The tourism component is composed of the leisure and entertainment facilities on board cruise ships

and the tourist hinterland of each port of call that passengers visit on cruises.

The vast majority of research studies on the cruise industry thus far have focused on the tourism component. However, in recent years, this trend has changed. Research studies associated with the maritime component of the cruise industry have increased, focusing mainly on cruise ports. Some of these studies include the following themes: relevant factors in the site selection of cruise terminals [9], the cruise industry's selection criteria for being a homeport [10, 1], the incentive mechanism in concession agreements for cruise terminal activities [27] and determinants of cruise traffic that is registered by a port [3, 6]. This paper focuses on the maritime component of the cruise industry, specifically on cruise ports.

The core element of the cruise industry is its itinerary system, which involves selling a set of ports and destinations that comprise the itinerary rather than a single destination or port. In 2015, three cruise regions accounted for 67% of the deployed capacity. The Caribbean was the main region, with a share of 36%, followed by the Mediterranean and Northern Europe, with 20% and 11% of the deployed capacity, respectively. In the period 2004-2014, Europe was the driving force for cruising: the total number of passengers increased by 136.2% as further interest in cruises in the region provided the incentive for cruise lines to create more itineraries throughout the continent, especially in the Mediterranean Sea [19]. During the first 15 years of the 21st century, the Mediterranean was the most dynamic region, with an average annual growth rate of 9.4%. The Western Mediterranean had the largest cruising activity, with 70% of cruise passenger movements occurring during the period of 2000-2015 [13, 16]. In this section of the Mediterranean Sea are the tourist powerhouses of Italy and Spain with the highest and second highest cruising activity, respectively, in the Mediterranean basin.

With the growth in the cruise business, cruise lines have had to seek new ports to meet demand and satisfy first-time cruise passengers and repeat cruise passengers by attempting to offer differentiated products based on the ports that comprise the itinerary. This article analyses a sample of 29 Western Mediterranean ports in seven countries. The purposes of the article are as follows: (a) to determine patterns of change in the cruise traffic of the ports in the sample during the period of 2000-2015, (b) to sort the destinations by port size to identify the distribution of the observed evolution and to identify the size with the best results in cruise activity, and (c) to determine the cooperative/competitive relationships among the largest ports that combine homeport passenger movements and transit passenger movements. The main contributions of this study, from a cruise itinerary viewpoint, are as follows: (1) an analysis of a sample of ports belonging to seven countries, (2) the presentation of a model to determine the cooperative/competitive relationships between cruise ports, and (3) the identification of the best group sizes and the relationships with other ports to offer better information to cruise port managers that would be useful for developing future strategies for cruise business.

The remainder of the paper is structured as follows. Section 2 is devoted to a literature review of cruise ports, spatial dependence in the configuration of a cruise itinerary and the concept of cooptation. Section 3 presents the analysis methodology. In section 4, the main results and its discussion are presented. Section 5 concludes the paper.

LITERATURE REVIEW

In cruise shipping, the port is very important for all stages of the cruise ship operation. Ports serve as bases for embarkation and debarkation — homeports — but they also serve as intermediate destinations — ports of call — for shore excursions and resupply along the cruise route [12]. In designing an itinerary, first, the cruise line selects the destination region. The next step involves selecting the homeport(s), depending on whether the itinerary is open or closed, from which the itinerary will be developed. *Closed itineraries* only have one homeport because the itinerary starts and ends at this port; in this case, the itinerary is a closed loop. *Open itineraries* have two homeports — the itinerary starts and ends at different ports. Ports of call are then needed to complete the itinerary. According to Marti [11], the geographic concepts of 'site' and 'situation' can contribute to a better understanding of the cruise-ship port selection process. 'Site', a physical factor, is obviously of great significance to the origin and evolution of cruise ports. 'Situation' can comprise either physical or cultural qualities. The location of embarkation ports relative to destination ports in addition to vessel speed and the number of days allocated to complete each round-trip voyage also governs the number of ports that can be visited [11].

In a set of ports of call, there may be a mix of 'must-see' ports/marquee ports and discovery ports; each type differs according to the tourism attractiveness of the port. 'Must-see' locations/marquee ports are world-famous ports that are absolutely necessary for every itinerary. A discovery port is one that is not world-famous but offers the sense of discovering an unknown treasure [22]. In addition, some discovery ports feature technical calls to obtain a balance between sailing time and shore time, especially between two 'must-see' port calls. Some ports — homeport or ports of calls — are marquee destinations. The concept of marquee destinations is related to tourist attractions located outside the port city and is linked to the port — for example, Civitavecchia (Rome), Livorno (Florence, Pisa) or Motril (Granada). 'Must-see' locations/marquee ports/destinations underline that the concept of itineraries is still bound to the concept of the destination and that itineraries can be more effectively sold if they include some specific destinations [21] because these destinations attract passengers and generate the most sales for the cruise itinerary.

The decision for a cruise line to call at a specific port or, more importantly, to establish a homeport for their vessels depends on whether the area in which the port is located is attractive for cruise itineraries. A port cannot be attractive

if it is not located close to or in an area where there are other available cruise ports with which to design an itinerary. Thus, a cruise port needs to be located close to or within an area where cruise ships operate [12]. The above geographic constraint can be referred to as a geographic constraint at the global level in terms of designing an itinerary, but there is also a strong spatial dependence on the configuration of a cruise itinerary within the cruise destination region or the specific sector of a cruise destination. This geographical dependence results in a negative spatial relationship with the range of short distances between ports, which becomes positive at intermediate distances and negative again at large distances [7]. Cruise ports need one another to survive according to a 'mutual benefit' principle [1]. Additionally, the optimisation of sailing distances in designing an itinerary is a key question because fuel costs have a major impact on the total shipping costs because fuel consumption has an exponential dependence on sailing speed.

The presence of sufficient port-specific and port-related infrastructures, the absence of intense use that may lead to congestion and process disruption, and the modernisation of infrastructures and processes to provide efficient and effective port services are key to including a port as part of an itinerary. While principal cruise ports serve derived demand, their own competitiveness is, to a certain degree, a draw for attracting cruise calls. In seeking to develop a new product, cruise lines have added and continue to search for new cruise ports to add to itineraries and attract land-based holidaymakers or cruises that wish to return [19]. Rodrigue and Notteboom [21] note that the cruise industry works in a 'supply push mechanism' as cruise lines aim to generate demand for cruises by providing new products (itineraries) with a larger and more diversified range of ships. Therefore, the cruise industry continually needs to introduce new itineraries and ships with new amenities and destinations as well as redeploying older and smaller vessels on other itineraries [1]. Furthermore, cruise lines wish to create itineraries that include ports of different sizes, as each type of port provides different types of experiences by blending different types of attractiveness and permitting future passengers to select from among various options to access the departing port [19]. In addition, cruise lines in the process to seek new destinations keep in mind the geopolitical factors and institutional stability of the cruise destination and, also, the security level of ports and tourist hinterlands in order to provide 'secure-comfortable' itineraries. These factors influence both the sustained development of a cruise destination and the success of a particular itinerary.

Strong growth in Mediterranean cruises in the past several years has increased congestion at several ports, both on the maritime side (piers) and on the land side (adjacent touristic districts). This may create constraints in the establishment of itineraries because only a limited number of slots to visit ports of call may be available; adding ports of call may require additional costs and even a bidding process to guarantee access [21]. The possibility of being included in itineraries that involve several ports is a vital parameter, particularly for the development of a non-marquee cruise port [19].

Cruise ports compete within the limits of certain geographic regions. These limits are mainly shaped according to the location of the regional homeports [1]. There is an interdependent relationship between cruise ports; it is necessary to see these ports of call from the point of view of the itineraries as a whole rather than as isolated destinations. This then leads to complex relationships between the cruise ports. Competition and cooperation simultaneously occur between two or more rival ports in a given market. The competition is more intense between ports of the same category [19]. In the case of cruising, the close relationship that is necessary between ports to create attractive itineraries can be described as the perfect case of 'coopetition'. Branderburger and Nalebuff [2] defined 'coopetition' as a mix of the verbs 'cooperation' and 'competition' to describe the 'win-win' strategy used by ports that are very close to one another and must cooperate and compete simultaneously for a sustainable market share. Furthermore, according to Song [24], cooperation is an action by which ports work together to further the general interest of all ports and in which ports increase their market power through collaboration.

This phenomenon has long been observed in cargo ports, especially container ports. Song [23] states that 'coopetition' is a way of *collaborating to compete*. Such collaboration may prevent mutually destructive competition between players. A strategic alliance can strengthen both partners against outsiders even if it weakens partner individually [8]. Furthermore, a collaborative strategy is more additive than a competitive strategy. Interfirm 'coopetition' is highly compatible, and mutually beneficial strategies with different objectives can be strengthened when players work together. This approach can be applied in the configuration of a cruise itinerary with ports of different sizes, technical features and tourist attractiveness. Furthermore, port coopetition results in stronger bargaining powers against government-mandated trade, investment barriers, mega-carriers and shipping alliances [23]. Bearing this background in mind, the methodology for classifying the ports in the sample according to size is presented next to analyse the evolution of cruise traffic in these ports and the proposed cooperation/competition dynamic model.

METHODOLOGY

The criterion used to select the ports in the sample is the registration of more than 7500 average total cruise passenger movements per year between 2000 and 2015; 29 ports meet this criterion. Regarding the cruise activity in the Western Mediterranean Sea, 48 ports in 2015 registered cruise passenger movements [16]. The criterion chosen to classify ports by size is associated with the annual cruise passenger movements. In the literature, one can find the following classification structures according to size. MedCruise used a classification that is divided in two categories, *Category A* and *Category B*. *Category A* is composed of ports with traffic from more than 130,000 cruise passengers in 2013,

more than 80,000 cruise passengers in 2014 and more than 100,000 cruise passengers in 2015. *Category B* is composed of ports with traffic from less than 130,000 cruise passengers in 2013, less than 80,000 cruise passengers in 2014 and less than 100,000 cruise passengers in 2015 [14, 15, 16]. Rodriguez et al. [22] proposed a classification that is divided into five sizes: ‘small’ (less than 100,000 passenger movements/year), ‘medium’ (100,000 to less than 250,000 passenger movements/year), ‘large’ (250,000 to less than 500,000 passenger movements/year), ‘very large’ (500,000 to 1 million passenger movements/year), and ‘huge’ (more than 1 million passenger movements/year). Furthermore, Pallis [19] applied a similar classification to the latter that was structured based on five sizes and with the same cruise passenger movements for each size; the difference lies in the name of the largest size, ‘major’. The classification proposed in this paper follows an approach similar to the latter two, which is structured as follows. ‘Small’ (less than 100,000 passenger movements/year), ‘medium’ (100,000 to 500,000 passenger movements/year), and ‘major’ (more than 500,000 passenger movements/year).

Once the 29 ports of the sample are classified by size, the next step of the analysis consists of carrying out a shift-share analysis to determine the changes in cruise passenger movements that are registered at the intergroup and intragroup level. This analysis is performed to identify the size with the best results and, within each size group, the individual behaviour of each port.

Shift-share analyses have been used extensively to analyse the differences between regional and national growth rates in variables such as export growth, employment and productivity [28]. The ‘share’ effect reflects the expected growth of cruise passenger movements in a seaport if it were to simply maintain its market share and, as a consequence, evolves in the same way as the port size group as a whole (the same growth rate as the groups). The total ‘shift’ reflects the total number of cruise passenger movements that a port has actually lost to or won from competing ports in the same port size group, with the expected cruise passenger movements (share effect) as a reference. The sum of the shift effects of all ports/size groups considered equals zero. The components of the shift-share analysis can be calculated with the following expressions:

$$\begin{aligned} ABSGR_i &= CRUPAX_{it_1} - CRUPAX_{it_0} \\ &= SHARE_i + SHIFT_i \end{aligned} \quad (1)$$

$$SHARE_i = \left(\frac{\sum_{i=1}^n CRUPAX_{it_1}}{\sum_{i=1}^n CRUPAX_{it_0}} - 1 \right) CRUPAX_{it_0} \quad (2)$$

$$\begin{aligned} SHIFT_i &= \\ CRUPAX_{it_1} - \frac{\sum_{i=1}^n CRUPAX_{it_1}}{\sum_{i=1}^n CRUPAX_{it_0}} \cdot CRUPAX_{it_0} \end{aligned} \quad (3)$$

where $ABSGR_i$ is the absolute growth of cruise passenger movements in port i for the period t_0-t_1 , $SHARE_i$ is the share-effect of port i for the period t_0-t_1 that is expressed in cruise passenger movements, $SHIFT_i$ is the total shift of port i for the period t_0-t_1 that is expressed in cruise passenger movements, $CRUPAX_i$ is the cruise passenger movements of port i , and n is the number of ports in each size group.

Next, two measures of market concentration are applied to calculate the distribution of the changes in cruise traffic in the sample of Western Mediterranean ports. Furthermore, the aim of the concentration analysis aims to determine whether the gain or loss obtained in the shift-share changes the concentration of the Western Mediterranean cruise port market. The measure is applied to the whole sample. The Herfindahl-Hirschman Index (HHI) and Gini coefficient (G) are used. The HHI is useful for identifying the degree of concentration within a port system [18]. The HHI is calculated as

$$HHI = \sum_{i=1}^N S_i^2, \quad (4)$$

where HHI is the concentration index for the cruise port sample, S_i is the market share for port i of the port sample and N is the number of ports in port sample. If the total traffic structure is completely dominated by one specific cruise port, the index has a maximum value of one (full concentration). If, on the other hand, the traffic structure within the port sample is equally divided among all cruise ports such that no seaport dominance exists, the index equals its minimum value of $1/n$.

The Gini coefficient is a widely used index that measures the percentage departure from a perfectly uniform distribution [18]. The G coefficient is calculated as follows,

$$G = 1 + \frac{1}{N} - \frac{2}{N^2 \bar{Y}} (Y_1 + 2 Y_2 + \dots + n Y_n), \quad (5)$$

where N is the number of cruise market share observations (i.e., number of ports); \bar{Y} is the arithmetic mean of the market share; and Y_n are the market share numbers in decreasing order. If all the ports in the port sample have the same market share, the Gini coefficient will equal zero. In the event that one port accounts for the total cruise market share (full concentration), the Gini coefficient equals unity.

The last step of the analysis consists of establishing a dynamic model to determine the cooperative/competitive relationships between the ports of the size with the best results that have both homeport passengers and transit passengers. The application of the model aims to determine the type of relationship that prevails between the best sized ports. The calculation premise used to formulate the dynamic model assumes that the market shares of the ports are interrelated, i.e., that there is a linear relationship between the market shares registered by the ports. This calculation premise is made because there is high spatial interdependence between ports in

designing cruise itineraries and because ports depend on each other; the product offered by the cruise industry is the entire itinerary and not just a single port or destination. Therefore, the market share of each port is selected as a dynamic variable. Similar approaches are applied in cooperative/competitive dynamic models for container ports that share the same hinterland [25]. The model is as follows:

$$\frac{dx}{dt} = A'x \quad x(0) = x_0 \quad (6)$$

where t is time, x is the vector of market shares, is the system matrix for identification, and x_0 is the vector of the initial values. By applying simple difference approximations for the derivatives obtained, for each time step Δt , the following relationships are calculated:

$$b_n = Ax_n \quad b_n \equiv x_{n+1} - x_n \quad A \equiv \Delta t A'. \quad (7)$$

The model can be reformulated as

$$b_n = X_n a. \quad (8)$$

Next, if the observed market shares are taken as the solution, then an overdetermined system, Eq. (9), is obtained, which may be solved by the least-square method. The sum of the squares of the errors should be minimal; see Eqs. (10) and (11).

$$\begin{matrix} a_{11}x_1 + a_{12}x_2 + \dots + a_{1n}x_n = b_1 \\ \vdots \\ a_{m1}x_1 + a_{m2}x_2 + \dots + a_{mn}x_n = b_m \end{matrix} \quad (9)$$

where m and n are the sub-indices of the interrelated ports.

$$\|Ax - b\|_2 = \min. \quad (10)$$

$$\|Ax - b\|_2^2 = (Ax - b)^T (Ax - b) = x^T A^T Ax - 2x^T A^T b + b^T b. \quad (11)$$

Minimization yields a system of equations,

$$A^T Ax = A^T b, \quad (12)$$

from which a can be calculated. The model proposed is tested with the market shares of ports of the best size that combine both homeport passenger movements and transit passenger movements in the period of 2001-2015. Only off-diagonal coefficients are interpreted; the interpretation criterion is

ports that are connected by a positive coefficient as cooperative and ports connected by a negative coefficient as competitive.

RESULTS AND DISCUSSION

The application of the proposed classification in three size categories, which is partially based on Rodrigue et al. [22] and Pallis [19], as mentioned in the methodology section, to the sample of the ports yields the following results. The 'medium' group is the largest, with 14 ports in seven countries: Cádiz, Cannes-Antibes, Gibraltar, Ibiza, La Goulette, La Spezia, Málaga, Messina, Monaco, Palermo, Toulon, Valencia, Valletta and Villefranche. This is followed by the 'major' group, with eight ports in three countries: Barcelona, Civitavecchia, Genoa, Livorno, Marseille, Naples, Palma de Mallorca and Savona. The remaining seven ports of the sample are encompassed in the 'small' group: Alicante, Almería, Cagliari, Cartagena, Mahón, Motril and Nice.

The first stage of the shift-share analysis consisted of an intergroup analysis by size group. The net result for the whole period of 2001-2015 yields 'major' ports as the best size, with a positive shift of 659,019 passenger movements. This gain has been at the expense of 'medium' and 'small' ports because both saw a negative shift over the period. The former saw a decrease of 568,718 passenger movements and the latter a decrease of 90,301 passenger movements. The general trend throughout the period was that the year in which the 'major' ports won passenger movements was when 'medium' ports lost movements and vice versa; see Figure 1.

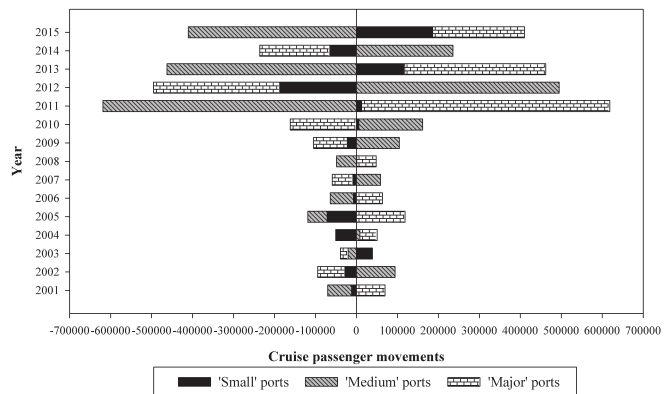


Fig. 1. Shift analysis for three size groups for Western Mediterranean cruise ports

The second stage of the shift-share analysis consisted of an intragroup analysis to determine the behavioural pattern of each port within the group. Among 'major' ports, Marseille had the greatest gain; see Figure 2. This gain is the picture of the growth in the French source market, in which the number of French cruise passengers in 2015 was approximately three times the number registered in 2003. In addition, the creation of French brands/cruise lines — such as Croisières de France (CDF), which belongs to the Royal Caribbean Cruises Limited group — is also influential. Furthermore, Marseille is the main gateway to Mediterranean itineraries for the French

source market. Source markets, whenever possible, prefer to embark at national ports. Moreover, since 2009, there has been a private terminal operator that is integrated from three cruise lines: Costa Crociere, 40%; MSC, 40%; and Louis Cruises, 20% [27]. According to Esteve-Perez and Garcia-Sanchez [6], the intervention of a private terminal operator has a positive bearing on the number of cruise passengers. In Marseille, this effect has been observed: from 2010, an increase in passenger movements has been registered.

Civitavecchia and Barcelona are also high-ranking ports. Civitavecchia is a gateway port to the must-see destination of Rome. The high tourist attractiveness of this destination makes Civitavecchia one of the attraction poles for cruises in the Western Mediterranean. Moreover, since 2006, there has been an intervention of private terminal operators in Civitavecchia that are integrated three cruise lines, each with a share of 33.33%: Costa Crociere, RCCL and MSC [27]. Barcelona is a must-see port in the Western Mediterranean with a market share of 14.49% during the period of 2000-2015, the highest share in the sample of 29 ports. In addition, since 2000, Barcelona has had private terminal operators for its cruise terminals. This port, coupled with Civitavecchia, constitutes the two main attraction poles for Western Mediterranean itineraries. The success of the two ports can be associated with two concepts: high tourism attractiveness (Barcelona and Rome) and adequate cruise infrastructures that are adapted to the growth of the cruise industry. Barcelona and Civitavecchia are ports that generate greater sales for certain itineraries.

The positive shift from Palma de Mallorca is associated with its 'must-see' port character and its strategic geographical position in the Central Western Mediterranean. The low gains recorded are mainly associated with losses for seven years in a row, from 2003 to 2009, and two years in a row, from 2011 to 2012, switching to wins during 2013-2015.

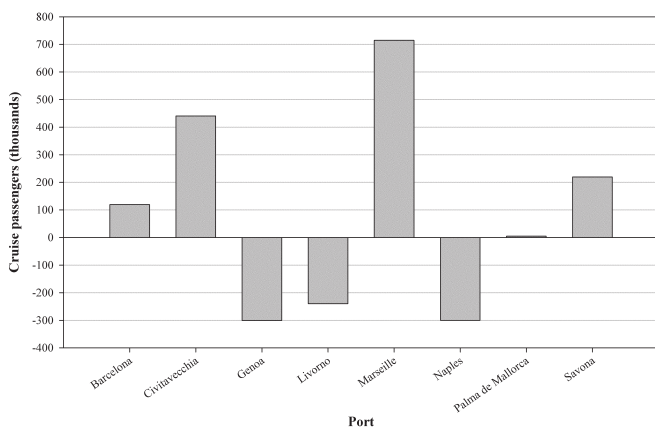


Fig. 2. Intragroup shift analysis for the 'major' group, net results for period 2001-2015

In contrast, the ports of Genoa, Livorno and Naples recorded losses. In both Genoa and Livorno, signs of congestion are seen in the last period of the analysis. In fact, these data are associated with gains from Savona, which

serves as an alternative to Genoa due to the short distance that separates them (19 nautical miles).

In the 'medium' group, two behaviour patterns are seen. A set of ten ports is located in the spectrum of a shift of +/- 100,000 passenger movements, in which six have losses and the remaining four have wins. The second behaviour pattern is characterised by a shift of higher magnitude; see Figure 3. La Spezia is the port with the largest gain; its geographical proximity to Livorno, coupled with congestion symptoms recorded in Livorno in recent years, make it an alternative to the Livorno dock — hence a noteworthy gain is seen. Valencia is the second port with higher gains. In recent years, there has been an increase in cruise infrastructure in the port of Valencia. The average annual growth of this maritime traffic was 44.55% during the period of 2000-2015. Valencia also acts as a homeport mainly for the Spaniard source market. More specifically, Valencia acts as a homeport for Spaniards living in the centre of the Iberian Peninsula due to the good connections via high-speed railways and motorways between the centre of Spain and Valencia.

The loss of 846,781 cruise passenger movements in La Goulette is extremely significant. The causes of this loss are associated with the political instability associated with the Arab Spring during 2010 and 2011 and the terrorist attacks in Tunis in March 2015. These events resulted in a remarkable loss of 667,499 passenger movements in 2011 and 420,427 passenger movements in 2015. Villefranche experienced a negative shift of 349,176 cruise passenger movements. The reasons for this loss are associated with the high growth of Marseille and its lack of berthing facilities. The call at Villefranche requires the use of anchoring and tendering services. The trend of increases in the sizes of cruise ships that have been put into service in recent years means that port facilities must adapt to the new generation of mega-cruise ships.

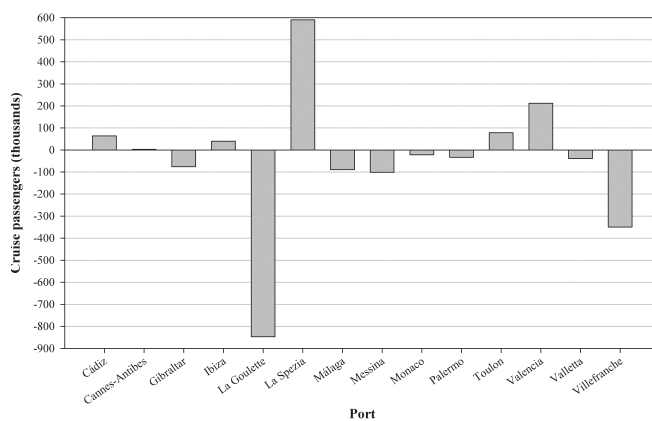


Fig. 3. Intragroup shift analysis for the 'medium' group, net results for period 2001-2015

Regarding 'small' group, only two ports have seen increasing shifts in the period of 2000-2015; see Figure 4. Cagliari has had the highest gains; its growth rate during this period was 36.82%. A partial influence for this gain is the reconfiguration of itineraries that had calls in La Goulette,

as lots of calls were cancelled after the terrorist attacks in Tunis in 2015 and part of the vessels were redirected to Cagliari. Also, the reconfiguration of these itineraries has mostly benefited Valletta and the ports of Sicily and Sardinia. These changes in the itineraries respond to the search for 'secure-comfortable' calls. Furthermore, in Cagliari, a private terminal operator has been operating since 2012. The company terminal operator is a partnership between RCCL and *Venezia Terminal Passeggeri Spa* [19]. In 2013 and 2015, Cagliari registered positive net shifts of 61,591 and 175,127 cruise passenger movements, highlighting the positive effect of the intervention of a private terminal operator. Cartagena developed a number of commercial strategies to promote cruise traffic on their docks during the period of 2000-2015, and the sample shows growth of 20.03% during 2000-2015. In addition, in 2016, the milestone of becoming an interporting port for Princess Cruises was attained.

Nice has seen the highest negative shift of the 'small' group, with a loss of 161,779 cruise passenger movements. Nice can be affected negatively by the growth of Marseille and the technical limitations of its cruise port facilities. The maximum ship dimension per berth in Nice is 210 meters in length; anchorage is also available [17]. The vast majority of contemporary cruise vessels cannot call at this port because the ship lengths are greater than 210 meters. In this particular case, the call would require anchoring and use tendering services.

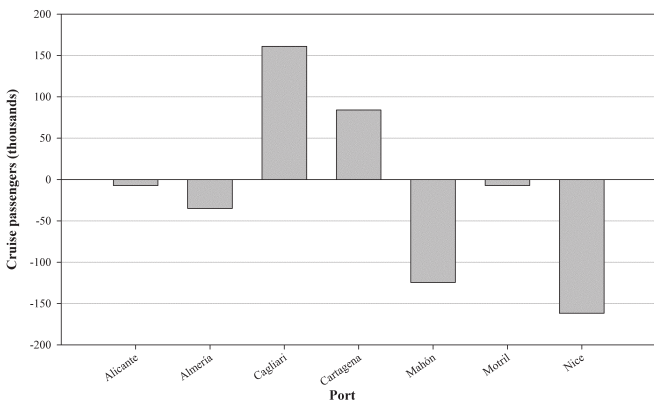


Fig. 4. Intragroup shift analysis for the 'small' group, net results for period 2001-2015

The shift data obtained indicate that the process of win or loss between ports is not based on removing market participants; all ports require one other because the cruise industry sells itineraries rather than single port destinations. In addition, it should be kept in mind that the sample of ports analysed is part of the Western Mediterranean cruise port market. Then, some traffic might have shifted to other ports, like North Corsican ports and North Sardinian ports, that are situated in the Western Mediterranean but are not part of the sample of ports analysed.

Figure 5 shows the Herfindahl-Hirschman indices and Gini coefficient values for the entire sample of ports. The Herfindahl-Hirschman indices for the entire Western Mediterranean are extremely stable over time, with an average

value of 0.073 during the period of 2000-2015. Changes in the values of HHI, with an average annual increase of 0.57%, indicate a modest trend towards a less evenly distributed market. Pallis and Arapi [20] obtained similar results for the Western Mediterranean sector by applying HHI to cruise passenger movements that are registered between 2005 and 2014.

The values of the Gini coefficient confirm the conclusions obtained by the HHI regarding the evolution of cruise port market concentrations; see Figure 5. Since 2000, the entire sample of ports has remained virtually at the same level of concentration with minor fluctuations towards concentration, with an average annual change rate of 0.32%.

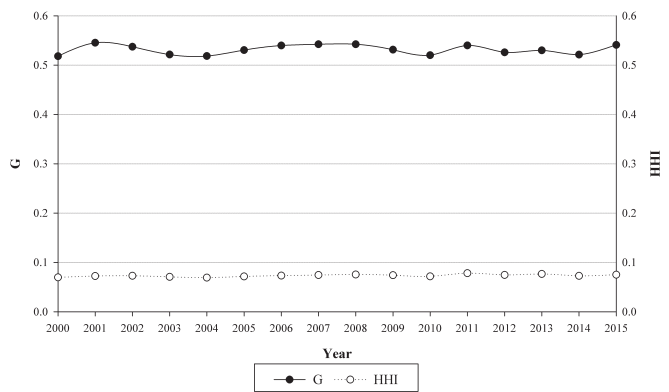


Fig. 5. Values of HHI and G coefficients for the whole sample of ports for period 2000-2015

Among the ports of the 'major' group, six have registered both homeport and transit passenger movements: Barcelona, Civitavecchia, Genoa, Marseille, Palma de Mallorca and Savona. Cooperation can be performed at the inter- and intra-itinerary levels, which is why the study of cooperation models focus on ports sharing homeport traffic and transit traffic. Therefore, the dynamic model is created with these six ports while focusing on the three main ports via market share: Barcelona, Civitavecchia and Palma de Mallorca. The first application of the dynamic model only focuses on these three ports because they are must-see ports, gateways to world-famous tourist destinations, leaders throughout the period in accumulating two-thirds of the market share of 'major' ports that combine homeport and transit traffic, and have more than one million average cruise passenger movements during the period of 2001-2015. The application of the model seeks to determine the type of relationships that predominate among the largest 'major' ports. Particularising the dynamic model proposed in equation (9) with the six ports that comprise the analysis yields the following results.

Barcelona shows high degree of cooperation with the other ports, both for homeport traffic and port-of-call traffic. This result can be interpreted as follows: if the remaining ports experience more cruise traffic, Barcelona hosts more transit ship calls or more itineraries that start and/or end at Barcelona with calls in other ports. Moreover, Barcelona is the main homeport and the second port of call of the six ports under analysis, with an average market share of 31.3% and

25.6%, respectively, during 2001-2015. Thus, it has significant bargaining power to concentrate itineraries in its berths. Barcelona has excellent cruise infrastructures for hosting homeport operations with high numbers of cruise passengers. In addition, these cruise facilities are adapted for mega-cruise ships. Furthermore, the high tourism attractiveness of Barcelona makes this port one of the favourite calls for cruise lines in attempting to garner greater sales of the itinerary. Transit traffic represented 45.5% of all cruise traffic registered in Barcelona during 2001-2015.

The results of these calculations for the homeport are shown in Table 1.

Table 2 shows the results with transit cruise passenger movements.

traffic. Palma de Mallorca is the second homeport and the third port of call for the six ports under analysis, with a market share of 17.1% and 17.9%, respectively, during 2001-2015. Palma de Mallorca has competitive homeport relationships with its closest geographically ports, Barcelona and Marseille, because they constitute alternative gateways to itineraries in the northwestern sector of the Western Mediterranean. The share of homeport traffic in Palma de Mallorca is 47.5%. On the other hand, the growth of transit calls in Barcelona, Marseille, Savona and Genoa benefit Palma de Mallorca because it hosts more transit calls as a result. The competitive relationship with Civitavecchia may be associated with the fact that Palma de Mallorca and Civitavecchia are the most geographically distant (459 nautical miles).

Tab. 1. Cooperative/competitive relationships among the largest 'major' Western Mediterranean ports for the homeport category during the period of 2001-2015

	Barcelona	Civitavecchia	Palma de Mallorca	Marseille	Savona	Genoa
Barcelona		<i>Cooperative</i> (0.510)	<i>Cooperative</i> (0.353)	<i>Cooperative</i> (0.145)	<i>Cooperative</i> (0.084)	<i>Cooperative</i> (0.314)
Civitavecchia	<i>Cooperative</i> (0.083)		<i>Cooperative</i> (0.089)	<i>Cooperative</i> (0.195)	<i>Cooperative</i> (0.274)	<u>Competitive</u> (-0.054)
Palma de Mallorca	<u>Competitive</u> (-0.340)	<i>Cooperative</i> (0.135)		<u>Competitive</u> (-0.300)	<i>Cooperative</i> (0.403)	<i>Cooperative</i> (0.760)

Note: coefficient values in brackets.

Tab. 2. Cooperative/competitive relationships among the largest 'major' Western Mediterranean ports for the transit category during the period of 2001-2015

	Barcelona	Civitavecchia	Palma de Mallorca	Marseille	Savona	Genoa
Barcelona		<i>Cooperative</i> (0.046)	<i>Cooperative</i> (0.291)	<i>Cooperative</i> (0.079)	<u>Competitive</u> (-0.405)	<i>Cooperative</i> (0.305)
Civitavecchia	<i>Cooperative</i> (0.190)		<i>Cooperative</i> (0.527)	<u>Competitive</u> (-0.490)	<i>Cooperative</i> (0.308)	<u>Competitive</u> (-0.597)
Palma de Mallorca	<i>Cooperative</i> (0.456)	<u>Competitive</u> (-0.333)		<i>Cooperative</i> (0.802)	<i>Cooperative</i> (0.216)	<i>Cooperative</i> (0.168)

Note: coefficient values in brackets.

Civitavecchia has high degree of cooperation with other ports in terms of homeport traffic; however, the cooperation degree is slightly lower for port of call traffic. Thus, the positive development of cruise traffic in the other ports has a positive effect on Civitavecchia. This is the main port of call and the third homeport among the six ports of analysis, with a market share of 29.9% and 16.6%, respectively, during 2001-2015. The high tourism attractiveness of the 'must-see' destination of Rome generates 65.4% of cruise traffic in Civitavecchia as transit traffic. Thus, it has significant bargaining power in concentrating itineraries in its berths, mainly as transit calls. Moreover, the competitive relationship with Marseille can be related with the high share of transit traffic in the two ports: Marseille has 71.1% transit traffic. Both ports have the highest shares of transit traffic. Genoa is the geographically closest port under analysis with respect to Civitavecchia (205 nautical miles); therefore, the competitive relationship obtained can be related to this geography factor.

Palma de Mallorca shows a high degree of cooperation in transit traffic, which is slightly lower in terms of homeport

CONCLUSIONS

The dynamism of the cruise industry requires that cruise lines seek new ports to design new itineraries and meet demand. The increased supply of itineraries attempts to create differentiated products based on ports that comprise the itinerary. The design of new itineraries is always performed with the idea that the cruise industry sells itineraries rather than single ports/destinations. The Western Mediterranean is a pole of attraction for cruise itineraries that are associated with its tourist attractions, which has allowed a greater number of ports to host cruise ships. The size classification proposed in this paper reveals the significant heterogeneity of cruise ports in the Western Mediterranean based on the passenger movements recorded.

'Major' ports grew at the expense of 'medium' and 'small' ports during the period of 2001-2015. 'Major' ports thus show hierarchical dominance over the 'medium' and 'small' categories. The results of the shift-share analysis highlight that

the process of gain or loss does not seek to destroy market participants but rather reduce their market shares because ports need each other to generate itineraries. Among the causes of the most important losses are geopolitical instability events and a lack of adequate facilities for the new generation of large cruise ships and mega-cruise ships that have been put into service in recent years. Mega-cruise ships have had an increasing presence in the cruise fleet. If the cruise facilities of ports are not adapted to the new large sizes, their cruise business strategies should be reoriented to smaller sizes, which are primarily associated with luxury, upper premium and premium segments rather than contemporary segments. The positive shifts have the intervention of a private terminal operator in several ports as a common element in recent years. Moreover, in some cases, the private terminal operator is a cruise line or a cruise line partnership, indicating a process of vertical integration in the cruise industry. Furthermore, in 2012, losses in 15 of the 29 ports analysed can be attributed to the effects of the Costa Concordia ship disaster.

The concentration in the sample of 29 ports during the first 15 years of the 21st century has remained stable over time, according to the changes in the values of HHI and G. The concentration analysis allows us to determine that the gains of 'major' ports is not so high (8.5% of the average total passenger movements of this port group during 2000-2015) as to vary the concentration. The concentration does not vary significantly because ports need one another. The central element around which the cruise industry is structured, the itineraries, has led to complex cooperative/competitive relationships between ports. These relationships can be seen at the inter- or intra-itinerary level. The results obtained show cooperative relationships between the three largest cruise ports of the 'major' group. Therefore, the largest 'major' ports perceive other ports as collaborators based on the principle that the element marketed by the cruise industry is the itinerary.

BIBLIOGRAPHY

1. Bagis, O.; Dooms, M.: Turkey's potential on becoming a cruise hub for the East Mediterranean Region: The case of Istanbul. *Research in Transportation Business & Management*, vol. 13, pp. 6-15, 2014.
2. Branderburger, A.; Nalebuff, B.: *Co-opetition*. Doubleday, New York 1996.
3. Castillo-Manzano, J.I.; Fageda, X.; Gonzalez-Laxe, F.: An analysis of the determinants of cruise traffic: An empirical application to the Spanish port system. *Transportation Research Part E*, vol. 66, pp. 115-125, 2014.
4. CLIA (Cruise Lines International Association): *2016 cruise industry outlook*. CLIA, Washington 2016.
5. Cruise Market Watch: Growth of the Cruise Line Industry [online]. Available from: <http://www.cruisemarketwatch.com/growth/>. [Accessed 31 May 2016].
6. Esteve-Perez, J.; Garcia-Sanchez, A.: Cruise market: Stakeholders and the role of ports and tourist hinterlands. *Maritime Economics & Logistics*, vol. 17(3), pp. 371-388, 2015.
7. Esteve-Perez, J.; Garcia-Sanchez, A.: *La industria de cruceros: características, agentes y sus funciones*. Fundación Valenciaport, Valencia 2015.
8. Hamel, G.; Doz, Y.; Prahalad, C.: Collaborate with your competitors—and win. *Harvard Business Review*, vol. 67, pp. 133-139, 1989.
9. Lau, Y.; Tam, K.; Ng, A.K.Y.; Pallis, A.A.: Cruise terminals site selection process: An institutional analysis of the Kai Tak Cruise Terminal in Hong Kong. *Research in Transportation Business & Management*, vol. 13, pp. 16-23, 2014.
10. Lekakou, M.B.; Pallis, A.A.; Vaggelas, G.K.: An analysis of cruise industry's selection criteria. Paper presented at the International Association of Maritime Economists Annual Conference, June 24-26. Copenhagen, Denmark, 2009.
11. Marti, B.E.: Geography and the cruise ship port selection process. *Maritime Policy & Management*, vol. 17(3), pp. 157-164, 1990.
12. McCalla, R.J.: An Investigation into Site and Situation: Cruise Ship Ports. *Tijdschrift voor Economische en Sociale Geografie*, vol. 89(1), pp. 44-55, 1998.
13. MedCruise: *The New Medcruise Statistic Report*. MedCruise, Barcelona 2011.
14. MedCruise: *Cruise activities in MedCruise ports: Statistics 2013*. MedCruise, Piraeus 2014.
15. MedCruise: *Cruise activities in MedCruise ports: Statistics 2014*. MedCruise, Piraeus 2015.
16. MedCruise: *Cruise activities in MedCruise ports: Statistics 2015*. MedCruise, Piraeus 2016.
17. MedCruise: French Riviera Ports-Ports facts [online]. Available from: <http://www.medcruise.com/port/488/french-riviera-ports/information>. [Accessed 27 June 2016].
18. Notteboom, T.E.: Concentration and load centre development in the European container port system. *Journal of Transport Geography*, vol. 5(2), pp. 99-115, 1997.
19. Pallis, A.A.: *Cruise Shipping and Urban Development: State of the Art of the Industry and Cruise Ports*. International Transport Forum, Paris 2015.

20. Pallis, A.A.; Arapi, K.P.: A Multi-Port Cruise Region: Dynamics and Hierarchies in the Med. *Tourismos*, vol. 11(2), pp. 168–201, 2016.
21. Rodrigue, J.P.; Notteboom, T.: The geography of cruises: Itineraries, not destinations. *Applied Geography*, vol. 38, pp. 31–42, 2013.
22. Rodrigue, J.P.; Comtois, C.; Slack, B.: *The geography of transport systems* (3rd ed.). Routledge, Abingdon 2013.
23. Song, D.W.: Port co-opetition in concept and practice. *Maritime Policy and Management*, vol. 30(1), pp. 29–44, 2003.
24. Song, D.W.: Regional container port competition and co-operation: the case of Hong Kong and South China. *Journal of Transport Geography*, vol. 10, pp. 99–110, 2002.
25. Twrdy, E.; Batista, M.: Competition between container ports in the Northern Adriatic. *International Journal for Traffic and Transport Engineering*, vol. 4(4), pp. 363–371, 2014.
26. UNCTAD (United Nations Conference on Trade And Development): *Review of Maritime Transport 2015*. UNCTAD, Geneva 2015.
27. Wang, G.W.Y.; Pallis, A.A.; Notteboom, T.E.: Incentives in cruise terminal concession contracts. *Research in Transportation Business & Management*, vol. 13, pp. 36–42, 2014.
28. Wilson, P.; Chern, T.S.; Ping, T.S.; Robinson, E.: A Dynamic Shift-Share Analysis of the Electronics Export Market 1988–2001: Can the NIEs Compete with China?. SCAPE Working Paper Series, Paper No. 2005/07, May 2005.

CONTACT WITH THE AUTHORS

Jeronimo Esteve-Perez

e-mail: jeronimo.esteve@upct.es

Universidad Politécnica de Cartagena
Department of Naval Technology
Paseo Alfonso XIII, 52, 30203 Cartagena

SPAIN

Antonio Garcia-Sanchez

e-mail: a.garciasanchez@upct.es

Universidad Politécnica de Cartagena
Department of Economics
Calle Real, 3, 30201 Cartagena

SPAIN

AN OPTIMIZATION APPROACH TO THE INTERMODAL TRANSPORTATION NETWORK IN FRUIT COLD CHAIN, CONSIDERING COST, QUALITY DEGRADATION AND CARBON DIOXIDE FOOTPRINT

Qianli Ma

Wenyuan Wang

Yun Peng

Xiangqun Song

Dalian University of Technology, Dalian, China

ABSTRACT

This model optimizes port hinterland intermodal refrigerated container flows, considering both cost and quality degradation, which is distinctive from the previous literature content in a way that it quantifies the influence of carbon dioxide (CO₂) emission in different setting temperature on intermodal network planning. The primary contribution of this paper is that the model is beneficial not only to shippers and customers for the novel service design, but also offer, for policy-makers of the government, insights to develop inland transport infrastructures in consideration of intermodal transportation. The majority of models of multimodal system have been established with an objective of cost minimization for normal commodities. As the food quality is possible to be influenced by varying duration time required for the storage and transportation, and transportation accompanied with refrigeration producing more CO₂ emission, this paper aims to address cost minimization and quality degradation minimization within the constraint of CO₂ footprint. To achieve this aim, we put the quality degradation model in a mixed-integer linear programming model used for intermodal network planning for cold chain. The example of Dalian Port and Yingkou Port offer insight into trade-offs between transportation temperature and transport mode considering CO₂ footprint. Furthermore, the model can offer a useful reference for other regions with the demand for different imported food, which requires an uninterrupted cold chain during the transportation and storage.

Keywords: intermodal transport network; quality model; refrigerated container; fruit cold chain; integer linear programming

INTRODUCTION

Global fruit and vegetable production has experienced remarkable growth with the rate of some 6 percent per annum over the past two decades. Transportation and storage of fresh fruits and fresh vegetables are challenging and risky operations due to the highly perishable nature of such products. Distribution of fresh products falls in the category of cold chains in which the products are conserved at low temperature. For 20% amount of the fruits and vegetables, an efficient cold chain is essential to preserve their quality and to their shelf life in order to reduce food losses. Moreover,

lots of other food cargoes, such as seafood, dairy product, red wine and chocolate, are also traded across borders via cold chain transport. Compared with most supply chains, food cold chain is often more difficult and complex to manage because food is perishable and has a short shelf life.

Due to the rapid development of food cold chain and the enormous success of containerization, the use of refrigerated containers has shown a continuous growth during the past two decades. The massive growth of trade in refrigerated containers depends on many factors, mostly economic and technological. In China, to integrate into the Belt and Road (B&R) Initiative actively, Dalian Port and Yingkou Port have

opened up some new international logistic channels, such as Liaoning-Manchuria-Europe Channel, Liaoning-Sea-Europe and China-South Korea-Russia. Especially, Dalian Port has opened a new domestic cold-chain model with refrigerated container train for sea-rail intermodal transport.

Intermodal transport is a term used to describe the movement of goods in an identical loading unit or vehicle which uses various modes of transport (road, rail, air and sea) successively without any handling of the freights themselves during transfers between modes. It can save time and money by integrating freight, simplifying complex loading and unloading steps, and protecting freight from extreme weather and damage (Min, 1991).

The scheduling of intermodal network for normal commodities has drawn a lot of interest in academic research field. The majority of models of intermodal network scheduling have been established with a single objective, such as cost minimization (Iannone and Thore, 2010; Wang and Yun, 2013), time minimization (Zhang et al., 2010) and CO₂ emission (Liao et al., 2009). Some other authors integrated transit time, storage time or transportation distance into the multiple target system with a cost minimization (Yang et al., 2011; Zhang et al., 2011; Lam and Gu, 2016; Rahimi et al., 2008). However, with the food quality in the cold chain logistics gaining increasing attention, very few papers studied the design of intermodal network for refrigerated containers and took the quality level of the food in the refrigerated containers into consideration in targets of the optimization. For individual refrigerated containers, approximately 19% of the energy use related to its journey is used for refrigeration purposes (Fitzgerald et al., 2011). Due to the importance of refrigeration and transportation to CO₂ footprint, the environmental protection has become a key concern in the cold chain logistics.

Taking the research gaps into account, this paper develops a novel optimization model for the scheduling of the intermodal network of a container port hinterland. The final aim of this model is to put forward an innovative intermodal network scheduling which can help the shipper to achieve cost minimization, quality degradation minimization, and CO₂ footprint to better meet market needs.

PROBLEM DESCRIPTION

QUALITY DEGRADATION PROBLEM

Generally, quality degradation of food in transport and storage is dependent on time t , temperature T , and other constants (activation energy and gas constant), which can be described by the equation:

$$\frac{dq}{dt} = kq^n \quad (1)$$

Where q is the quality, k – the rate of decay, and n – the power factor. For food where quality degradation is related to microbial growth (e.g., meat and fish), the quality degradation follows the first-order reactions shown by the line F in Fig. 1, while other food (e.g., fresh fruits and vegetables) follow the zero-order reactions shown by the line Z.

Prediction of food quality is a complicated problem because of the range and diversity of food features and their transport and storage conditions. Plenty of models have been established for specific kinds of food (Vankerschaver et al., 1996; McDonald and Sun, 1999; Lukasse and Polderdijk, 2003). From the above mentioned models we can know that temperature is a leading factor affecting food quality in supply chains. The rate of quality degradation k is dependent on the Arrhenius equation:

$$k = k_0 \cdot \exp[-E_a/RT] \quad (2)$$

where k_0 is a constant, E_a – the activation energy, R – the gas constant, and T – the absolute temperature.

We can estimate the food quality at a certain location, based on Eq. (1) dependent on an initial quality q_0 , time interval t_i , degradation rate k_i (related to T_i), getting:

$$q = q_0 - \sum_{i=1}^m k_i t_i \quad (3)$$

for zero-order reactions and:

$$q = q_0 \cdot \exp\left[-\sum_{i=1}^m k_i t_i\right] \quad (4)$$

for first-order reactions.

Substituting the Eq. (2) we get:

$$q = q_0 - \sum_{i=1}^m k_0 t_i \cdot \exp[-E_a/RT_i] \quad (5)$$

and:

$$q = q_0 \cdot \exp\left[-\sum_{i=1}^m k_0 t_i \cdot \exp[-E_a/RT_i]\right] \quad (6)$$

For a given temperature, according to above given equations we can get the quality change during a time period, which leads to the quality change Δq for a time period τ and temperature T :

$$\Delta q(\tau, T) = -k_0 \tau \cdot \exp[-E_a/RT] \quad (7)$$

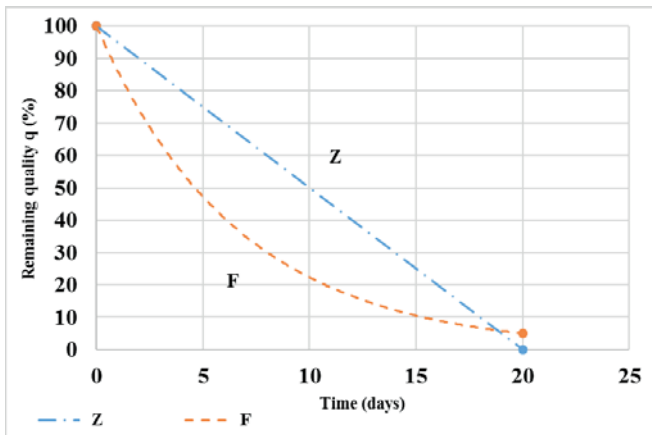


Fig. 1. Illustration of quality degradation

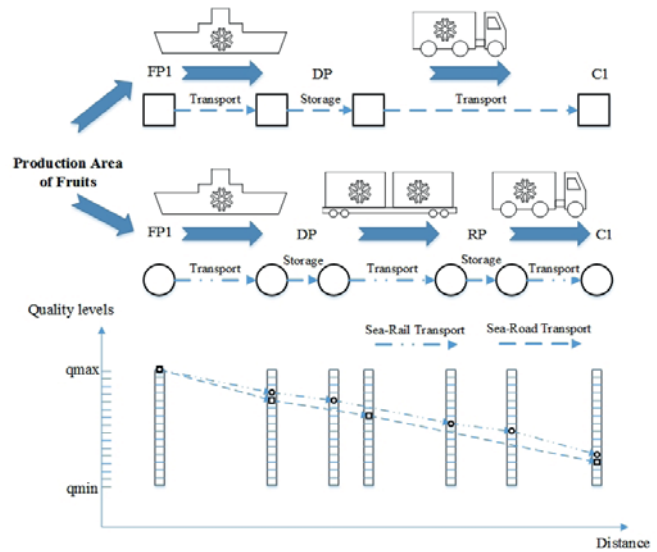


Fig. 3. The intermodal transport route from FP1 to C1 (see Notation, Sets)

PROBLEM OF PORT HINTERLAND INTERMODAL NETWORK SCHEDULING

The intermodal network in food cold chain is illustrated in Fig. 2. Refrigerated containers with fresh food are shipped from foreign seaports to domestic ones. After discharge at the domestic ports, refrigerated containers can be transferred to distribution centres in inland cities by rail or truck (Fig. 3). Without rail facilities, refrigerated containers could also be transported from ports to inland cities all the way by truck.

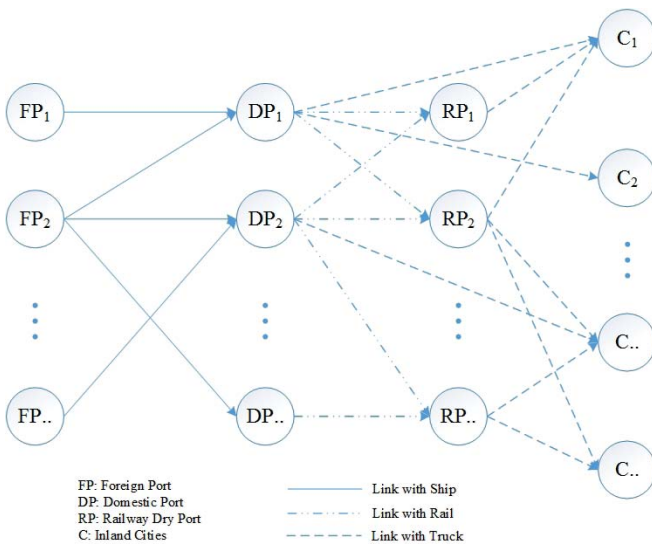


Fig. 2. The intermodal transport network of a container port hinterland

A BI-OBJECTIVE OPTIMIZATION MODEL

1) Notation

Indices	Description
i	Node index
i, j	Index of pair (i, j) , referring to an arc from node i to node j
q	Quality index
k	Temperature index

Sets	Description
FP	Set of foreign ports
DP	Set of domestic ports
RP	Set of railway dry ports
C	Set of inland cities
N	Set of all nodes: $N=FP \cup DP \cup RP \cup C$
A	Set of all arcs: $A=A_{FPDP} \cup A_{DPRP} \cup A_{RPC} \cup A_{DPC}$, for each $(i, j) \in A_{XY}$, (i, j) denotes the arc from $i \in X$ and $j \in Y$, and $X, Y \in \{FP, DP, RP, C\}$

Transport cost minimization and quality degradation minimization are included in the objective of this model. In actual realities, transport cost and quality degradation should be used to deal with the optimization by decision makers.

Decision variable	Description
$f_{i,j,q,k}$	Flow quantities in TEU on arc (i, j) with temperature level k , quality level q at the starting node i , $(i, j) \in A$

Parameter	Description
G	Average CO ₂ emission limitation of this network per TEU in kg
$u_{i,j}$	Distance from node n_i to n_j in km, $(i, j) \in A$

Parameter	Description
$f_{i,j,k}$	Cost for transporting one TEU per km on arc (i, j) at temperature level k , $(i, j) \in A$
CHC_i	Container handling cost in node n_i per TEU, $n_i \in DP \cup RP$
$g_{i,k}$	Cooling cost for facility i at temperature level k , $n_i \in DP \cup RP$
SF_i	Cost for storing one TEU in facility i , $n \in DP \cup RP$
CS	Cost for import container per TEU, including customs clearance cost, container inspection fee, document fee, and port security fee, etc.
$CEQ_{i,j,k}$	Transportation CO ₂ emission from node n_i to n_j with temperature k in kg per TEU, $(i, j) \in A$
$CES_{i,k}$	Storage CO ₂ emission in node n_i with temperature k per TEU, $n_i \in DP \cup RP$
Δq_k	Quality degradation with temperature k per TEU per hour
$\Delta q_{i,k}$	Quality degradation in facility i , $n_i \in DP \cup RP$
$\Delta q_{i,j,k}$	Quality degradation on arc (i, j) , $(i, j) \in A$
q_0	Initial quality
q_{\min}	Minimum quality level for products
SPM_i	Container supply quantity of node n_i in TEU, $n_i \in FP$
DMM_i	Container demand quantity of node n_i in TEU, $n_i \in C$
CAP_i	Container throughput capacity of node n_i in TEU, $n_i \in DP \cup RP$
TTP_{ij}	Transportation time from node n_i to n_j in hours per TEU, $(i, j) \in A$
THT_i	Container handling time in node n_i per TEU, $n_i \in DP \cup RP$
TST_i	Container storage time in node n_i per TEU, $n_i \in DP \cup RP$

2) Model assumptions

To facilitate the modelling, we make the following assumptions:

- The goods in different pallets in one refrigerated container are in the same temperature.
- There are only one-way (inbound) flows for the intermodal network in food cold chain.
- There is sufficient capacity of transportation market to meet the demand of available vehicles for refrigerated container transport.
- The uncertainty of quality loss for the items in port area is ignored. Although there are some probable situations leading to quality loss during loading, intra-port transporting, switching-on/off the container to/from an electricity source, veterinary and custom inspection (Filina-Dawidowicz, 2014), container handlings in port area during intermodal transportation are relatively consistent.

3) Model formulation

Two objective functions:

$$\text{MinimiseTransC} = \left(\begin{aligned} & \sum_k \sum_q \sum_{(i,j) \in A} \hat{f}n_{i,j,q,k} \times u_{i,j} \times f_{i,j,k} \\ & + \sum_k \sum_q \sum_{(i,j) \in A} \hat{f}n_{i,j,q,k} \times (CHC_i + CHC_j) \\ & + \sum_k \sum_q \sum_{(i,j) \in A} (g_{i,k} \times \hat{f}n_{i,j,q,k} + SF_i \times \hat{f}n_{i,j,q,k}) \\ & + \sum_k \sum_q \sum_{(i,j) \in A_{FP}} \hat{f}n_{i,j,q,k} \times CS \end{aligned} \right) \div \sum_{i \in F} SPM_i \quad (8)$$

$$\text{MinimiseQualD} = \left(\begin{aligned} & \sum_k \sum_q \sum_{(i,j) \in A} \hat{f}n_{i,j,q,k} \times \frac{\Delta q_{i,j,k}}{q_0} \\ & + \sum_k \sum_q \sum_{(i,j) \in A_{FP} \cup A_{DP} \cup A_{RP}} \hat{f}n_{i,j,q,k} \times \frac{\Delta q_{i,k}}{q_0} \end{aligned} \right) \div \sum_{i \in F} SPM_i \quad (9)$$

with the constraints:

$$\sum_k \sum_q \sum_{(i,j) \in A} \hat{f}n_{i,j,q,k} = SPM_i, \quad \forall n_i \in FP \quad (10)$$

$$\sum_k \sum_{q \geq q_{\min}} \sum_{(i,j) \in A} \hat{f}n_{i,j,q,k} = DMM_j, \quad \forall n_j \in C \quad (11)$$

$$\sum_k \sum_q \sum_{(i,j) \in A} \hat{f}n_{i,j,q,k} \leq CAP_i, \quad \forall n_i \in DP \cup RP \quad (12)$$

$$\sum_k \sum_q \sum_{(i,j) \in A} ((CEQ_{i,j,k} + CES_{i,k}) \times \hat{f}n_{i,j,q,k}) \div \sum_{i \in F} SPM_i \leq G \quad (13)$$

$$\sum_k \sum_i \hat{f}n_{i,j,q,k} = \sum_k \sum_l \hat{f}n_{j,l,q-M_{j,l,k}-M_{j,l,k}}, \quad n_i \in FP \cup DP \cup RP, \forall n_j \in DP \cup RP \quad \forall q \quad (14)$$

$$\Delta q_{i,k} = (THT_i \times 2 + TST_i) \times \Delta q_k, \quad \forall n_i \in DP \cup RP \quad (15)$$

$$\Delta q_{i,j,k} = TTP_{ij} \times \Delta q_k, \quad \forall (i, j) \in A \quad (16)$$

$$\hat{f}n_{i,j,q,k} \in \mathbb{Z}^+, \quad \forall (i, j) \in A, \forall q, \forall k \in \{k_1, k_2, \dots, k_n\} \quad (17)$$

are formulated.

4) Corresponding explanations

The model can be applied to the intermodal transportation network design in food cold chain. We take the inbound container flows in the formulation of this model. The objective function (8) minimizes unit costs of refrigerated containers flowing through the network, which includes costs of: transportation, refrigeration, terminal handling, storage and customs clearance. The objective function (9) minimizes total unit quality degradation including the loss in transportation and storage. The definition of average quality degradation is used in this model. The total quality degradation is the sum of loss of food in each refrigerated container routing through all the network. Then the total loss is divided by the total container amount to get the unit quality degradation. The constraint (10) and (11) are supply and demand constraints of refrigerated containers. The constraint (12) specifies the capacity of each transport nodes. The constraint (13) represents the CO₂ emission restrictions regulated by the government. The constraint (14) reflects the

balance of cargo in flows and out flows at each node with quality degradation. The constraint (15) and (16) represent the quality degradation in a node and on an arc, respectively. The constraint (17) is the non-negativity constraint and integer restriction on the decision variables.

Similar to the viewpoint about capacity constraint expressed by H.J. Kim et al. (2008), we calculate the capacity of each domestic port by:

$$CAP_i = \alpha_i \times CAP_i^* \quad (18)$$

where α_i is the proportion of the cargo volume related to the intermodal transport among the total throughput at port i and CAP_i^* is the capacity corresponding to the transport of refrigerated containers of the port gotten after removing the trans-shipment cargoes.

This model is a bi-objective MILP problem including minimizing cost and quality degradation simultaneously and the CO₂ emission requirements are set as a constraint in this model. The model was implemented in IBM ILOG CPLEX Optimization Studio 12.6 which is an optimization software program. Though large-scale cases need some meta-heuristic algorithms, most medium or small-size problems can be solved directly and efficiently by the CPLEX solver. The test runs were performed on a 3.50Ghz Xeon PC (with 16.0 GB RAM). The network resulted in a problem instance with tens of thousands of constraints and a few ten thousand variables (around 1500 integer) and was solvable well within limits acceptable for decision support in the industrial practice.

MODEL APPLICATION AND ILLUSTRATIVE CASE STUDY

In this section a case study on the refrigerated container cargo shipment in China is performed. As China strives to achieve more regional cooperation, its “Belt and Road” initiative will not only drive domestic development but will also influence its foreign policy. At sea, it will focus on jointly building smooth, secure and efficient transport routes connecting major sea ports and increase connectivity of customs clearance, reloading and multimodal transport between countries.

In this case we set the hinterland area of Dalian Port and Yingkou Port in Northeast China as the backyard of our study. As the most important container port in Northeast China, Dalian Port cooperates with more than 100 container shipping lines. Over 90 percent of the international containers in three north-eastern provinces need to be trans-shipped in Dalian Port. Not far away from Dalian Port, Yingkou Port was ranked as the 9th container port since 2015. We choose two domestic ports, Dalian Port and Yingkou Port, as an example. Rapid container traffic growth has taken place in the two ports over the past ten years. In this example two foreign ports, i.e. Laem Chabang and Manila are involved in China’s international cold chain trade for bananas. According to the

hinterland situation, we include two main inland transport modes, namely, truck and rail.

The selected hinterland areas of Dalian and Yingkou ports include Liaoning Province, Jilin Province and Heilongjiang Province. Nine big cities are chosen as inland city nodes. Based on the current situation of transportation infrastructure in Northeast China, we consider two railroad dry ports in Shenyang and Changchun. Data on distance parameters were collected from “SeaRates.com”, “www.12306.cn” and “www.amap.com”.

We assume that refrigerated container is 100% laden for import, and customs clearance cost amounts to \$100 per TEU. Other port handling cost is \$160 per TEU. Every inland city has its own demand in accordance with the different urban development level. Other parameters are given in Tab. 1.

Tab. 1. Transport parameters

Mode	Ship	Rail	Truck
Variable transportation cost (\$/km)	0.2	0.5	1.5
Average speed (km/h)	40	40	60
CO ₂ footprint (kg/ton × km)	0.084	0.208	0.796

QUALITY DEGRADATION

Investing more resources in preservation efforts, by using a faster transportation mode or lower setting temperature, helps to keep quality degradation to a minimum (Cai et al., 2010). Although palletized bananas have been mainly transported on specialized vessels in the past, the transportation mode is shifting to refrigerated containers on shipping companies’ vessels, which allows to take a more flexible reaction to fluctuating market volumes. For bananas, colour and weight are two important factors determining quality, green life and market value. According to the quality degradation of fruits (see Sec. 2.1), the quality is a linear function of temperature. The optimum temperature range for bananas is between 10 °C ~15 °C . The green life period of bananas for each temperature option (take 11 °C , 13 °C and 15 °C just to distinguish the effect of different temperature on cost and CO₂ emission in the optimum range) is shown in Tab. 2 (Jedermann et al., 2014).

Tab. 2. Estimated quality degradation for bananas at different temperature levels

Temperature (°C)	11	13	15
Green life period (days)	52	45	38
Quality degradation per day (Δq)	0.96%	1.104%	1.316%

RELATIVE COOLING COST AND CO₂ FOOTPRINT

The cost of transportation depends on the setting temperature. We take the thermal characteristics of cooling processes into consideration in order to determine the cost. The coefficient of performance (COP) for refrigeration is calculated as follows (Wang, 2000).

$$COP = \frac{Q_L}{W} = \frac{T_L}{T_H - T_L} \quad (19)$$

Where W is the input energy, Q_L – the amount of heat transferred from a lower temperature environment to a higher one, T_H – higher temperature and T_L – lower temperature – both measured in Kelvin. The COP means that, for each unit of energy drawn from an electricity source, the coolant can absorb as much as COP units of heat from the inside of the refrigerator. For example, if $T_H=298\text{K}$ (25°C), and $T_L=284\text{K}$ (11°C), then COP is 20.29.

If we assume the cost of electric energy at 11°C equal to 1, then the relative cost at other temperature can be calculated by multiplying the cost with the ratio of COP. For instance, with the COP at 11°C (20.29) and the COP at 13°C (23.83), we get the ratio of $20.29/23.83=0.85$. The results for other temperature levels are shown in Tab. 3.

Tab. 3. The relative transportation cost and CO₂ footprint values for different temperature values, using 11°C as a reference

Temperature ($^\circ\text{C}$)	11	13	15
Relative transportation costs	1	0.85	0.70
Relative CO ₂ footprint	1	0.85	0.70

THE SCENARIO WITH BI-OBJECTIVE OPTIMIZATION

To analyze the trade-offs between transport cost and quality degradation, we give the results of the bi-objective optimization shown in Fig. 4, 5 and 6. When transport cost is the only objective, the railway transport mode with the highest setting temperature which generates the lowest CO₂ emission is the most preferred one. When quality degradation is the only objective, the truck transport mode with the lowest setting temperature which generates the highest CO₂ emission is the most preferred.

The usage rate of truck is still higher while the usage rate of train is relatively low because many cities do not have railway links to domestic ports or the capacity of existing railway dry ports is limited with the growing rail-sea intermodal transportation volumes. The inland transportation network of Dalian Port and Yingkou Port is composed of railway, highway and state roads, which covers the whole Northeast China hinterland. The capacity of railway dry port will keep pace with the increasing of transportation demand for containers according to the economic and social development planning.

In the sea leg, optimization objectives also affect the route for cargo. Dalian Port is an integral part of Dalian Northeast Asian International Shipping Centre. For import containers to the port hinterland, many shipping lines call Dalian Port first and then Yingkou Port, or link Dalian and Yingkou ports with feeder services. If a customer needs to receive cargoes at a lower quality loss, container must be discharged at Dalian Port and then trucked to Yingkou, otherwise his containers can be discharged at Yingkou Port.

SENSITIVITY ANALYSIS OF CO₂ EMISSION RESTRICTIONS

According to Sec. 2.3, G represents the average CO₂ emission limitation per TEU which reflects the restriction

on CO₂ emission. In order to illustrate the impact of G value, we obtain modelling results at four sets of G value. In CO₂ requirements I, II and III, G values are set to 20830 kg, 22370 kg and 23910 kg, respectively. In CO₂ requirements IV, G value is set to 32040 kg or more. When G value is greater than 32040 kg (When this result is obtained, we take some other small values at equal intervals just to contrast the effect of CO₂ emission on modelling results), the change of G value will not impact the Pareto Frontier.

We can note that the usage of train increases and the setting temperature rises when G value decreases. The usage of truck increases and the setting temperature decreases when G value increases. This finding is in conformity with the common sense that train is more environmentally friendly than truck and higher temperature causes less greenhouse emissions.

It is noted that a small change in CO₂ emissions will have a significant effect on the results. The sea transport distance takes a primary share in the total intermodal chain's mileage because majority of CO₂ emission is from the sea transport. Thus, addressing environmental protection into intermodal network design, we can reduce the truck mileage for inland transport, which can also save cost. However there must be done substantial improvements in inland intermodal transport infrastructures, including railways and dry ports.

Tab. 4. Transport quantity via railroad ports

Railway dry port	Capacity (TEU)	Usage (TEU)			
		G= 20830kg	G= 22370kg	G= 23910kg	G≥32040kg
Shenyang	600	600	0	0	0
Changchun	450	450	450	209	0
Total	1050	1050	450	209	0

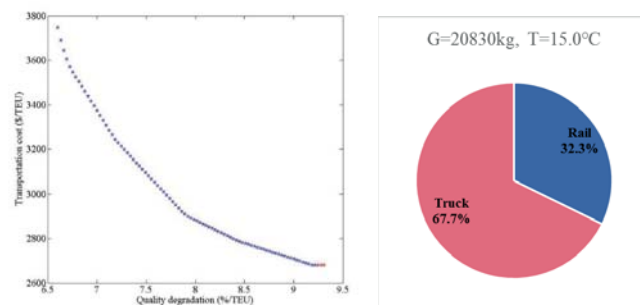


Fig. 4. Modelling results at CO₂ Emission Constraint I ($G=20830$ kg)

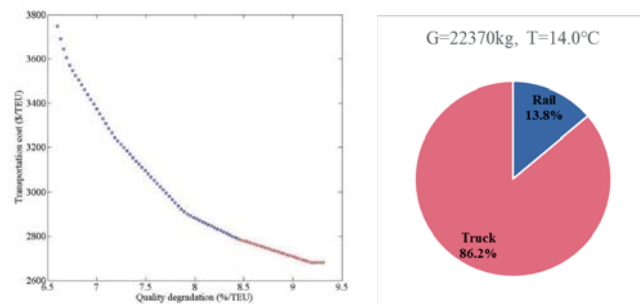


Fig. 5. Modelling results at CO₂ Emission Constraint II ($G=22370$ kg)

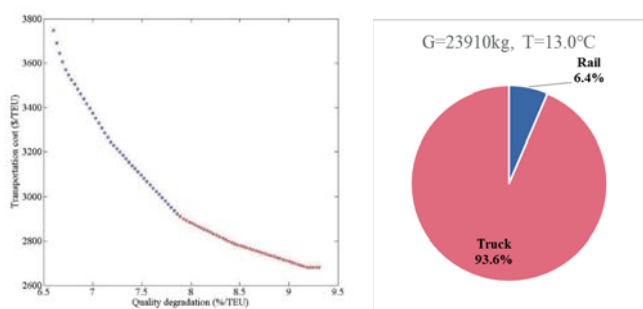


Fig. 6. Modelling results at CO₂ Emission Constraint III (G=23910 kg)

$$Z = A + Bx + C / y + Dx^2 + E / y^2 + Fx / y + Gx^3 + H / y^3 + Ix / y^2 + Jx^2 / y \quad (20)$$

where : Z is the transportation cost, x - the average quality degradation and y - the ambient temperature. A, B, C, D, E, F, G, H, I, J are parameters of the fitting equation (20). The fitting parameters of the three-dimensional curved surface are shown in Tab. 6.

Tab. 6. Fitting parameters of three-dimensional curved surface

A	B	C	D
3.33×10 ⁴	-5.29×10 ³	-8.79×10 ⁵	773.88
E	F	G	H
3.20×10 ⁷	-1.04×10 ⁵	-38.37	-2.39×10 ⁷
I	J	R ²	
-3.03×10 ⁵	7.23×10 ³	0.994	

FITTING ANALYSIS IN AMBIENT TEMPERATURES

Based on the description given in Sec. 3.2, it is known that we use 25 °C as the ambient temperature. However, there will be different ambient temperatures in different seasons with global periodic climate change. Relative transportation costs and relative CO₂ footprint in different ambient temperatures are shown in Tab. 5.

Fig. 7 summarizes the results for four different ambient temperatures. It clearly shows that the increase in ambient temperature leads to the increase in cost under the same average quality degradation. The difference between the ambient temperature and the temperature in refrigerated containers has an obvious effect on cost because the higher the temperature difference the more energy burnt by the vehicle.

Tab. 5. The relative transportation cost and CO₂ footprint values, using 11 °C as the reference for different ambient temperatures

Ambient temperature (°C)		Setting Temperature (°C)		
		11	13	15
Relative transportation costs or Relative CO ₂ footprint	21	1	0.79	0.59
	23	1	0.83	0.66
	25	1	0.85	0.70
	27	1	0.87	0.74

The outlining characters of the three-dimensional curved surface are analyzed. Based on the fitting curved surface, a new calculating method for the cost is presented (Eq. 20).

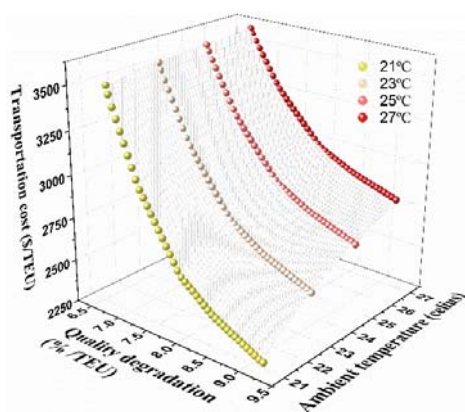


Fig. 7. Modelling results for different ambient temperatures

CONCLUSIONS AND FUTURE RESEARCH

This research has provided a novel approach to the intermodal network design problem for refrigerated container shipment considered from the tactical level point of view, based on an optimization model. The shippers need to know how to optimize transport planning based on customer requirements and transportation infrastructure. In the market driven business environment, they have to optimize total cost and also to meet quality requirement given by customers. Especially for high value-added products, they have to take fully the influence of temperature and time on the quality of commodities into account. In the meantime, they are required to comply with CO₂ emission restrictions as commodity refrigeration produces more CO₂ emission during transportation. Roads and railways are the most common modes for container land transportation with their imperfections and suitability. As discussed in the former sensitivity analysis, the CO₂ emission restriction for cold chain transportation in the intermodal network can be adjusted to accommodate different situations. First, the shippers should utilize railways as the primary transportation mode and set the higher temperature to lower cost and CO₂ emissions whenever inland railways are available. Second, they are recommended to use trucks and set lower temperature selectively when quality of commodities is a major concern from the side of customers. Third, tighter environment regulations on CO₂ emissions favour rail transport and higher temperature setting, and a little change in the CO₂ emission restriction will have a significant impact on the range of feasible solutions. Thus, the shipper ought to adopt a better approach by flexible taking cost, quality and CO₂ emission into consideration for the intermodal network planning. The preference choices of the model for the cold chain design (Sea-Rail Transport and Sea-Road Transport) are a combination of these factors

for the mutual relationship among transportation modes, quantities and setting temperatures.

Furthermore, shippers can use the optimization model for investment and service planning before they enter a new market. In the numerical example, Harbin-Dalian Railway, G1 Highway, G2 Highway and other important passages serve as a corridor linking coastal ports in Liaoning Province and Northeast China hinterland. Actually, the Chinese government has realized that insufficient transport infrastructure hinders the economic development of Northeast China. The central committee of the Communist Party of China, announced a plan to revitalize the old industrial base of Northeast China, largely focusing on its transport facilities. Li Keqiang stressed that the government should invest more in public facilities such as transport, water projects and railways, and also called for innovation in investment and financing – to attract more social investment.

There are some contributions made by this research not only to the academic field but also the transportation industry. As an academic contribution, this model fills the gaps in the subject-matter literature, because it optimizes port- hinterland intermodal flows of refrigerated containers considering both cost and quality degradation. Moreover, this study is distinctive from the previous literature in a way that it quantifies the influence of CO₂ emission in different setting temperatures on intermodal network planning. Also, the numerical example provides an illustration of the intermodal network planning in Northeast China. Furthermore, the model can offer a useful reference for other regions with the demand for different imported food which requires an uninterrupted cold chain during the transportation and storage. The primary contribution of this paper is that the model is beneficial not only to shippers and customers for the novel service design, but also offer insights for the governmental policy-makers to attract attention to developing inland transport infrastructure when considering intermodal transportation.

There are also some limitations in this study. On one hand, the uncertainty factors, such as demand, supply and transit time have not been considered in this study. On the other hand, in this model we do not combine the inbound and outbound container flows, which means that the developed formula represents only one-way flow. All of these issues are valuable research directions to be undertaken in the future.

ACKNOWLEDGMENT

The authors would like to acknowledge the support of National Natural Science Foundation of China (Projects No. 51309049 and No. 51279026). In addition, we acknowledge the Research Centre for Port Development at Dalian University of Technology for partial funding and devices.

REFERENCES

1. FAO: FAO Statistical Yearbook 2014 (FAO ed.).
2. H. Min : [International intermodal choices via chance-constrained goal programming](#). Transportation Research Part A General. 25(6), 1991, pp.351-362.
3. Flannone and S Thore: An economic logistics model for the multimodal inland distribution of maritime containers. International Journal of Transport Economics. 37, 2010 , pp. 281-326.
4. W.F. Wang and W.Y. Yun : Scheduling for inland container truck and train transportation. International Journal of Production Economics. 143, 2013, pp. 349-356.
5. R. Zhang, W.Y. Yun , H. Kopfer: Heuristic-based truck scheduling for inland container transportation. Or Spectrum. 32 , 2010, pp. 787-808.
6. C. Liao, P. Tseng and C. Lu: Comparing carbon dioxide emissions of trucking and intermodal container transport in Taiwan. Transportation Research Part D : Transport and Environment,14, 2009, pp. 493-496.
7. X.J. Yang, J. Low and L.C. Tang: Analysis of intermodal freight from China to Indian Ocean: A goal programming approach. Journal of Transport Geography, 19, 2011, pp. 515-527.
8. R.Y. Zhang, W.Y. Yun , I.K. Moon: Modelling and optimization of a container drayage problem with resource constraints. International Journal of Production Economics,133, 2011, pp. 351-359.
9. J. Lam and Y. Gu : A market-oriented approach for intermodal network optimisation meeting cost, time and environmental requirements. International Journal of Production Economics,171, 2011, pp. 266-274.
10. M. Rahimi, A. Asef-Vaziri and R. Harrison: An Inland Port Location-Allocation Model for a Regional Intermodal Goods Movement System. Maritime Economics & Logistics, 10 , 2010, pp. 362-379.
11. W.B. Fitzgerald, O. Howitt , I.J. Smith, et al. : Energy use of integral refrigerated containers in maritime transportation. Energy Policy,39, 2011, pp. 1885-1896.
12. K. Vankerschaver, F. Willocx, C. Smout, et al. : Mathematical modelling of temperature and gas composition effects on visual quality changes of cut endive. Journal of Food Science, 61,1998, pp. 613.

13. K. McDonald and D.W. Sun : Predictive food microbiology for the meat industry: a review. *International Journal of Food Microbiology*, 52 , 1999, pp. 1-27.
14. L. Lukasse and J.J. Polderdij : Predictive modelling of post-harvest quality evolution in perishables, applied to mushrooms. *Journal of Food Engineering*, 59, 2003, pp. 191-198.
15. H.J. Kim, Y.T. Chang , T.W. Lee, et al. : Optimizing the transportation of international container cargoes in Korea. *Maritime Policy & Management*, 35, 2008, pp. 103-122.
16. Filina-Dawidowicz L. : Rationalization of servicing reefer containers in sea port area with taking into account risk influence. *Polish Maritime Research*, 21, 2014, pp. 76-85.
17. X.Q. Cai, J. Chen , Y.B. Xiao, et al. : Optimization and Coordination of Fresh Product Supply Chains with Freshness-Keeping Effort. *Production and Operations Management*, 19, 2010, pp. 261-278.
18. R .Jedermann, U. Praeger , M. Geyer, et al. : Remote quality monitoring in the banana chain. *Philosophical Transactions of the Royal Society a-Mathematical Physical and Engineering Sciences*, 372, 2014.
19. S.K. Wang : *Handbook of Air Conditioning and Refrigeration*. Ed.S.K. Wang, 2000.

CONTACT WITH THE AUTHORS

Qianli Ma

e-mail: qianlima@mail.dlut.edu.cn
 Dalian University of Technology
 Linggong Road, 116024 Dalian
CHINA

Wenyuan Wang

e-mail: wangwenyuan@dlut.edu.cn
 Dalian University of Technology
 Linggong Road, 116024 Dalian
CHINA

Yun Peng

e-mail: yun_peng@dlut.edu.cn
 Dalian University of Technology
 Linggong Road, 116024 Dalian
CHINA

Xiangqun Song

e-mail: sxqun@dlut.edu.cn
 Dalian University of Technology
 Linggong Road, 116024 Dalian
CHINA

SELECTION OF MAIN ENGINES FOR HOPPER SUCTION DREDGERS WITH THE USE OF PROBABILITY MODELS

Damian Bocheński
Gdańsk University of Technology, Poland

ABSTRACT

This paper presents a new original method of selection of main engines for hopper suction dredgers with regard to probabilistic models. It was proposed to use the normal distribution to describe the operational loads of the main receivers. The principles for determination of parameters of load distribution and design power of the main engines were formulated. Lastly, the principles of selection of the size and number of main engines has been proposed.

Keywords: hoppers suction dredgers, main engines, design

INTRODUCTION

The selection of main engines for hopper suction dredgers, due to the large number of main types of energy receivers and the significant variability of energy demand in particular the operating states, is one of the most difficult tasks in the design of marine power plants.

On the hopper suction dredgers one can find four main types of energy receivers, which are [9]:

- receivers for self-propulsion, dredging and maneuvering (propulsors and bow thrusters),
- receivers connected with the break-up, grounding and transport of the soil (dredge pumps and jet pumps).

On the hopper suction dredges, very often the drive of several major energy consumers is used by one main engine (centralized drive of main power receivers). In many cases, the main engine may have a nominal power less than the combined power of the main power receivers (this is the result of variability of the load of this type of main receivers during the work involved in dredging works).

Design of dredger power systems requires the use of appropriate pre-design methods when deciding on the size and number of main and auxiliary engines.

In currently used shipbuilding engine design methods [10, 11, 12, 13, 14, 15, 16, 17] and in the recommendations of marine engine manufacturers [18, 19, 20, 21, 22], deterministic methods are used for the selection of main engines. This is based on the assumptions used for calculations, established working conditions and related equipment parameters corresponding to the most unfavorable energy situation.

According to the author, significant advances in dredging machine initialization methods and in solving a number of exploitation problems are due to the use of probabilistic models containing random variables or random functions. Probabilistic models will better describe the complex and variable realities of dredger operation, which are strongly influenced by casual factors rather than deterministic models.

On the basis of the author's research, published in [3, 4, 6, 9], it can be assumed that to describe the operating load power of the main power dredgers receivers (or groups

of auxiliary energy receivers), which are random variables one may use normal or close to normal distribution. Additionally, there is the possibility of assuming independence between the simultaneous power loads of the main power receivers.

The justification for assuming that load distributions of these receivers (or groups of receivers) can be described by normal distribution (or close to normal) is the fact that their load affects many randomly varying volumes. For example, they may be external conditions (winds, currents, waves, etc.), dredging conditions (bottom shape, length of pipelines, type of dredging). They significantly affect the load of the main receivers. Power loads are dependent on the demand generated by numerous (about several hundred) auxiliary energy receivers operating independently.

OPERATIONAL LOADS OF MAIN POWER RECEIVERS

The main energy receivers of the hopper suction dredgers are characterized by different power loads in the individual jobs of the “dredging” work [3,4,5,9]. Therefore, the confirmation of the assumption concerning the normality of load distributions of the main energy receivers of dredgers was related to the construction of models of their exploitation loads, taking into account the components of state of “dredging works” [9].

As regards dredger suction dredgers, “dredging works” are divided into the following works [9]:

In regards to hopper suction dredgers, “dredging works” are divided into the following works [9]:

- loading (the dredger moves at 2-3 knots with lowered suction pipes, loading of the hopper with dredge pumps, the jet pumps help to break the soil to the bottom, positioning the dredger using the bow thrusters);
- sailing between places of loading and unloading (dredger moving at the speed of several knots, distance from several to over 100NM);
- unloading of the hopper (unloading by pumping the excavated material with the dredge pumps, jet pumps diluting the ground in the hopper, dynamic positioning the dredger with the bow thrusters).

The results of in-service research have allowed us to develop methods of forecasting operational loads of main dredger energy receivers [7, 8, 9]. These studies have identified the relationship between the load distribution parameters of the main dredger receivers (N_{MR}^{us} , σ_{MR}) and their nominal useful power ($N_{MR}^{us})^{nom}$.

The useful power of the dredge and jet pumps is determined by the dependence [4,9]:

$$\left. \begin{aligned} N_{DP}^{us} &= P_{DP}^w \cdot Q_{DP}^w \\ N_{JP}^{us} &= P_{JP} \cdot Q_{JP} \end{aligned} \right\} \quad (1)$$

where:

P_{DP}^w – dredge pump pressure specified for water,

Q_{DP}^w – volume efficiency of the dredge pump specified for water,

P_{JP} – pressure of the jet pump,

Q_{JP} – volume efficiency of the jet pump.

The power of the propulsor can be considered the towing power of the dredger hull N_{HD}^{us} expressed in dependence [7, 9]:

$$N_{HD}^{us} = R_{HD} \cdot v_{DR} \quad (2)$$

where:

R_{HD} – dredger hull resistance at assumed speed of movement,

v_{DR} – assumed speed of movement.

In the design assumptions for the needs of the shipowner for the hopper suction dredges, only the required speed of the dredger v_{DR} is given. As a result, it is necessary to look for the possibility of determining the drag resistance of the dredger hull. The author proposes the use of modified Admiralty method [1, 9], where the size of the suction hopper dredger will be the capacity of the hopper V_{HP} .

In the case of bow thrusters, useful power output use has been abandoned (not given in the technical dossier dredgers) in favor of nominal power thrusters, always given in the dredgers technical specification.

Tab. 1 gives linear regression equations describing the parameters of load distributions of main energy receivers of hopper suction dredger for individual works belonging to the state of “dredging works” [7, 8, 9].

Tab. 1. Linear regression equations that determine the load distribution parameters of the main power receivers of the hopper suction dredgers during the work involved in dredging works

Main receiver	Work type	Form of dependence
Propulsors of the main drive	Sailing between load and unload places	$(N_{PR}^{mn})^{sail} = 7,57 + 0,014 \cdot [(V_{HP})^{2/3} \cdot (v_{DR})^{2,5}]$
		$\sigma_{PR}^{sail} = -6,64 + 0,0024 \cdot [(V_{HP})^{2/3} \cdot (v_{DR})^{2,5}]$
	Loading	$(N_{PR}^{mn})^{load} = 18,41 + 0,01 \cdot [(V_{HP})^{2/3} \cdot (v_{DR})^2]$
		$\sigma_{PR}^{load} = -5,32 + 0,0015 \cdot [(V_{HP})^{2/3} \cdot (v_{DR})^2]$
Dredge pumps	Loading	$(N_{DP}^{mn})^{load} = 1,32 \cdot (N_{DP}^{us})^{load} - 26,34$
		$\sigma_{DP}^{load} = 0,041 \cdot (N_{DP}^{us})^{load} + 17,1$
	unloading	$(N_{DP}^{mn})^{unload} = 0,712 \cdot (N_{DP}^{us})^{unload} + 2,43$
		$\sigma_{DP}^{unload} = 0,076 \cdot (N_{DP}^{us})^{unload} + 22,01$
Jet pumps	Loading and unloading	$N_{JP}^{mn} = 0,89 \cdot N_{JP}^{us} + 6,46$
		$\sigma_{JP} = 0,036 \cdot N_{JP}^{us} + 2,57$
Bow thrusters	Loading	$(N_{BT}^{mn}) = 0,685 \cdot N_{BT}^{nom}$
		$\sigma_{BT} = 0,1 \cdot N_{BT}^{nom}$
	unloading	$(N_{BT}^{mn}) = 0,503 \cdot N_{BT}^{nom}$
		$\sigma_{BT} = 0,09 \cdot N_{BT}^{nom2}$

Acceptable ranges of variable values independent of the equations given in tab. 1 are shown in tab. 2.

Tab 2. Acceptable ranges of variable values independent of the equations given in tab. 1

Independent variable	Value range
V_{HP}	350–13700 m ³
V_{DR}	9–15,5 knots
$(N_{DP}^{us})^{load}$	68,2–1817 kW
$(N_{DP}^{us})^{unload}$	203,5–5084 kW
(N_{JP}^{us})	25–1290 kW
N_{BT}^{nom}	350–1000 kW

OPERATION PARAMETERS OF MAIN ENGINE LOADS

In general, the main engine of the main propulsion system maintains the main drive for the energy receivers and may, to a certain extent, cover the energy demand generated by the groups of auxiliary electric power generators. The parameters of the total load distribution of the main engines for the considered operating state, according to the general principle determining the parameters of the combined normal distribution [1, 9], will be:

$$\left. \begin{aligned} N_{ME,\Sigma}^{mn} &= \sum_{i=1}^n \frac{N_{MR,i}^{mn} \cdot \lambda_{MR,i}^{os}}{(\eta_{MR}^{TM})_i} + \varphi_e \cdot \frac{N_{EL}^{mn} \cdot \lambda_{GP}^{os}}{\eta_{GP} \cdot \eta_{GB}} \\ \sigma_{ME,\Sigma} &= \sqrt{\sum_{i=1}^n \left(\frac{\sigma_{MR,i} \cdot \lambda_{MR,i}^{os}}{(\eta_{MR}^{TM})_i} \right)^2 + \left(\varphi_e \cdot \frac{\sigma_{EL} \cdot \lambda_{GP}^{os}}{\eta_{GP} \cdot \eta_{GB}} \right)^2} \end{aligned} \right\} \quad (3)$$

where:

$N_{ME,\Sigma}^{mn}, \sigma_{ME,\Sigma}$ – mean value and standard deviation of the normal total load distribution of the main engine,

$N_{MR,i}^{mn}, \sigma_{MR,i}$ – mean value and standard deviation of the normal load distribution of the i-th main receiver,

N_{EL}^{mn}, σ_{EL} – mean value and standard deviation of the normal distribution of electricity demand generated by all groups of auxiliary receivers, the method of determining the electrical demand of the hopper suction dredgers is presented in [2,9],

φ_e – coefficient determining the share of electrical power demand covered by generators (or power hydraulics pumps) driven by the main engine,

$\lambda_{MR,i}^{os}, \lambda_{GP}^{os}$ – coefficients determining the share of working time of the i-th main energy receiver, e.g. generator or pump driven by the main engine in the considered operating state,

$(\eta_{MR}^{TM})_i$ – efficiency of the power transmission system to drive the i-th main power receiver,
 η_{GP}, η_{GB} – generator (pump) efficiency, gearbox efficiency.

Parameters of load distribution with the power of the main engines refer to the engine operating time during the “dredging” condition ($\tau_{ME}^{dr} = \lambda_{ME}^{dr} \cdot \tau_{dr}$), to the power of the main engine coupler (main engine couplings). In the case of hopper suction dredgers, “dredging works” are to be divided into three works performed during these activities: loading, hydraulic unloading and moving between the loading and unloading sites. Hence, the operating time of the main engines for this type of dredgers will be defined as: $\tau_{ME}^{load}, \tau_{ME}^{unload}, \tau_{ME}^{sail}$.

The impact of variants of energy system solutions is expressed in different, depending on the variant, values $(\eta_{MR}^{TM})_i$ of individual major energy consumers. Major receivers of this kind may, in certain applications, be driven in a variety of complex power transmission systems. The efficiency of such a system (composed of j elements loaded simultaneously – the serial functional structure) is [9]:

$$\eta_{MR}^{TM} = \prod_{j=1}^n (\eta_j) \quad (4)$$

where: η_j – efficiency of the j-th power transmission system element.

Each applied element of this system is characterized by a specific course of its performance depending on the load being transferred. Knowing the performance characteristics of the individual components of a complex power transmission system, it is possible to determine the course of the power transmission performance across the power range $(N_{MR}^{TM})_{\min} \div (N_{MR}^{TM})_{\max}$ using the relationship (4).

If the efficiency difference of the power transmission system $\Delta \eta_{MR}^{TM}$ is small (generally no more than 5-10% [9]), then the mean $(\eta_{MR}^{TM})_{mn}$ of the efficiency can be used. The average value is calculated as the weighted average [9]:

$$(\eta_{MR}^{TM})_{mn} = \frac{\sum_{i=1}^n (\eta_{MR}^{TM})_i \cdot p_i}{\sum_{i=1}^n p_i} \quad (5)$$

where:

$(\eta_{MR}^{TM})_i$ – Performance of the power transmission system in the i-th range $(N_{MR}^{TM})_{\min} \div (N_{MR}^{TM})_{\max}$,

p_i – load frequency in the i-th main receiver load range.

The coefficient φ_e in equation (3) informs the variant of the solution of the dredging power system in the sense of the principles of electric power generation by the main propulsion system, to cover its demand for auxiliary energy receivers. The value of this factor $0 \leq \varphi_e \leq 1$ [9].

Definitely most of the power solutions of hopper suction dredgers are the power plants characterized by a high degree of centralization of the drive of main receivers and a high degree of integration of power systems. In such systems there is one main engine, or equivalent main engine multi-engine, to drive all the main dredgers present in the dredge, simultaneously covering the electricity demand generated by the auxiliary energy receivers. Trapezoidal suction dredges are commonly used for twin-screw propulsion systems, so there are no single-engine propulsion systems.

In this case, we can talk about four possible variants of the power plant solutions for hopper suction dredgers:

- variant I in which all the energy needed to drive all the main receivers as well as the auxiliary energy receivers is generated by 2-3 generating sets (diesel-electric power station) – fig. 1;
- variant II, in which propulsors of the main propulsion are driven by two main engines in the diesel-mechanical systems (through mechanical transmissions), and the remaining main propulsors of the propulsion are driven by diesel-electric systems (fig. 2);
- variant III, in which two main energy receivers: main propulsors and dredge pumps, are driven by two main engines in the diesel-mechanical systems; the other energy receivers are driven by diesel-electric systems (fig. 3);
- variant IV, where up to three main energy receivers (main propulsors, dredge and jet pumps) are driven by two main engines in the diesel-mechanical systems, and bow thrusters are driven by diesel-electricity system. One main engine drives propulsion through the gearbox and the other through a multi-speed gear pump, the second engine also propels the propulsor and uses a second gearbox to propel the jet pumps (fig. 4).

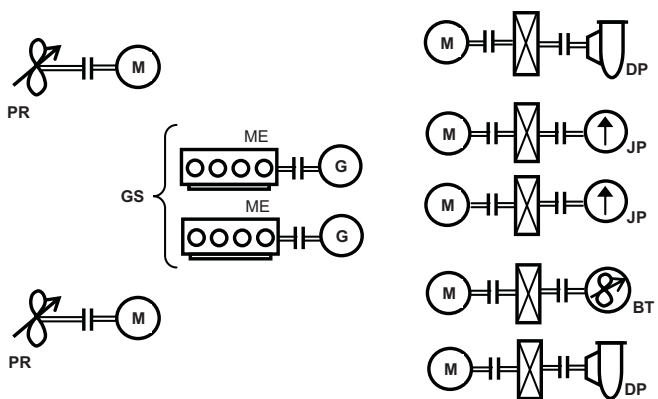


Fig. 1. Schematic diagram of variant I of the power plant; GS – gensets, ME – main engine, PR – propulsor, DP – dredge pump, JP – jet pump, BT – bow thruster

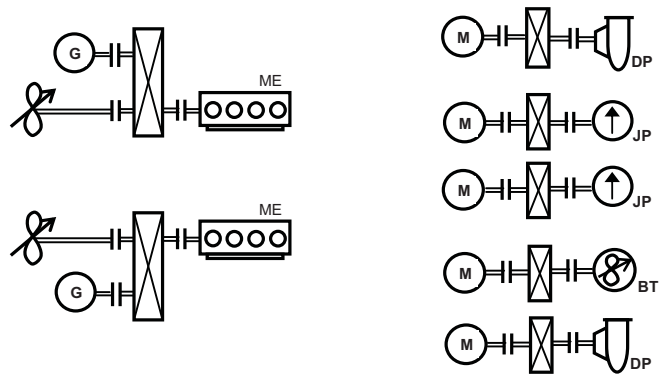


Fig. 2. Schematic diagram of variant II of the power plant; ME – main engine, PR – propulsor, DP – dredge pump, JP – jet pump, BT – bow thruster

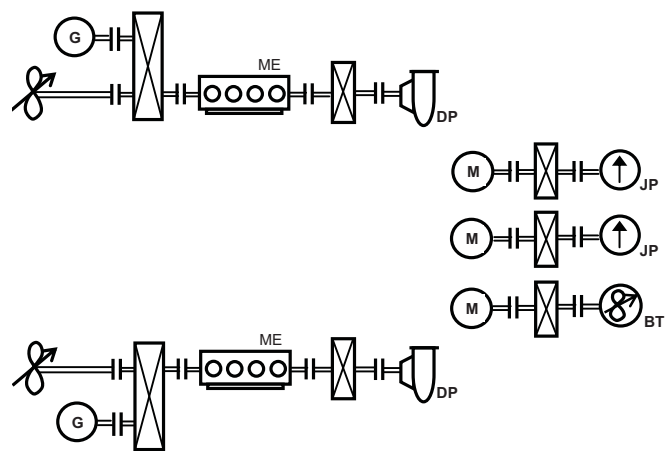


Fig. 3. Schematic diagram of variant III of the power plant; ME – main engine, PR – propulsor, DP – dredge pump, JP – jet pump, BT – bow thruster

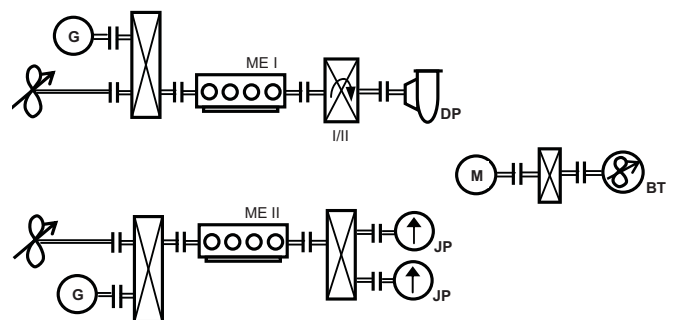


Fig. 4. Schematic diagram of variant IV of the power plant; ME – main engine, PR – propulsor, DP – dredge pump, JP – jet pump, BT – bow thruster

By limiting to these four variants of the engine room solutions of the hopper suction dredgers, dependencies (3) can be transformed into dependencies describing the parameters of the load distribution of the main engines for the three works belonging to the “dredging” state. For variants I, II and III these will be [9]:

– loading ground cargo hold

$$\left. \begin{aligned} (N_{ME}^{mn})^{load} &= \frac{(N_{PR}^{mn})^{load} \cdot \lambda_{PR}^{load}}{\eta_{PR}^{TM}} + \frac{(N_{DP}^{mn})^{load} \cdot \lambda_{DP}^{load}}{\eta_{DP}^{TM}} + \frac{(N_{JP}^{mn})^{load} \cdot \lambda_{JP}^{load}}{\eta_{JP}^{TM}} + \frac{(N_{BT}^{mn})^{load} \cdot \lambda_{BT}^{load}}{\eta_{BT}^{TM}} + \varphi_e \cdot \frac{N_{EL}^{mn} \cdot \lambda_{GP}^{load}}{\eta_{GP} \cdot \eta_{GB}} \\ (\sigma_{ME}^{load}) &= \sqrt{\left(\frac{\sigma_{PR}^{load} \cdot \lambda_{PR}^{load}}{\eta_{PR}^{TM}}\right)^2 + \left(\frac{\sigma_{DP}^{load} \cdot \lambda_{DP}^{load}}{\eta_{DP}^{TM}}\right)^2 + \left(\frac{\sigma_{JP}^{load} \cdot \lambda_{JP}^{load}}{\eta_{JP}^{TM}}\right)^2 + \left(\frac{\sigma_{BT}^{load} \cdot \lambda_{BT}^{load}}{\eta_{BT}^{TM}}\right)^2 + \left(\varphi_e \cdot \frac{\sigma_{EL} \cdot \lambda_{GP}^{load}}{\eta_{GP} \cdot \eta_{GB}}\right)^2} \end{aligned} \right\} (6)$$

– hydraulic unloading

$$\left. \begin{aligned} (N_{ME}^{mn})^{unload} &= \frac{(N_{DP}^{sr})^{unload} \cdot \lambda_{DP}^{unload}}{\eta_{DP}^{TM}} + \frac{(N_{JP}^{mn})^{unload} \cdot \lambda_{JP}^{unload}}{\eta_{JP}^{TM}} + \frac{(N_{BT}^{mn})^{unload} \cdot \lambda_{BT}^{unload}}{\eta_{BT}^{TM}} + \varphi_e \cdot \frac{N_{EL}^{mn} \cdot \lambda_{GP}^{unload}}{\eta_{GP} \cdot \eta_{GB}} \\ (\sigma_{ME}^{unload}) &= \sqrt{\left(\frac{\sigma_{DP}^{unload} \cdot \lambda_{DP}^{unload}}{\eta_{DP}^{TM}}\right)^2 + \left(\frac{\sigma_{JP}^{unload} \cdot \lambda_{JP}^{unload}}{\eta_{JP}^{TM}}\right)^2 + \left(\frac{\sigma_{BT}^{unload} \cdot \lambda_{BT}^{unload}}{\eta_{BT}^{TM}}\right)^2 + \left(\varphi_e \cdot \frac{\sigma_{EL} \cdot \lambda_{GP}^{unload}}{\eta_{GP} \cdot \eta_{GB}}\right)^2} \end{aligned} \right\} (7)$$

– moving between loading and unloading

$$\left. \begin{aligned} (N_{ME}^{mn})^{sail} &= \frac{(N_{PR}^{mn})^{sail} \cdot \lambda_{PR}^{sail}}{\eta_{PR}^{TM}} + \varphi_e \cdot \frac{N_{EL}^{mn} \cdot \lambda_{GP}^{sail}}{\eta_{GP} \cdot \eta_{GB}} \\ (\sigma_{ME}^{sail}) &= \sqrt{\left(\frac{\sigma_{PR}^{sail} \cdot \lambda_{PR}^{sail}}{\eta_{PR}^{TM}}\right)^2 + \left(\varphi_e \cdot \frac{\sigma_{EL} \cdot \lambda_{GP}^{sail}}{\eta_{GP} \cdot \eta_{GB}}\right)^2} \end{aligned} \right\} (8)$$

For variant IV for moving between loading and unloading relation (8) is valid, for the other two works applies dependency [9]:

– loading ground cargo hold

$$\left. \begin{aligned} (N_{ME}^{mn})_I^{load} &= \frac{(N_{PR}^{mn})^{load} \cdot \lambda_{PR}^{load}}{2 \cdot \eta_{PR}^{TM}} + \frac{(N_{DP}^{mn})^{load} \cdot \lambda_{DP}^{load}}{\eta_{DP}^{TM}} + \varphi_e \cdot \frac{N_{EL}^{mn} \cdot \lambda_{GP}^{load}}{2 \cdot \eta_{GP} \cdot \eta_{GB}} \\ (\sigma_{ME}^{load})_I &= \sqrt{\left(\frac{\sigma_{PR}^{load} \cdot \lambda_{PR}^{load}}{2 \cdot \eta_{PR}^{TM}}\right)^2 + \left(\frac{\sigma_{DP}^{load} \cdot \lambda_{DP}^{load}}{\eta_{DP}^{TM}}\right)^2 + \left(\varphi_e \cdot \frac{\sigma_{EL} \cdot \lambda_{GP}^{load}}{2 \cdot \eta_{GP} \cdot \eta_{GB}}\right)^2} \end{aligned} \right\} (9)$$

$$\left. \begin{aligned} (N_{ME}^{mn})_{II}^{load} &= \frac{(N_{PR}^{mn})^{load} \cdot \lambda_{PR}^{load}}{2 \cdot \eta_{PR}^{TM}} + \frac{(N_{JP}^{mn})^{load} \cdot \lambda_{JP}^{load}}{\eta_{JP}^{TM}} + \frac{(N_{BT}^{mn})^{load} \cdot \lambda_{BT}^{load}}{\eta_{BT}^{TM}} + \varphi_e \cdot \frac{N_{EL}^{mn} \cdot \lambda_{GP}^{load}}{2 \cdot \eta_{GP} \cdot \eta_{GB}} \\ (\sigma_{ME}^{load})_{II} &= \sqrt{\left(\frac{\sigma_{PR}^{load} \cdot \lambda_{PR}^{load}}{2 \cdot \eta_{PR}^{TM}}\right)^2 + \left(\frac{\sigma_{JP}^{load} \cdot \lambda_{JP}^{load}}{\eta_{JP}^{TM}}\right)^2 + \left(\frac{\sigma_{BT}^{load} \cdot \lambda_{BT}^{load}}{\eta_{BT}^{TM}}\right)^2 + \left(\varphi_e \cdot \frac{\sigma_{EL} \cdot \lambda_{GP}^{load}}{2 \cdot \eta_{GP} \cdot \eta_{GB}}\right)^2} \end{aligned} \right\} (10)$$

– hydraulic unloading

$$\left. \begin{aligned} (N_{ME}^{sr})_I^{unload} &= \frac{(N_{DP}^{mn})^{unload} \cdot \lambda_{DP}^{unload}}{\eta_{DP}^{TM}} + \varphi_e \cdot \frac{N_{EL}^{mn} \cdot \lambda_{GP}^{unload}}{2 \cdot \eta_{GP} \cdot \eta_{GB}} \\ (\sigma_{ME}^{unload})_I &= \sqrt{\left(\frac{\sigma_{DP}^{unload} \cdot \lambda_{DP}^{unload}}{\eta_{DP}^{TM}}\right)^2 + \left(\varphi_e \cdot \frac{\sigma_{EL} \cdot \lambda_{GP}^{unload}}{2 \cdot \eta_{GP} \cdot \eta_{GB}}\right)^2} \end{aligned} \right\} (11)$$

$$\left. \begin{aligned} (N_{ME}^{mn})_{II}^{unload} &= \frac{(N_{JP}^{mn})^{unload} \cdot \lambda_{JP}^{unload}}{\eta_{JP}^{TM}} + \frac{(N_{BT}^{mn})^{unload} \cdot \lambda_{BT}^{unload}}{\eta_{BT}^{TM}} + \varphi_e \cdot \frac{N_{EL}^{mn} \cdot \lambda_{GP}^{unload}}{2 \cdot \eta_{GP} \cdot \eta_{GB}} \\ (\sigma_{ME}^{unload})_{II} &= \sqrt{\left(\frac{\sigma_{JP}^{unload} \cdot \lambda_{JP}^{unload}}{\eta_{JP}^{TM}}\right)^2 + \left(\frac{\sigma_{BT}^{unload} \cdot \lambda_{BT}^{unload}}{\eta_{BT}^{TM}}\right)^2 + \left(\varphi_e \cdot \frac{\sigma_{EL} \cdot \lambda_{GP}^{unload}}{2 \cdot \eta_{GP} \cdot \eta_{GB}}\right)^2} \end{aligned} \right\} (12)$$

SELECTION OF NUMBER AND SIZE OF MAIN ENGINES

The design value (nominal) of power of the main engine in the case of a single-engine powertrain can be determined from the dependence [9]:

$$(N_{ME}^{nom})^{design} = \frac{N_{ME}^{mn}}{(\bar{N}_{ME}^{mn})^{design}} \quad (13)$$

In the case of a group consisting of several engines, the power given by the relation (13) allows to determine the total nominal power (design) of the main engines ($\sum N_{ME}^{nom})^{design}$. This value corresponds to the combined nominal power of the largest number of operating engines and to the drive of certain main receivers and suspended generators.

The dependent (13) value $(\bar{N}_{ME}^{mn})^{design}$ is determined on the basis of the operating values \bar{N}_{ME}^{mn} of the main engines tested [6,7,9], taking into account the value of the ratio $N_{ME}^{max} / N_{ME}^{nom}$ (which is the ratio of the maximum operating power of the main motors to their nominal power) and the acceptance at an appropriate level of main engine power reserve ΔN_{ME} . The value of this reserve depends on the operating conditions and the nature of the load changes driven by the main engine of the main power receivers. The value ΔN_{ME} of power systems with a high degree of centralization of the main receivers and a high degree of integration of power systems is 0.15 [9], hence the value $(\bar{N}_{ME}^{mn})^{design}$ can be assumed to be 0.65-0.7 [9].

The second way to determine the design value of the nominal power of the main engine is to determine it from the dependence [9]:

$$(N_{ME}^{nom})^{design} = (N_{ME}^{mn} + \beta_{ME} \cdot \sigma_{ME}) + \Delta N_{ME} \quad (14)$$

where:

β_{ME} – coefficient of relative range of maximum loads, acceptance of value $\beta = 3$ allows to determine the maximum load with probability 0,997;

ΔN_{ME} – reserve power of the main engine.

For variants I, II and III the number of main engines in the case of the selection of identical engines, their calculated nominal power will be [9]:

$$(N_{ME}^{nom})_m^{design} = \frac{(\sum N_{ME}^{nom})^{design}}{m} \quad (15)$$

where: $m = 1, 2, \dots$

In the case of selection of engines of different sizes (variant I only) [9]:

$$\sum_{m=1}^n (N_{ME}^{nom})_m^{design} = (\sum N_{ME}^{nom})^{design} \quad (16)$$

In case of variant IV we can say that we have two different single-engine power trains in which the nominal power of the main engine is determined by the dependence (13).

It should be noted, that if one analyzes different variants of drive solutions for major energy receivers, the values $(\sum N_{ME}^{nom})^{design}$ will differ from one another because of different efficiency values $(\eta_{MR}^{TM})_m$ (bypassing the potential demand for auxiliary power receivers). This means that the analyzed variants of the main propulsion drive solutions will be equivalent in nominal power to the main receivers and will differ by the total nominal power of the main engines.

CONCLUSIONS

The presented method can be applied in design practice, mainly at the initial stages of designing hopper suction dredgers. The advantages of the method are:

- the use of probabilistic models, better describing the complex and variable realities of exploitation of dredgers,
- use experimental research to build the above models,
- the need to know only those parameters that are given in the ship's design assumptions.

Using the proposed method, one can analyze many different variants of the engine solutions in different configurations of the main engines. The objective of choosing the best solution is to use the economic efficiency indicator method, which will take into account the investment and operating costs of the variants.

BIBLIOGRAPHY

1. Balcerski A.: *Modele probabilistyczne w teorii projektowania i eksploatacji spalinowych siłowni okrętowych*. Gdańsk: Wyd. Fundacji Promocji Przemysłu Okrętowego i Gospodarki Morskiej 2007.
2. Bocheński D.: *Demand determination for electrical energy for trailing suction hopper dredgers*. W: [Mat.] IV International Scientific-Technical Conference EXPLO DIESEL & GAS TURBINE '05, Gdańsk-Międzyzdroje-Kopenhaga 2005.
3. Bocheński D.: *Operational loads of diesel engines on trailing suction hopper dredgers in their main service states*. Journal of Polish CIMAC, Energetic Aspects vol. 3, nr 1, Gdańsk 2008.
4. Bocheński D.: *Operational loads of dredge pumps in their basic service states on selected types of dredgers*. Journal of Polish CIMAC, Energetic Aspects vol. 3, nr 1, Gdańsk 2008.
5. Bocheński D.: *Eksplatacyjne obciążenia śrub napędowych pogłębiarek różnych typów w podstawowych stanach ich eksploatacji*. Zesz. Nauk. Akademii Morskiej w Szczecinie 2009, nr17 (89), XXIX Sympozjum Siłowni Okrętowych SymSO 2008.
6. Bocheński D.: *Operational loads of diesel engines on trailing suction hopper dredgers in their main service states*. Journal of Polish CIMAC, Energetic Aspects vol. 3, nr 1, Gdańsk 2008.
7. Bocheński D.: *Określanie parametrów rozkładów eksploatacyjnych obciążeń napędu własnego pogłębiarek ssących nasiębiernych podczas robót pogłębiarskich*. Zesz. Nauk. Akademii Marynarki Wojennej w Gdyni 2009, nr 178/A, XXX Sympozjum Siłowni Okrętowych SymSO 2009.
8. Bocheński D.: *Determination of operational load parameters of dredge pumps under dredging operations*. Journal of Polish CIMAC, Energetic Aspects vol. 4, nr 1, Gdańsk 2009.
9. Bocheński D.: *Projektowanie wstępne siłowni pogłębiarek z zastosowaniem metod i modeli probabilistycznych*. Politechnika Gdańska, seria monografie 142, Gdańsk 2013.
10. Harrington R. L.: *Marine Engineering*. The Society of Naval Architects and Marine Engineers 1992.
11. Jamroz J., Swolkień T., Wieszczyński T.: *Projektowanie siłowni okrętowych*. Gdańsk: Wyd. Polit. Gdańskiej 1992.
12. Taylor D. A.: *Introduction to Marine Engineering*. Oxford: Elsevier Butterworth-Heinemann 1996.
13. Urbański P.: *Podstawy napędu statków*. Gdynia: Wyd. Rozwoju AM w Gdyni 2005.
14. Woud H. K., Stapersma D.: *Design of propulsion and electric power generation systems*. London: IMarEST 2002.
15. Vlasblom W. J.: *Designing dredging equipment*. Lecture notes Wb3408, TUDelft 2003-05.
16. Vlasblom W. J., Pinkster J.: *Dredgers*, chapter 51 "Ship design and construction" vol. II. The Society of Naval Architects and Marine Engineers, New York 2004.
17. Welte A.: *Nassbaggertechnik*. Karlsruhe: Institut für Maschinenwesen in Baubetrieb, Universität Fridericiana 1993.
18. Project Guide PROPAC, Wartsila Finland 2006.
19. Project Guide Wartsila 32, Wartsila Finland Oy 2010.
20. Project Guides 2008. DVD Video, MAN Diesel 2008.
21. Wartsila 20-Product Guide, Wartsila Finland Oy 2009.
22. Wartsila 26-Product Guide, Wartsila Finland Oy 2009.

CONTACT WITH THE AUTHORS

Damian Bocheński

Gdańsk University of Technology
11/12 Narutowicza St.
80 - 233 Gdańsk
POLAND

SELECTED PROBLEMS OF SENSITIVITY AND RELIABILITY OF A JACK-UP PLATFORM

Bogdan Rozmarynowski
Tomasz Mikulski
Gdańsk University of Technology, Poland

ABSTRACT

The paper deals with sensitivity and reliability applications to numerical studies of an off-shore platform model. Structural parameters and sea conditions are referred to the Baltic jack-up drilling platform. The study aims at the influence of particular basic variables on static and dynamic response as well as the probability of failure due to water waves and wind loads. The paper presents the sensitivity approach to a generalized eigenvalue problem and evaluation of the performance functions. The first order time-invariant problems of structural reliability analysis are under concern.

Keywords: Random variables, Structural reliability, Simulation methods, Offshore structures

INTRODUCTION

Off-shore platforms belong to the group of structures that work in strong technological and environmental regimes. Methods of probabilistic engineering mechanics applied in the analysis of these structures seem to be the most versatile [1]. This observation comes from the non-deterministic nature of the sea environment, exposing the platform structures to extreme sea waves, wind, current, seismic actions, ice, loads, ship collisions, technological impacts due to drilling works, etc. The requirements of severe environmental conditions and growing expectations of strong offshore industry contribute to the development of various structural systems, consequently invented, designed and operated on the basis of safety factor idea [2]. Valuable views on different offshore engineering problems can be found in [3], [4], [5], [6], [7], [8] and [9].

The paper presents a numerical approach to sensitivity and reliability problems of the Baltic steel drilling platform. This is

a jack-up type platform, originally intended to operate under the Baltic Sea (Fig. 1). In a thirty-year period the platform has been involved in intensive exploration within the Polish Baltic zone, contributing in the development of oil and gas industry in Poland.

Key structural action has been recently undertaken for the structural rearrangement of the platform in order to implement its new drilling stationary functions.

In the analysis of offshore structures there are many engineering problems of high importance, e.g. the structure-sea-subsoil interactions, determination of hydrodynamic, aerodynamic and seismic loads, determination of subsoil parameters, fatigue analysis, safety evaluation, etc. Due to the complexity of the mentioned problems no exact solutions are available, therefore, in order to assess the risk of failure of offshore platforms, approximate procedures must be used. In the paper structural sensitivity theory, e.g. [10], [11] and structural reliability analysis [1], [12] are applied.

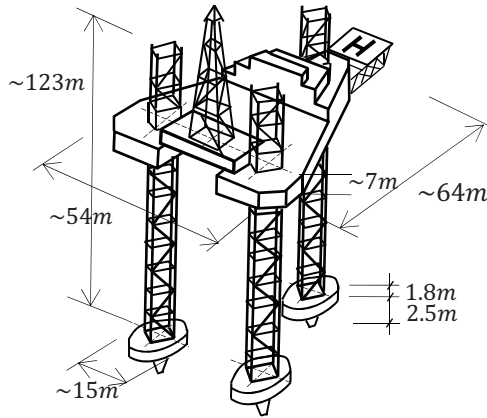


Fig. 1. General view of the Baltic drilling platform (dimensions in meters)

A numerical example deals with sensitivity and reliability computations due to parameters of the Baltic drilling platform [13], [14]. Thus it is the example of real engineering tasks with structural specifications of an existing system.

Sensitivity analysis of the structural response (i.e. displacements, internal forces, reactions, free vibration frequency of space frames and trusses) was performed due to variations of the basic (design) variables [15] was performed. Global structural geometry, cross-sectional dimensions, material constants, support spring constants as well as external loads define basic variables. The computer program for statics and harmonic vibrations of space frames was developed. The sensitivity approach makes it possible to formulate performance functions (failure functions) further applied in reliability analysis. The first order approximation of failure probability is linearization of the performance surface in the domain of standard normal variables, i.e. replacing it by a hyperplane. The design point on the limit-state surface is the point of minimum distance to the origin. Two methods are used in searching the design point, i.e. the method known as the HL-RF method [16] and the directional simulation method, where failure probability in each sample is computed conditionally in a direction in the standard normal space [17] and [18]. These two methods are employed in the author software (cf. [19]).

STRUCTURAL MODEL

The platform is discretized by means of the Finite Element Method [20]. Linear space beam or truss models can be used. Structural parameters (i.e. geometry of the structure, cross-sectional dimensions, length of elements, material constants and support spring constants) and the external loads are considered basic variables. Reliability analysis employs random modelling of the external loads and the subsoil parameters. Loads are assumed point forces with random intensities acting at nodes of the discrete model. Statistical parameters of the load intensity distribution, i.e. the mean value and standard deviation are defined on the basis of static

solution and spectral properties of the load process (the spectral approach was used in the papers of Jesień, 1987 and Rozmarynowski, 1990). The performance functions, created with the help of sensitivity-directed software, express either maximum horizontal deck displacement or flexural load-bearing capacity of the beam cross-section.

STRUCTURAL DATA

Figure 2 presents the discrete model with 72 degrees of freedom and all structural, subsoil, wave and wind parameters used in the analysis [13].

DESCRIPTION OF LOADS

Specification of random loads, i.e. names, distribution types, mean values and standard deviations of the corresponding random variables are shown in the Table 1. The subscript in each variable indicates the appropriate node number due to FEM discretization.

The mean values of particular random variables are evaluated on the basis of static analysis of the Baltic platform [21]. The standard deviations of the wind and wave loads in the considered case are computed using spectral characteristics of the load processes (cf. [13] and [14]). The coefficient of variation of the self-weight was assumed 10%. Fig.2 includes the following wave field data parameters: \bar{H} , \bar{T} , \bar{L} , are mean height, mean period and mean length for long-crested waves, respectively; C_M' , C_M'' , C_D are empirical inertia and drag coefficients of the Morison equation [22].

In the case of slender enough and vertical cylinders, fixed in the sea bottom, the equation takes the form:

$$d\mathbf{P}_H(x,t) = d\mathbf{P}_{HI}(x,t) + d\mathbf{P}_{HD}(x,t) = \rho \frac{\pi d^2}{4} \left\{ C_M' \frac{\partial \mathbf{v}_n(x,t)}{\partial t} + C_M'' \left(\frac{\partial \mathbf{v}_n(x,t)}{\partial t} - \frac{\partial \dot{\mathbf{q}}_n(x,t)}{\partial t} \right) \right\} + \frac{1}{2} d C_D (\mathbf{v}_n(x,t) - \dot{\mathbf{q}}_n(x,t)) \|\mathbf{v}_n(x,t) - \dot{\mathbf{q}}_n(x,t)\| dx \quad (1)$$

where $d\mathbf{P}_H(x,t)$ is the wave force (the hydrodynamic load vector) normal to the local axis Ox of the cylinder of a length dx . This force is aligned with the direction of wave propagation. $d\mathbf{P}_{HI}$ is the inertia force and $d\mathbf{P}_{HD}$ denotes the drag force; ρ is the density of water; d is the diameter of the submerged cylinder; subscript n denotes "normal" to the cylinder axis; $\mathbf{v}(x,t)$ stands for the water particle velocity in the undisturbed wave field; $\dot{\mathbf{q}}(x,t)$ defines the cylinder response (velocity); C_M'' is the added mass coefficient – part of the Eqn. (1), involving the cylinder acceleration, complements suitable terms of the structural mass matrix; $\partial/\partial t$ denotes the partial derivative.

The last term of the Morison Eqn. (1) is non-linear, it represents the hydrodynamic drag forces. This term was studied in detail in [14]. If the analysis covers static (and free undamped vibration) computations, the following terms from Eqn. (1) are required:

$$\mathbf{P}_{HI}^i = \int_{-l/2}^{l/2} d\mathbf{P}_{HI}^i = C_M \frac{\rho g}{l} \mathbf{V}_i H K_I \quad (2)$$

$$\mathbf{P}_{HD}^i = \int_{-l/2}^{l/2} d\mathbf{P}_{HD}^i = \frac{1}{2} C_D \frac{\rho g}{l} \mathbf{A}_i H^2 K_D$$

where l is the element length; g stands for the acceleration of gravity; \mathbf{V}_i denotes the volume of the submerged element associated with the i -th node of the discrete model; H is the wave height and:

$$K_I = \frac{1}{2} k \int_{-l/2}^{l/2} \frac{\cosh(k(x+h))}{\cosh(kh)} \sin\left(-\frac{2\pi t}{T}\right) dx$$

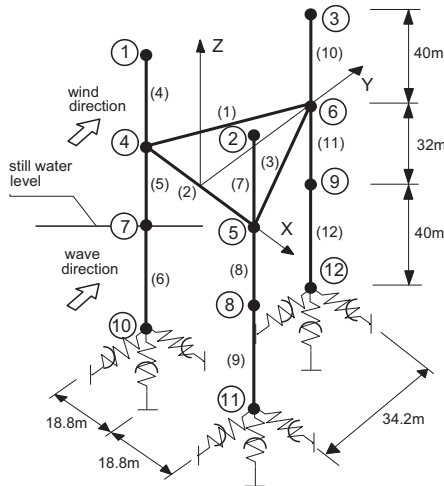
where $k = 2\pi/L$, h is the depth of the sea, x indicates the local axis variable, T denotes the wave period; \mathbf{A}_i is the projected area of the submerged element:

$$K_D = \frac{1}{4} k \int_{-l/2}^{l/2} \frac{\cosh^2(k(x+h))}{\sinh(kh)\cosh(kh)} \left| \cos\left(\frac{2\pi t}{T}\right) \right| \cos\left(\frac{2\pi t}{T}\right) dx$$

The engineering applications of Eqns. (2) direct the investigation to extreme values. Additionally, these extremes do not occur simultaneously. The appropriate factor to reduce their combination depends on the ratio $C_M d / C_D H$. The inertia and drag forces obtained this way (after integration from the sea bottom to the free sea elevation, with respect to the length of the beam finite elements) results in the load mean values.

D_z specified in Fig. 2 is an equivalent diameter of the platform leg composed of four cylinders, each of diameter d .

Wind field data parameters (Fig. 2): \bar{V}_{10} is the mean speed at a height of 10m above the surface; χ denotes the surface drag coefficient, L is the length scale of turbulence, a, b, c are



SUBSOIL PARAMETERS:
 $E = 60 \text{ MPa}$, $\nu = 0.4$, $E(G) = 21.4 \text{ MPa}$
 $\sigma_G = 10,7 \text{ MPa}$

empirical coefficients in the Davenport's formula expressing the cross-spectral density of the along-wind fluctuating velocity [23], C_{DA} is the drag coefficient .

THE SUBSOIL PROPERTIES

The subsoil parameters are assumed deterministic or random. In both variants the subsoil is assumed a homogeneous linear half-space defined by shear modulus G and Poisson's ratio ν . It is assumed that in the second variant of the subsoil model, shear modulus is random, whereas Poisson's ratio is deterministic. The soil-structure interaction is simulated by a system of springs. The mean values and the variances of the spring coefficients are [13], [24]:

$$K_{iX}^H = K_{iY}^H = \frac{8r_0}{2-\nu} E(G), K_{iZ}^V = \frac{4r_0}{1-\nu} E(G),$$

$$K_{iX}^R = K_{iY}^R = \frac{8r_0^3}{3(1-\nu)} E(G), K_{iZ}^T = \frac{16r_0^3}{3} E(G) \quad (3)$$

$$\sigma_{K_H}^2 = \frac{64r_0^2}{(2-\nu)^2} \sigma_G^2, \sigma_{K_V}^2 = \frac{16r_0^2}{(1-\nu)^2} \sigma_G^2,$$

$$\sigma_{K_R}^2 = \frac{7.11r_0^6}{(1-\nu)^2} \sigma_G^2, \sigma_{K_T}^2 = 28.44r_0^6 \sigma_G^2$$

where the superscripts H , V , R and T denote horizontal, vertical, flexural and torsional components of the spring stiffnesses, respectively; r_0 is the radius of the disc, $E(\bullet)$ denotes mathematical expectation and σ_G^2 is the variance of shear modulus G , i stands for the node number at the bottom. It results in the values shown in Table 2.

STRUCTURAL PARAMETERS:

1. Element stiffnesses

Part	$EA [MN]$	$GJ_s [MNm^2]$	$EJ [MNm^2]$
Deck	$8.40 \cdot 10^5$	$1.94 \cdot 10^6$	$2.53 \cdot 10^6$
Legs	$0.79 \cdot 10^5$	$6.86 \cdot 10^5$	$8.93 \cdot 10^5$

2. Lumped masses (translational)

Node	Mass [Mg]
1 (2, 3)	300
4 (5, 6)	1800
7 (8, 9)	310
10 (11, 12)	160
Total	$2570 \times 3 = 7710$
Hydrodynamic masses	550
Deck exploitation mass	1700

WAVE FIELD PARAMETERS:

$$\bar{H} = 14m, \bar{T} = 10s, \bar{L} = 180m$$

$$C_M' = C_M'' = C_D = 1$$

WIND FIELD PARAMETERS:

$$\bar{V}_{10} = 40 \text{ m/s}, L = 1200m, \chi = 0.005, a = b = c = 1, C_{DA} = 1,$$

$$D_z = 4m$$

Fig. 2. Space beam discrete model of the platform

SENSITIVITY OF THE EIGENVALUE PROBLEM

The solution to the generalised eigenproblem of the model in Fig. 2 provides to the following natural frequencies (see Table 4). The sensitivity analysis deals with the first natural frequency and the corresponding eigenmode, this is presented in Fig. 3

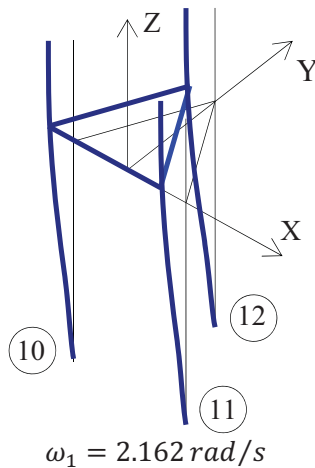


Fig. 3. The analysed first eigenfrequency and eigenmode

In the present example the support spring constraints in nodes 10, 11 i 12 were taken into account as design variables. The variation of natural frequency is as follows

$$\frac{\delta\omega_1}{\omega_1} = \sum_{j=1}^n W_{1j} \frac{\delta x_j}{x_j} \quad (4)$$

where W_{1j} stands for the first-order sensitivity coefficient of the design variable x_j . The sensitivity coefficients for the spring stiffnesses at the indicated nodes are collected in Table 3.

According to Fig. 3 the first eigenmode, shows flexural deformation type along the OX axis, the sensitivity coefficients are presented in Table 3 for perpendicular directions, i.e. K_Y (nodes 10, 11, 12) and K_Z (node 12), as well as for rotations along the OX axis, i.e. K_{φ_X} and the OZ axis, i.e. K_{φ_Z} , are equal zero.

The framed sensitivity coefficients in Table 3 reveal the influences of rotational and translational springs, i.e. K_{φ_Y} and K_Z , on variations of the first eigenfrequency and eigenmode. The obtained results are drawn in Fig. 4 with respect to the node no 10. Similar results were obtained for the remaining support nodes, i.e. no 11 and no 12.

Additionally, Fig. 4 shows that the eigenmode sensitivity is highly affected by translational spring variation, the impact of the rotational one is lower. This is a key practical conclusion, while one of the platform legs meets a weak subsoil layer, a consequent, sudden break may cause structural instability.

Limiting the set of design variables to these related to the vertical components of spring supports in nodes 10, 11 and

12 in terms of the assumed variations, i.e. $\delta K_{10Z} = 0.2K_{10Z}$, $\delta K_{11Z} = -0.2K_{10Z}$, $\delta K_{12Z} = 0.1K_{10Z}$, the comparative sensitivity computations are depicted in Fig. 5.

The direct eigenmode solution indicated in Fig. 5 is an alternative approach used in the study to compare the sensitivity results.

Generally, the first-order variations of the structural response (i.e. displacements, cross-sectional forces, support reactions, free vibration frequencies) due to variations of the basic (design) variables (i.e. loads, Young's modulus, Poisson's ratio, mass density constant, sectional shear distribution factor or cross-sectiona dimensions) can be analysed with the help of the author software developed for statics and harmonic vibrations of space frames.

RELIABILITY ANALYSIS

In the reliability analysis assumptions upon the performance functions are required. In the paper these functions are assumed to take the following two conditions:

Displacement barrier (stiffness condition):

$$g_1(d_p, \mathbf{X}) = 1 - \frac{q(\mathbf{X})}{d_p} \quad (5)$$

where \mathbf{X}^T is the vector of random variables including: vave and wind loads described in Table 1, where v_{X_i} denotes the coefficient of variation of the random variable X_i , self-weight loads modelled by the normal distribution with the mean values computed with the help of lumped masses data presented in Fig. 2 and the coefficient of variation equal 10% and spring stiffnesses replaced by the normal distribution with the mean values shown in Table 2 and the coefficient of variation 50%, $q(\mathbf{X})$ denotes the response (displacement) function, d_p is the maximum allowable drift of the platform.

Cross-section capacity condition:

$$g_2(M_p, N_p, \mathbf{X}) = 1 - \left\{ \left[\frac{M(\mathbf{X})}{M_p} \right]^{\alpha_1} + \left[\frac{N(\mathbf{X})}{N_p} \right]^{\alpha_2} \right\} \quad (6)$$

in which α_1 and α_2 are constant coefficients, $M(\mathbf{X})$ and $N(\mathbf{X})$ are the bending moment and axial force, $M_p = WR_{pl}$, $N_p = AR_{pl}$, where W and A are section modulus and cross-section area, R_{pl} is the yield stress. The parameters of the performace functions in Eqs. (5) and (6), i.e. d_p , W , A and R_{pl} can be generally considered random variables.

In the example the yield stress is assumed Gaussian random variable of the following statistical characteristics:

$$E(R_{pl}) = 250MPa,$$

$$\sigma_{R_{pl}} = 0.125 \cdot E(R_{pl}) = 31.25MPa$$

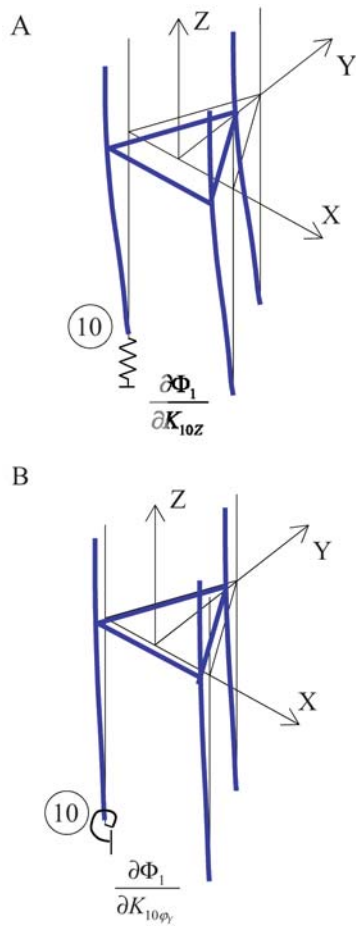


Fig. 4. Sensitivity coefficients of the first eigenmode for the node Nr 10

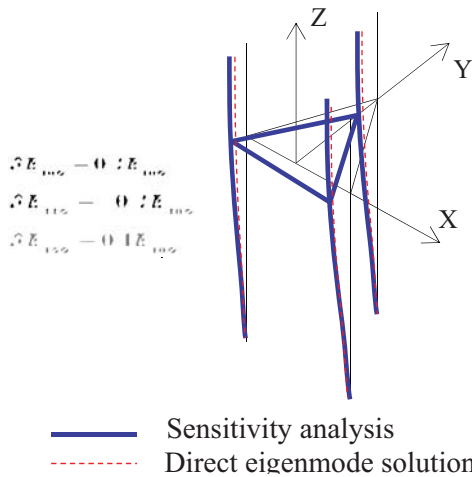


Fig. 5. Comparison of the results

The remaining parameters are taken arbitrarily, based on structural data, i.e. $W = 1.27m^3$, $A = 0.38m^2$ and $\alpha_1 = 1$, $\alpha_2 = 2$ (cf. [25]).

Assume that $S(\mathbf{X})$ is the following general function of the response variables, i.e. $S(\mathbf{X}) = q_{6Y}(\mathbf{X})$ in Eq. (5), where $q_{6Y}(\mathbf{X})$ is the horizontal displacement in Y-direction at the

deck node Nr 6 (Fig. 2) and $S(\mathbf{X}) = \{M(\mathbf{X}), N(\mathbf{X})\}$ in Eq. (6). Let Taylor's series expansion of $S(\mathbf{X})$ exist at the mean value point $\mu_{\mathbf{X}} = E(\mathbf{X})$:

$$S(\mathbf{X}) = S(\mu_{\mathbf{X}}) + \sum_{i=1}^n \left(\frac{\partial S}{\partial X_i} \right) \cdot (X_i - \mu_{X_i}) + \Psi(\mathbf{X}) = \quad (7)$$

$$= a_0 + \sum_{i=1}^n a_i X_i + \Psi(\mathbf{X})$$

where $\Psi(\mathbf{X})$ represents the higher-order terms.

The coefficients in Eq. (7) can be computed in several ways including direct differentiation method, iterative perturbation algorithms [26], [27] and sensitivity methods, i.e. the adjoint method [10] with the use of finite-element procedures. In the paper the sensitivity approach was applied. It yields the statement that the influence of the self-weight variability of loads on the structural response is negligible. It means that the space of basic random variables can be reduced to those representing wind and wave loads and spring stiffnesses. It is assumed that random variables are uncorrelated or correlated.

A basic problem within structural reliability is to evaluate the probability of failure:

$$P_f = P[g_i(\mathbf{X}) \leq 0] = \int_{g_i(\mathbf{X}) \leq 0} f(\mathbf{x}) d\mathbf{x} \quad (8)$$

where $f(\mathbf{x})$ stands for the joint probability density function of $\mathbf{x} \in \mathbf{X}$, $g_i(\mathbf{X})$, $i=1,2$, are the performance functions formulated such that $g_i(\mathbf{X}) \leq 0$ defines failure of the structure and $g_i(\mathbf{X}) > 0$ denotes its survival. To set up the joint probability distribution the Nataf's multivariate distribution model with determined marginal distributions and covariances between them was implemented [28].

The main results of the reliability computation for the platform numerical model presented in Fig. 2 are given in Table 5 and Table 6, where First Order Reliability Method (FORM) and Second Order Reliability Method (SORM) were employed. Probabilities of separate failure modes are presented for uncorrelated and correlated random variables representing wind and wave loads. The maximum allowable displacement was assumed $d_p = 0.5m$.

The HL-RF method originally proposed by Hasofer and Lind and extended by Rackwitz and Fiessler was applied in the presented analysis because experience shows [16] that this method requires small amounts of storage and computation in each step, moreover, in most situations this method converges rapidly.

The Monte Carlo directional simulation method (MCDS) was applied herein in order to compare the results of the HL-RF method. The method is generally applicable for time-invariant reliability integration. The importance sampling technique used in directional sampling in the case of convex polyhedral failure [17] set results in considerably reduced number of trials. In the analysed numerical example the number of trials did not exceed 1000.

CONCLUDING REMARKS

The paper presents the first-order sensitivity and time-invariant reliability approaches of the Baltic drilling platform subjected to wind and wave loads. On the basis of the analysis, it is possible to formulate the following conclusions.

1. All random variables do not act equally on structural reliability. Sensitivity methods may be practically used to quantify the influence of each basic random variable. In the numerical example presented, the self-weight took a negligible influence on response variations. Thus the space of basic random variables was considerably reduced.
2. The data in the numerical example made the displacement-based performance function (stiffness condition) decisive in the structural safety assessment.
3. The probability of the first failure mode increases when the correlation coefficient between the wind and wave loads increases. An opposite tendency one can observe in the second failure mode.
5. Greater probabilities of failure were obtained when the subsoil model has random parameters (cf. Table 6 and [29]).
6. In the considered problem the directional simulation method worked well, compared to the HL-RF method. The limit of 1000 trials was sufficient to achieve accepted convergence. Simulations by classical Monte Carlo method required ten times more trials.

REFERENCES

1. Chandrasekaran S.: *Offshore structural engineering. Reliability and risk assessment*. Taylor and Francis Group, 2016.
2. Chakrabarti S.K.: *Handbook of offshore engineering*. Vol. 1, 2, Elsevier, 2005.
3. Chakrabarti S. K.: *Nonlinear Methods in Offshore Engineering*, Developments in Marine Technology, 5, Elsevier, 1990.
4. Faltinsen O.M.: *Sea loads on ships and offshore structures*. Cambridge University Press, 1990.
5. Clauss G., Lehmann E., Ostergaard C.: *Offshore structures*. Vol. 1, 2. Springer, 1992.
6. Gran S.: *A Course in Ocean Engineering*. Developments in Marine Technology, Elsevier, 1992.
7. Moan T. *Reliability and Risk Analysis for Design and Operations Planning of Offshore Structures*. Structural Safety and Reliability, ICOSSAR'93, 1, Balkema, Rotterdam, 1994, pp.21-43.
8. Wilson J.F.: *Dynamics of offshore structures*. John Willey & Sons, 2003.
9. Bai Y., Bai Q.: *Subsea engineering handbook*. Elsevier, 2012.
10. Haug E. J., Choi K. K. and Komkov V.: *Design Sensitivity Analysis of Structural Systems*. Academic Press, New York, 1986.
11. Szymczak Cz.: *Elementy teorii projektowania* (in Polish). PWN, Warszawa 1988.
12. Melchers R.E.: *Structural reliability and predictions*. John Wiley & Sons, Chichester, 1999.
13. Jesień W.: *Random Vibrations of the Baltic Drilling Platform Subjected to Wind Loads and Water Waves*. Earthquake Engineering and Structural Dynamics, 15, 1987, pp. 595-617.
14. Rozmarynowski B.: *Averaged Damping in Random Vibrations of the Baltic Drilling Platform*. Journal of Sound and Vibration 139(3), 1990, pp. 437-458.
15. Mikulski T. and Szymczak Cz.: *Sensitivity Analysis of Free Vibration Frequencies of Frames including Shear Rotary Inertia Effects*. Proceedings of XI International Conference on Computer Methods in Mechanics, Szczecin-Swinoujście, 14-20 May 1990.
16. Liu P.-L. and Der Kiureghian A.: *Optimization Algorithms for Structural Reliability*. Structural Safety, 9, 1991, pp. 161-177.
17. Bjerager P.: *Probability Integration by Directional Simulation*. Journal of Engineering Mechanics, ASCE, 114(8), 1986, pp.1285-1302.
18. Shao S. and Murotsu Y.: *Reliability of Complex Systems Using an Efficient Directional Simulation*. Structural Safety and Reliability, ICOSSAR'93, 3, Balkema, Rotterdam, 1994, pp.1529-1534.
19. Liu P.-L., Lin H.-Z., Der Kiureghian A.: *CALREL user manual*. Report No. UCB/SEMM-89/18, Berkely 1989.
20. Jesień W., Rozmarynowski B. and Wizmur W.: *Dynamical response of the Baltic drilling platform loaded by wind waves and wind*. Proceedings of an International Conference on Computer Modelling in Ocean Engineering, Venice, 19-23 Sept., Balkema, Rotterdam, 1988, pp. 531-537.
21. Wizmur M., Jesień W. and Rozmarynowski B.: *Static and dynamic algorithms for the Baltic platform structure - deterministic approach*. Internal working report, (in Polish), Gdańsk, 1981.
22. Morison, J.R., O'Brien, M.P., Johnson, J.W. and Schast, S.A.: *The forces exerted by surface waves on piles*. PetroleumTrans., ASME, 189, 1950, pp. 149-154.

23. Davenport A. G.: *The Spectrum for Horizontal Gustiness near the Ground in High Winds*. Quarterly Journal of the Royal Meteorological Society , 87, 1961, pp.194-211.
24. Clough R.W. and Penzien J.: *Dynamics of Structures*. McGraw-Hill, New York, 1975.
25. Sokol L.: *Sollicitations ultimes dans une section circulaire*. Construction Metallique (in French). No. 2, 1988, pp. 73-80.
26. Dias J., Nagtegaal J. and Nakazawa S.: *Iterative perturbation algorithms in probabilistic finite analysis*. Computational Mechanics of Probabilistic and Reliability Analysis, Elmpress International, Virginia, 1989, pp. 211-230.
27. Wu Y.-T., Millwater H. R. and Cruse T. A.: *Advanced probabilistic structural analysis method for implicit performance functions*. AIAA Journal, 28(9), 1990, pp. 1663-1669.
28. Liu P.-L. and Der Kiureghian A.: *Multivariate distribution models with prescribed marginals and covariances*. Probabilistic Engineering Mechanics, 1(2), 1986, pp. 105-112.
29. Rozmarynowski B.: *Reliability analysis of a stochastically non-linear structural system*. Proceedings of the International Conference on Safety and Reliability, ESREL'97, Vol. 2, Lisbon, Portugal, 1997, pp. 1509-1517.
30. Breitung K.: *Asymptotic approximations for multinormal integrals*. Journal of Engineering Mechanics, ASCE 110(3), 1984, pp. 357-366.

CONTACT WITH THE AUTHORS

Bogdan Rozmarynowski
Tomasz Mikulski

Gdańsk University of Technology
11/12 Narutowicza St.
80-233 Gdańsk
POLAND

Tab. 1. Random variables X_i and their statistical parameters X_{0i} , v_{Xi}

X_i variable ¹	Name	Distribution	$X_{0i} = E(X_i)$ [kN]	v_{Xi}
$Y_1, Y_2, Y_3, Y_4, Y_5, Y_6$	Wind load	Gumbel	280.6	1.25.
Y_7, Y_8, Y_9	Wave load	Log-normal	446.	2.60
Y_{10}, Y_{11}, Y_{12}	Wave load	Log-normal	290.6	2.60

Tab. 2. Mean values of stiffnesses of the suport springs

Type of the spring displacement	Stifness
Translational horizontal K_{ix}, K_{iy} [Mn/m]	783.3
Translational vertical K_{iz} [Mn/m]	1044.4
Rotational horizontal K_{ix}^R, K_{iy}^R [Mn/m]	37204.2
Rotational vertical K_{iz}^R [Mn/m]	44645.0

Tab. 3 Sensitivity coefficients of the eigenfrequency

Spring constraint	Node 10	Node 11	Node 12
K_x	0.00589	0.00589	0.00457
K_y	0.00003	0.00003	0.00000
K_z	0.05536	0.05536	0.00000
$K_{\varphi x}$	0.00015	0.00015	0.00000
$K_{\varphi y}$	0.10694	0.10694	0.09590
$K_{\varphi z}$	0.00000	0.00000	0.00000

Tab. 4. Natural frequencies of the model with elastic supports.

$\omega_1 = 2.162$ rad/s	$\omega_2 = 2.163$	$\omega_3 = 3.445$	$\omega_4 = 9.434$
--------------------------	--------------------	--------------------	--------------------

Tab. 5. Probabilities of failure modes, $d_p = 0.5m$, deterministic spring stiffnesses. FORM

Method	Correlation coefficient between wind and wave loads			
	0.0		0.20	
	P_{f1}	P_{f2}	P_{f1}	P_{f2}
HL-RF	$1.413 \cdot 10^{-3}$	$1.693 \cdot 10^{-5}$	$2.550 \cdot 10^{-3}$	$1.593 \cdot 10^{-5}$
MCDS ²	$1.585 \cdot 10^{-3}$	$1.823 \cdot 10^{-5}$	$2.879 \cdot 10^{-3}$	$1.691 \cdot 10^{-5}$

Tab. 6. Probabilities of failure modes, $d_p = 0.5m$, random spring stiffnesses. FORM/SORM

Method	Correlation coefficient between wind and wave loads			
	0.0		0.20	
	P_{f1}	P_{f2}	P_{f1}	P_{f2}
HL-RF	$2.343 \cdot 10^{-3}$	$1.593 \cdot 10^{-3}$	$4.055 \cdot 10^{-3}$	$1.530 \cdot 10^{-3}$
MCDS and IB ³	$2.485 \cdot 10^{-3}$	$1.572 \cdot 10^{-3}$	$4.379 \cdot 10^{-3}$	$1.394 \cdot 10^{-3}$

Footnotes:

- ¹ Subscript indices of the variables refer to the node Nr indicated in Fig. 2.
- ² MCDS denotes Monte Carlo Directional Simulation method.
- ³ The probabilities P_{f2} were obtained by applying improved Breitung (IB) formula [30].

CONCEPT OF DEVICE TO INSPECT INTERNAL TECHNICAL CONDITION OF MARINE PIPELINE

Danuta Warnke

Gdańsk University of Technology, Poland

ABSTRACT

The article presents a concept of the device to inspect technical condition of the interior of a marine pipeline. The design assumption was that the vehicle would be built for a specific existing pipeline, which is the Nord Stream gas pipeline. Based on the analysis of operating parameters and dimensions of the pipeline, the economic diameter and the medium flow velocity were calculated. The shape of the structure was proposed, and the measuring instruments and materials for manufacturing the vehicle were selected. The problems of energy supply during vehicle operation, and its installation inside the pipeline were solved.

Keywords: Nord Stream, marine pipeline, PIG-s inspection

INTRODUCTION

Pipeline diagnostics has never been an easy task, especially when the diagnosed object is situated at the bottom of the Baltic Sea. Due to different pipe diameters and types of transported media, each pipeline should have its individual inspection vehicle. The goal of the present work was working out a concept of the device to inspect technical condition of the Nord Stream gas pipeline.

The pipelines can be divided into three categories:

- a) Raw material pipelines – for transporting crude oil or gas;
- b) Product pipelines – for transporting finished products to storage and distribution points;
- c) Technological pipelines – such as cooling installations in nuclear refineries, for instance.

The Nord Stream pipeline belongs to the first category. Modern pipelines offer the possibility of checking their technical condition from inside, without disconnecting them from service (so-called In Line Inspection). The inspection devices, co-called “smart PIGs”, find places on pipe walls which need careful monitoring or repair. Smart

pistons are intended to perform two basic functions, which are inspection of pipeline interior and removal of deposits and dirt [1]. The pipeline can be cleaned mechanically or chemically. Here, three types of drives for cleaning devices can be named:

- a) mechanical drive (for instance a rope tied to pull the access eye along the pipe),
- b) hydraulic drive (medium is used as the drive for smart pistons),
- c) pneumatic drive (with compressed air as the driving medium).

The designed device will have hydraulic drive.

In general, external offshore diagnostics can be done by divers, but at larger depths unmanned devices are used which are remotely controlled from the ship. Internal inspection of the pipeline is usually done using probes and smart pistons, also referred to as PIGs [8].

A list of detected inner damages of the pipeline includes:

- a) corrosion,
- b) material losses,
- c) shape changes,
- d) cracks.

A similar list of the detected external pipeline damages includes:

- a) corrosion,
- b) mechanical damages caused by marine vehicles or animals,
- c) human error – material defects, badly prepared foundation.

There are several types of smart pistons used for inspecting inner walls. Their division can base on the used measuring technology:

- a) Mechanical devices – which inspect changes of inner geometry and/or mechanical damages;
- b) Magnetic devices – making use of magnetic field technology to assess corrosion and cracks;
- c) Ultrasound devices – used for measuring pipe wall thickness;
- d) Electromagnetic devices – making use of so-called Foucault currents [19].

The designed device belongs to the first group: mechanical inspection devices.

STRUCTURE OF TYPICAL MECHANICAL PIG

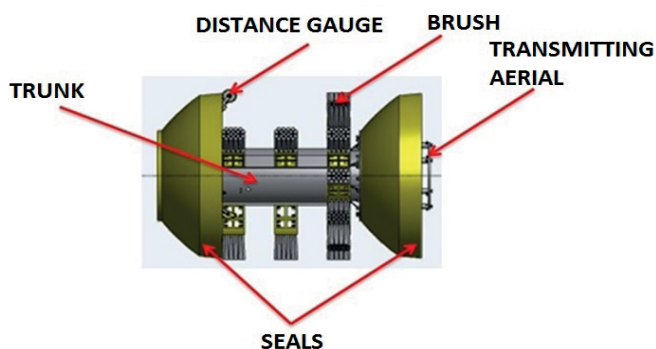


Fig. 1 Structure of typical PIG [18]

The medium flowing in the pipeline drives the device, due to the presence of tightly fitting elements – collars. A large number of cleaning brushes are usually used in oil pipelines, in which more impurities are collected than in gas pipelines [4]. Distance meters are used for determining the current position of the device. The used transmitting antenna makes it possible to localise the PIG in an emergency situation. Searching for the lost device is rather troublesome, as the signal transmitted by the antenna is relatively low. That is why this method works well in ground pipelines. All electronics of the device is placed inside the tight casing, which should also have space for a relatively large battery supplying the deck computer used for recording signals coming from the measuring sensors. The length of the diagnostic devices can reach as much as 4 m. The larger the number of measuring segments, the more precise image of inner pipeline walls is recorded. A longer device is more likely to be wedged inside the pipe, therefore the pipeline is to be cleaned up before inserting the smart piston into it. This can be done with the

aid of cleaning PIGs, having the form of a sphere, or a double piston [2]. Their task is to remove methane hydrates created as a result of connection of methane and water molecules. This connection of molecules is facilitated by low temperature and high-pressure which occur in each marine pipeline. The creation of hydrated decreases the transporting cross-section. Another method to eliminate methane hydrates is removal of water from the transported medium, or adding methanol or ethylene glycol to the medium. The amounts of hydrate deposits are to be monitored and removed at least once a year. Attention should also be paid to the starting and finishing stations used for inserting the vehicle in the pipeline and removing it. A standard scheme of inserting the device in the pipeline is shown in Fig. 2 and described below:

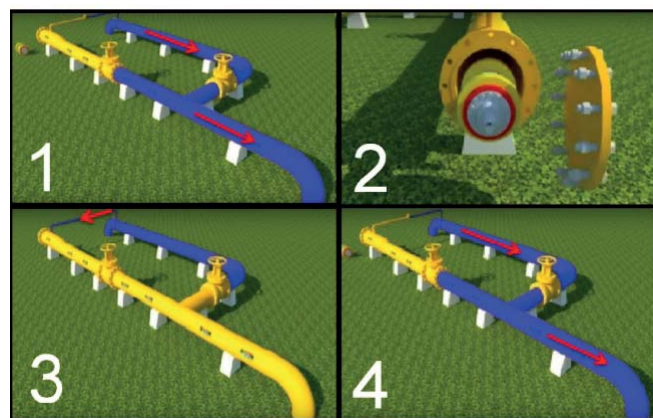


Fig. 2 Stages of placing the device Dacon [16]

Phase one: Standard pipeline operation. The medium flows in the direction indicated by the red arrow.

Phase two: Opening the hatch and inserting the diagnostic device.

Phase three: Closing the right large valve. The gas flow direction changes, which is indicated by the red arrow in Frame 3. The inflowing medium drives the inserted diagnostic device. After opening the left large valve, PIG leaves the driving station and moves with the medium.

Phase four: Opening the right valve to return to the initial flow [17].

PARAMETERS OF THE NORD STREAM GAS PIPELINE

Marine pipelines are extremely difficult to inspect. The Nord Stream gas pipeline has been laid at the bottom of the Baltic Sea and its task is to transport natural gas from Russia to Europe. This extremely large structure consists of two identical legs. The length of a single leg is 1224 km, the inner diameter is 1.153 m, and the thickness of walls varies from 27mm to 41mm. When designing the pipeline, the pressure drop of the transported medium was taken into account which resulted in different wall thicknesses. The gas flow is generated by a set of compressors situated at the pipeline inlet.

Laying the entire two-leg pipeline from Vyborg to Greifswald required the use of 202 000 pipe segments of 24 000 kg in weight each.



Fig. 3 The Nord Stream route [5]

Natural gas is a mixture of light saturated hydrocarbons, mainly methane. Since the molecular formula of the medium (natural gas) transported via the Nord Stream pipeline is a protected secret, the design calculations were to be preceded by molecular weight assessment of the flowing gas. The informational catalogue of DNV says that this is a dry gas with low sulphur content (95% methane content, the minimum). Table 1 collates the molecular weight assessment according to PGNiG (Polish Petroleum and Gas Mining) for high-methane natural gas [14,15].

ECONOMIC DIAMETER

The reliable input data used in economic diameter and gas flow velocity calculations corresponded to the calculation model described in [13].

Table 1. Assessing molecular weight of the deposit, acc. to [2]

Gas mixture component	Molecular weight of gas component M_{cg}	Relative density of gas component G_n [-]	Volumetric fraction of gas component in unit volume of mixture (acc. to PGNiG) x_{vg} [-]	Molecular weight fraction of gas component in mixture (M_{cg}) [kg/mol]	Relative density fraction of gas component in mixture (G_n) _i [-]
Methane	16,14	0,56	0,978	15,785	0,545
Ethane	30,07	1,04	0,010	1,323	0,046
Propane	44,10	1,52			
Butane	58,12	2,01			
Nitrogen	28,01	0,97	0,010	0,280	0,010
Carbon dioxide	44,01	1,52	0,002	0,088	0,003
Total			1,000	$M_{cg}^{(m)} = 17,476$	$G_n^{(m)} = 0,603$

$$G_n = \frac{M_{cg}}{M_{cp}} \frac{M_{cg}}{M_{cp}^{(m)}} \frac{M_{cg}}{M_{cg}^{(m)}} \frac{G_n}{G_n} \quad \text{where:} \quad \begin{array}{l} M_{cg} \text{ molecular weight of gas [kg/kmol],} \\ M_{cp}^{(m)} \text{ molecular weight of air 28,964 [kg/kmol],} \\ M_{cg}^{(m)} \text{ molecular weight of mixture of gases [kg/kmol],} \\ G_n \text{ relative density fraction in the mixture [-].} \end{array} \quad (1)$$

The economically justified inner diameter of the pipeline was calculated using formula (2) (with the temperature expressed in Kelvin degrees):

$$D_{ek}^{(g)} = 0,397 \cdot 10^{-2} \cdot M_n^{0,448} \cdot G_n^{0,132} \cdot (\mu_d^{(g)})^{0,025} \left(\frac{T \cdot Z}{P}\right)^{0,316} \quad (2)$$

where:

$D_{ek}^{(g)}$ economically justified inner diameter of the pipeline [m]

M_n volumetric gas flow rate (flow capacity of the pipeline) in normal conditions $T_n = 273,15$ K ($t_n = 0$ °C), $P_n = p_{at} = 101,325$ kPa [m^3/h],

G_n relative gas density in normal conditions ($T_n = 273,15$ K ($t_n = 0$ °C), $p_n = 101,325$ kPa) ($G = 1$ for air)[-]

$\mu_d^{(g)}$ dynamic viscosity coefficient of gas [MPa · s],

T absolute gas temperature [K]

Z gas compressibility ratio [-],

P absolute gas pressure [kPa].

Based on the Nord Stream report by DNV, the outlet gas temperature was assumed constant and equal to -1 °C. Changing to Kelvin degrees gives:

$$T = 273,15 + (-1) = 272,15 \text{ K} \quad (3)$$

The assumed pressure value needed in formula (1) is the arithmetic mean of the pipeline inlet and outlet pressures:

$$P = \frac{p_1 + p_2}{2} = \frac{22 + 17,75}{2} = 19,87 \text{ MPa} = 19870 \text{ kPa} \quad (4)$$

The DNV report on Nord Stream construction says that the flow capacity of one pipeline leg in normal conditions is:

$$\begin{aligned} M_n &= 27,5 \left[\text{mld} \frac{\text{m}_n^3}{\text{year}} \right] \\ &= 3,14 \left[\text{mln} \frac{\text{m}_n^3}{\text{h}} \right] \\ &= 3139269,4 \left[\frac{\text{m}_n^3}{\text{h}} \right] \end{aligned} \quad (5)$$

The relative density of gas in normal conditions is:

$$\begin{aligned} G_n &= \frac{M_{cg}}{M_{cp}} = \frac{17,476 \text{ [kg/kmol]}}{28,964 \text{ [kg/kmol]}} \\ &= 0,603 [-] \end{aligned}$$

The dynamic viscosity coefficient values are:

a) Beginning of the route: Vyborg. Maximal operating temperature:

$$\begin{aligned} T_{\max} &= 40^\circ\text{C} = 313,15 \text{ K} \\ \mu_d^{(gt)} &= 0,0119 \text{ [mPa} \cdot \text{s]} \\ &\text{(the value read from Diagram 1)} \end{aligned}$$

b) End of route: Greifswald. Minimal operating temperature:

$$\begin{aligned} T_{\min} &= -1^\circ\text{C} = 272,15 \text{ K} \\ \mu_d^{(gt)} &= 0,0107 \text{ [mPa} \cdot \text{s]} \\ &\text{(the value read from Diagram 1)} \end{aligned}$$

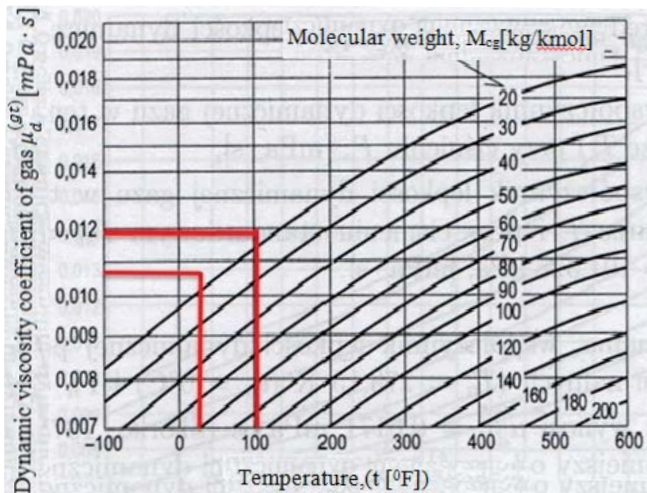


Diagram 1. Dynamic viscosity coefficient of gas vs. temperature and molecular weight of gas at atmospheric pressure [13].

To read the data from Diagram 1, the temperature was to be recalculated to Fahrenheit degrees:

a) Inlet temperature:

$$(40^\circ\text{C} \cdot 1,8) + 32 = 104^\circ\text{F}$$

b) Outlet temperature:

$$(-1^\circ\text{C} \cdot 1,8) + 32 = 30,2^\circ\text{F}$$

The pseudocritical parameters of the gas mixture were calculated as:

$$T_{kr}^{(p)} = \sum_{i=1}^{n_g} (T_{kr})_i \cdot (x_{vg})_i \quad (6)$$

$$P_{kr}^{(p)} = \sum_{i=1}^{n_g} (P_{kr})_i \cdot (x_{vg})_i \quad (7)$$

$T_{kr}^{(p)}$ pseudocritical temperature of natural gas as the mixture of gas hydrocarbon substances [K],

$P_{kr}^{(p)}$ absolute pseudocritical pressure of natural gas as the mixture of gas hydrocarbon substances [MPa]

$(T_{kr})_i$ absolute critical temperature of i-th natural gas component [K]

$(P_{kr})_i$ absolute critical pressure of i-th natural gas component, [MPa],

$(x_{vg})_i$ volumetric fraction of i-th gas component in the mixture [-].

Critical parameters of particular natural gas components are given in Table 2.

Table 2. Selected physical parameters of hydrocarbons and other compounds [13]

Name	Critical temperature	Critical pressure
Methane	191,11	4,64
Ethane	305,0	4,88
Propane	370,0	4,25
Butane	425,56	3,80
Nitrogen	126,11	3,39
Carbon dioxide	304,44	7,40

$$\begin{aligned} T_{kr}^{(p)} &= 0,978 \cdot 191,11 + 0,01 \cdot \frac{305 + 370 + 425,56}{3} \\ &\quad + 0,01 \cdot 126,11 + 0,002 \cdot 304,44 \\ &= 192,44 \text{ [K]} \end{aligned}$$

$$\begin{aligned} P_{kr}^{(p)} &= 0,978 \cdot 4,64 + 0,01 \cdot \frac{4,88 + 4,25 + 3,80}{3} + \\ &\quad 0,01 \cdot 3,39 + 0,002 \cdot 7,40 = 4,63 \text{ [MPa]} \end{aligned}$$

The calculated values of the reduced temperature and pressure are:

$$T_{zr}^{(p1)} = \frac{T_1}{T_{kr}^{(p)}} = \frac{313,15}{192,44} = 1,63 \quad (2)$$

$$P_{zr}^{(p1)} = \frac{P_1}{P_{kr}^{(p)}} = \frac{22}{4,63} = 4,75 \quad (2)$$

where:

- T_1 inlet temperature,
- P_1 inlet pressure,
- $T_{zr}^{(p1)}$ reduced pseudocritical temperature of natural gas at pipeline inlet [-]
- $P_{zr}^{(p1)}$ reduced pseudocritical pressure of natural gas at pipeline inlet [-]

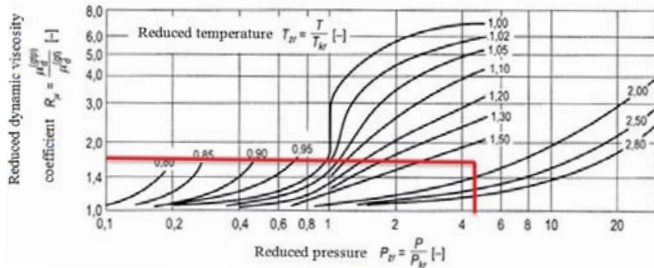


Diagram 2. Effect of the reduced pressure and reduced temperature on the dynamic viscosity coefficient of gas [13].

The read value of the dynamic viscosity coefficient of gas is:

$$R_\mu = \mu_d^{(gtp)} / \mu_d^{(gt)} = 1,6 \quad (8)$$

where:

- $\mu_d^{(gtp)}$ dynamic viscosity coefficient of gas at temperature T and pressure P [MPa · s]
- $\mu_d^{(gt)}$ dynamic viscosity coefficient of gas at temperature T and standard pressure $P_{st} = 101\,325$ [mPa · s]

The viscosity coefficient in flow conditions was assessed as:

$$\mu_d^{(g)} \equiv \mu_d^{(gtp)} = R_\mu \cdot \mu_d^{(gt)} = 1,6 \cdot \mu_d^{(gt)} = 1,6 \cdot 0,0119 = 0,01904 \text{ [mPa} \cdot \text{s]}$$

The compressibility ratio of the real gas was read from Diagram 3.

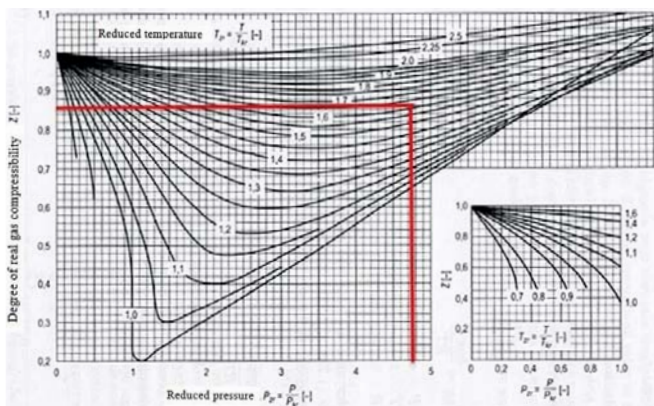


Diagram 3. Gas compressibility ratio vs. reduced pressure and temperature [13].

The read value: $Z = 0,855$

The economic diameter of the pipeline was calculated from the formula:

$$D_{ek}^{(g)} = 0,397 \cdot 10^{-2} \cdot M_n^{0,448} \cdot G_n^{0,132} \cdot (\mu_d^{(g)})^{0,025} \cdot \left(\frac{T \cdot Z}{P}\right)^{0,316}$$

$$D_{ek}^{(g)} = 0,397 \cdot 10^{-2} \cdot 3139269,4^{0,448} \cdot 0,603^{0,132} \cdot (0,01904)^{0,025} \cdot \left(\frac{272,15 \cdot 0,855}{19870}\right)^{0,316}$$

$$= 0,67 \text{ m} \approx 0,7 \text{ m}$$

Unlike liquid media, the transported natural gas is compressible, therefore of high importance is placing in the above formula real temperature and pressure values, as they are the only parameters reflecting real flow conditions in the pipeline, while the remaining parameters refer to normal conditions, i.e.: ($T_n = 273,15$ K ($t_n = 0^\circ$ C), $P_n = p_{at} = 101,325$ kPa). The volume of the transported gas depends on its temperature and pressure, therefore normal calculating conditions were introduced to standardise particular parameters and thus provide opportunities for comparing, for instance, volumetric flow rates or densities with other gas media. The inner diameter of the Nord Stream gas pipeline is 1,153 m, while the calculated economic diameter was only 0,67 m. That means that the real diameter is larger by 41,9% than the economic diameter. This discrepancy can result from calculating the economic diameter with the aid of the formula created based on the steel pipeline production costs recorded in the USA in 1975. For gas pipelines produced in those years the formula worked very well, with the difference between real and economic diameter not exceeding a few percent. The author of [13] quotes that the steel pipe production cost increased by 5% until 1998, while the cost of electrical energy, taken into account in the formula, increased by 10%. The Nord Stream pipeline is an undersea pipeline, which has been built since 2010. The production costs were extremely high, and the predicted operation time is equal to 50 years. In case of such investment projects, in the initial phase the economically justified diameter is calculated based on material costs, operating time, etc., and only in the next phase the operating diameter is calculated. These two diameter values can differ.

GAS FLOW VELOCITY IN NORD STREAM PIPELINE

The medium flow velocity in the Nord Stream gas pipeline was calculated from formula (9) [2]:

$$v_g = 0,131 \cdot 10^{-3} \cdot \left(\frac{M_n \cdot T \cdot Z}{P \cdot (D_w^{(g)})^2} \right) \quad (9)$$

where:

- v_g natural gas flow velocity [m/s],
- M_n volumetric gas flow rate [m³/h],
- T absolute gas temperature [K],
- Z gas compressibility ratio [-],
- P absolute gas pressure [kPa],
- $D_w^{(g)}$ inner diameter of pipeline [m].

$$v_g = 0,131 \cdot 10^{-3} \cdot \left(\frac{M_n \cdot T \cdot Z}{P \cdot (D_w^{(g)})^2} \right) =$$

$$0,131 \cdot 10^{-3} \cdot \left(\frac{3139269,4 \cdot 272,15 \cdot 0,855}{19,875 \cdot (1,153)^2} \right) = 3,62 \left[\frac{m}{s} \right]$$

The diagnostic PIG is assumed to move with the same velocity as that of the transported medium (here: natural gas).

ELEMENTS OF DESIGNED DEVICE

The diameter of the designed device is equal to the inner diameter of the Nord Stream pipeline. This condition is essential, as the measuring, cleaning and driving elements should be in tight contact with the pipeline wall to work properly. The length of the device mainly results from space requirements for the container with electronics and the battery for supplying measuring instruments during the inspection. The calculated capacity of the battery is 28,8 kWh, and its weight is 274,28 kg. The battery consists of 4 packages of 178 small batteries and 1 package of 67 small batteries. The energy stored in the battery is sufficient for 4 days of device operation.

The designed smart device consists of four indispensable sections.

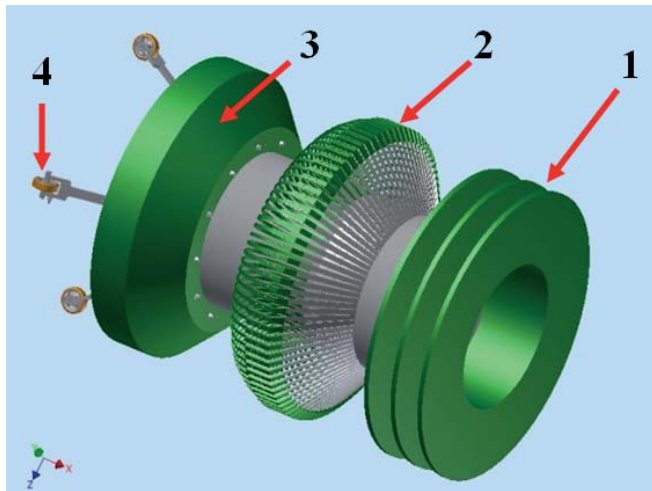


Fig. 4. Complete diagnostic device [10]

1 - cleaning seal, 2 - measuring element, 3 - driving seal, 4 - distance gauge.

Functions performed by the device include:

- pipeline cleaning from dirt,
- measuring the covered distance,
- detecting gas pipeline diameter changes.

Planned tasks:

- PIG is expected to perform internal inspection of the pipeline for which it was built. The inspection consists in detecting material losses, cracks, and/or tarnishes. Fast detection of defects will make it possible to avoid gas pipeline unsealing and the resultant ecological disaster,

- Overall diagnostics and precise location of places which need intervention,

- Location of hydrate concentration places.

The number of functions and tasks directly affects the number of segments used in the device. The first element is the cleaning seal. It is situated in the front part of the vehicle and its task is to collect tarnishes and dirt remaining after the previous cleaning. This element consists of three discs, which makes its structure more rigid and the cleaning process more precise. The discs have empty space in the centre, to limit the mass of the device. Moreover, this space plays the role of a container for collected dirt, thanks to which the wedges of the cleaning discs will not get clogged. The second element of the device is the section with the glued strain gauge bridges. It detects dents, lumpy tarnish and dirt on pipeline walls. The perimeter of this section contains 90 measuring loop-like elements mounted every 4 degrees around the perimeter of the device casing.

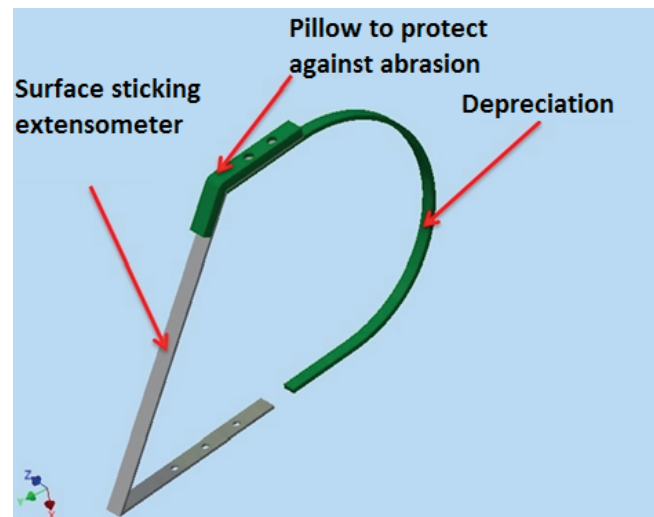


Fig. 5 Measuring element [10]

The error of perimeter imperfection detection was calculated in the following way:

Length along perimeter:

$$L = 2 \cdot \pi \cdot r$$

$$L = 2 \cdot \pi \cdot 576,5 = 3622,26 \text{ mm}$$

where:

r inner diameter of pipeline,

90 number of measuring elements,

20mm width of measuring element,

$$90 \cdot 20 = 1800 \text{ mm}$$

$$3622,26 - 1800 = 1822,26 \text{ mm}$$

$$\frac{1822,26}{90} = 20,24 \text{ mm}$$

The width of the gaps between the measuring elements is equal to 20,24 mm. This accuracy is sufficient for detecting

significant defects. A strain gauge bridge is glued to each measuring element. Proper selection and arrangement of these bridges enables to detect pipeline diameter changes, and further precise analysis of the detected pits, tarnishes and corrosion, and the current condition of welded joints. High sensitivity of strain gauge bridges provides opportunities for precise tracking of changes on pipeline walls [11]. The third part of the inspection device is the sealing element. It prevents the natural gas from seeping behind the element, thanks to which the entire mass of gas presses into the front wall of the inspection device and moves it downstream. The fourth section of the device consists of rolls, mounted every 90 degrees and fitting to the gas pipeline walls. The motion of the designed device makes the rolls rotate, and thus measure the distance covered by the PIG. Figure 6 shows the positions of the measuring rolls and inductive sensors.

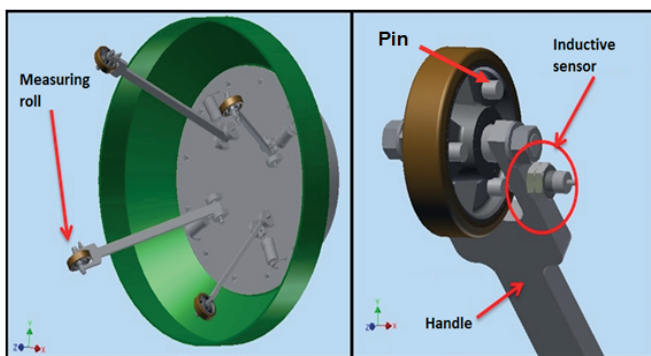


Fig. 6 The distance meter [10].

The inductive sensor is screwed into the fork (measuring roll handle), at a distance of 4 mm from the pin. This distance is sufficient for safe counting of the number of sensor's meetings with the pin. Each disc with the rolls has 3 metal pins, fastened every 120 degrees. Counting the average number of revolutions recorded by 4 rolls makes it possible to calculate precisely the current position of the device. The device project assumes installing the sensor IS-12-H1-S1 made by Simex [12]. The measuring rolls work in difficult conditions and they should be reliable and resistant to damages. When selecting this element, it is advisable to take into account rolls used in forklift trucks. They reveal good adhesion and low abrasibility, and are offered in many sizes on the market. The rolls selected for the device project were made by Eles-Ganter [20]. Along with the measuring elements, the potentiometer is used for detecting pipeline diameter changes (dents, welds, thick tarnish). However, in this case it also plays another function. Each diameter change may cause vibrations or jumps of the rolls measuring the distance covered by the device, which may lead to the accumulation of errors in device position estimation. In this situation the potentiometer helps to identify and properly correct the accumulated position errors [6,7]. The inspection device is also equipped with a spring shock absorber, the task of which is to keep four forks in such a position that all measuring rolls are pressed to pipeline walls. Proper tension of the spring keeps the

forks in correct positions, and thus makes the rolls be in tight contact with the walls. The designed shock absorber consists of the spring, a piston and a mandrel screwed into it. Its casing is assumed to be airtight, to protect the shock absorber interior from fouling. The number of movements of the PIG device is limited, as the pipeline in which it moves constitutes a sort of track for it. The device is solely driven by the medium flowing in the pipeline. The only independent movement which PIG can make is changing the rotation angle around its own axis, which is facilitated by axial symmetry of the device along its length. Theoretically, the rotational position of the inspection probe can be measured using oscillatory or liquid inclinometers. They work well on slow ships, where the reading of the measuring element is obtained directly. Nevertheless, for higher speeds and accuracies, other types of inclinometers are recommended. A place for this measuring instrument is provided in the airtight container for electronics. The project assumes the use of one-dimensional inclinometer IS1SP360-BL produced by WObit. Its measuring range is up to 360 degrees, and its accuracy is very high. The sensor is factory calibrated. According to the producer, it works very well in difficult conditions. The natural gas pressure in the Nord Stream pipeline is sufficiently high to introduce the PIG device for inspection purposes. However, to move properly, the device should have a relevant "driving surface", which means that the gas flowing in the pipeline should press the inspection device evenly and thus generate a relevant driving force. The speed of motion of the inspection device is assumed to be approximately equal to that of the flowing medium. The role of driving surface is played in the device by the driving seal. It is in permanent tight contact with pipeline walls, thus blocking the pipeline cross section and generating the maximum driving force. A set of three discs is also mounted in the front part of the device body. They have two tasks to perform, which are driving and cleaning. Since the gas pipeline is not as heavily fouled as the oil pipeline, a decision was made to resign from installing cleaning brushes on the device body.

SUMMARY

The designed inspection device consists of three decouplable segments, which means that it can be disassembled into three main parts: stern part with the driving seal and instrumentation, middle part with the measuring elements, and front part with a set of polyurethane discs. The three-part structure was designed with an intention of easy replacement of individual elements. The system of measuring elements distributed around the device perimeter has a wide inspection range. Substantial damages should be detected. Indeed, the measuring elements will be subject to wear, which first of all means abrasion of measuring element shields. When their thickness decreases to the height of the countersunk head of the fastening rivet, the polyurethane shield is to be replaced. The external potentiometer is also exposed to quick damage. Acting within a small angular range, it is exposed

to so-called “erasing wear”. That is why of high importance is visual examination of the device after each inspection operation. As for the distance meter, its fastening on the steel fork can be replaced by laminate elements, which reveal high strength and material elasticity. The designed inspection device had no assumed weight limits, therefore the applied mechanical structure of the distance meter support has no contraindications concerning its use. What is more, it is relatively simple and cheap to manufacture. When selecting the inclinometer, of high importance was to know its structure and principle of operation. The pipeline will be a sort of screen for the inclinometer, therefore its operation should base on the acceleration due to gravity. The inclinometer selected for the project is reliable and relatively small, and has a wide operating range.

Based on simple solutions, a device was designed which performs cleaning and inspection tasks in functional and reliable way. Its servicing should not pose a problem, as all elements are easily replaceable. Moreover, by using smaller or larger sealing discs and different sizes of measuring element shock absorbers, the designed PIG device can be easily adapted for operation in pipelines with other inner diameters. Here, the only limitation is the diameter of the container for electronics and battery.

BIBLIOGRAPHY:

1. <http://osfm.fire.ca.gov/pipeline/pdf/conferece/inlineinspection.pdf>,
2. <http://www.peg-germany.de/en/products/pipeline-products/pipeline-spheres.html>,
3. Rowiński L.: Deep-water vehicles: structure and equipment (in Polish), WiB Gdansk 2008,
4. <http://www.inlineservices.com/pipeline-pig-brushes>,
5. <https://deutsch.rt.com/wirtschaft/49870-ostsee-pipeline-nord-stream-2-trotz-sanktionen-gebaut-russland-deutschland/>
6. <http://rab.ict.pwr.wroc.pl/~arent/rr/mpr/czujniki2.html>,
7. <http://www.tme.eu/pl/details/cw-18-10k-p6/potencjometry-jednoobrotowe-cermetowe/telpod/>,
8. Hupka J.: Pipeline operation related technical problems (in Polish), Department of Chemical Technology, Faculty of Chemistry, Gdansk University of Technology.
9. Gerwatowski D.: Linear flow resistance coefficient vs. system flow capacity, with the Yamal pipeline as an example of transit pipeline system (in Polish), EuRoPol GAZ SA, Warsaw.
10. Figures from Inventor programme.
11. <http://automatykab2b.pl/technika/3095-czujniki-tensometryczne-czyli-co-o-pomiarach-siy-powinien-wiedzie-automatyk#.VmstudLhC00>,
12. <http://www.simex.pl/produkt/3313>,
13. Magda W.: Marine pipelines (in Polish), Wydawnictwo techniczne, Warsaw 2004.
14. Nord Stream - Espoo Report, <https://www.nord-stream.com>
15. <http://www.nord-stream.com/>
16. https://www.youtube.com/watch?v=55wa_CvA7UA,
17. <http://www.bc.pollub.pl/Content/254/korozja.pdf>
18. <http://www.tdwilliamson.com/SolutionsEngine?condition=99&industry=9>,
19. <http://www.rosen-group.com/global/solutions/pipeline-systems.html>,
20. <http://www.elesa-ganter.com/pl/28/sp/9563/4/120/kolaz-nalewanym-wie%C5%84cem-poliuretanowym/re.f5/eg/>,

CONTACT WITH AUTHOR

Danuta Warnke

e-mail: danwarnk@pg.gda.pl

Gdansk University of Technology
ul. Narutowicza 11/12
80-233 Gdansk

INVESTIGATION METHOD AND MATHEMATICAL MODEL OF PRESSURE LOSSES IN HYDRAULIC ROTARY MOTOR

Agnieszka Maczyszyn

Gdańsk University of Technology, Poland

ABSTRACT

This paper presents a way of determining the coefficient k_8 of the pressure losses Δp_{Mp} (flow drag) in internal ducts of SWSB-63 hydraulic motor. The coefficient is determined at a flow rate equal to the theoretical capacity Q_{p1} of the pump feeding the motor, the losses are related to the nominal pressure p_n in the hydraulic system. The investigations followed a model of energy performance of hydraulic rotary motor, proposed by Z. Paszota.

Keywords: hydrostatic drive, power values of energy losses, hydraulic rotary motor, pressure losses, pressure efficiency

INTRODUCTION

Basic units of hydraulic systems are : drive and control systems. Drive systems are composed of pump units serving as converters of mechanical energy into liquid flow energy, units of hydraulic motors serving simultaneously as consumers of liquid flow energy and converters of the energy into mechanical one, as well as control units, e.g. those controlling motion speed or direction. The three groups are mutually connected by conduits and supplemented by auxiliary units.

The hydraulic rotary motors are used in hydrostatic drives which – in case of marine applications – can transfer large amounts of power and simultaneously have compact structure resulting in a small area required for their location on deck. This is one of many advantages of hydrostatic drive.

The pressure losses Δp_{Mp} in internal ducts of hydraulic motor have a great influence on total efficiency of displacement machine, which in turn impacts working parameters of hydrostatic system.

Pressure losses constitute drag of working medium flow through internal ducts and distributor of displacement machine, hydraulic motor in this case. Geometry of the ducts

is characteristic for a given design solution. The losses Δp_{Mp} in the motor result to a large degree from local pressure losses which arise from changes in flowing flux direction and velocity. The pressure losses Δp_{Mp} depend mainly on the flow rate Q_M of oil and its viscosity ν [7].

The pressure losses Δp_{Mp} can be expressed as follows :

$$\Delta p_{Mp} = \Delta p_{Mp1} + \Delta p_{Mp2} = f(Q_M, \nu) \quad (1)$$

where:

Δp_{Mp1} - pressure losses in inlet duct (occurring between liquid inflow point to hydraulic motor and working chambers);

Δp_{Mp2} - pressure losses in outlet duct (occurring between working chambers and liquid outflow point from hydraulic motor).

In general, the pressure losses power ΔP_{Mp} is the product of the pressure loss Δp_{Mp} and liquid flow rate Q_M , namely:

$$\Delta P_{Mp} = \Delta p_{Mp} Q_M \quad (2)$$

The power ΔP_{Mp} of pressure losses in hydraulic motor is sum of the power ΔP_{Mp1} of pressure losses in inlet duct and the power ΔP_{Mp2} of pressure losses in outlet duct of the motor :

$$\Delta P_{Mp} = \Delta P_{Mp1} + \Delta P_{Mp2} \quad (3)$$

As a result, the formula describing the power ΔP_{Mp} of pressure losses in hydraulic motor takes the form as follows :

$$\Delta P_{Mp} = \Delta P_{Mp1} + \Delta P_{Mp2} = \Delta p_{Mp1} Q_M + \Delta p_{Mp2} Q_{M2} \quad (4)$$

In rotary motor in which the liquid flow rate Q_{M2} in outlet duct is practically equal to the liquid flow rate Q_M in inlet duct (i.e. the motor absorbing capacity Q_M) $\rightarrow Q_{M2} = Q_{M1} = Q_M$, the pressure losses power ΔP_{Mp} in the motor takes the form:

$$\Delta P_{Mp} = (\Delta p_{Mp1} + \Delta p_{Mp2}) Q_M = \Delta p_{Mp} Q_M \quad (5)$$

KNOWN METHODS FOR DESCRIPTION OF PRESSURE LOSSES

The pressure losses Δp_{Mp} in ducts presented in Fig. 3 make it possible to determine the value of the exponent a_{vp} equal to $\sim 0,25$ for the motor absorbing capacity Q_{Mt} . The obtained value allows to state that we deal with a not fully developed flow. It can be confirmed by the fact that, according to the Darcy-Weisbach formula for fully developed turbulent flow, the expression for pressure losses is of the following form:

$$\Delta p = \lambda \frac{1}{d} \frac{\rho v^2}{2}, \quad (6)$$

where:

- λ - stands for linear drag coefficient which varies depending on value of Reynolds number (Re),
- l - the length of the pipe [m];
- d - diameter of the pipe [m];
- ρ - fluid density [kgm⁻³],
- v - linear speed of fluid [ms⁻¹].

Transforming the relation (10) into a function depending on the flow rate Q , one obtains the formula:

$$\Delta p = \lambda \frac{8}{\pi^2} \rho \frac{1}{d^5} Q^2 \quad (7)$$

In the dependence of the linear drag coefficient λ on Re, presented in [9], four zones are distinguished. In the first zone for $Re < Re_{kr}$ laminar flow occurs (where λ is described by the relations: $\lambda = \frac{64}{Re}$ or $\lambda = \frac{75}{Re}$). In the second (transition) zone liquid flow is unstable, i.e. either laminar or turbulent flow may happen. Transition from laminar flow to turbulent not fully developed one occurs suddenly. The third zone is characteristic of a not fully developed turbulent flow. In this zone the linear drag coefficient λ for a hydraulically smooth

conduit was described by the following empirical formula according to Blasius:

$$\lambda = \frac{0,3164}{Re^{0,25}} \quad (8)$$

Substituting the relation (8) into the Darcy-Weisbach formula (6) and transforming the so obtained relation into a function of flow rate, one achieves the following :

$$\Delta p = 0,2414 \frac{l\rho}{d^{4,75}} v^{0,25} Q^{1,75} \quad (9)$$

According to the relation (9), in case of a not fully developed flow the pressure losses does not depend, a. o., on the viscosity ν and the liquid flow rate Q . The power exponents which appear in this formula, take, for various flow conditions (e.g. conduit roughness), values different from those given in the formula (9).

The fourth zone is characteristic of a fully developed turbulent flow. In this zone the linear drag coefficient λ depends only on the relative roughness defined by the ratio ϵ/d of the absolute roughness ϵ and the conduit internal diameter d . Flows at so large values of Reynolds number rather do not happen in hydrostatic drives. In case of fully developed turbulent flow, λ has a constant value independent on Re.

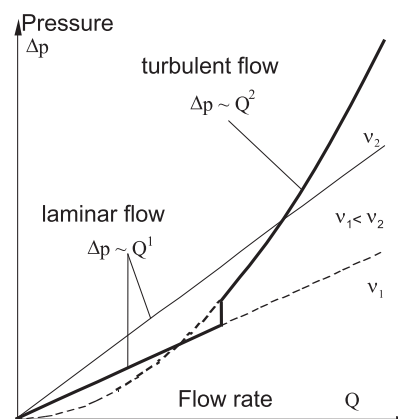


Fig. 1 Relation between the pressure loss Δp and the flow rate Q [3]

In Fig. 1 the above considered relations which describe pressure losses in function of flow rate are depicted as follows: for laminar flow - by a linear function dependent also on oil viscosity, and for fully developed turbulent flow - by a square function.

In the literature sources [10 ÷ 14] another way of determining the pressure losses ΔP_{Mp} in displacement machine internal ducts can be found, as follows :

$$\Delta p_{Mp} = C_t \cdot \rho \cdot Q^2 + C_l \cdot \nu \cdot \rho \cdot Q \quad (10)$$

The formula makes it possible to determine the pressure losses Δp_{Mp} when working liquid parameters such as its density ρ and viscosity ν as well as flow rate Q are known. Values of the constants C_t and C_l can be achieved from the trend line of the characteristics $\Delta p_{Mp} = f(Q)$ representing the

pressure losses Δp_{Mp} in displacement machine internal ducts in function of its absorbing capacity Q .

In the literature sources [13, 14] the pressure losses Δp_{Mp} in hydraulic motor are described as follows :

$$\Delta p_{Mp} = C_{ich} \cdot \rho \cdot \omega^2 \cdot \sqrt[3]{\left(\frac{V_t}{2 \cdot \pi}\right)^2} \quad (11)$$

where :

- C_{ich} – coefficient of proportionality;
- ω – angular speed of displacement machine shaft;
- V_t – theoretical working space.

To increase precision of description of dependence of hydraulic motor energy efficiency on the motor absorbing capacity Q_M in a wide range of changes in hydraulic oil viscosity ν , it is proposed to apply the simulation description of relation of the pressure losses Δp_{Mp} in motor ducts, given by Z. Paszota in [7]. In the case of the considered SWSB-63 motor it turned out that in its ducts a not fully developed turbulent flow occurs.

The model of the pressure losses Δp_{Mp} , proposed by Z. Paszota [7], can be presented as follows:

$$\Delta p_{Mp} = k_8 p_n \left(\frac{Q_M}{Q_{Pt}}\right)^{a_{qp}} \left(\frac{\nu}{\nu_n}\right)^{a_{vp}}, \quad (12)$$

Where the coefficient:

$$k_8 = \frac{\Delta p_{Mp}|_{Q_M=Q_{Pt}, \nu_n}}{p_n} \quad (13)$$

determines the pressure losses Δp_{Mp} in hydraulic motor internal ducts and distributor, which would appear at the motor absorbing capacity Q_M equal to the theoretical capacity Q_{Pt} of the pump feeding the motor, related to the nominal pressure p_n of the system in which the hydraulic motor is used.

Application of the dimensionless ratios Q_M/Q_{Pt} and ν/ν_n in the mathematical model (12) makes it possible to determine the exponent a_{qp} of influence of the liquid flow rate Q_M in ducts on the pressure losses Δp_{Mp} , as well as the exponent a_{vp} of influence of the working liquid viscosity ν on the pressure losses Δp_{Mp} , hence it allows to precisely describe the relation Δp_{Mp} in function of Q_M and ν .

The equation (13) defining the coefficient k_8 as well as the mathematical model (12) combine description of the pressure losses Δp_{Mp} in motor ducts with magnitude of the theoretical capacity Q_{Pt} of the pump and the nominal pressure p_n of the hydrostatic system [11].

WAY OF MEASURING THE PRESSURE LOSSES Δp_{Mp} IN SWSB-63 MOTOR

Fig. 2 presents a way of measuring the pressure losses Δp_{Mp} in ducts of SWSB-63 motor. Working elements of the motor were disassembled from it to form free flow of working medium. This way the flow conditions close to real ones were reached, i.e. those when distributor's elements rotate with the speed which

corresponds to the motor absorbing capacity Q_M . The pressure losses Δp_{Mp} in ducts of SWSB-63 motor were calculated as the differential pressure :

$$\Delta p_{Mp} = \Delta p_{de} - \Delta p_{AC} \quad (14)$$

where:

- Δp_{AC} – pressure loss measured in the section A – C of liquid flow in the space limited by the drum, which was negligible;
- Δp_{de} – pressure loss measured in points d and e (based on fig. 1)[6].

Tab. 1 shows principal working parameters of SWSB-63 motor.

Tab. 1 The principal working parameters of SWSB-63 motor

	q_{Mt} [m ³]	n_{Mn} [s ⁻¹]	ν_n [mm ² s ⁻¹]	p_n [MPa]	M_{Mt} [Nm]	P_{Mc} [kW]
SWSB 63 motor	639·10 ⁻⁶	2,67	26	6,2	617,8	10,6

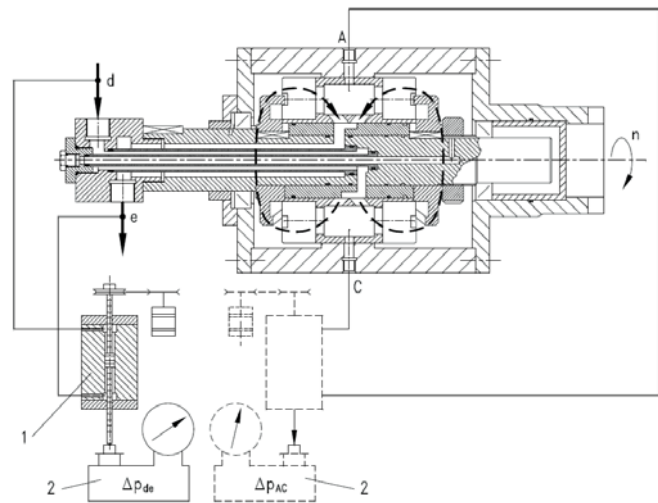


Fig. 2 The SWSB motor adjusted to measuring the pressure losses in internal ducts [6]: 1 – piston pressure gauge serving to measure differential pressure; 2 – tangent balance

PRESSURE LOSSES IN SWSB-63 HYDRAULIC MOTOR

In order to determine characteristics which make it possible to obtain pressure losses in the tested motor it was necessary to determine in advance parameters of its nominal running. Based on the results of the SWSB-63 motor tests contained in [1], the motor theoretical absorbing capacity Q_{Mt} equal to

the pump theoretical capacity Q_{pt} ($Q_{M1} = Q_{pt} = 1,71 [dm^3 \cdot s^{-1}]$) was assumed. The SWSB-63 motor was tested under changeable oil kinematic viscosity ν (in the range from $13 \text{ mm}^2 \cdot \text{s}^{-1}$ to $150 \text{ mm}^2 \cdot \text{s}^{-1}$), hence the reference viscosity ν_n was taken equal to $26 \text{ mm}^2 \cdot \text{s}^{-1}$. The remaining working parameters are given in Tab. 1.

Fig. 3 shows the characteristics of the pressure losses Δp_{Mp} in ducts of SWSB-63 motor in function of the motor absorbing capacity Q_M ($\Delta p_{Mp} = f(Q_M)$), at selected constant values of the hydraulic oil kinematic viscosity ν .

And, Fig. 4 presents the characteristics of the pressure losses Δp_{Mp} in ducts of SWSB-63 motor in function of the coefficient of oil kinematic viscosity ν/ν_n ($\Delta p_{Mp} = f(\nu/\nu_n)$), at constant values of the motor absorbing capacity Q_M . The curves were obtained on the basis of the characteristics (Fig. 3) expressing the pressure losses Δp_{Mp} in function of the motor absorbing capacity Q_M ($\Delta p_{Mp} = f(Q_M)$).

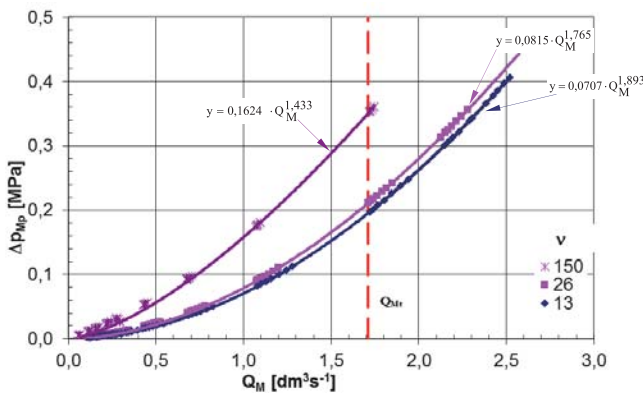


Fig. 3 The pressure losses Δp_{Mp} in motor ducts in function of the SWSB-63 motor absorbing capacity Q_M at selected constant values of the hydraulic oil viscosity ν [4, 5]

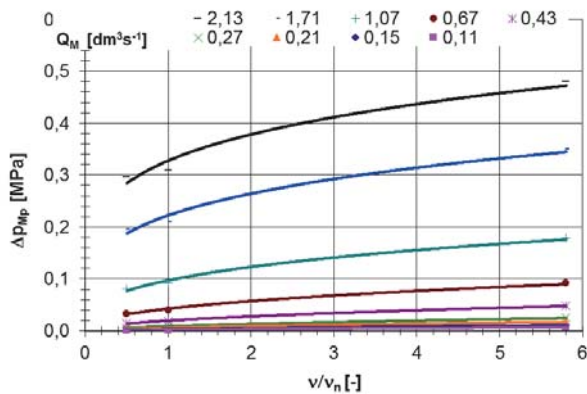


Fig. 4 The pressure losses Δp_{Mp} in motor ducts in function of the oil viscosity coefficient ν/ν_n , at selected values of the motor absorbing capacity Q_M [4]

DETERMINATION OF THE COEFFICIENT k_8 OF THE PRESSURE LOSSES Δp_{Mp} IN SWSB-63 MOTOR AS WELL AS THE EXPONENTS a_{QP} AND a_{NP}

The model of pressure losses Δp_{Mp} in hydraulic motor (proposed by Z. Paszota in [7]) takes into account: possible application of it to a model of the motor total efficiency η_M as well as to a model of the efficiency η of hydrostatic drive in which the motor is used, and also possible modification of the model on the basis of laboratory tests of pressure losses in ducts of displacement machine (pump, hydraulic motor) with the aim of increasing accuracy of description of losses in motor of a given construction as well as in the range of changes in oil viscosity occurring in drive system under operation. Knowledge of value of the dimensionless coefficient k_8 for a given motor will make it possible to compare types of motors and their proper assessment during selecting an appropriate motor for a given drive system.

On the basis of the depicted characteristics (Fig. 3 ÷ 6), values of the pressure losses coefficient k_8 (acc. (13)) as well as of the power exponents: a_{QP} – which determines impact of the liquid flow rate Q_M in ducts on the pressure losses Δp_{Mp} in hydraulic motor, and a_{vp} – which determines impact of the working liquid viscosity ν on the pressure losses Δp_{Mp} in hydraulic motor.

From Fig. 4 which was depicted for the nominal working parameters of motor (Tab. 1), the value of the pressure loss Δp_{Mp} equal to 0,21 [MPa] was read. By relating the obtained value to the nominal pressure p_n the following value of the pressure losses coefficient k_8 was achieved in accordance with the formula (13):

$$k_8 = \frac{\Delta p_{Mp|Q_M=Q_{pt}, \nu_n}}{p_n} = \frac{0,21}{6,2} = 0,034, \quad (15)$$

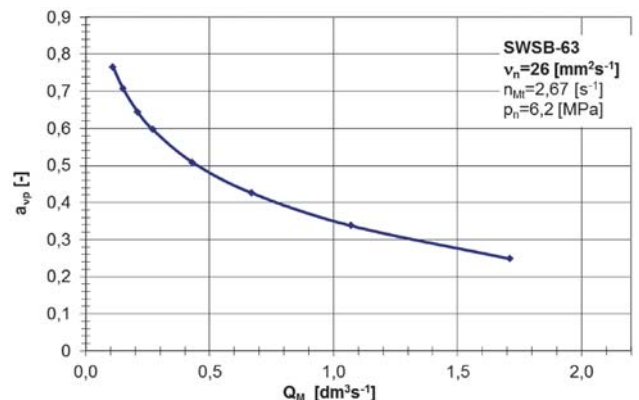


Fig. 5 The exponent a_{vp} (appearing in the power function $\Delta p_{Mp} = k_8 p_n (Q_M/Q_{pt})^{a_{QP}} (\nu/\nu_n)^{a_{vp}}$ which describes the relation between the pressure losses Δp_{Mp} in motor ducts and the ratio of Q_M and pump theoretical capacity Q_{pt} expressed in function of the motor absorbing capacity Q_M [4].

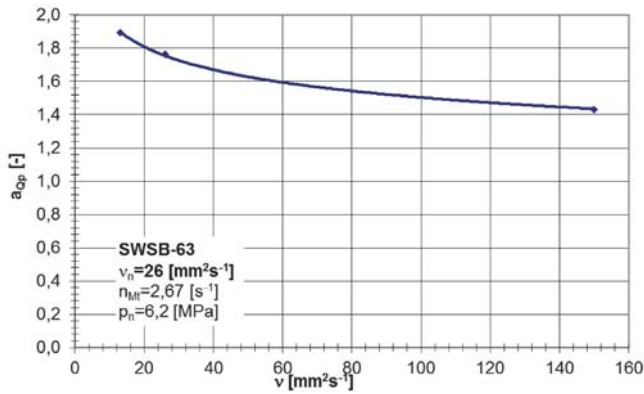


Fig. 6 The exponent a_{Qp} (appearing in the power function $\Delta p_{Mp} = k_p p_n (Q_M/Q_{Pt})^{a_{Qp}} (v/v_n)^{a_{vp}}$ which describes the relation between the pressure losses Δp_{Mp} in motor ducts and the ratio of Q_M and pump theoretical capacity Q_{Pt}) expressed in function of the working liquid viscosity v , [4]

As a result, the simulation formula for determining the pressure losses Δp_{Mp} in ducts of SWSB-63 motor at changeable viscosity v , takes the following form :

$$\Delta p_{Mp} = 0,034 p_n \left(\frac{Q_M}{Q_{Pt}} \right)^{1,77} \left(\frac{v}{v_n} \right)^{0,25} \quad (16)$$

Simulation calculations of the pressure losses were performed by using the formula (9). Their results are presented in Fig. 7.

Comparing the characteristics of pressure drops in the motor with results of the simulation calculations, one can observe that differences in values of pressure drops amount to 1% on average.

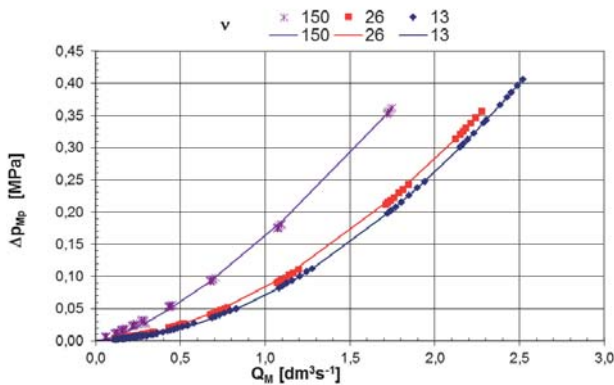


Fig. 7 Comparison of the working medium pressure losses Δp_{Mp} in ducts of SWSB-63 motor, described by the mathematical model (9) (continuous lines) with the results of measurements (points on the curves) [1]

CONCLUSIONS

1. The investigations on pressure losses in SWSB-63 hydraulic motor at three values of oil viscosity, conducted within frames of the work [1], revealed that the losses follow the relation: $\Delta p_{Mp} \sim Q^{1,77}$. The

results confirmed that in the ducts of the tested machine a not fully developed turbulent flow occurs. The similar confirmation can be found from the tests of pressure losses in PTO2-16 hydraulic axial piston motor of constant absorbing capacity per rotation at the recommended viscosity $v_n = 35 \text{ mm}^2 \text{ s}^{-1}$ of L-HL46 hydraulic oil (9 equal to abt. 46°C), carried out by M. Czyński within the frames of the work [2] - the tests showed that the losses in question follow the relation:

2. From the characteristics (Fig. 3) presenting the pressure losses Δp_{Mp} in ducts in function of the SWSB-63 motor absorbing capacity Q_M it can be observed that the value of the exponent a_{Qp} decreases along with viscosity increasing. This confirms that the formulae (7) and (9) interpreted in Fig. 1, are correct, i.e. that in the case of the relation $\Delta p_{Mp} \sim Q^1$ we deal with laminar flow, and in the case of $\Delta p_{Mp} \sim Q^2$ - with fully developed turbulent flow.
3. The impact of the working liquid viscosity v on the pressure losses Δp_{Mp} in internal ducts (Fig. 4), at $v_n = 26 \text{ [mm}^2 \text{ s}^{-1}]$ and the motor theoretical absorbing capacity $Q_{Mt} = 1,71 \text{ [dm}^3 \text{ s}^{-1}]$, is determined by

the value of the power exponent a_{vp} appearing in the function $\Delta p_{Mp} \sim \left(\frac{v}{v_n} \right)^{a_{vp}}$, where $a_{vp} \approx 0,249$.

And, value of the exponent increases at decreasing absorbing capacity, hence at $Q_M = 0,11 \text{ [dm}^3 \text{ s}^{-1}]$ it amounts to $a_{vp} \approx 0,764$. The values of the exponent a_{vp} allow to conclude that the pressure losses Δp_{Mp} in internal ducts have character of a disturbed flow with a decreasing degree of the disturbance which accompanies the lowering of absorbing capacity.

BIBLIOGRAPHY

1. Balawender A., Osiecki A., Paszota Z., Klimkiewicz W., Ciepielowski J.: Tests of SWSB-63 large-torque medium-pressure hydraulic motor (in Polish). Scientific research work, Gdańsk 1972
2. Czyński M.: Laboratory tests of a model of energy efficiency of hydrostatic transmission (in Polish). Doctor's degree thesis. Szczecin University of Technology. Faculty of Ship Engineering. Szczecin 2005
3. Koralewski J.: Impact of viscosity on energy losses in changeable capacity piston pump (in Polish). Essential report on the promoting research project No. N N504 4684 33, ?
4. Maczyszyn A., Energy analysis of construction of displacement rotary machines applicable to hydrostatic transmissions (in Polish). Doctor's degree thesis, Gdańsk

University of Technology, Faculty of Ocean Engineering and Ship Technology, Gdańsk 2014

5. Maczyszyn A.: Evaluation of losses in a hydraulic motor based on the SWSB - 63 motor tests. Polish Maritime Research, Vol. 17, No 4, 2010, pp. 46-53,
6. Paszota Z. : Aspects energetiques des transmissions hydrostatiques (in French) . Publ. Gdańsk University of Technology, Gdańsk 2002
7. Paszota Z., Energy losses in hydrostatic drive. Drive investigation method compatible with diagram of power increase opposite to the direction of power flow . Lambert Academic Publishing, Saarbrucken 2016
8. Skorek G.: Laboratory tests of pressure losses in displacement pump (in Polish), Hydraulika i Pneumatyka 2, 2005.
9. Stryczek S.: Hydrostatic drive, Vol. 2 : Systems (in Polish), Scientific Technical Publishers (WNT) , Warsaw 1997
10. Sliwinski P.: New satellite pumps. Key Engineering Materials, No. 490/2012
11. Sliwinski P.: The basics of design and experimental tests of the commutation unit of a hydraulic satellite motor. Archives of Civil and Mechanical Engineering, No. 16/2016, DOI:[1016/j.acme.2016.04.003](https://doi.org/10.1016/j.acme.2016.04.003).
12. Sliwinski P.: The flow of liquid in flat gaps of satellite motors working mechanism. Polish Maritime Research, 2, 2014.
13. Sliwinski P.: The influence of water and mineral oil on volumetric losses in a hydraulic motor. Polish Maritime Research, Special issue S1 (93), Vol. 24, 2017, DOI: 10.1515/pomr-2017-0041.
14. Sliwinski P.: The influence of water and mineral oil on mechanical losses in hydraulic motor. Chinese Journal of Mechanical Engineering. (*article in print*).

CONTACT WITH THE AUTHOR

Agnieszka Maczyszyn

e-mail: agnieszka.maczyszyn@pg.edu.pl

Gdańsk University of Technology
11/12 Narutowicza St.
80 - 233 Gdańsk
POLAND

RESEARCH OF DEPOSIT ACCUMULATED ON HEAT EXCHANGE SURFACES IN THE LIGHT OF THERMAL DEGRADATION OF HEAT EXCHANGE APARATUS OF STEAM POWER PLANTS

PART I: STUDY OF REAL SEDIMENTS

Tomasz Hajduk
Gdynia Maritime University, Poland

ABSTRACT

The presence of deposits on heat exchange surfaces in condensers and regenerative exchangers of ship and land steam power plants is always connected with the increase of the wall temperature on the water vapor side due to additional thermal resistances resulting from accumulated deposits. This increase always results in an increase in the condensing pressure, which results in the deterioration of the condensation process of the water vapor, leading to thermal degradation of a given heat exchanger. In addition, the resulting deposits form unevenness with a diversified, often stochastic, geometric structure of the surface layer surface, whose measure is most often the roughness parameters, describing the geometric structure of the surface. In addition, the increase in surface roughness of the heat transfer surface on the water vapor side promotes the formation of a thicker layer of condensate, thus worsening the organization of condensate runoff, which results in interference of the thermal degradation phenomenon of a given heat exchange apparatus. As a result, these phenomena lead to a reduction in the efficiency of a given thermal system, and thus entail an increase in the costs of energy conversion and consequently cause an increased degradation of the natural environment. In the article, based on the results of the author's own experimental research, the types of pollution accumulating on heat exchange surfaces on the water vapor side of heat exchange apparatus in marine and land steam power plants and quantitative measures of the unevenness of the surface layer of these sediments are presented.

Keywords: steam power plants, heat exchangers, deposits, spectral analysis, surface geometric texture

INTRODUCTION

In the theory of heat exchange, the term “fouling” according to Knudsen, is designated as a substance that accumulates on the surface of heat exchange, which at the same time puts additional thermal resistance in the heat transfer processes. As a result, thermal degradation of a given exchanger occurs [12]. Pollutants are often referred to as deposits, although the name, as Taborek notes [21], should belong only to impurities occurring in the form of a solid.

In spite of maintaining the recommended methods of chemical correction of feed water, boiler water, condensate and water vapor, during the operation of power units of steam power plants, sedimentary phenomena occur and

corrosion processes in water-steam cycles [22]. As a result of these processes, deposits are deposited on the heat exchange surfaces both on the water side and on the steam side. The serious operational difficulties resulting from this influence the setting of increasingly stringent requirements in relation to the quality of water and the quality of water vapor [2]. Moreover, filling the cycle with water properly cleaned and chemically prepared does not guarantee proper operation of steam power plant devices, because high temperature and pressure, as well as high thermal load of the heat exchange surface cause a series of complex physicochemical changes, changing water properties and its reactivity to construction materials of energy devices. The mechanism of these changes is not completely recognized. Therefore, it is necessary to

constantly check the quality of the circulating medium and correct its composition so that the devices can be operated in accordance with the guidelines of designers and manufacturers. Typically, the processes of deposit formation on heat exchange surfaces and corrosion processes are closely related [20].

The chemical composition of deposits formed on the water side depends also to a large extent on the construction type of the heat exchanger itself and its function (condensers, low and high pressure regeneration heat exchangers) [21]. The basic contaminants present in water include salts and gases dissolved in it, as well as some organic substances, i.e. calcium, sodium, potassium, magnesium, manganese, iron salts, calcium sulfates, calcium chloride, silica and silicates (so-called water glass). In addition, impurities may occur in the liquid phase (turbine oil) and gas, as so-called non-condensing gases (air) [19].

In the literature on the subject concerning deposits from the steam heat exchange surface of low and high pressure regeneration heat exchangers as well as condensers of land and sea steam power plants, it is shown that these types of sediments mainly consist of iron oxides in the form of: Fe_3O_4 , $FeO \cdot Fe_2O_3$, Fe_2O_3 and FeO and copper compounds. The percentage of these compounds in the deposits varies and depends on the material of the heat exchanger pipe [15].

An additional problem in the operation of heat exchangers used in energy block systems are microorganisms that form biological pollutants in the form of deposits (biofouling), e.g. mussels, crustaceans, fungi, algae and bacterial colonies. The important microorganisms responsible for corrosion phenomena include bacteria oxidizing iron and manganese compounds: *Thiobacillus ferrooxidans*, *Ferrobacillus ferrooxidans*, *Metalogenium symbioticum* [9].

In addition, the resulting pollutants usually form unevenness with different geometric structure of the surface layer surface both on the heat transfer surfaces of shell and tube exchangers as well as plate exchangers [11, 14, 23]. An interesting fact is that the irregularity of the external heat exchange surface created by the depositing deposits, on the one hand, may intensify the heat exchange process, and on the other hand may contribute to an additional increase in thermal degradation of the exchanger [6, 8, 24]. For example, Brahim et al [3] studied the influence of the shape of the geometric structure of the deposit surface collected from the cooling water side of the heat exchanger on the course of time characteristics of thermal resistance of impurities. These tests have shown that a greater unevenness of heat exchange surfaces from the cooling water side of the exchanger causes a smaller increase in the thermal resistance of pollutants over time, however, the increase in roughness is also combined with an increase in flow resistance.

On the other hand, the studies of Förster and Bohnet [8] regarding the influence of surface heat exchange surface roughness on the course of time characteristics of thermal resistance showed that larger irregularities of this surface cause a significant increase in thermal resistance of pollutants over time. For example, in the initial stage of salt precipitation

from water, in the so-called induction time τ_{ind} , they are deposited in the form of flakes tightly adhering to the surface of the pipe. They are a form of microchips, which on one hand develop the surface of heat exchange, and on the other, act as flow turbulizers breaking the laminar boundary layer, which results in the intensification of heat exchange. Therefore, some authors call τ_{ind} time as the period of intensification of heat exchange [26]. It is worth adding that extension of the τ_{ind} period is one of modern strategies against thermal degradation of heat exchangers [8].

The influence of wall impurities on a single pipe is often taken into account by means of corrections, referred directly to the calculated coefficient of heat transfer α_v from the condensing side of steam. Especially when it is difficult to distinguish the influence of the thermal resistance of the deposit layer from the influence of surface roughness. For example, Kutateladze recommends correction of the coefficient α_v with the indicator ϵ (tab.1), the value of which depends on the type of material and the condition of the pipe surface. However, it is a relationship presented only in a descriptive way. For example, for a steel pipe, covered with a thin deposit of deposit, the index ϵ is 0.67 - however, the author does not specify how thick the deposit layer is and what is the irregularity of its surface [10].

Tab. 1. The values of the correction factor ϵ depending on the material and condition of the pipe surface for the heat transfer coefficient on the water vapor side, according to [10]

ϵ	Pipe type
1.36	surface ground to a mirror shine
1.00	smooth brass pipes
0.83	Normal or drawn steel pipes
0.79	pipes coarsely cleaned with sandpaper
0.67	steel pipes covered with thin deposit coating

In addition, the increase in surface roughness of the heat transfer surface on the water vapor side promotes the formation of a thicker layer of condensate, thus worsening the so-called conditions of run-off during the condensation process of water vapor. This phenomenon can be explained by the fact that the formed deposits on the side of the pair create, in a sense, quasi-ribs, which can lead to a process of flooding intercostal canals well-known in literature. This phenomenon has an adverse effect on the operation of a single pipe, because the bottom layer of condensation, with a thickness approximately equal to the height of the ribs, constitutes an additional thermal resistance [4, 25].

Summing up, the issues aimed at identifying substances constituting deposits on heat exchange surfaces of heat exchangers of steam power plants and the quantitative description of the structure of the surface layer of deposits are a vital research issue. Knowledge of physico-chemical properties and the structure of the surface layer of the resulting deposits supports the quality of mathematical models, taking into account the features of thermal degradation, resulting from the deposition of pollutants on heat exchange surfaces of heat exchangers of steam power plants. It is worth emphasizing that these models have extremely important

practical importance, as they are used in thermal and flow diagnostics and in the planning of repair actions of these devices [5, 13, 27].

The author of this work carried out experimental research on deposits formed on the surfaces of heat exchange on the water vapor side. These studies were carried out in two stages, the first of which concerned the identification of chemical compounds of deposits, the second – the assessment of the surface layer of deposits.

RESEARCH ON THE CHEMICAL COMPOSITION OF DEPOSITS

In the research identifying the chemical composition of deposits accumulating on the heat exchange surfaces in steam power plants, the spectral analysis method based on the analysis of the X-ray spectrum was used. The purpose of this analysis is to detect elements or chemical compounds of the test sample (qualitative analysis) and to determine the quantitative composition of the sample by measuring the intensity of radiation at a specific wavelength (quantitative analysis) [7].

RESEARCH METHODOLOGY

Spectral analysis of the chemical composition of deposits was carried out by measuring the emission of characteristic EDS radiation, with the use of the semi-quantitative method [7]. The tests were carried out at the Department of Materials Engineering at the Faculty of Mechanical Engineering at the Gdańsk University of Technology. To identify the elemental composition of the tested samples and determine their quantitative composition, high-quality scientific-research equipment was used, i.e. an environmental scanning microscope type FEI XL 30 ESEM manufactured by Philips. The basic data of this device is included in table 2 [29].

Experimental tests were carried out for individual pipes from heat exchangers of three different steam power plants, which were coded as: RFS#02, RFS#07, RFS#12. Basic information about research materials along with their sensory characteristics is given in Table 3.

Tab. 2. Nominal characteristics of the scanning microscope, Philips, type FEI XL 30 ESEM, acc. [29]

Feature	Characteristic
Accuracy	< 1% measured quantity
Operating mode	I. High vacuum – conductive specimen; II. Low vacuum – non-conductive specimen
Control	Computer, Windows® NT environment software
Electronic cannon	Tungsten cathode with automatic setting, saturation and alignment
Resolution	3.5 nm @ 30 kV (low and high vacume); 15 nm @ 3 kV (low vacume)
Detectors	Built-in EDX spectrometer detector
Magnification	6×1 200 000 high vacume; 250×400 000 environmental mode
Vacuum system	Turbomolecular pumps, vacuum recovery time: a) high: 3.5 min, b) low: 2.5 min.

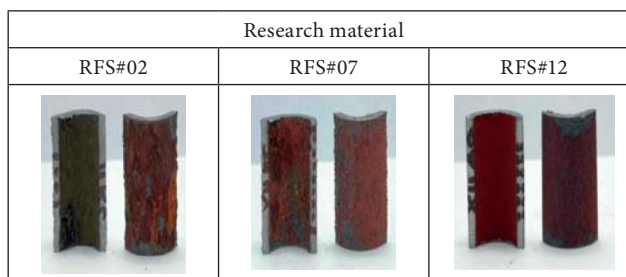
Feature	Characteristic
Presentation and recording of the image	15 „LCD monitors, 7” HD photomonitor with a 35mm SLR camera, digital image recording: HDD, FDD, CDR

Tab. 3. Sensory characteristics of sediments formed on the water vapor side of the tested samples RFS#02, RFS#07, RFS#12, according to [self.]

Sample	Color	Roughness	Origin
RFS#02	brown-yellow	irregular	HR-HP; EC 100 MW; Donator: KR
RFS#07	rusty-blue	fairly regular	HR-LP; E 200 MW; Donator: KR
RFS#12	purple	regular	HR-LP; E 100 MW; Donator: AG

Samples for testing were prepared in accordance with the applicable experimental measurements procedure in quantitative X-ray microanalysis. The limitations resulting from the geometry of the environmental chamber of the Philips FEI XL 30 ESEM scanning microscope were taken into account. Table 4 shows photos of RFS#02, RFS#07 and RFS#12 deposit samples. They were made from a tripod with a Nikon D70S camera with a MicroNikkor 105 mm – 1:2.8D lens (settings: white balance – user, ISO – 200, diaphragm – 32, time – 1s).

Tab. 4. Photographs of deposit samples for testing the chemical composition by spectral analysis, according to [self.]



RESULTS OF SPECTRAL ANALYSIS

The results of research on spectral analysis of the sediments of the tested samples RFS#02, RFS#07 and RFS#12 are presented in Table 5.

Tab. 5. Results of spectral analysis for deposit samples from steam engine heat exchangers, according to [self.]

RFS#02		RFS#07		RFS#12	
Element	Wt %	Element	Wt %	Element	Wt %
O K	21.92	O K	20.21	O K	18.57
Si K	0.34	Si K	0.72	Fe K	79.30
P K	0.53	Mn K	0.62	Co K	2.12
S K	0.38	Fe K	64.84	Total	100.00
Mn K	1.38	Cu K	13.61		
Fe K	75.45	Total	100.00		
Total	100.00				

An exemplary spectrogram of the tested sediments for the RFS#07 sample is shown in Figure 1.

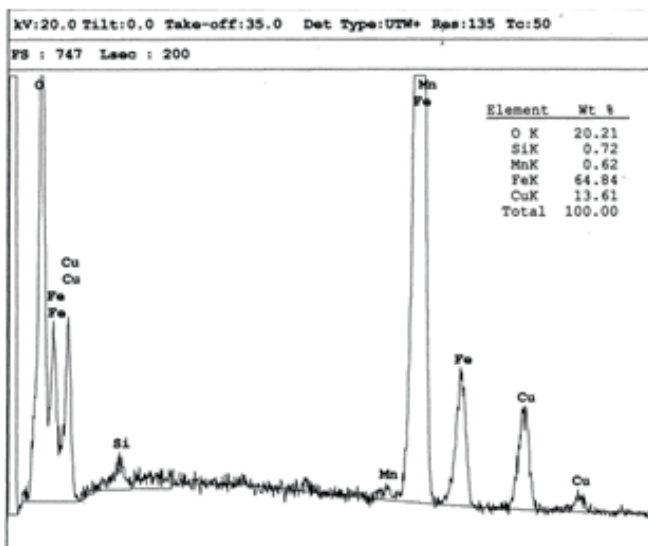


Fig. 1. Spectrograph of the sample deposits of RFS#07 obtained with the Philips EI XL 30 ESEM scanning microscope, according to [self]

INTERPRETATION OF TEST RESULTS

The identification of deposits of the analyzed samples was based on the stoichiometric analysis method [17]. Comparisons of the number of moles of the forecasted compounds with the theoretical values of quantitative relations that exist in chemical compounds have been made, i.e. in compounds that, according to literature, potentially constitute deposits on the water vapor side of heat exchange surfaces of heat exchange devices in land and marine steam power plants. The theoretical values of stoichiometric relations sr_T in chemical compounds forming deposits on heat exchange surfaces of heat exchangers in steam power plants are presented in Table 6 [17].

Tab. 6. Values of stoichiometric relations sr_T (theoretical) chemical compounds, according to [17]

Deposit	FeO	Fe ₂ O ₃	CuO	Cu ₂ O
relation sr_T	Fe:O 1:1	Fe:O 2:3	Cu:O 1:1	Cu:O 2:1
value sr_T	1.00	0.67	1.00	2.00

The number of real $n_{s_{Ei}}$ moles of the i -th element E contained in the sample was determined based on the dependence:

$$n_{s_{Ei}} = \frac{m_{Ei}}{M_{Ei}} \quad (1)$$

where:

m – mass of the E_i element in the sample [g],
 M – the molar mass of the E_i element [g/mol].

The molar ratio $mrs_{Ei:Ej}$ between i -th and j -th element in the sample is expressed:

$$mrs_{Ei:Ej} = \frac{n_{s_{Ei}}}{n_{s_{Ej}}} \quad (2)$$

An exemplary analysis of the identification of chemical compounds constituting deposits was carried out for the RFS#07 sample. Taking into account the results of tests from tab. 5 and formula 1, the number of moles n_{s_p} of the elements is:

$$n_{s_O} = \frac{m_O}{M_O} = \frac{20.21}{16.00} = 1.263;$$

$$n_{s_{Fe}} = 1.161; n_{s_{Cu}} = 0.214;$$

$$n_{s_{Si}} = 0.026; n_{s_{Mn}} = 0.011.$$

On the basis of formula 2 and the values of moles determined above, and taking into account theoretical values from table 6 of stoichiometric ratios, the following chemical compounds were evaluated as the tested deposit:

– iron compounds,

$$mrs_{Fe:O} = \frac{n_{s_{Fe}}}{n_{s_O}} = \frac{1.161}{1.161} = 1.00$$

It was identified as iron oxide (II). For further analysis, 0.102 moles of oxygen remain at the disposal ($0.102 = 1.263 - 1.161$). Hence, another compound was sought among copper oxides:

– copper compounds,

$$mrs_{Cu:O} = \frac{n_{s_{Cu}}}{n_{s_O}} = \frac{0.214}{0.102} = 2.09 \approx 2.00$$

It was estimated that it is copper oxide (I). The remaining elements (Si, Mn) occurred in trace amounts and could be “broken” from the tube material during the test. All results of the identification of chemical compounds included in the deposits on heat exchange surfaces of the tested samples are included in Table 7.

Tab. 7. Identification of chemical compounds constituting deposits of the tested samples RFS#02, RFS#07, RFS#12, according to [self]

Sample	Number of moles	Recognition
RFS#02	$n_{s_O}=1.37, n_{s_{Fe}}=1.35,$ other elements in trace amounts	FeO
RFS#07	$n_{s_O}=1.26, n_{s_{Fe}}=1.16, n_{s_{Cu}}=0.21,$ other elements in trace amounts	FeO, Cu ₂ O
RFS#12	$n_{s_O}=1.16, n_{s_{Fe}}=1.42,$ other elements in trace amounts	not determined

EXAMINATION OF THE SURFACE LAYER OF DEPOSITS

The actual surface of the solid body is the boundary between it and the surrounding center. It is an integral, external part of the surface layer. The top layer, which was created under certain technological conditions, is called technological surface layer. However, the layer that was created under operating conditions is the so-called operational top layer [18]. The structure of the external surface is determined by the geometric structure of the surface (SGP). It is assumed that the state of SGP consists of four classes of irregularities, I) shape outlines, II) surface waviness, III) surface roughness,

and IV) surface microroughness [1, 16]. In the experimental studies, the author assumed to determine as equivalent: the surface layer of deposits and the heat exchange surface on the water vapor side of the steam engine heat exchangers.

RESEARCH METHODOLOGY

The measure of irregularities in the surface layer of deposits can be characterized by a set of parameters whose values depend on the properties of the material constituting the deposit and on the conditions in which the deposit was formed. The assessment of the geometric structure of the deposit surface was made on the basis of the theory that is valid for the assessment of surface microgeometry for machinery elements that cooperate with each other. The issues related to metrology, shaping and the influence of the geometric structure of the surface on the operational properties of machines are a very complex problem and considerably extend beyond the scope of research undertaken by the author of this article [1, 16, 18]. In own research, the author limited himself to the use of several basic parameters in the field of the assessment of the geometric structure of the surface for the unevenness of the 3rd class of the surface layer. The following roughness measures [1, 28] were accepted for the description of the tests:

1. The average arithmetic deviation of the profile Ra :

$$Ra = \frac{1}{N} \sum_{i=1}^N |Y_i| \quad (3)$$

2. The average square deviation of the profile Rq :

$$Rq = \sqrt{\frac{1}{N} \sum_{i=1}^N Y_i^2} \quad (4)$$

3. The maximum height of the profile Rz :

$$Rz = \frac{1}{n} \sum_{i=1}^n Rz_i \quad (5)$$

4. The maximum height of the peak Rp :

$$Rp = \frac{1}{n} \sum_{i=1}^n Rp_i \quad (6)$$

5. Maximum height of the recess Rv :

$$Rv = \frac{1}{n} \sum_{i=1}^n Rv_i \quad (7)$$

6. The average width of the profile elements Rsm :

$$Rsm = \frac{1}{m} \sum_{i=1}^m Xs_i \quad (8)$$

where:

- Y_i – absolute values of profile's deviations R ,
- Rz_i – the largest height of the roughness profile for the elementary section,
- Rp_i – the largest elevation of the roughness profile for the elementary section,
- Rv_i – the largest depression of the roughness profile for the elementary section,
- Rsm – the average value of the width of the Xs profile elements inside the elementary segment,
- n – number of elementary sections.

The texture parameter K of the top deposit layer was calculated by the Förster and Bohnet formula:

$$K = (Rz \cdot Rsm)^{-1} \quad (9)$$

Förster and Bohnet [8] showed in their research that the texture parameter K has a significant effect on the value of the induction time τ_{ind} . They obtained an empirical positive correlation between the time of deposit excitation τ_{ind} (in hours) and the texture parameter K assuming values from 0 to $0.8E10 \text{ m}^{-2}$:

$$\tau_{ind} = 7.0789 \cdot 10^{-9} \cdot K + 12.8 \quad (10)$$

The shortest period τ_{ind} was characterized by the surface with the highest irregularity of the structure of the surface layer (small K values), while the longest period τ_{ind} was characterized by the surface with the least irregularity (high K values).

RESEARCH STAND

Roughness measurements were made by contact method, two-dimensional surface registration technique in the Laboratory of Cavitation of the Center of Liquid Mechanics at IMP PAN in Gdańsk. The test stand for surface unevenness consisted of two main parts: a roughness measuring instrument - a surface-contact profilometer of the Mitutoyo manufacturer, type SJ-301 (fig. 2) and Mitutoyo ver. 3.20 for acquisition and processing of measurement data [30].

Each measurement of the surface roughness of the deposit was preceded by a visual assessment of the test sample, thanks to which the direction of the measurement was determined and the measurement section was selected. Measurements of microgeometry of the surface of the samples were carried out on their cylindrical surface, in the longitudinal direction to the axis of the samples. For each sample, measurements were taken for three different measurement sections.



Fig. 2. Mitutoyo SJ-301 Surface Roughness Tester stand, by [self]

These sections were selected from two cross-sections of the research material. They arose from the intersection of the surface of the cylindrical tube with the plane at the central angles: $\alpha=0^\circ$, $\beta=120^\circ$ and $\gamma=240^\circ$ (Figure 3). The value of the arithmetic mean of the parameters measured in the given planes was used for the analysis.

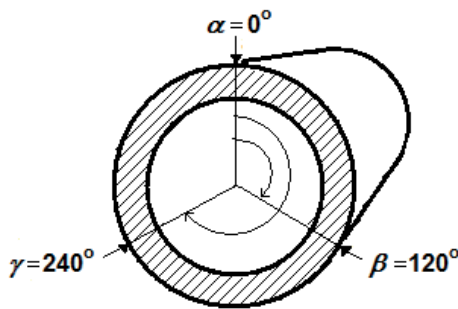


Fig. 3. Plots defining the places of roughness measurement of the tested deposit, according to [self]

To describe the microgeometry of the surface layer of deposits, the following settings were selected in the Mitutoyo ver. 3.20: measured profile R , amplitude permeation filter GAUSS, length of the elementary measuring section $l_r=0.8$ mm, total measuring length $l_n=4.0$ mm (times $n=5$), length of the run-up section $\lambda_c/2=0.4$ mm and length of the coasting section $\lambda_c/2=0.4$ mm, while λ_c is the filter cut-off length equal to l_r [30].

Tab. 8. Measured in the planes of the center angles α , β , γ and averaged (av) values of the surface profile parameters of the tested samples RTS#00, RFS#02, RFS#07 and RFS#12, "b.d." no data, according to [self]

Measure [μm]	Research material															
	RTS#00				RFS#02				RFS#07				RFS#12			
	av	α	β	γ	av	α	β	γ	av	α	β	γ	av	α	β	γ
R_a	0.96	0.53	1.14	1.21	7.76	9.61	7.11	6.57	7.07	4.45	11.78	4.98	6.22	4.24	8.57	5.84
R_q	1.33	0.73	1.59	1.69	9.95	12.65	9.38	7.81	8.85	5.60	14.17	6.79	7.78	5.27	10.55	7.52
R_z	6.62	4.47	7.52	7.88	40.78	54.10	38.27	29.96	37.17	23.10	54.95	33.47	34.81	23.31	49.02	32.09
R_p	3.11	1.99	3.79	3.54	19.83	23.02	20.84	15.65	17.23	11.61	25.43	14.64	17.68	12.63	24.08	16.34
R_v	3.52	2.47	3.73	4.35	20.94	31.08	17.43	14.31	19.94	11.49	29.51	18.83	17.12	10.68	24.94	15.75
R_{sm}	161	161	b.d.	b.d.	b.d.	b.d.	b.d.	b.d.	330	279	382	b.d.	255	200	368	198

The deposit roughness tests were carried out on specially prepared samples, due to constraints conditioned by the maximum permissible length of the profilograph measuring section ($l_{n,max} \leq 12.5$ cm). In addition, an important problem was the leveling of the tested material, when its length is much higher than $l_{n,max}$. The tests were carried out for samples, of which one RTS#00 was free from deposits (reference sample), while the remaining three samples: RFS#02, RFS#07 and RFS#12 came from the heat exchange apparatus for regeneration of low and high pressure steam power plants.

RESULTS OF THE SURFACE LAYER TESTING

After reaching the stability status within each measurement series, an electronic test protocol was prepared by a measurement data acquisition system. Table 8 shows the measured roughness parameters and their average values. Moreover, scanning photos of the surface layer of the tested samples were recorded using the Philips FEI XL 30 ESEM scanning microscope (Fig. 4, Fig. 5, Fig. 6). The measure of irregularities of the surface layer of heat exchange surface on the water vapor side for a pipe without sediments (sample RTS#00) and for pipes with sediments (samples RFS#02, RFS#07, RFS#12) was determined based on the texture parameter K and presented in Table 9. In addition, taking into account the correlation (10), the hypothetical deposit excitation time τ_{ind} for a pipe without deposit (reference, RTS#00) was estimated at about 20 hours.

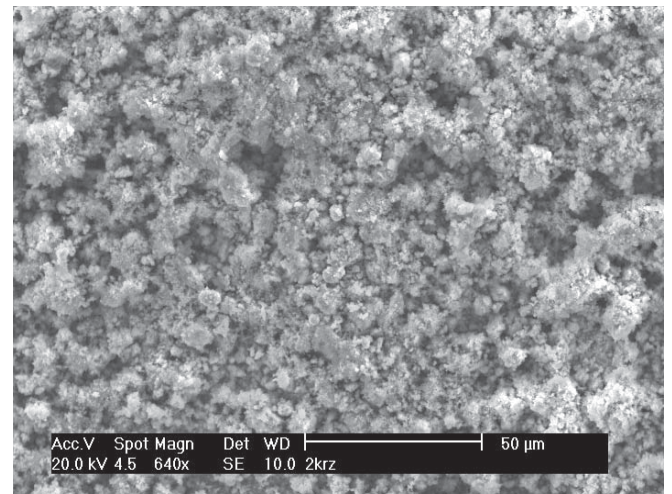


Fig. 4. Scanning image of the surface layer of the sample deposits of the RFS#02 in an enlargement of 640 \times , according to [self]

Tab. 9. Values of the texture parameter K of the top layer of the deposits of the tested samples RTS#00, RFS#02, RFS#07 and RFS#12, according to [self]

Texture parameter	Research material			
	RTS#00	RFS#02	RFS#07	RFS#12
$K \times 10^{-10} [m^{-2}]$	0.094	b.d.	0.008	0.013

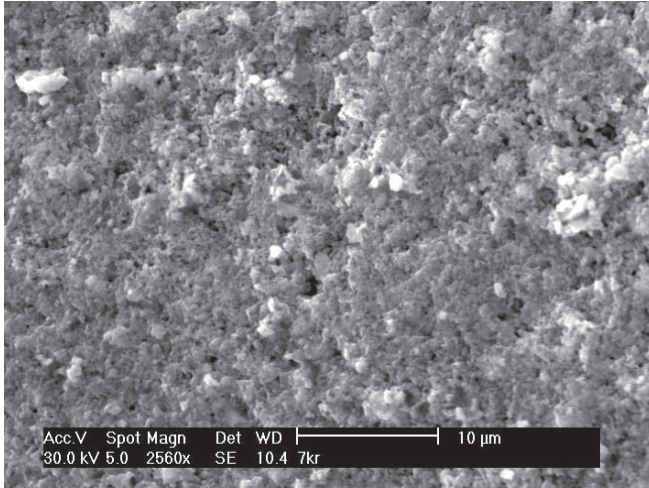


Fig. 5. Scanning photo of the surface layer of the sample deposits of RFS#07 at 2560x enlargement, according to [self]

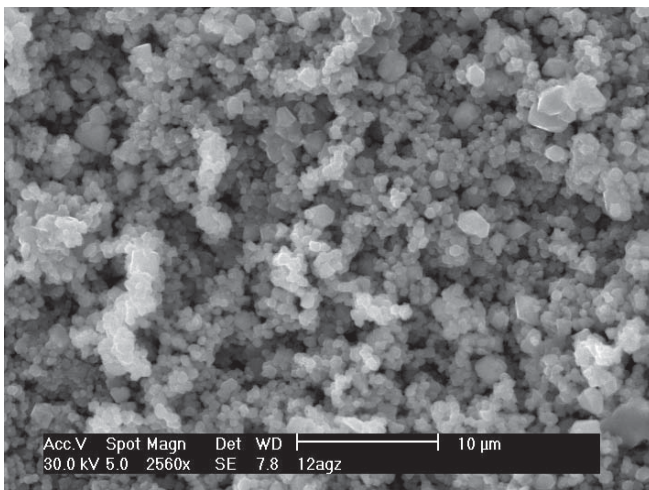


Fig. 6. Scanning photo of the surface layer of the sample deposits of RFS#12 at 2560x enlargement, according to [self]

DISCUSSION

Tests identifying the chemical composition of sediments accumulating on the water vapor side on heat exchange surfaces of heat exchangers of steam power plants have shown that the elements with the largest mass fraction were: iron, oxygen and copper. The results of the spectral analysis also showed the presence of trace elements of, i.e. cobalt, manganese, silicon, phosphorus and sulfur. The reason for the presence of these elements on spectrograms could be their removal from the tube material. On the basis of the obtained

spectra of the chemical composition of the deposits studied, an attempt was made to identify the chemical compounds that create them. Two compounds have been identified, i.e. iron oxide (II) (more frequently occurring) and copper oxide (I). It should be added that the shape of the spectral analysis results was influenced by the type of method adopted – a semi-quantitative method without a pattern. This method is considered to be less accurate than the full quantitative method with the pattern, nevertheless, the obtained results of empirical studies confirmed compliance with the results presented in literature on deposits accumulating on the water vapor side on heat exchange surfaces of land heat and marine steam power plants.

The second stage of the empirical research concerned the assessment of the structure of the surface layer of the tested deposits. The tests showed that the pipe without deposits was characterized by the lowest vertical irregularity of the surface, i.e. the Ra and Rz values for the RTS#00 sample reached values by an order of magnitude smaller than those for pipes with deposits. The results of the research also confirmed greater variation in the structure of the surface layer for pipes covered with deposits, i.e. RFS#07 and RFS#12. The texture parameter K of the pipes with deposits was smaller than the parameter K for the pipe without deposits, respectively about 12 and 7 times (in the case of the RFS#02 sample, the Rsm parameter and therefore the parameter K) could not be determined. Moreover, comparing the texture parameter K between the deposits of the RFS#07 and RFS#12 pipes, it was found that the irregular structure of the top layer, about 60% irregular, was characterized by the RFS#12 pipe. In operational practice, this state of things may result in a significant deterioration of the organization of condensate runoff from a single pipe. This phenomenon occurs due to flooding of intercostal microspheres, while generating additional thermal resistance. This resistance ultimately leads to an increase in the thermal degradation of a given heat exchange apparatus.

CONCLUSIONS

In conclusion, the influence of the presence of deposits accumulated on heat exchanger surfaces of steam-exchangers on the condensation of water vapor, due to the overlap of many phenomena at the same time, is a large issue in terms of research and complexity in the phenomenological explanation. In the author's conviction, a more detailed recognition of the type of accumulating deposits on heat exchange surfaces contributes to a more precise determination of their physical and chemical properties (quantitative aspect). On the other hand, systematic studies of the structure of the surface layer of deposits based on roughness parameters (quantitative aspect) can significantly contribute to the enhancement of the description of the phenomenon of steam condensation of energy heat exchange apparatus. The above results in the potential improvement of mathematical models of heat exchange devices, which ultimately leads to improvement of procedures for handling heat exchangers

of steam power plants according to the technical condition with control of parameters.

LITERATURE

1. Adamczak S.: Ocena chropowatości i falistości powierzchni. Informacje podstawowe. *Mechanik*, 2005, nr 5-6, s. 492-495.
2. Bednarek G., Maciejko M.: Reżim chemiczny stosowany w eksploatacji bloków energetycznych o mocy 360 MW w Elektrowni Bełchatów. *Energetyka*, 2003, rok XLVIII, nr 5, str. 309-321.
3. Brahim F., Augustin W., Bohnet M.: Numerical simulation of the fouling structured heat transfer surfaces. ECI Conference on Heat Exchanger Fouling and Cleaning. *Fundamentals and Applications*, 2003, pp. 121-129.
4. Butrymowicz D.: Influence of fouling and inert gases on the performance of regenerative feedwater heaters. *Archives of Thermodynamics*, 2001, Vol. 23, No. 1-2, pp. 127-140.
5. Butrymowicz D., Głuch J., Hajduk T., Trela M., Gardzilewicz A.: Analysis of fouling thermal resistance of feed-water heaters in steam power plants. *Polish Maritime Research*, 2009, Special issue S1, pp. 3-8.
6. Butrymowicz D., Hajduk T.: Zagadnienia degradacji termicznej wymienników ciepła. *Technika chłodnicza i klimatyzacyjna*, 2006, rok XIII, nr 3(121), s. 111-117.
7. Cygański A.: Metody spektroskopowe w chemii analitycznej. WNT, 1993, Warszawa.
8. Förster M., Bohnet M.: Modification of the interface crystal/heat transfer surface to reduce heat exchanger fouling. (ed.) Müller-Steinhagen H., *Heat Exchanger Fouling. Fundamental Approaches & Technical Solutions*, 2002, pp. 27-34.
9. Giebień R.: Biokorozja w energetyce. *Energetyka*, 2002, nr 8, str. 579-586.
10. Hobler, T.: Ruch ciepła i wymienniki. WNT, 1986, Warszawa.
11. Kazi S.N., Duffy G.G., Chen X.D.: A study of fouling and fouling mitigation on smooth and roughened metal surfaces and a polymeric material. (ed.) Müller-Steinhagen H., *Heat Exchanger Fouling. Fundamental Approaches & Technical Solutions*, 2002, pp. 65-72.
12. Knudsen J.G.: Fouling in Heat Exchangers. Overview and Summary. (ed.) Hewitt G.F., *Handbook of heat exchanger design*, Begell House Inc., 1992, New York, pp. 3.17.1.1-7.5.
13. Krzyżanowski J.A., Głuch J.: Diagnostyka cieplno-przepływowa obiektów energetycznych. Wydawnictwo IMP PAN, 2004, Gdańsk.
14. Kukulka D.J., Devgun M.: Fouling surface finish evaluation. *Applied Thermal Engineering*, 2007, Vol. 27, pp. 1165-1172.
15. Łodej M.: Nowa metoda chemicznego oczyszczania regeneracyjnych podgrzewaczy wysokoprężnych po stronie parowej. *Energetyka*, 2002, rok XLVII, nr 10/11, str. 809-811.
16. Nowicki, B.: Chropowatość i falistość powierzchni. WNT, 1991, Warszawa.
17. Pauling L., Pauling P.: *Chemia*. Wydawnictwo Naukowe PWN, 1998, Warszawa.
18. Senatorski J. K.: Podnoszenie tribologicznych właściwości materiałów przez obróbkę cieplną i powierzchniową. Instytut Mechaniki Precyzyjnej, 2003, Warszawa.
19. Stańda J.: Woda do kotłów parowych i obiegów chłodzących siłowni cieplnych. WNT, 1999, Warszawa.
20. Śliwa A.: Wpływ stopnia czystości pary na procesy korozyjne występujące w części przepływowej turbiny. *Energetyka*, 2003, nr 6, str. 407-410.
21. Taborek J.: Effects of Fouling and Related Comments on Marine Condenser Design. Marto P.J., Nunn R.H. (eds.): *Power Condenser Heat Transfer Technology*. Hemisphere Publishing Co., 1981, pp. 425-430.
22. Twardowski S., Maciejko M., Kozupa M.: Nowoczesne środki aminowe do korekcji czynnika roboczego w obiegach bloków energetycznych. *Energetyka*, 2000, Vol. LIV, nr 9, str. 75-79.
23. Wajs J., Milkielewicz D.: Influence of metallic porous microlayer on pressure drop and heat transfer of stainless steel plate heat exchanger. *Applied Thermal Engineering*, 2016, Vol. 93, pp. 1337-1346.
24. Wajs J., Milkielewicz D.: Effect of surface roughness on thermal-hydraulic characteristics of plate heat exchangers. *Key Engineering Materials*, 2014, Vol. 597, pp. 63-74, doi: 10.4028/www.scientific.net/KEM.597.63
25. Webb R.L.: The use of enhanced surface geometries in condensers. An overview. (eds) Marto P.J., Nunn R.H.: *Power Condenser Heat Transfer Technology*, 1981, pp. 353-366.
26. Xu Z.M., Wang J.G., Chen F.: A new predictive model for particulate fouling. (ed.) Bott T.: *Understanding Heat*

Exchanger Fouling and Its Mitigation. 1999, New York, pp. 185-192.

27. Zbroińska-Szczuchura E., Dobosiewicz J.: Uszkodzenia i diagnostyka wymienników ciepła w elektrociepłowniach. Energetyka, 2004, nr 12, str. 796-800.

28. DIN-EN ISO 4288, GPS – Surface texture: Profile method. Rules and procedures for assessment of surface texture, 1998.

29. Gdańsk University of Technology, Faculty of Mechanical Engineering, www.pg.gda.pl/~kkrzysztof/struktura.html

30. Surface Roughness Tester SJ-301: User's Manual.

CONTACT WITH THE AUTHOR

Tomasz Hajduk

e-mail: t.hajduk@wm.am.gdynia.pl

Faculty of Marine Engineering
Gdynia Maritime University
Morska 81-87, 81-225
POLAND

THE EFFECT OF OXYGENATED DIESEL-N-BUTANOL FUEL BLENDS ON COMBUSTION, PERFORMANCE, AND EXHAUST EMISSIONS OF A TURBOCHARGED CRDI DIESEL ENGINE

Gvidonas Labeckas

Stasys Slavinskas

Aleksandras Stulginskis University, Lithuania

Jacek Rudnicki

Gdańsk University of Technology, Poland

Ryszard Zadrąg

Polish Naval Academy, Gdynia, Poland

ABSTRACT

The article deals with the effects made by using various n-butanol-diesel fuel blends on the combustion history, engine performance and exhaust emissions of a turbocharged four-stroke, four-cylinder, CRDI 1154HP (85 kW) diesel engine. At first, load characteristics were taken when running an engine with normal diesel fuel (DF) to have 'baseline' parameters at the two ranges of speed of 1800 and 2500 rpm. Four fossil diesel (class 1) and normal butanol (n-butanol) fuel blends possessing 1 wt%, 2 wt%, 3 wt%, and 4 wt% (by mass) of n-butanol-bound oxygen fractions were prepared by pouring 4.65 wt% (BD1), 9.30 wt% (BD2), 13.95 wt% (BD3), and 18.65 wt% (BD4) n-butanol to diesel fuel. Then, load characteristics were taken when an engine with n-butanol-oxygenated fuel blends at the same speeds. Analysis of the changes occurred in the autoignition delay, combustion history, the cycle-to-cycle variation, engine efficiency, smoke, and exhaust emissions NO_x, CO, THC obtained with purposely designed fuel blends was performed on comparative bases with the corresponding values measured with 'baseline' diesel fuel to reveal the potential developing trends.

Keywords: Diesel engine; Diesel-n-butanol blends; Combustion phenomenon; Performance efficiency; Smoke; Pollutant emissions

INTRODUCTION

Growth of the economy and living standards of the population increase the need of people's and goods transportation by sea, railroads, the air, and highways. As a result, increases the need to use more ships, trains, airplanes, heavy-duty trucks, self-powered machines, city busses, and light-duty passenger cars. Unavoidably increases the demand of the fuel to be consumed, however the natural oil-resources are largely exhausted over hundreds of years. Moreover, the increased consumption of a fossil-origin fuel creates the urgent environment pollution problems and climate change. The automotive air-pollution problem emerged already in the 1940s in the Los Angeles basin [8]. The first

Clean Air Act enacted by Congress of the United States on July 14, 1955 identified the environmental air pollution related problems [17]. The Air Pollution Control Act documented the dangers to the public health and welfare, injury to agricultural crops and livestock, damage and deterioration of property, and hazards to the air, marine, and ground transport. This perception was the turning point at which the industrial, agricultural, and transportation infrastructure started to move towards green energy policy.

A legacy of the 20th century we still have today and the climate changes even more intensively over the last decades. Fulfilling historical agreement on curbing the climate change achieved in Paris (2015), the 195 Countries have made an important progress on the control of automotive emission and

set up increasingly strict emission regulations to reduce the human-made harm for the environment. Detailed analysis of the reasons leading to climate change, negotiations on reduction of carbon emissions and development of solutions for a gradual switch to renewable energy systems provides review [5]. Many of the research projects have been done to replace a fossil diesel fuel with renewable fuels such as neat oil derived from biomass of various origins, biodiesel, and ethanol. Using of renewable, oxygenated and sulphur-free fuels in internal combustion engines in a neat form or in blends with traditional diesel fuel saves fossil-fuel energy resources and makes less harm to the environment. 1-Butanol, also known as n-butanol, has a straight-chain structure with a hydroxyl group at the terminal carbon, and it has wide industrial applications. Butanol has attracted attention as an alternative biofuel because of its various advantages over other biofuels. The advances in butanol production were recently introduced to improve genetic modification of butanol-producing strains, and fermentation technology of butanol [27].

The influence of the addition of n-butanol on fuel properties, combustion, and emission characteristics for a diesel engine was studied and the engine performance and emissions were tested under nine loads at speed of 1200 rpm. The results showed that kinematic viscosity, net heating value, closed-cup flash point, density, and cetane number presented downward trends of varying degree with the increase in n-butanol content. Hydrocarbon (HC), carbon monoxide (CO), and particulate matter emissions decreased, while nitrogen oxides (NO_x) emissions and fuel consumption increased [25]. Lapuerta et al. [14] demonstrated that the increase of alcohol content in diesel or biodiesel, led to an increase in autoignition times. Such increase was not a linear but sharper for high alcohol contents, and was higher with ethanol than with butanol. For butanol blends, the increase in delay time was very similar when diesel or biodiesel were used. The maximum combustion pressure decreases as the alcohol content was increased, especially in the case of ethanol, as consequence of energy, chemical and dilution effects [14, 22]. The experiments of four-cylinder, four-stroke, turbocharged, CR diesel engine running with diesel and n-butanol blend with a volume ratio of 70:30 (D70B30) and a blend of diesel and gasoline with a volume ratio of 70:30 (D70G30) showed that the D70B30 blended fuel soot emission reduced more at the EGR ratio smaller than 25% and a constant speed of 1600 rpm. [10].

Normal butanol (CH₃CH₂CH₂CH₂OH – 74.0 g/mol) is an alcoholic-origin colourless liquid with a harsh fusel with banana odour, which possess 21.62 wt% of fuel-bound oxygen and differs as having low flash point of 28.9 °C and the boiling point of 117.7 °C at 760 mm Hg. On the one part, n-butanol added to commercial diesel fuel reduces density, viscosity, C/H atoms ratio and provides fuel-bound oxygen that along with good evaporative properties improves both the air and fuel vapours mixing rate and the combustion of fuel blend leading to more environment friendly exhaust. On the other part, the presence of a lighter and oxygenated

n-butanol reduces the cetane number, net heating value and thus mass of the fuel consumed per unit of energy developed by an engine. The sensitive interaction between advantages and disadvantages properties of n-butanol added to diesel fuel may lead to ambiguous development trends combustion, heat release rate and engine out emissions.

The purpose was to study the effects of oxygenated diesel-n-butanol fuel blends on the auto-ignition delay, combustion history, maximum heat release rate, burn angles MBF 50, MBF 90, brake specific fuel consumption, engine efficiency, smoke, and NO_x, CO, THC emissions of a turbocharged CRDI diesel engine running at various loads (bmep) and speeds of 1800 and 2500 rpm.

EXPERIMENTAL ENGINE TEST SET UP AND RESEARCH METHODOLOGY

A four-cylinder, turbocharged, CRDI diesel engine FIAT 1.9 JTD 8V 115 HP (85 kW) with a swept volume of 1.91 dm³ and compression ratio of 18:1 was used for the experimental tests. The uncooled air entered the capacity chamber and the cylinder at a controllable boost pressure of 0.160 MPa and the temperature of 85 °C. The EGR system was switched off to eliminate the potential side effects on the engine performance. Whereas the electronic control unit EDC-15C7 CR governed the timing and the duration of the fuel injection. The test setup contained a diesel engine, an engine test bed, the AVL indicating system, air and fuel mass consumption measuring equipment, a gas analyser, and a smoke meter as shown in Fig. 1. Specifications of an engine and fuel injection system are listed in Table 2.

Load characteristics with a fossil diesel fuel (DF) EN 590 (class 1) as a 'baseline' fuel and its 95.375/4.625 wt% (DB1), 90.749/9.251 wt% (DB2), 86.124/13.876 wt% (DB3) and 81.499/18.501 wt% (DB4) blends with n-butanol (B) components were taken at speeds of 1800 rpm and 2500 rpm. Changes in combustion, heat release characteristics, engine performance, smoke, and exhaust emissions revealed when using fuel blends DB1, DB2, DB3 and DB4 involving 1 wt%, 2 wt%, 3 wt% and 4 wt% of butanol-oxygen were compared with the respective values the reference diesel fuel develops for various brake mean effective pressures (bmep) at engine speeds of 1800 and 2500 rpm.

Tab. 1. Engine specifications

Engine code	192A1000
Engine brand / model	FIAT 1.9JTD 8v 115 HP (85kW)
Engine type	Four-cylinder engine, in line, turbocharged, JTD
Turbine code	712766-1
Turbocharger	A variable geometry Garret GT1749V
Fuel injection system	Common rail, direct injection (DI)
Cylinder bore x piston stroke	82 mm x 90.4 mm
The length of connecting rod	144.5 mm
Total displacement volume	1910 cc
Compression ratio	18.0±0.45:1

Combustion chamber	The OMEGA-shaped in a piston head
Rated power	85 kW (115 HP) at 4000 rpm (bmep = 1.335 MPa)
Maximum torque	255 Nm (EEC) at speed of 2000 rpm
Idle speed	850±20 rpm
SOHC – Intake timing angles	Opens before TDC at 0°; closes after BDC at 32°
SOHC – Exhaust timing angles	Opens before BDC at 40°; closes after TDC at 2°
The gas exchange system	OHC with the four vertical valves per cylinder
Fuel injection system	Common rail, Bosch
Maximum injection pressure	1400 bar (140±0.5 MPa)
Codes injection pump / injectors	0445010007 / 0445110119 – with 6 injection holes

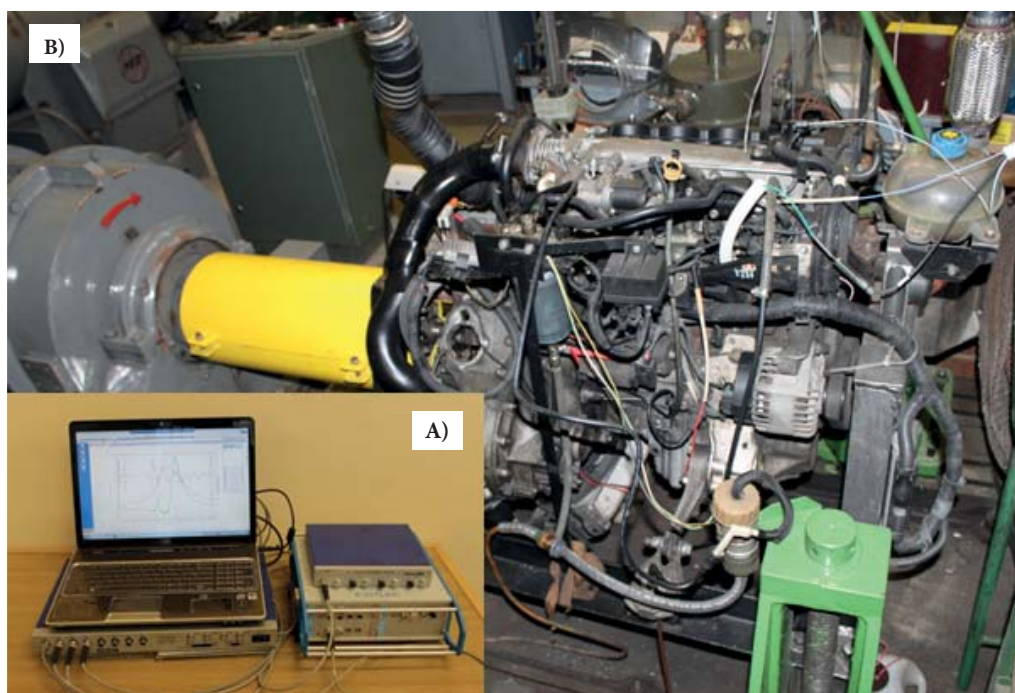


Fig. 1. Picture of the arrangement of the engine test stand: A) Measuring and recording apparatus; B) Research engine Fiat 1.9JTD 8v

A high-speed indicating system, which included the AVL angle encoder 365C and pressure transducer GU24D coupled to the AVL microIFEM piezoelectric amplifier and signal acquisition platform IndiModul 622, was introduced for the recording, acquisition, and processing of fast crank-angle gas pressure signals in the first cylinder. The single indicator diagrams, which reflected in-cylinder individual pressure signals over 100 cycles versus crank angle, were in series recorded for each fuel blend at every load-speed setting point of an engine. The data post-processing Software AVL CONCERTO™ advanced version 4.5 was used to increase productivity and improve measurement accuracy of the test results. The net heat release rate was calculated by using the AVL BOOST program. Summarized over the 100 engine-cycles in-cylinder pressure-data, instantaneous cylinder volume, and their first order derivative with respect

to crank angle have been used to calculate the heat release characteristics.

The engine torque was measured with an electric dynamometer KS-56-4 with a definition rate of ±1 Nm, and the speed with the AVL crank angle encoder 365C. A real-time air mass flow into the cylinders was measured with the AVL air mass flow meter and fuel mass consumption were recorded for every load-speed setting point with the AVL dynamic fuel balance 733S flex-fuel system. The fuel system was cleaned up after every test set and the engine operated for about 15 min intervals between test-series to consume the fuel remaining from the previous test and reach steady-state coolant temperature of 88–90 °C.

The start of injection (SOI) was recorded by using the Kistler piezoelectric pressure sensor ASMB 470004-1 connected on a high-pressure tube in front of the injector. The pressure sensor was coupled to the Kistler 2-channel charge amplifier-module 4665 mounted on the signals conditioning platform-compact 2854A to record high-pressure history at the injector with an accuracy of ±0.5% in the pressure range of 0–200 MPa.

The autoignition delay determined as a period in CADs between the start of injection (SOI) and the start of combustion (SOC) with an accuracy of ± 0.1°. As the start of injection was taken crank angle, at which the fuel pressure in a high-pressure tube drops temporally down due to the opening of the nozzle-needle-valve of the injector. As the start of combustion taken crank angle, at which the total heat release-rate crosses the zero line and changes its value from the minus side to the plus side. The definition of the autoignition delay time is shown in graphs of Fig. 2.

Using the data post-processing software AVL CONCERTO™ advanced edition provided higher productivity and accuracy of the test results. The crank angles values of MBF 50 and MBF 90 for 50% and 90% of the mass burned fraction, net heat release versus crank angle, the total amount of heat released over an engine cycle, and heat losses to the cooling system were determined by using the AVL BOOST simulation software to improve accuracy of the calculated results. The accuracies of the measured experimental data of the combustion process and engine performance parameters and the uncertainties of the calculated test results are listed in Table 2.

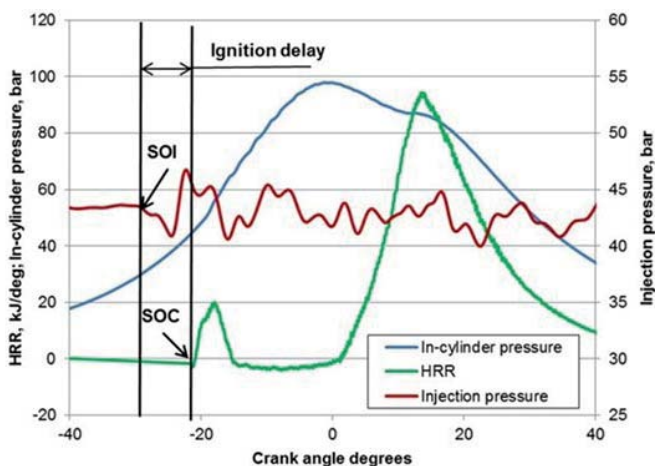


Fig. 2. Definition of the autoignition delay: the period expressed in crank angle degrees (CADs) between start of injection (SOI) and start of combustion (SOC).

Tab. 2. The accuracy of the measured engine performance and emission parameters and the uncertainty of the computed experimental results

Measurements	Accuracy
Engine torque	±1%
Engine speed	±0.1%
In-cylinder gas pressure	±0.1 MPa
Start of injection (SOI)	±0.1° (CADs)
Start of combustion (SOC)	±0.1° (CADs)
Calculated results	Total uncertainty
Engine power output	±1 %
Air mass flow rate	±1 %
Fuel mass flow rate	±0.1 %
Brake specific fuel consumption	±1.5 %
Brake thermal efficiency	±1.5 %

ANALYSIS OF MAIN PARAMETERS OF THE TESTED FUEL BLENDS

Conventional automotive fossil-origin diesel fuel (class 1) was produced at the oil refinery “Orlen Lietuva” and it satisfied the requirements of standard EN-590:2009+A1. Its composition consisted of C/H = 0.8608/0.1299 and the remaining 0.0093 was water, sulphur, and other impurities as determined at the refinery’s laboratory. The n-butanol (CH₃CH₂CH₂CH₂OH) was produced in Germany (Seelze) at Ltd. „Sigma-Aldrich” and satisfied the requirements of specification 1.00988.6025 1-Butanol EMPROVE® ESSENTIAL NF. At the respective producers’ laboratories, properties of the diesel fuel and n-butanol were examined by using the EU standards. These properties were approved with the certificates of quality analysis. Molecular weight of diesel fuel is about 180 [13] and that of 74 for n-butanol. Kinematic viscosity of a fossil diesel fuel (class 1) is 2.13 mm²/s at 40 °C whereas that of n-butanol compiles 2.97 mm²/s at 20 °C. Lubricity, HFRR VSD at 60 °C of n-butanol is lesser

(622 μm) than that (459 μm) of diesel fuel, but small amounts of n-butanol added to diesel fuel do not provide a risk to the reliability of the fuel system. More about properties of a fossil diesel, n-butanol and diesel-n-butanol fuel blends can be found in Table 1.

Tab. 3. Basic properties of a fossil diesel fuel, n-butanol and diesel-n-butanol fuel blends

Property parameters	Diesel fuel (class 1) C13H24	N-butanol (CH ₃ CH ₂ CH ₂ CH ₂ OH)	Diesel-n-butanol DB1	Diesel-n-butanol DB2	Diesel-n-butanol DB3	Diesel-n-butanol DB4
Oxygen, max wt%	0.00	21.62	1.0	2.0	3.0	4.0
Percentage of butanol in blend, wt%	-	-	4.625	9.251	13.876	18.501
Density at 20 °C, kg/m ³	832.7	811.0	831.7	830.7	829.7	828.7
Cetane number	51.4	25.0	50.2	49.0	47.7	46.5
Carbon, max wt%	86.67	64.87	85.66	84.65	83.65	82.64
Hydrogen, wt%	13.33	13.51	13.34	13.35	13.35	13.36
Carbon-to-hydrogen ratio (C/H)	6.50	4.80	6.42	6.34	6.27	6.19
Stoichiometric air-fuel ratio, kg/kg	14.685	12.220	14.53	14.37	14.21	14.05
Net heating value, kJ/kg	43.00	33.10	42.54	42.08	41.63	41.17

The engine tests started with conventional diesel fuel (class 1) to determine the combustion, performance and emissions characteristics constituting the “baseline” level that was used for monitoring of developing trends of parameters measured when operating with diesel-n-butanol fuel blends involving 1.0, 2.0, 3.0 and 4.0 wt% of n-butanol-oxygen at the same test conditions. Stable fossil diesel and n-butanol oxygenated fuel blends DB1, DB2, dB3 and DB 4 were premixed in the pre-set proportions by mass without using of any co-solvents because n-butanol mixes properly with diesel fuel and does not show any signs of phase separation at the temperature of 20 °C.

Renewable n-butanol or n-butyl alcohol or normal butanol is a primary alcohol with a 4-carbon structure and the chemical formula C₄H₉OH. It is built up from straight chain hydrocarbons, contains 21.62 wt% of fuel-bound oxygen and practically free of aromatics, nitrogen, and sulphur and possess the cetane numbers value of 25.0 that is threefold higher than that of ethanol (Table 3). Initial/final boiling points of diesel fuel (177.8 / 345.0 °C) are higher than a single boiling point of 117.7 °C of n-butanol. This means that n-butanol added to diesel fuel contributes to faster evaporation and enhances mixing rate of the air and fuel vapours and thus homogeneity of combustible mixture. Butanol is miscible with hydrocarbons therefore it mixes well with the ‘baseline’ diesel fuel too [10]. After diesel-n-butanol

fuel blends were prepared, the canisters were splashed for a while to avoid phase separation.

The density and kinematic viscosity of fuel blends were measured by using the laboratory device Anton Paar density/viscosity meter SVM 3000 with an accuracy of $\pm 0.0002 \text{ g/cm}^3$ and 0.1%, respectively, at the temperature of $40 \pm 0.001 \text{ }^\circ\text{C}$. Whereas the cetane number of oxygenated diesel-n-butanol fuel blends was computed by using typical methodology developed in the U.S. at the National Renewable Energy Laboratory [26]. This methodology assumes that the cetane number of obtained blend is a linear combination of the cetane numbers of the original fuel-components in its composition. The added n-butanol portions to diesel fuel the cetane number of the tested fuel blends reduced by 2.3%, 4.7%, 7.2%, and 9.5%, respectively. This data will be used for comparative analysis and qualitative evaluation of the relative changes occurred in the combustion process, engine efficiency, and exhaust emissions.

RESULTS AND DISCUSSION

Fig. 3 shows how oxygenated diesel-n-butanol fuel blends affects the autoignition delay when running under various engine loads (bmep) and the two ranges of speed of 1800 and 2500 rpm. At first, it should be noted that the start of injection (SOI) of a pilot fuel portion was under computer control to be automatically advanced by 15.0° and 6.0° CADs with the engine load (bmep) increased within the tested ranges at the respective speeds. This means that the SOI occurred earlier in the cycle BTDC to ensure well-timed autoignition and complete combustion of more fuel injected per cycle needed to develop higher load. This is the answer to the question why the autoignition delay progressively increased with increasing engine load, - because the oxidation reactions of the fuel started at lower both pressure and temperature inside the cylinder. However, the research did not intend to examine the changes occurred in engine load or speed, since the investigation was focused mainly on the comparative analysis of the fuel properties-evoked and n-butanol-oxygen-made effects on the ignition delay and following combustion processes.

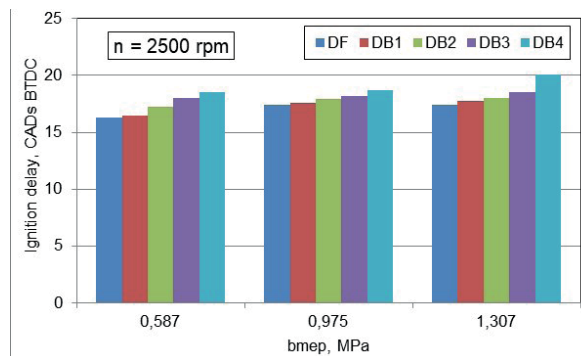
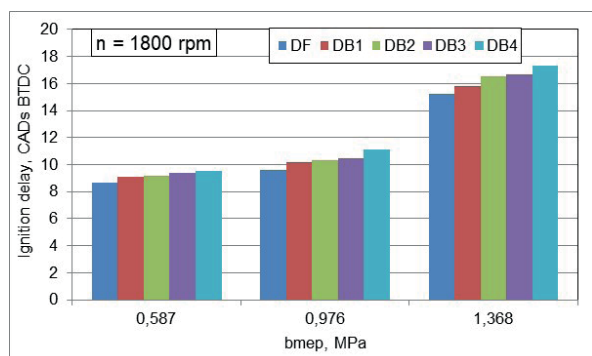


Fig. 3. The autoignition delay period in CADs as a function of engine load (bmep) at speeds of 1800 and 2500 rpm.

The autoignition delay time of diesel-n-butanol fuel blends DB1-DB4 increased by 4.6-9.2%, 7.4-16.8% and 3.9-13.8% against those values, 8.7° , 9.5° and 15.2° CADs, normal diesel fuel (DF) auto-ignites under respective 0.587, 0.978 and 1.368 MPa loads at the low speed of 1800 rpm. This pre-combustion period also increased by 1.2-13.5%, 1.1-7.5% and 2.3-15.5% when running with diesel-n-butanol fuel blends DB1-DB4 against, 16.3° , 17.4° and 17.4° CADs, diesel fuel auto-ignites under respective 0.587, 0.975 and 1.307 MPa loads at a higher speed of 2500 rpm. The obtained results show that the autoignition delay was always longer when running a turbocharged CRDI diesel engine with n-butanol-oxygenated fuel blends than with normal oxygen-free (class 1) diesel fuel. The longer auto-ignition delay for diesel-n-butanol fuel blends DB1, DB2, DB3 and DB4 can be directly attributed to the lower cetane number of the tested blends as compared to normal diesel fuel (Table 3). The next reason why the auto-ignition delay of diesel-n-butanol fuel blends was longer can be attributed to latent heat of vaporisation of n-butanol, 581.4 kJ/kg , being 2.15 times higher than, 270 kJ/kg , of diesel fuel. Finally, despite of a higher volatility, the auto-ignition temperature of alcoholic origin n-butanol is about $385 \text{ }^\circ\text{C}$, which is much higher than that, $250 \text{ }^\circ\text{C}$, of a fossil diesel fuel.

The ignition delay period was also longer when running a naturally aspirated diesel engine D-243 with various ethanol-diesel-biodiesel blends under 'lambda' of 5.5, 3.0 and 1.5 at speeds of 1400, 1800 and 2200 rpm [13]. The negative impact on the ignition delay time of using oxygenated diesel-HRD fuel blends involving ethanol or biodiesel was also observed when running a turbocharged CRDI diesel engine FIAT 1.9JTD 8v 115 HP (85kW) under 'lambda' of 1.30, 1.25 and 1.20 at the respective speeds of 1500, 2000 and 2500 rpm [6]. To having longer auto-ignition delay of oxygenated fuel blends perhaps contributed n-butanol-bound oxygen the presence of which reduced net heating value of fuel blends. In result, the higher was engine load (bmep) and, hence, more fuel injected per cycle, the greater was evaporative cooling effect. This resulted in the difference in auto-ignition delay periods between the combustion of a 'baseline' diesel fuel and oxygenated diesel-n-butanol fuel blends being more perceptible when running with the most oxygenated fuel

blend DB4 (4 wt% oxygen) at both engine speeds. Besides, the relative increase in the ignition delay period was greater when running under both the lowest and the highest loads at high speed of 2500 rpm, because the effect of cetane number is always greater if time needed to preheat, evaporate of the fuel droplets, and auto-ignite of air-fuel vapours is extremely limited.

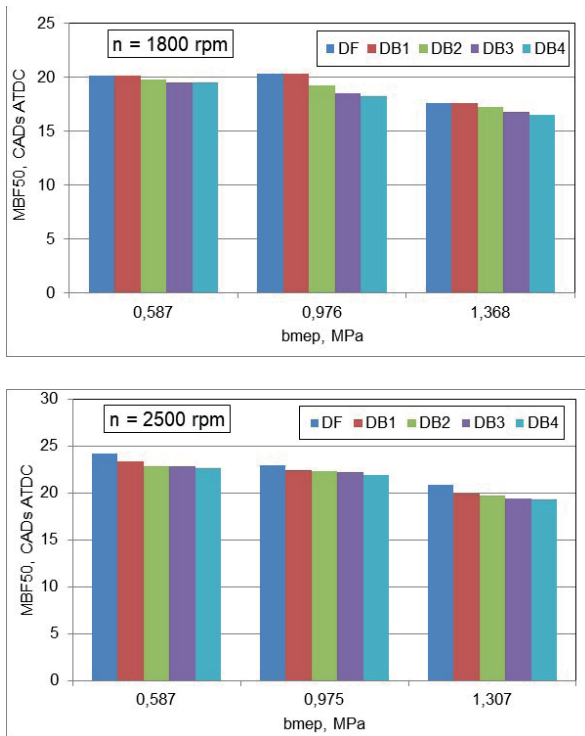


Fig. 4. Burn angle MBF 50 as a function of engine load (bmep) when running with oxygenated diesel-n-butanol fuel blends under various loads (bmep) and speeds of 1800 and 2500 rpm.

It is important to evaluate changes in burn angle MBF 50 caused by the combustion of various diesel-n-butanol fuel blends because this angle represents the centre of a gravity of heat release rate (HRR) characteristic and, thus, affects fuel-energy conversion efficiency of an engine. The shorter is the crank angle ATDC at which the 50% of energy releases in the cycle, the lower will be heat losses of the expansion stroke and thus higher engine efficiency can be attained. Nevertheless, angle MBF 50 should be neither too short, nor too long, but just as needed to harmonise sensitive interaction between the engine efficiency and the maximum torque (load) developed. Whereas the burn angle $AHRR_{max}$ should be approximately equal to 8° CADs ATDC as recommended by the AVL User's Guide instruction [2]. Burn angle MBF 50 decreased by 0.0–3.2%, 0.0–10.5%, 0.0–6.5% and 3.2–6.3%, 2.5–4.6%, 4.7–7.6% when running with oxygenated fuel blends DB1-DB4 against those values of 20.2° , 20.4° , 17.7° and 24.2° , 23.0° , 20.9° CADs the 50% of diesel fuel gets burned under the respective loads and engine speeds of 1800 and 2500 rpm (Fig. 4).

Again, the lover was the cetane number of fuel blends and, thus, the longer the ignition delay time available to improve the quality of air-fuel mixture, the higher was maximum heat release rate and the sooner in the cycle 50% of fuel-heat

releases from combustion of the most oxygenated fuel blend DB4 for the respective engine loads and speeds. To enhance the oxidation reactions, the n-butanol-based oxygen content should be progressively increased, 1, 2, 3 and 4 wt%, with increasing engine load to accelerate heat release rate against that the combustion of diesel fuel suggests for similar engine loads. Thus, burn angle MBF 50 can be shortened by 10.5% and 7.6% when running with the most oxygenated diesel-n-butanol fuel blend DB4 under medium load, 0.976 MPa, at speed of 1800 rpm and the high load, 1.307 MPa, at speed of 2500 rpm, respectively.

When running with a 'baseline' diesel fuel the end of combustion took place 4.2° (8.4%), 7.9° (15.8%) and 3.0° (5.6%), 8.1° (15.3%) CADs later in the cycle compared with that, 50.1° and 53.1° CADs, due to engine load increased from 0.587 MPa to 0.978, 1.368 MPa and from 0.587 MPa to 0.975, 1.307 MPa at the respective speeds of 1800 and 2500 rpm. The burn angle MBF 90 increased because burning of a bigger fuel portion delivered per cycle lasts always longer due to the reduced availability of air-born oxygen needed to complete combustion. However, a single-bound n-butanol-oxygen accelerated the combustion reactions to make a difference between oxygen-free diesel fuel and oxygenated diesel-n-butanol blends. Burn angle MBF 90 representing the end of combustion decreased by 1.4–3.4%, 3.7–30.2%, 2.1–26.7% and 0.0–1.5%, 2.0–2.1%, 1.0–6.5% when running with oxygenated fuel blends DB1-DB4 against those values of 50.1° , 54.3° , 58.0° and 53.1° , 56.1° , 61.2° CADs the combustion of diesel fuel ends up for the respective loads and speeds (Fig. 5).

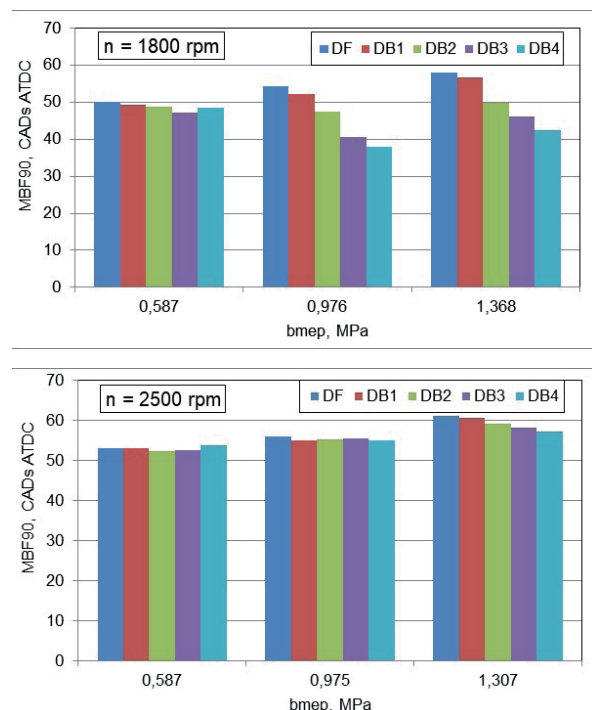


Fig. 5. Burn angle MBF 90 as a function of engine load (bmep) when running with oxygenated diesel-n-butanol fuel blends under various loads (bmep) and speeds of 1800 and 2500 rpm.

The end of combustion occurred by 2.7° – 12.2° and 0.2° – 7.6° CADs earlier in the cycle ATDC when running with oxygenated diesel-n-butanol fuel blends DB2-DB4 under medium (0.976 MPa) and high (1.368 MPa) loads than, 50.1° CADs, the combustion of diesel fuel proceeds under light (0.587 MPa) load and speed of 1800 rpm. This means that the combustion reactions of richer air-diesel-n-butanol fuel mixtures advanced with a higher average flame speed than normal air-diesel fuel mixture burns under easy loading conditions. Positive changes in the end of combustion of diesel-n-butanol fuel blends can be attributed to the longer auto-ignition delay (Fig. 3) that provides more time needed to improve the homogeneity of combustible mixture. In result, oxygenated air-diesel-n-butanol fuel mixtures burned with a higher flame speed than a straight diesel affords to cope with a problem at the respective loads and speeds. Next, n-butanol-oxygen contributed with an essential help accelerating the combustion reactions mainly at the low speed of 1800 rpm because of a lower turbulence intensity, swirl, and temperature inside the cylinder. Whereas the role of n-butanol-oxygen at the end of combustion seems to be less significant when running at the high speed of 2500 rpm.

The positive effect of using n-butanol-oxygen on combustion reactions decreased significantly when the turbulence intensity, swirl, and temperature inside the cylinder increased at a higher engine speed of 2500 rpm. Nevertheless, the positive development trends in the end of combustion remained in value when running under high load and speed too because of extremely limited real time to accomplish the cycle (Fig. 5). Comparison of data in Figs. 4 and 5 shows that the end of combustion representing angle MBF 90 is more sensitive to changes in engine load, speed, and n-butanol-oxygen content than angle MBF 50, which represents a half (50%) fuel portion burned in the cylinder. This is because the oxidation reactions decrease for the end of combustion due to limited availability of air-born oxygen and a lower mixing rate of the air and fuel blends at the late stages of the expansion stroke. Because the air-born oxygen was about utilised for the end of combustion there emerged a chance for fuel-oxygen to show the own potentials in accelerating combustion.

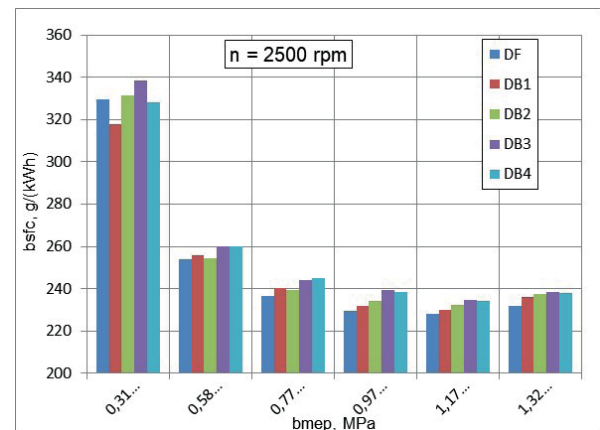
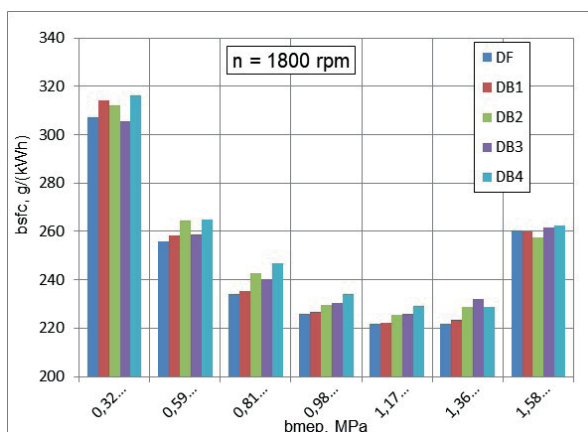


Fig. 6. The brake specific fuel consumption (bsfc) as a function of engine load (bmep) when using various diesel-n-butanol fuel blends at speeds of 1800 and 2500 rpm.

Columns of the brake specific fuel consumption (bsfc) in g/kWh as a function of engine load (bmep) obtained during operation with diesel fuel and diesel-n-butanol fuel blends at speeds of 1800 and 2500 rpm have been superimposed as shown in Fig. 6. As obvious from the figures, the bsfc decreased with the increasing load to the value that depends on the engine load, speed, and fuel blend used sustaining at the highest level for the most oxygenated and thus less calorific blend DB4 (4.0 wt% oxygen). The lowest brake specific fuel consumption of 221.6 g/kWh was obtained for diesel fuel and 223.3 g/kWh (0.8% higher) for slightly oxygenated (1.0 wt%) diesel-n-butanol blend DB1 when running under rational load of $bmep = 1.1362$ MPa at speed of 1800 rpm. The bsfc gradually increased to 228.8 (3.2%), 231.9 (4.6%) and 228.9 g/kWh (3.3%) against the respective value of diesel fuel due to lower heating value of oxygenated fuel blends DB2, DB3 and DB4. The amount of fuel blend DB2 (2.0 wt% oxygen) consumed per unit of energy developed increased with the lowest increment rate of 14.1% reaching 257.5 g/kWh against that of 260.5 g/kWh of diesel fuel needed to maintain the highest load of $bmep = 1.590$ MPa at the low speed of 1800 rpm. Further air-diesel-n-butanol mixture enrichment, and particularly air-diesel fuel mixture, was limited by critically high levels of smoke (Fig. 11).

The noted bsfc development trends with engine load remained in value when running with diesel fuel and oxygenated diesel-n-butanol fuel blends under various loads and speed of 2500 rpm. Again, the bsfc increased to 230.0 (0.9%), 232.3 (1.9%), 234.5 (2.9%), and 234.4 g/kWh (2.8%) for oxygenated fuel blends DB1, DB2, DB3, and DB4 against that, 228.0 g/kWh, a straight diesel consumes to develop reasonable load of $bmep = 1.174$ MPa at considered revolutions. However, the brake specific fuel consumption increased to 236.1 (1.8%), 237.7 (2.5%), 238.2 (2.7%), and 237.9 (2.5%) for the respective fuel blends DB1, DB2, DB3, and DB4 against that of 232.0 g/kWh a straight diesel consumes to maintain the highest load of $bmep = 1.320$ MPa at high speed of 2500 rpm. Specific fuel consumption increased mainly due to lower net heating value of oxygenated fuel blends (Table 3). Nevertheless, the revealed

tendency to reduce specific fuel consumption by using the most oxygenated (4.0 wt%) fuel blend DB4 was profitably utilised when running at the high engine load and speed. This was because the increased auto-ignition delay time (Fig. 3) provided advantages to improve quality in preparing air-fuel mixture, then the oxidation reactions proceed faster (Figs. 4) and the combustion ended up earlier in the cycle (Fig. 5) that enhanced engine efficiency (Fig. 7), reduced CO (Fig. 9), THC emissions (Fig. 10) and smoke of the exhaust (Fig. 11).

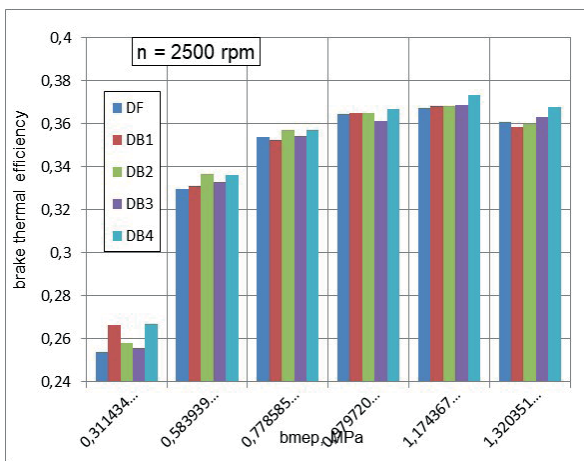
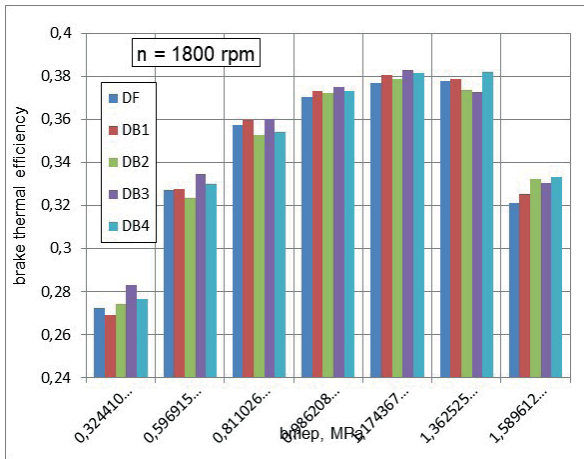


Fig. 7. The brake thermal efficiency (bte) as a function of engine load (bmep) when using various diesel-n-butanol fuel blends at speeds of 1800 and 2500 rpm.

The brake specific fuel consumption and net heating value of each fuel blend were evaluated to calculate brake thermal efficiency of an engine. As columns in Fig. 7 show, the engine efficiency progressively increased with increasing load reaching the highest brake thermal efficiency of 0.383 for diesel-n-butanol fuel blend DB3 (3.0 wt% oxygen) and 0.377 for a straight diesel running at $bmep = 1.174$ MPa and speed of 1800 rpm (Fig. 7). As engine load further increased to maximum of $bmep = 1.363$ and 1.590 MPa, the leader's position took over the most oxygenated blend DB4 (4.0 wt%) suggesting the best engine efficiency of 0.382 (1.0%) and 0.333 (3.7% higher) than the respective values, 0.378 and 0.321, a straight diesel produces from combustion

of critically enriched air-fuel mixture. It is worth to note that no decrease in engine efficiency was observed and fuel consumption increased proportionally to its lower heating value when diesel-n-butanol fuel blends up to 20% (by volume) were used in a Euro 6 engine following the New European Driving Cycle [15].

It is obvious from figures that the brake thermal efficiency depends on engine load, speed and the fuel used. At a higher speed of 2500 rpm, the need for fuel-bound oxygen increased with load, therefore the highest efficiency values produced the combustion of fuel blends DB1 (0.266), DB2 (0.337, 0.357), and the most oxygenated DB4 (0.367, 0.373, 0.368). The highest efficiency values from combustion of diesel-n-butanol fuel blend DB4 (4.0 wt% oxygen) were 0.8%, 1.6% and 1.9% higher than, 0.364, 0.367 and 0.361, a straight diesel develops for the respective loads of $bmep = 0.980$, 1.174 and 1.320 MPa. The obtained results proved that there does not exist an exceptional blend using of which could ensure the best possible engine efficiency within wide ranges of loads and speeds. The matter is that the amount of fuel-bound oxygen needed for complete combustion depends on load and thus availability of air-born oxygen as well as engine speed, turbulence intensity, swirl, and temperature inside the cylinder. The bigger is a lack of air-born oxygen inside the cylinder, the greater the need for the fuel-bound oxygen to burn the fuel completely and ensure engine efficiency.

The NO_x production depends on the ignition delay time and the amount of the fuel premixed for rapid combustion, maximum heat release rate, pressure inside the cylinder, and adiabatic flame temperature [4]. Analysis of biodiesel and second-generation biofuels showed that the NO_x emissions have trends to increase with increasing biodiesel blend level, but the magnitude of this effect differs for different feedstocks, engines, and cycles [7]. A review of the effects of biodiesel on NO_x emissions shows that the NO_x increased with increasing unsaturation, but they decrease with increasing chain length [9]. Heterogeneous air-fuel mixture contributes to uneven temperature distribution in the cylinder and thus stimulates the formation of NO , which always dominates in NO_x production [8]. In this case, the changes in NO_x emissions are largely determined by sensitive interaction between the longer auto-ignition delays (Fig. 3) and the shorter combustion durations specified by burn angle MBF 90 (Fig. 5). For similar reasons, the NO_x emissions (in g/km) remained unchanged with n-butanol addition to diesel fuel up to 20% (by volume) when running a Euro 6 diesel engine in the New European Driving Cycle [15].

As columns in [Fig. 8 show, the temperature related NO_x production increased with engine load and was higher when running with diesel fuel and all fuel blends tested at speed of 1800 rpm. The combustion of oxygenated diesel-n-butanol fuel blend DB2 (2.0 wt%) generated NO_x emissions 5.2%, 3.4%, 4.8%, 6.3%, 7.9%, 5.1% and 3.7% more than a straight diesel produces, 225, 415, 583, 828, 1207, 1438 and 970 ppm, for respective loads at the low speed of 1800 rpm. Despite of a higher brake thermal efficiency (Fig. 7), the combustion of oxygenated blends DB3 and DB4 produced almost always

NO_x emissions less than blend DB2 does because of a shorter burn angle MBF 90 (Fig. 5) and thus reduced residence time left for the combustion reactions [23]. The NO_x emissions reached the lowest level of 955 ppm when running under the highest load of bmep = 1.590 MPa with the most oxygenated blend DB 4 (4.0 wt%) at the low speed of 1800 rpm.

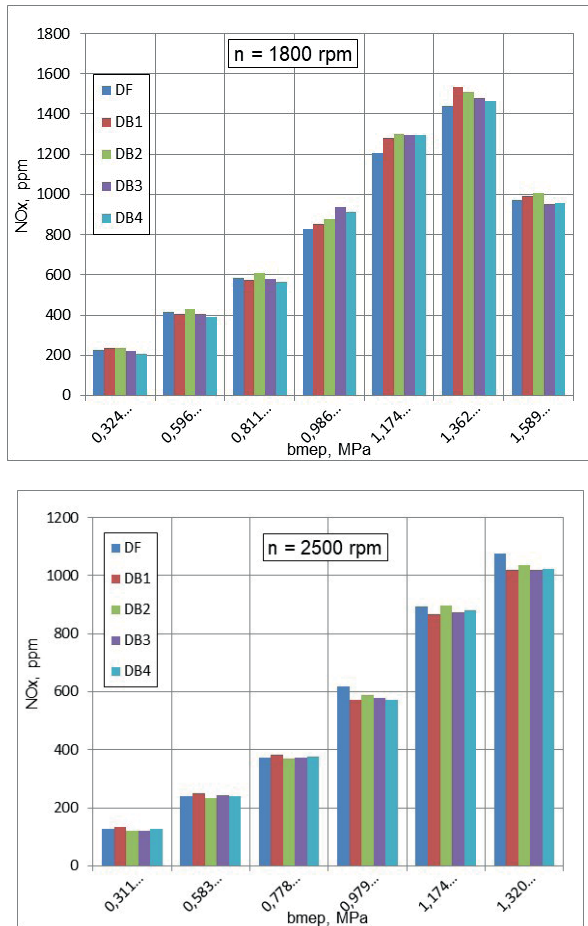
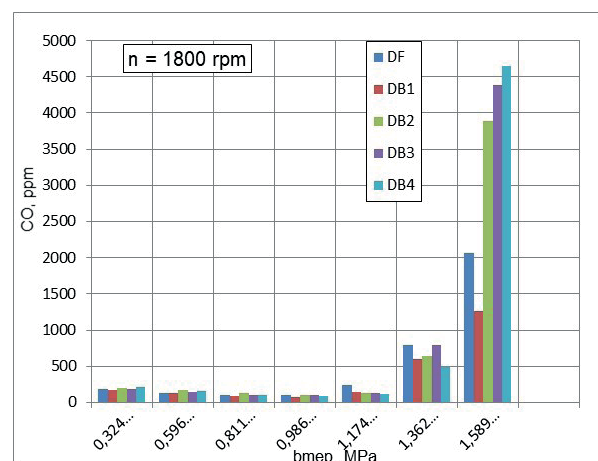


Fig. 8. The nitrogen oxide emissions (NO_x) as a function of engine load (bmep) when using various diesel-n-butanol fuel blends at speeds of 1800 and 2500 rpm.

The NO_x emissions decreased when running at speed of 2500 rpm because of the volumetric efficiency reduced and thus in-cylinder pressure was lower since boost pressure remained at the same level of 0.16 bar to eliminate the potential effects of the intake temperature on auto-ignition delay, combustion, and NO_x production. The positive effect of using oxygenated fuel blends on the NO_x production was less discernible due to shorter combustion duration in units of time at a higher speed. Therefore, the NO_x emissions produced from combustion of fuel blend DB1 (1.0 wt%) increased by 3.9%, 3.8% and 2.1% only when running under light loads of bmep = 0.311, 0.583 and 0.778 MPa against, 128, 240 and 374 ppm, a straight diesel produces at speed of 2500 rpm. Whereas the biggest NO_x emissions of 618, 892 and 1075 ppm emerged namely from combustion of oxygen-free diesel fuel when running under higher loads of bmep = 0.979, 1.174 and 1.320 MPa at the latter speed.

The combustion of fuel blend DB2 generated NO_x emissions similar as a straight diesel does, but slightly more, 588, 897 and 1036 ppm, than the remaining diesel-n-butanol blends DB1, DB3 and DB4 produce for considered test conditions. Thus, the NO_x emissions changing behaviour shows that the increased fuel-bound oxygen mass content is important, but evenly important is air-to fuel equivalence ratio 'lambda' (load) and the temperature inside the cylinder on which the NO_x production mainly depends [8].

The production of CO emissions depends on engine load, speed and the availability of air-borne oxygen in the cylinder. When running with diesel-n-butanol blends, an extra fuel-bound oxygen comes with an essential help to burn the fuel completely and reduce CO emissions when in the combustion chamber is a lack of air-borne oxygen and time needed for oxidation reactions is limited at a high speed. The effect of n-butanol-oxygen was minor because of the presence of air-borne oxygen in the cylinder when running a turbocharged CRDI diesel engine under light loads and the low speed of 1800 rpm. Emissions of CO decreased from 180 to 100 ppm for a straight diesel and from 210 to 90 ppm for the most oxygenated fuel blend DB4 due to bmep increased from 0.324 to 0.986 MPa and higher temperature inside the cylinder. The need for fuel-bound oxygen increased with engine load and, thus, CO emissions produced from combustion of diesel-n-butanol fuel blends were 54.2% (DB4), 38.0% (DB4) and 38.8% (DB1) lower than the respective values of 240, 790 and 2060 ppm a straight diesel produces for bmep = 1.174, 1.363 and 1.590 MPa at the latter speed. Whereas CO emissions progressively increased to 3890 (93.2%), 4390 (2.1 times) and 4650 ppm (2.3 times) when running with more oxygenated fuel blends DB2, DB3 and DB4 under the highest load, bmep = 1.590 MPa, and the low speed of 1800 rpm.



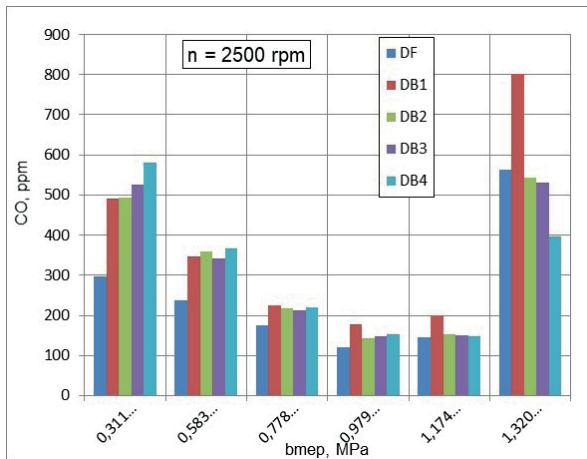


Fig. 9. The carbon monoxide emissions (CO) as a function of engine load (bmeP) when using various diesel-n-butanol fuel blends at speeds of 1800 and 2500 rpm.

Emissions of CO from combustion of diesel fuel decreased from 300 ppm to 235, 175, 120 ppm with engine load changed from bmeP = 0.311 MPa to 0584, 0.779, 0.980 MPa to increase again to 145 and 560 ppm for higher bmeP = 1.174 and 1.320 MPa when running at high speed of 2500 rpm. These species are always higher when running at light loads because of too low temperature inside the cylinder to burn the fuel completely whereas the following CO emissions increase with engine load caused the lack of air-borne oxygen needed to convert all carbon in the fuel to CO₂ and all oxygen to H₂O. For these reasons, the CO production increased by 63.3% (DB1), 65.0% (DB2), 75.0% (DB3) and 93.3% (DB4) with increased fuel-oxygen content because n-butanol added to diesel fuel reduced net heating value of the fuel and thus temperature inside the cylinder for low load of bmeP = 0.311 MPa. Whereas the CO production progressively decreased from the highest value of 800 ppm (DB1) to 545 (DB2), 530 (DB3) and 395 ppm (DB4) with adding of n-butanol to diesel fuel when running under the highest load of bmeP = 1.320 MPa at speed of 2500 rpm. Thus, using of oxygenated fuel blends DB2, DB3 and DB4 CO emissions reduced by 2.7%, 5.4% and 29.5% against, 560 ppm, a straight diesel produces at high bmeP = 1.320 MPa and speed of 2500 rpm. Naturally, the need for fuel-bound oxygen increased with increasing speed of an engine because time available to burn the fuel completely was extremely limited.

Small 2.0 wt% content of n-butanol added to diesel fuel the THC production increased 7.6, 2.9, 2.3 times and by 8.8% and 39.1% against the respective values a straight diesel produces running under bmeP = 0.324-1.174 MPa and the low speed of 1800 rpm. However, THC emissions sustained at the lowest levels of about 80 ppm and were from 2.0 to 4.3 times lower when using the most oxygenated fuel blend DB4 (4.0 wt% oxygen) at the respective loads. Moreover, THC emissions decreased by 35.1% (DB1), 27.3% (DB2), 26.0% (DB23) and 43.4% (DB4) when using oxygenated fuel blends against that value of 3960 ppm a straight diesel produces for the highest

load of bmeP = 1.590 MPa at the low speed of 1800 rpm (Fig. 10).

Especially big THC emissions increase 5.3, 4.1, 3.9, 4.5, 4.0 and 2.1 times against that the normal diesel produces for the respective loads of bmeP = 0.311-1.320 emerged when running with slightly (1.0 wt%) oxygenated fuel blend DB1 at the higher speed of 2500 rpm. Moreover, the increased THC emissions were accompanied by a bigger exhaust smoke emerged from incomplete combustion of fuel blend DB1 under considered test conditions (Fig. 11). However, using more oxygenated fuel blends DB2, DB3 and DB 4 the production of THC emissions reduced 2.4, 2.0 and 3.7 times, respectively, against that value of 260 ppm a fully loaded, bmeP = 1.320 MPa, straight diesel produces at a higher speed of 2500 rpm.

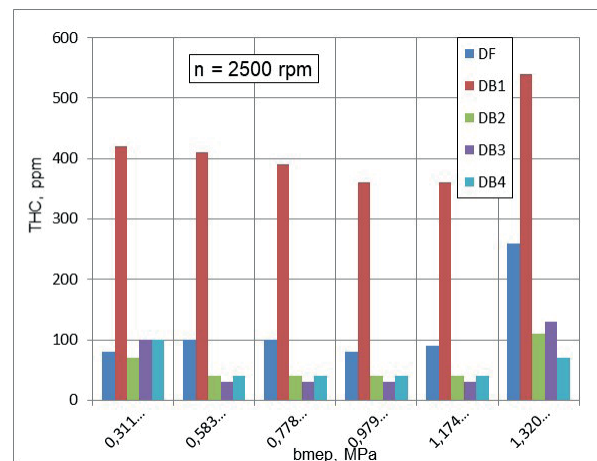
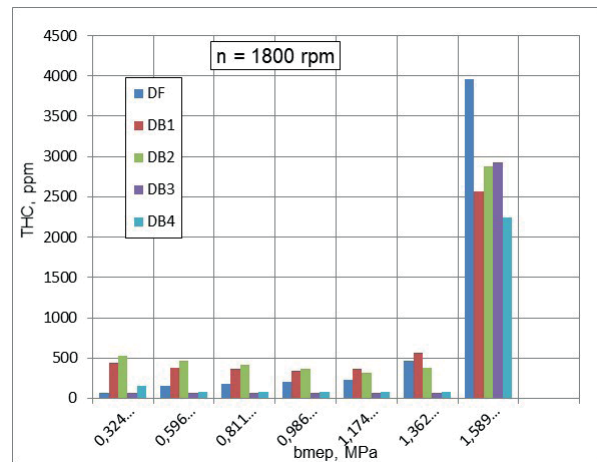


Fig. 10. The total unburned hydrocarbons (THC) as a function of engine load (bmeP) when using various diesel-n-butanol fuel blends at speeds of 1800 and 2500 rpm.

Smoke of the exhaust was at negligible and varied between 3.2-10.5% when running with normal diesel fuel under light and medium loads of bmeP = 0.324-1.362 MPa at low 1800 rpm speed (Fig. 11). Transparency of the exhaust further improved 1.5-2.8 times using of the most oxygenated fuel blend DB4 (4 wt% oxygen) against that a straight diesel produces for considered test conditions. As could be expected, the biggest positive effect of using diesel-n-butanol fuel blends

was achieved when running a turbocharged CRDI diesel engine under the highest load of $b_{mep} = 1.590$ MPa. Using oxygenated fuel blends DB1, DB2, DB3 and DB4 smoke of the exhaust reduced by 6.2%, 26.0%, 20.1% and 24.8%, respectively, against that value of 77.5% the combustion of diesel fuel generates for the highest load at the low speed of 1800 rpm. Apart from the help of fuel-bound oxygen in the combustion reactions, to having lower smoke contributed all of them, - lower density, C/H atoms ratio and stoichiometric air-fuel ratio of the tested fuel blends that reduced the need for air-borne oxygen on which transparency of the exhaust mainly depends.

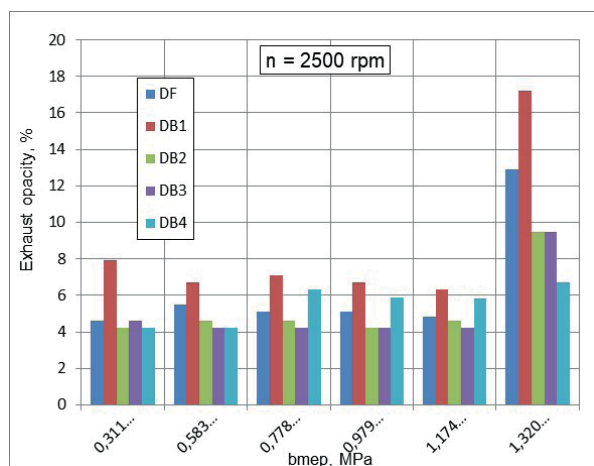
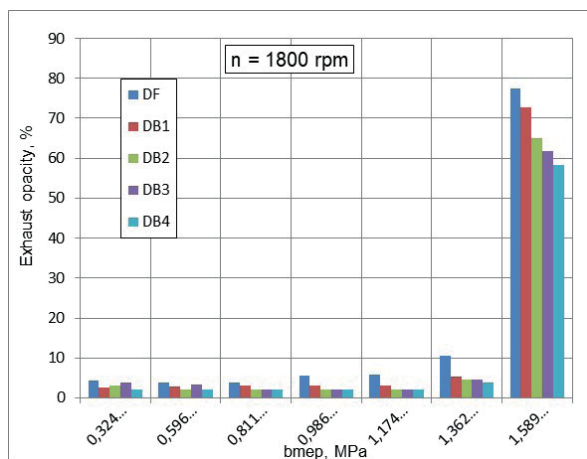


Fig. 11. The nitrogen oxide emissions (NO_x) as a function of engine load (b_{mep}) when using various diesel-n-butanol fuel blends at speeds of 1800 and 2500 rpm.

As swirl, squish and turbulence intensity of in-cylinder compressed air increased, smoke of the exhaust from a straight diesel did not change greatly and varied between 4.6-5.5% reaching the biggest value of 12.9% for the highest load, $b_{mep} = 1.320$ MPa, at high speed of 2500 rpm (Fig. 11). On the contrary, smoke of the exhaust increased by 71.7%, 21.8%, 39.2%, 34.0%, 28.6% and 33.3% when using slightly oxygenated fuel blend DB1 against the respective values the combustion of oxygen-free diesel fuel produces for the tested engine loads. Moreover, the higher smoke opacity was accompanied by

spontaneous eruption of unburned hydrocarbons as can be seen in Fig. 10. Apart of fuel-bound oxygen, the production of smoke depends on many variables, some of which are not fully understood. Therefore, it is difficult to reveal a real reason of this phenomenon. The increase in smoke opacity and, with some exceptions in THC, was also observed when running with slightly (0.91 wt%) ethanol-oxygenated diesel-HRD fuel blends a turbocharged CRDI diesel engine under close to stoichiometric conditions, $\lambda = 1.30, 1.25$ and 1.20 , at speeds of 1500, 2000 and 2500 rpm [12].

A half fuel portion burned earlier (Fig. 4) and the end of combustion took place sooner in the cycle (Fig. 5) when running with more oxygenated fuel blends DB2, DB3 and DB4 under the highest load, $b_{mep} = 1.320$ MPa, at speed of 2500 rpm. The positive changes in combustion resulted in brake thermal efficiency higher (Fig. 7) owing to lower CO (Fig. 9), THC (Fig. 10) emissions and reduced by 25.6%, 26.4% and 48.1% lower smoke opacity against that, 12.9%, a straight diesel produces for considered test conditions. The matter is that diesel fuel contained allowable by standard EN 590 amounts of polycyclic aromatics and sulphur whereas an alcoholic origin n-butanol did not. Therefore, the effects of oxygenated diesel-n-butanol fuel blends on the auto-ignition delay, combustion reactions, engine efficiency, smoke and exhaust emissions depend on the composition of the tested fuel blends, their chemical and physical properties as well as on engine load, speed, availability of air-borne oxygen and temperature conditions inside the cylinder.

CONCLUSIONS

The auto-ignition delay period of a pilot diesel-n-butanol fuel blends DB1-DB4 portions increased by 3.9-13.8% and 2.3-15.5% against, 15.2° and 17.4° CADs, the normal diesel fuel auto-ignites when running a turbocharged CRDI diesel engine under full loads of $b_{mep} = 1.368$ and 1.307 MPa at the respective speeds of 1800 and 2500 rpm.

Burn angle MBF 50 occurred by 0.0-6.5% and 4.7-7.6% earlier in the cycle for oxygenated fuel blends DB1-DB4 than 17.7° and 20.9° CADs the 50% mass-portion of diesel fuel gets burned when running a fully loaded, $b_{mep} = 1.368$ and 1.307 MPa, turbocharged CRDI diesel engine at speeds of 1800 and 2500 rpm.

The combustion of air-fuel mixtures prepared over the longer ignition delay ended by 2.7° - 12.2° and 0.2° - 7.6° CADs earlier in the cycle ATDC when using fuel blends DB2-DB4 at medium ($b_{mep} = 0.976$ MPa) and high ($b_{mep} = 1.368$ MPa) loads than, 50.1° CADs, diesel fuel gets burned at light ($b_{mep} = 0.587$ MPa) load and speed of 1800 rpm. Whereas the effect of oxygenated fuel blends on the end of combustion was minor for all loads at a higher speed of 2500 rpm.

Brake specific fuel consumption decreased with engine load to 221.6 g/kWh for diesel fuel and 223.3 (0.8%), 228.8 (3.2%), 231.9 (4.6%) and 228.9 g/kWh (3.3%) for fuel blends DB1, DB2, DB3 and DB4 when running at $b_{mep} = 1.1362$ MPa and speed of 1800 rpm. The bsfc further increased to 230.0

(0.9%), 232.3 (1.9%), 234.5 (2.9%), and 234.4 g/kWh (2.8%), respectively, against, 228.0 g/kWh, a straight diesel consumes at bmep = 1.174 MPa and speed of 2500 rpm.

Brake thermal efficiency increased with engine load to reach maximum of 0.383 for diesel-n-butanol fuel blend DB3 (3.0 wt% oxygen) and 0.377 for a straight diesel running at bmep = 1.174 MPa and speed of 1800 rpm. Whereas the highest efficiency of 0.367 (0.8%), 0.373 (1.6%) and 0.368 (1.9%) suggested the most oxygenated blend DB4 (4.0 wt%) against, 0.364, 0.367 and 0.361, a straight diesel develops for bmep = 0.980, 1.174 and 1.320 MPa at speed of 2500 rpm.

The combustion of fuel blend DB2 (2.0 wt% oxygen) generated NO_x emissions 5.1% more than a straight diesel produces, 1438 ppm, for bmep = 1.362 MPa at the low speed of 1800 rpm. The NO_x emissions relatively decreased to the lowest levels of 955 (1.5%) and 1020 (5.1%) ppm when running a fully loaded engine, bmep = 1.590 and 1.320 MPa, with the most oxygenated fuel blend DB 4 (4.0 wt%) at the respective speeds of 1800 and 2500 rpm.

CO emissions increased to maximum of 3890 (93.2%), 4390 (2.1 times) and 4650 ppm (2.3 times) when running with oxygenated fuel blends DB2, DB3 and DB4 under the highest load, bmep = 1.590 MPa, and the low speed of 1800 rpm. Whereas CO emissions decreased by 2.7%, 5.4% and 29.5% against, 560 ppm, a straight diesel produces when running a fully loaded engine, bmep = 1.320 MPa, with diesel-n-butanol blends DB2, DB3 and DB4 at speed of 2500 rpm.

THC emissions decreased by 35.1% (DB1), 27.3% (DB2), 26.0% (DB3) and 43.4% (DB4) when using oxygenated fuel blends against, 3960 ppm, a straight diesel produces for the highest load of bmep = 1.590 MPa at the low speed of 1800 rpm. Using oxygenated fuel blends DB2, DB3 and DB 4 the THC production reduced 2.4, 2.0 and 3.7 times, respectively, against, 260 ppm, a fully loaded, bmep = 1.320 MPa, straight diesel produces at a higher speed of 2500 rpm.

BIBLIOGRAPHY

1. Armas O., García-Contreras R., Ramos A. *Pollutant emissions from New European Driving Cycle with ethanol and butanol diesel blends*. Fuel Processing Technology, 2014, Vol. 122, p. 64-71.
2. AVL Concerto User's Guide. Copyright, 2012, AVL List GmbH, Hans List Platz 1, 8020 Graz, Austria. -88 p.
3. Directive 2009/28/EC on the promotion of the use of energy from renewable sources and amending and subsequently repealing Directives 2001/77/EC and 2003/30/EC. 2009.04.23. Off J E. U 2009; L 140:16-62.
4. Emberger P., Hebecker D., Pickel P., Remmele E., Thuncke K. Emission behaviour of vegetable oil fuel compatible tractors fuelled with different pure vegetable oils. Fuel 2016, Vol. 167, Issue 3, p. 257-270.
5. Engels A. Review - Anthropogenic climate change: how to understand the weak links between scientific evidence, public perception, and low-carbon practices. Energy and Emission Control Technologies, Dove Medical Press Limited, 25 January 2016, Vol. 4, p. 17-26.
6. Giakoumis E.G., Rakopoulos C.D., Dimaratos A.M., Rakopoulos D.C. *Exhaust emissions with ethanol or n-butanol diesel fuel blends during transient operation: A review*. Renewable and Sustainable Energy Reviews. 2013, Vol. 17, p. 170-190.
7. Hajbabaie M., Johnson K.C., Okamoto R.A., Mitchell A., Pullman M., Durbin T.D. Evaluation of the Impacts of Biodiesel and Second Generation Biofuels on NO_x Emissions for CARB Diesel Fuels. Environmental Science and Technology, 2012, Vol. 46, Issue 16, p. 9163-9173.
8. Heywood J.B. Internal Combustion Engine Fundamentals. -Co - Singapore for manufacture and export (International edition) 1988. 930 p.
9. Hoekman S.K., Robbins C. Review of the effects of biodiesel on NO_x emissions. Fuel Processing Technology, 2012, Vol. 96, Issue 1, p. 237-249.
10. Huang H., Zhou C., Liu Q., Wang Q., Wang X. *An experimental study on the combustion and emission characteristics of a diesel engine under low temperature combustion of diesel/gasoline/n-butanol blends*. Applied Energy, 2016, Vol. 170, p. 219-231.
11. Labeckas G., Slavinskas S., Kanapkienė I. The individual effects of cetane number, oxygen content or fuel properties on the ignition delay, combustion characteristics, and cyclic variation of a turbocharged CRDI diesel engine – Part 1. Energy Conversion and Management, 2017, Vol. 148, Issue 10, p. 1003-1027.
12. Labeckas G., Slavinskas S., Kanapkienė I. The individual effects of cetane number, oxygen content or fuel properties on performance efficiency, exhaust smoke and emissions of a turbocharged CRDI diesel engine – Part 2. Energy Conversion and Management, 2017, Vol. 149, Issue 11, p. 442-466.
13. Labeckas G., Slavinskas S., Mažeika M. The effect of ethanol-diesel-biodiesel blends on combustion, performance, and emissions of a direct injection diesel engine. Energy Conversion and Management, 2014, Vol. 79, Issue 3, p. 698-720.
14. Lapuerta M., Hernandez J.J., Fernandez-Rodríguez D., Cova-Bonillo A. *Autoignition of blends of n-butanol and ethanol with diesel or biodiesel fuels in a constant-volume combustion chamber*. Energy, 2016, Vol. 118, p. 613-621.

15. Lapueta M., Hernandez J.J., Fernandez J.R., Barba J., Ramos A., Rodriguez D.F. Emission benefits from the use of n-butanol blends in a Euro 6 diesel engine. *International Journal of Engine Research*, 2017, p. 1-14, doi: 10.1177/1468087417742578.
16. Park S.H., Youn I.M, Lee C.S. *Influence of two-stage injection and exhaust gas recirculation on the emissions reduction in an ethanol-blended diesel-fuelled four-cylinder diesel engine*. *Fuel Processing Technology*, 2010, Vol. 91, Issue 11, p. 1753–1760.
17. Public Law 159 – July 14, 1955 (p. 322): An ACT to provide research and technical assistance relating to air pollution control. Chapter 360, July 15, 1955, 2 p.
18. Rakopoulos D.C., Rakopoulos C.D., Giakoumis E.G. Dimaratos A.M., Kyritsis D.C. *Effects of butanol–diesel fuel blends on the performance and emissions of a high-speed DI diesel engine*. *Energy Conversion and Management*, 2010, Vol. 51, p. 1989-1997.
19. Rakopoulos D.C., Rakopoulos C.D., Giakoumis E.G. *Impact of properties of vegetable oil, bio-diesel, ethanol and n-butanol on the combustion and emissions of turbocharged HDDI diesel engine operating under steady and transient conditions*. *Fuel*, 2015, Vol. 156, p. 1-19, DOI: 10.1016/j.fuel.2015.04.021.
20. Rakopoulos D.C., Rakopoulos C.D., Kyritsis D.C. *Butanol or DEE blends with either straight vegetable oil or biodiesel excluding fossil fuel: Comparative effects on diesel engine combustion attributes, cyclic variability, and regulated emissions trade-off*. *Energy*, 2016, Vol. 115, p. 314-325.
21. Rakopoulos D.C., Rakopoulos C.D., Papagiannakis R.G., Kyritsis D.C. *Combustion heat release analysis of ethanol or n-butanol diesel fuel blends in heavy-duty DI diesel engine*. *Fuel*, 2011, Vol. 90, p. 1855-1867.
22. Rogers D.R. *Engine Combustion: Pressure Measurement and Analysis*. SAE International, 400 Commonwealth Drive, Warrendale, PA 15096-0001-USA, 2010. 322 p.
23. Shahir S.A., Masjuki H.H., Kalam M.A., Imran A., Ashrafal A.M. Performance and emission assessment of diesel–biodiesel–ethanol/bioethanol blend as a fuel in diesel engines: A review. *Renewable and Sustainable Energy Reviews*, 2015, Vol. 48, Issue 8, p. 62-78.
24. Siwale L., Kristof L., Adam T., Bereczky A., Mbarawa M., Penninger A., Kolesnikov A. *Combustion and emission characteristics of n-butanol/diesel fuel blend in a turbo-charged compression ignition engine*. *Fuel*, 2013, Vol. 107, p. 409-418.
25. Yang M., Wang Z., Guo S., Xin X., Qi T., Lei T., Yan X. *Effects of fuel properties on combustion and emissions of a direct injection diesel engine fuelled with n-butanol-diesel blends*. *Journal of Renewable and Sustainable Energy*, 2017, Vol. 9, Issue 1, doi: <http://dx.doi.org/10.1063/1.4976714>.
26. Yanowitz J., Ratcliff M.A., McCormick R.L., Taylor J.D., Murphy M.J. *Compendium of Experimental Cetane Numbers*. Technical Report NREL/TP-5400-61693, August 2014. 62 p.
27. Zheng J., Tashiro Y., Wang Q., Sonomoto K. *REVIEW. Recent advances to improve fermentative butanol production: Genetic engineering and fermentation technology*. *Journal of Bioscience and Bioengineering*, 2015, Vol. 119, Issue 1, p. 1-9.
28. Zheng M., Li T., Han X. *Direct injection of neat n-butanol for enabling clean low temperature combustion in a modern diesel engine*. *Fuel*, 2015, Vol. 142, p. 28-37.

CONTACT WITH THE AUTHORS

Gvidonas Labeckas
Stasys Slavinskas

Aleksandras Stulginskis University
Power and Transport Machinery Engineering Institute
Studentu str. 11, Akademija
LT-53361 Kaunas distr.
LITHUANIA

Jacek Rudnicki

Gdańsk University of Technology
Faculty of Ocean Engineering and Marine Science
11/12 Narutowicza St.
80 - 233 Gdańsk
POLAND

Ryszard Zadrąg

Polish Naval Academy
Śmidowicza 69
81-127 Gdynia
POLAND

THE EFFECT OF NUMERICAL 2D AND 3D FEM ELEMENT MODELLING ON STRAIN AND STRESS DISTRIBUTIONS AT LASER WELD NOTCHES IN STEEL SANDWICH TYPE PANELS

Karol Niklas

Janusz Kozak

Gdańsk University of Technology, Poland

ABSTRACT

Like other means of transport, merchant ships face the problem of increasing requirements concerning the environment protection, which, among other issues, implies the reduction of fuel consumption by the ship. Here, the conventional approach which consists in making use of higher strength steels to decrease the mass of the ship hull can be complemented by the use of new steel structures of sandwich panel type. However, the lack of knowledge and experience concerning, among other issues, fatigue strength assessment of thin-walled sandwich structures makes their use limited. Untypical welds imply the need for individual approach to the fatigue analysis. The article presents the effect of numerical FEM modelling with the aid of two-dimensional (2D) and three-dimensional (3D) elements on the results of strain and stress distributions in the areas of toe and root notches of the analysed laser weld. The presented results of computer simulation reveal that modelling of strain and stress states in 2D (instead of full 3D) affects only the results in close vicinity of the notch, and the observed differences rapidly disappear at a distance of 0.05 mm from the bottom of the notch. The obtained results confirm the possibility of use of numerically effective 2D strain and stress state models for analysing the fatigue strength of laser weld according to local approach.

Keywords: ship structure, sandwich, panel, FEM, laser weld, stress, strain, notch, fatigue, lightweight structure, I-core, EEDI

INTRODUCTION

The maritime transport industry plays an important role in the present globalised world. Every day, huge amount of cargo is transported by sea. The total annual volume of the transported cargo is estimated as equal to 53.6 milliard tonnes-sea miles [1]. Despite clear slowdown of the rate of development in recent years, the long-distance maritime transport is irreplaceable, and what is more, is still remains most effective in economic terms. Taking into consideration the emission of greenhouse gases, CO₂ in particular, ships are nowadays the most ecological form of transport. Depending on the size, merchant ships emit from 3 to 8 grams of CO₂ per tonne-kilometre of transported cargo [2], while the

18-wheeler based road transport emits about 15 times as much, and the air transport about 80 times as much. In total, the maritime transport emits about 2.5% of all greenhouse gases [3] and still remains the sector which is least burdened with restrictive environment protection regulations. The most significant regulations which aim at reducing the emission of toxic substances (SO_x and NO_x in particular) during fuel combustion is the MARPOL convention and its Annex VI [4], which introduces limits for permissible emissions of toxic substances during fuel combustion (Tier I, II). Since September 2017, the limit Tier III will apply, which reduces by 70% the permissible emission of toxic substances by ships, compared to Tier II [5]. Although many ship owners make attempts to avoid environment protection related costs,

changes in nearest years are inevitable. EU has also introduced regulations for their maritime areas which reduce, since 2020, the content of sulphur in the fuel down to 0.5% [6]. The above regulations mainly refer to the quality of the combusted fuel and obligatory introduction of additional devices to capture toxic substances from the exhaust. Much more interesting changes have been brought by IMO regulations [4], which introduced obligatory requirements concerning ship energy efficiency in order to reduce their negative effect on the environment. A key element here are the Energy Efficiency Design Index (EEDI) [7]–[9] and the Ship Energy Efficiency Management Plan (SEEMP) [10], which entered into force in January 2013 and are obligatory for newly built ships. These regulations impose minimal EEDI values depending on ship's type and size. The planned grow of ship energy efficiency is expected to reach 10%, 20% and 30% until year 2020, 2025 and 2030, respectively. The introduced regulations do not impose the way in which they are to be met, therefore the abovementioned efficiency grow can result either from technological development, or from improvement in the ship maintenance area (better management, for instance).

Accordingly, there is a need for significant grow of economic efficiency of ships. A possible way to reduce fuel consumption and emission of greenhouse gases is decreasing the mass of the ship hull. For medium-size or small ships, there is economically justified possibility of use of aluminium alloys in the superstructure or entire structure of the ship hull. In the case of large merchant ships, so far, the most effective method to decrease the ship hull mass consists in the use of higher strength steels and decreasing the thickness of structural elements. The estimated reduction of ship hull mass resulting from the use of high tensile strength (HTS) steels is shown in Fig. 1. The yield point of HTS steels is 2–3 times as high as that of ordinary strength structural steel (235 MPa). At present, the contribution of higher strength steels in many newly built ships amounts to 80% of ship hull mass.

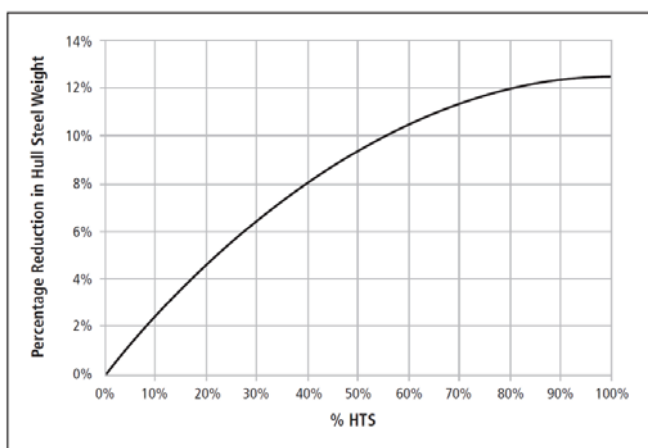


Fig. 1. The effect of HTS steel contribution on ship hull mass reduction [11]

Another way to reduce the ship hull mass is the use of new structural forms, so-called sandwich panel structures. These are multilayer panels made of higher strength steel,

but consisting of extremely thin sheets, of $t=1.5-5.0$ mm in thickness. The panel structure is designed taking into account its specific use and attributing it with the required mechanical and functional properties. The use of different cross-section shapes of internal stiffeners is possible, including I, Y, V, X, or O shapes. For instance, panels with X and Y type stiffeners (optionally with inner core) reveal higher ability to absorb energy during collision [12], [13], [14], [15], [16], [17]. Other variants of multilayer structures with advanced mechanical properties resulting from the use of light concrete as filling material can be found in [18], [19], [20]. Thus, depending on the planned application, sandwich structures can have different types of stiffeners, different dimensions of individual structural components, and additional inner space filling. What is of high importance here is the possibility to optimize the structure for selected design assumptions [21], [22], [23]. Within a huge variety of possible solutions, the most frequently used steel sandwich panel form is the I-core panel which consists of two layers of plating separated by internal flat-bar stiffeners. A sample I-core panel with plating thickness of $t=2.5$ mm, FB40x3 stiffeners, and the distance between stiffeners equal to $s=120$ mm, is shown in Fig. 2.

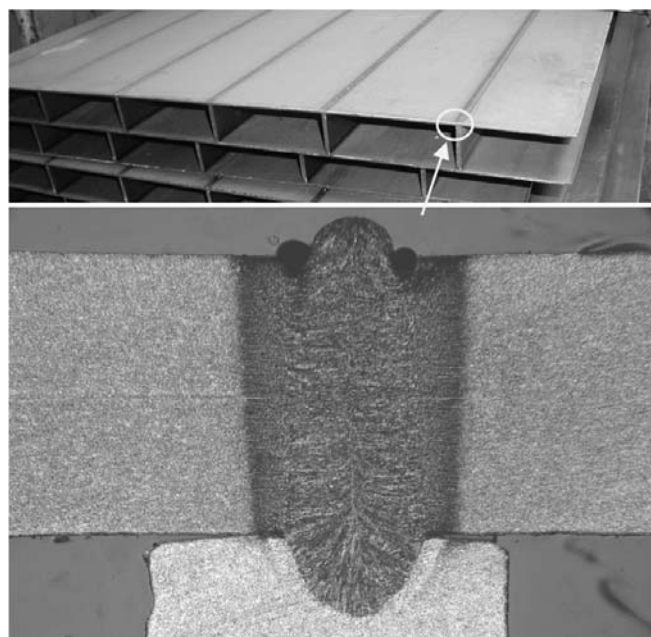


Fig. 2. Steel I-core panel and magnified image of the laser weld connecting the plating with the stiffener.

Despite very favourable mechanical properties and relatively low mass, the use of steel sandwich panels is rather limited now. Among other reasons, this results from the lack of knowledge and experience concerning the safety of use of this new structural solution. A key problem here is assessing the fatigue strength of untypical laser welds connecting the plating with the stiffeners – see Fig. 1. These welds are made using laser welding technology, or its hybrid version also making use of laser. The resultant welded joint has the geometry and material properties which differ much from conventional welds [24], [25], [26], [27]. This significantly

affects fatigue characteristics of the thin-walled sandwich structures. Theoretical and experimental research activities are in progress now which focus on assessing the fatigue life of laser welded sandwich structures [28], [29], [30], [31], [25], [32], [32], [32], [33], [34], [35]. The present state of the art in this area has not permitted development of a comprehensive calculation method for structures of this type. The calculated fatigue life of the analysed structures heavily depends on the assumed loading condition [30], [36], [37]. From among numerous possible methods to assess the fatigue life, the most frequent approach bases on local strains, or local stresses [38], [39], [40], [41], [42]. A crucial function in this method is played by stress and strain distributions in the geometric weld notch areas. The most effective way to determine the maximal stress and strain values is computer simulation making use of the Finite Element Method. Simultaneously, the use of the local stress based method requires an individual approach focused on analysing the effect of numerical modelling on the results. An interesting issue in this context is the effect of the computational grid in the notch area observed in analyses of geometric notches, [43] for instance. The dissimilarity of the analysed laser weld results from the use of untypical laser welding technology which consists in one-sided introduction of laser beam from the outer side of the plating and melting it together with the stiffener situated inside it. As a result, a welded joint with untypical geometry and material properties is formed. The effect of the material model on strain and stress distributions will be discussed in a separate paper, while the effect of the rounding radius of the notch on the geometric stress concentration factor was analysed in [44]. For a selected weld variant, the numerically simulated strain field in the notch area was compared with that recorded in the real-scale experiment [45]. As a continuation of earlier research activities in this field, the present article analyses the effect of numerical FEM modelling with the aid of 2D and 3D elements on stress and strain distributions in the notch areas of the analysed laser weld. The analysis is performed from the perspective of use of the determined strain and stress distributions for assessing the fatigue life in so-called local stress/strain approach.

THE EFFECT OF NUMERICAL FEM MODELLING MAKING USE OF 2D AND 3D ELEMENTS

Below described is the numerical model of laser weld in I-core panel. The performed analysis aimed at assessing the effect of the selected way of modelling (2D or 3D) on strain and stress results in the area of geometric toe and root notches of the laser weld. The use of 2D elements assumes the plain strain or stress state, while the use of 3D elements takes in to account the three-axial state of strain and stress.

NUMERICAL MODEL OF LASER WELD

The analysed laser weld was modelled using the FEM method in the computer programme ANSYS. The geometry of the modelled weld was assumed based on the measurements done on samples taken from real panels. The measurements made use of a computer programme and the 25 times magnified photo of the weld. When modelling, the symmetry of the weld geometry with respect to its axis was assumed. The computations were performed for nominal load $\sigma_x = 168$ MPa, introduced at the plating sheet edge at a distance from the analysed weld. A linear material model was used which corresponded to steel with Young's modulus $E=2.05e5$ MPa and Poisson's ratio equal to 0.3. The numerical model with the assumed load and boundary conditions is shown in Fig. 3. The model nodes situated along the weld axis were deprived of the degree of freedom in the x-axis direction, while those situated on the lower edge of the stiffener – in the y-axis direction. The coordinate system shown in the figure is coherent with that used during the presentation of results.

Three variants of numerical models were considered. The first model was created using 3D elements of SOLID186 type which take into account the three-axial strain and stress state. The element SOLID186 has 20 nodes, with three degrees of freedom at each node: in the x-, y-, and z-axis directions. This model was referred to as "solid". The second model, referred to as "pstress", was created using 2D elements of PLANE183 type, in the plain stress state on the xy-plane. The element PLANE183 has 8 nodes, with two degrees of freedom at each node: in the x- and y-axis directions. The last model was also created using the elements PLANE183. It assumed the plain strain state in the xy-plane and therefore was referred to as "pstrain". For all models, the calculations were performed for the same loads, boundary conditions, and discretisation. Below described is the effect of the model version on local strain and stress results in direct vicinities of geometric toe and root notches of the analysed weld.

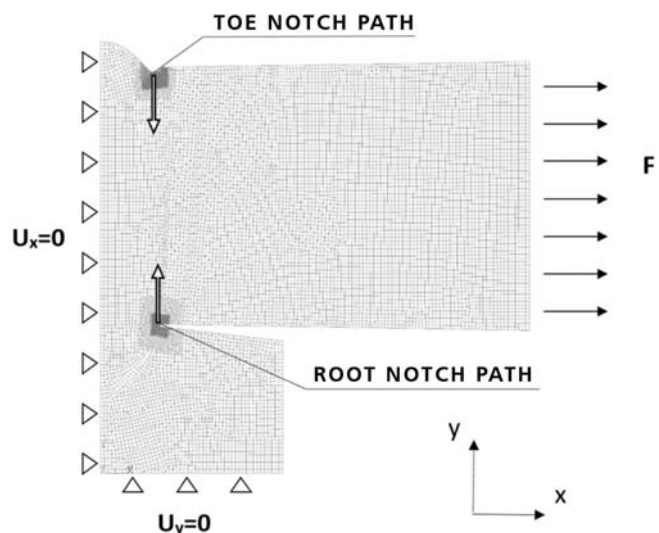


Fig. 3. Numerical FEM model with load and boundary conditions.

RESULTS AND DISCUSSION

The results are analysed along two paths. The first path begins at the weld toe notch and goes down vertically inside the material, while the second path begins at the bottom of the weld root notch and goes up vertically, in the material thickness direction. These two paths are shown in Fig. 3. The results are presented in the form of strain and stress diagrams: in Fig. 4 and Fig. 5 for the toe notch, and in Fig. 6 and Fig. 7 for the root notch. When analysing the results shown in the diagrams we can observe that:

- a) The maximal absolute strain and stress values for toe notches are larger than those for root notches. For the toe notch and three-axial strain and stress state modelling:
 - the maximal total strain in the x-axis direction is 0.004186 [-],
 - the maximal total strain in the y-axis direction is 0.002403 [-],
 - the maximal stress S_x in the x-axis direction is 533 MPa,
 - the maximal stress S_y in the y-axis direction is 38 MPa,
 Relative differences of maximal strain values in the x- and y-axis directions in the root notch area are equal to -24.6% and -41.6%, respectively, while for the stresses S_x and S_y they are equal to -7.8% and 109.9%, respectively. The stress values in the x-axis direction are 14 times as large for the toe notch and 6 times as large for the root notch as those in the y-axis direction. Based solely on the results of the numerical FEM analysis, the maximal strain and stress values are observed in the toe notch, and this notch can be indicated as the possible place of fatigue crack concentration. However, the experimental weld fatigue research shows that in practice, fatigue cracks are observed in both toe and root notches. There is no sufficient experimental evidence to indicate univocally the place in which the fatigue cracks occur much more frequently. This issue needs more experimental research.
- b) For both the toe and root notches, greater strain and stress values are observed in the x-axis direction. In three-axial strain and stress state modelling, the maximal toe notch strain value in the y-axis direction is equal to 57.4% of that in the x-axis direction. For the root notch this value is 44.5%. The maximal toe notch stress value in the y-axis direction is equal to 7.1% of that in the x-axis direction, while for the root notch this value is 16.2%. This results directly from the load direction assumed in the calculations, which was the x-axis direction. What is also noteworthy is large strain and stress values in the y-axis direction (perpendicular to the direction of load action).
- c) The results for the plain stress state at the notch bottom differ from the remaining values, but at the distance of 0.05 mm from the notch bottom this difference disappears. For instance, the relative difference of normal toe notch stress S_x between the plain stress state model and the three-axial stress state model is equal to 34.9%, while at the distance of 0.05 mm this difference drops down to as little as 8.3%.
- d) The plain strain state calculation variant gives the strain results close to those obtained in the three-axial strain and

stress state modelling. This is because of the assumed zero stress value in the direction normal to the finite element plane. Likewise, the plain stress state variant gives the stress results close to those obtained in the three-axial strain and stress state variant, due to the assumed zero strain value in the direction normal to the finite element plane.

- e) For all analysed variants, the compliance of strain and stress results is much better in the y-axis direction than that in the x-axis direction, which is related with the direction of load action. The effect of the assumed zero strain and stress values in the plain stress and strain variants, respectively, is less noticeable in the less heavily loaded direction.

The above results reveal that plain strain state modelling makes it possible to obtain local strain and stress results similar to those obtained in the three-dimensional model. In the fatigue analysis according to local approach, the effective notch stress is determined in accordance with the hypothesis of stress averaging at a virtual distance of microstructural support, or at a distance of fictional notch rounding radius [38]. In both cases the distance at which the results are averaged is greater than the distance from the notch bottom at which the effect of modelling on the results can be observed. Thus, from the practical point of view, the results of geometric stress concentration coefficients will be identical for all here analysed methods of modelling.

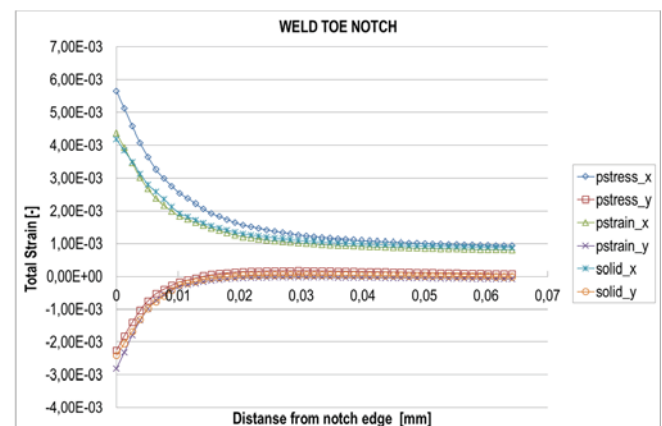


Fig. 4. Total strain in x- and y-axis directions for laser weld toe notch path

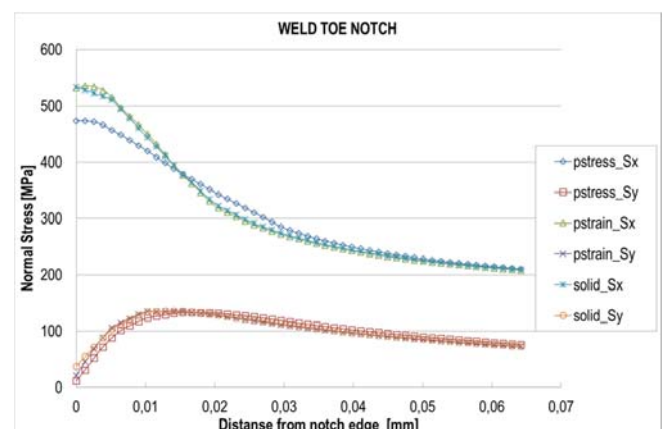


Fig. 5. Normal stress in x- and y-axis directions for laser weld toe notch path

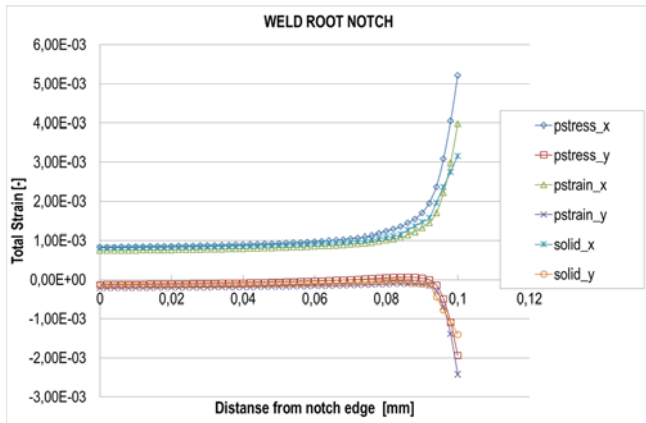


Fig. 6. Total strain in x- and y-axis directions for laser weld root notch path.

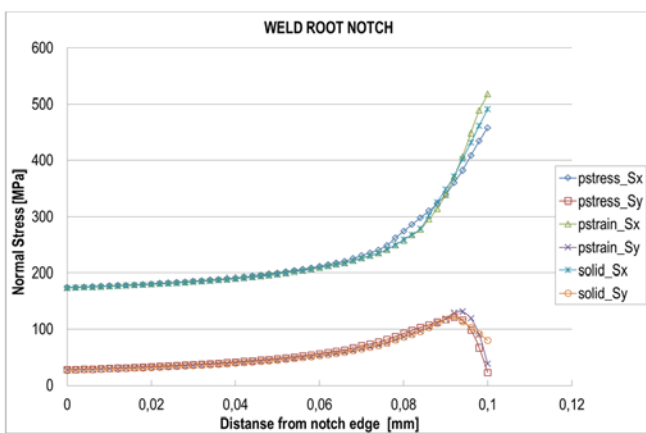


Fig. 7. Normal stress in x- and y-axis directions for laser weld root notch path.

SUMMARY AND CONCLUSIONS

The need to fulfil new requirements concerning ship energy efficiency improvement implies technological progress aiming at the reduction of fuel consumption and emission of greenhouse gases. Taking into account economic and ecological aspects, of high importance here is the reduction of ship hull mass. A commonly used approach to reach this goal is the use of higher strength steels. In many cases the contribution of HTS steels in the hull structure can reach as much as 60-80%. Cases have been reported when the ships were entirely (100%) built of higher strength steel. We can say that this method of ship hull mass reduction has been exploited. New opportunities are opened by the use of new structures, so-called sandwich panels. They are also made of higher strength steels, but the sandwich type structure makes it possible to reach much more favourable relation of strength properties (stiffness in particular) to mass. Research activities are in progress now which focus on determining a series of properties of sandwich structures in order to ensure safety of their use. An important aspect which needs a detailed analysis is the fatigue life of welds connecting structural elements of panels. Compared to typical joints,

these welds have considerably different geometry and material properties, which implies the need to examine the effect of these differences on the fatigue life of welds. The analysis can be performed using the local stress or local strain approach, whereas the strain or stress distributions at the notch are usually determined based on computer simulations performed with the aid of the Finite Element Method or the Boundary Element Method. The fatigue life calculation methodology is known for welds connecting structural elements of more than 5 mm in thickness. The application of this methodology for thinner elements, such as steel sandwich panels, implies the need for verifying the effect of particular aspects of numerical modelling on the obtained results. This article analysed the effect of 2D and 3D modelling on the strain and stress distributions at geometric nodes of the laser weld made in the steel I-core panel. The calculations were performed using the Finite Element Method in three variants characterised by: plain stress state, plain strain state, and three-axial strain and stress state. The obtained results have revealed that the effect of modelling method on the results at the bottom of the weld toe and root notch is small. The strain and stress results in the toe and root notch areas obtained using the plain strain and plain stress models are very close to those obtained using the three-axial strain and stress model. Differences in local strain or stress values disappear at such a small distance as about 0.05 mm from the notch bottom. When performing the fatigue analysis in accordance with the local approach (local strain or local stress), the effective stress values are determined at a virtual distance of microstructural notch support, or at a distance of fictional notch rounding radius. It is noteworthy that regardless of the stress averaging method, the distance at which it is done is greater than the distance from the notch bottom at which the effect of the modelling method on the values of the analysed strain or stress is noticeable. Therefore, the important practical conclusion is that the geometric stress concentration coefficient values calculated using 2D plain strain modelling, 2D plain stress modelling, and 3D three-axial strain and stress modelling will be very close to each other, and the possible effect of modelling method can be neglected. This justifies the use of much more effective 2D models for analysing strain and stress concentrations in laser weld toe and root notches.

ACKNOWLEDGEMENTS

The research was supported by the National Centre for Research and Development (NCRD) and the SmartPS project No. MARTECII/SmartPS/4/2016. The research was supported by the Academic Computer Centre in Gdansk (CI TASK). All support is highly appreciated by the author.

BIBLIOGRAPHY

1. UNCTAD, "Review of Maritime Transport 2016," 2016.
2. P. R. Cabezas and G. Kasoulides, "International Maritime Organization," *Int. J. Mar. Coast. Law*, vol. 3, no. 3, pp. 235–245, 2004.
3. T. W. P. Smith et al., "Third IMO Greenhouse Gas Study 2014," 2014.
4. IMO, "MARPOL Annex VI, Chapter 4," 2011.
5. IMO, "MEPC 69/21. Report of the Marine Environment Protection Committee on its sixty-ninth session," 2016.
6. European Parliament and Council of the European Union, "Directive 2012/33/EU of the European Parliament and of the Council," 2012.
7. IMO, "MEPC.215(93) – Guidelines for calculation of reference lines for use with the Energy Efficiency Design Index (EEDI)," 2012.
8. IMO, "MEPC.214(93) – 2012 Guidelines on survey and certification of the Energy Efficiency Design Index (EEDI)," 2012.
9. IMO, "MEPC.212(93) – 2012 Guidelines on the method of calculation of the attained Energy Efficiency Design Index (EEDI) for new ships," 2012.
10. IMO, "MEPC.213(93) – 2012 Guidelines for the development of a Ship Energy Efficiency Management Plan (SEEMP)," 2012.
11. American Bureau of Shipping, "Ship Energy Efficiency Measures - Status and Guidance," 2013.
12. H. Naar, P. Kujala, B. C. Simonsen, and H. Ludolphy, "Comparison of the crashworthiness of various bottom and side structures," *Mar. Struct.*, vol. 15, no. 4–5, pp. 443–460, 2002.
13. A. Klanac, S. Ehlers, and J. Jelovica, "Optimization of crashworthy marine structures," *Mar. Struct.*, vol. 22, no. 4, pp. 670–690, 2009.
14. P. Hogstrom and J. W. Ringsberg, "Assessment of the crashworthiness of a selection of innovative ship structures," *Ocean Eng.*, vol. 59, pp. 58–72, 2013.
15. V. Rubino, V. S. Deshpande, and N. A. Fleck, "The collapse response of sandwich beams with a Y-frame core subjected to distributed and local loading," *Int. J. Mech. Sci.*, vol. 50, no. 2, pp. 233–246, 2008.
16. L. St-Pierre, V. S. Deshpande, and N. A. Fleck, "The low velocity impact response of sandwich beams with a corrugated core or a Y-frame core," *Int. J. Mech. Sci.*, vol. 91, pp. 71–80, 2015.
17. S. Hou, S. Zhao, L. Ren, X. Han, and Q. Li, "Crashworthiness optimization of corrugated sandwich panels," *Mater. Des.*, vol. 51, pp. 1071–1084, 2013.
18. A. Christian and G. O. K. Chye, "Performance of fiber reinforced high-strength concrete with steel sandwich composite system as blast mitigation panel," in *Procedia Engineering*, 2014, vol. 95, pp. 150–157.
19. E. A. Flores-Johnson and Q. M. Li, "Structural behaviour of composite sandwich panels with plain and fibre-reinforced foamed concrete cores and corrugated steel faces," *Compos. Struct.*, vol. 94, no. 5, pp. 1555–1563, 2012.
20. T. J. Grafton and J. R. Weitzenböck, "Steel-concrete-steel sandwich structures in ship and offshore engineering," *Adv. Mar. Struct. - Proc. 3rd Int. Conf. Mar. Struct. MARSTRUCT 2011*, pp. 549–558, 2011.
21. J. Romanoff and P. Kujala, "OPTIMUM DESIGN FOR STEEL SANDWICH PANELS FILLED WITH POLYMERIC FOAM," in *FAST 2001 The 6th International Conference on Fast Sea Transportation*, 2001, no. September.
22. J. D. Poirier, S. S. Vel, and V. Caccese, "Multi-objective optimization of laser-welded steel sandwich panels for static loads using a genetic algorithm," *Eng. Struct.*, vol. 49, pp. 508–524, 2013.
23. J. Romanoff, "Optimization of web-core steel sandwich decks at concept design stage using envelope surface for stress assessment," *Eng. Struct.*, vol. 66, pp. 1–9, 2014.
24. D. Boroński, "Cyclic material properties distribution in laser-welded joints," *Int. J. Fatigue*, vol. 28, no. 4, pp. 346–354, 2006.
25. J. Kozak, "Selected problems on application of steel sandwich panels to marine structures," *Polish Marit. Res.*, vol. 16, no. 4, pp. 9–15, 2010.
26. H. Remes and P. Varsta, "Statistics of Weld Geometry for Laser-Hybrid Welded Joints and its Application within Notch Stress Approach," *Weld. World*, vol. 54, no. 7, pp. R189–R207, 2010.
27. R. Soltysiak and D. Boronski, "Strain analysis at notch root in laser welded samples using material properties of individual weld zones," *Int. J. Fatigue*, vol. 74, pp. 71–80, 2015.

28. N. A. McPherson, N. Suarez-Fernandez, D. W. Moon, C. P. H. Tan, C. K. Lee, and T. N. Baker, "Laser and laser assisted arc welding processes for DH 36 microalloyed steel ship plate," *Sci. Technol. Weld. Join.*, vol. 10, no. 4, pp. 460–467, 2005.
29. V. Caccese, P. A. Blomquist, K. A. Berube, S. R. Webber, and N. J. Orozco, "Effect of weld geometric profile on fatigue life of cruciform welds made by laser/GMAW processes," *Mar. Struct.*, vol. 19, no. 1, pp. 1–22, 2006.
30. C. M. Sonsino, M. Kueppers, M. Eibl, and G. Zhang, "Fatigue strength of laser beam welded thin steel structures under multiaxial loading," *Int. J. Fatigue*, vol. 28, no. 5–6, pp. 657–662, 2006.
31. K. Salonitis, P. Stavropoulos, A. Fysikopoulos, and G. Chryssolouris, "CO₂ laser butt-welding of steel sandwich sheet composites," *Int. J. Adv. Manuf. Technol.*, vol. 69, no. 1–4, pp. 245–256, 2013.
32. D. Frank, J. Romanoff, and H. Remes, "Fatigue strength assessment of laser stake-welded web-core steel sandwich panels," *Fatigue Fract. Eng. Mater. Struct.*, vol. 36, no. 8, pp. 724–737, 2013.
33. D. Frank, J. Romanoff, and H. Remes, "Fatigue life improvement of laser-welded web-core steel sandwich panels using filling materials," in *Analysis and Design of Marine Structures - Proceedings of the 5th International Conference on Marine Structures, MARSTRUCT 2015*, 2015.
34. A. T. Karttunen et al., "Fatigue strength of laser-welded foam-filled steel sandwich beams," *Mater. Des.*, vol. 115, pp. 64–72, 2017.
35. J. W. Sowards et al., "Low-cycle fatigue behavior of fiber-laser welded, corrosion-resistant, high-strength low alloy sheet steel," *Mater. Des.*, vol. 121, pp. 393–405, 2017.
36. W. Fricke, C. Robert, R. Peters, and A. Sumpf, "Fatigue strength of laser-stake welded T-joints subjected to combined axial and shear loads," *Weld. World*, vol. 60, no. 3, pp. 593–604, 2016.
37. D. Frank, P. Dissel, H. Remes, J. Romanoff, and O. Klostermann, "Fatigue strength assessment of laser stake-welded T-joints subjected to reversed bending," *Fatigue Fract. Eng. Mater. Struct.*, vol. 39, no. 10, pp. 1272–1280, 2016.
38. D. Radaj, C. M. Sonsino, and W. Fricke, *Fatigue assessment of welded joints by local approaches*. 2006.
39. D. Radaj, C. M. Sonsino, and W. Fricke, "Recent developments in local concepts of fatigue assessment of welded joints," *Int. J. Fatigue*, vol. 31, no. 1, pp. 2–11, 2009.
40. C. M. Sonsino, W. Fricke, F. De Bruyne, A. Hoppe, A. Ahmadi, and G. Zhang, "Notch stress concepts for the fatigue assessment of welded joints - Background and applications," *Int. J. Fatigue*, vol. 34, no. 1, pp. 2–16, 2012.
41. D. Frank, "Fatigue strength assessment of laser stake-welded T-joints using local approaches," *Int. J. Fatigue*, vol. 73, pp. 77–87, 2015.
42. K. Niklas, "Calculations of notch stress factor of a thin-walled spreader bracket fillet weld with the use of a local stress approach," *Eng. Fail. Anal.*, vol. 45, 2014.
43. A. Cichanski, "The influence of mesh morphology on the SCF in 2D FEM analysis of flat bars with opposite V-notch under tension," in *22nd International Conference on Engineering Mechanics*, 2016, pp. 110–113.
44. K. Niklas and J. Kozak, "Influence of the notch rounding radius on estimating the elastic notch stress concentration factor in a laser welded tee joint," vol. 726. 2012.
45. Niklas K.; Kozak J., "Comparison of strain results at a laser weld notch obtained by numerical calculations and experimental measurements," *AIP Conf. Proc.* 1780, Am. Inst. Phys., 2016.

CONTACT WITH THE AUTHOR

K. Niklas

e-mail: karnikla@pg.edu.pl

Faculty of Ocean Engineering and Ship Technology
Gdansk University of Technology
Narutowicza 11/12 Str.
80-233 Gdansk
POLAND

DETERMINING EFFECTIVE LENGTH FOR 40 HM-T STEEL BY USE OF NON-LOCAL LINE METHOD CONCEPT

Grzegorz Robak¹

Daniel Krzyżak¹

Artur Cichański²

¹ Opole University of Technology, Poland

² UTP University of Science and Technology, Bydgoszcz, Poland

ABSTRACT

In the paper, the concept of non-local line method is presented and used for determining the effective length for notched elements. Experimental tests and calculations were performed for 40 HM-T (42CrMo4+QT) steel made specimens of two types, i.e. smooth specimens, and notched specimens with notch radius equal to 0.2 mm, 0.5 mm, 0.8 mm, and 1 mm. The performed FEM calculations took into account the multi-linear hardening model and cyclic material properties. The concept of the presented non-local line method bases on finding the position of critical plane and determining the effective length, meant as the fracture process zone. During numerical stress gradient simulations, also the weight function was implemented. It was observed that the effective length increases as the load increases.

Keywords: weight function, effective length

INTRODUCTION

The fatigue phenomenon is very complex, and fatigue damage depends on many factors, such as the type and condition of the material, the geometry of the element, the type of load, and the state of stress [3, 9, 15, 21, 24]. Determining the fatigue life of notched elements is still a goal for many scientists [13, 16, 17]. Fatigue life calculation methods can be divided into local and non-local. In the local methods, only the effort at one point is considered, while the non-local methods, in contrast, take into account stress or strain gradients, and/or strain energy density. The fatigue life of notched elements can also be calculated using the Neuber fictitious radius method [14, 18, 20, 23], which can be perceived as a substitute of the non-local line method. In another work which deals with this method [11], the relation between the microstructural support length and the number of cycles of nominal stress is presented. The relation between the fracture process zone and the loading level is also presented in the papers which make use of the

non-local volume method [9, 18]. In those two papers, the variability of the fracture process zone is indicated for both the line method and the volume method. The known non-local methods assume that the effective length can depend on the notch radius [12, 16], the grain size [19], the plastic zone [22, 25], and the stress distribution [16]. The two first methods give good results only for brittle materials, while in the third method, also usually used for brittle materials, the critical plastic crack zone can be determined using the equation proposed by [7]

$$R_y = \mu \cdot \left(\frac{K_{IC}}{\sigma_Y} \right)^2, \quad (1)$$

where:

μ – parameter which depends on loading condition,
 K_{IC} – fracture toughness,
 σ_Y – yield stress.

Equation (1) can be converted and the critical distance d_0 can be calculated from the equation

$$d_0 = \frac{\xi}{\pi} \cdot \left(\frac{K_{IC}}{\sigma_Y} \right)^2, \quad (2)$$

where:

ξ – parameter determined based on author's research.

The main aspect of that approach was to determine the parameter ξ , because different values are proposed by different authors. The value of this parameter was determined based on experimental tests and simulations done for different materials, and it mainly depended on notch geometry.

Another way to determine the fracture process zone has been developed by [16]. This is a non-local volume method, nevertheless the effective distance concept can be meant as a part of the line methods. In that approach the authors made use of the effective distance to determine the fracture process zone, and then performed the calculations in this area. The effective distance was determined based on the relative stress gradient idea (Fig. 1).

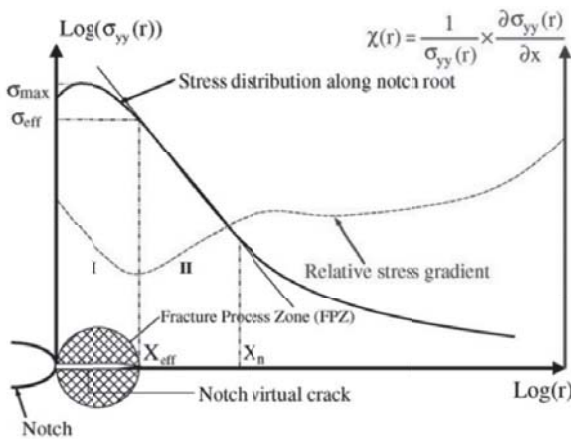


Fig. 1. Stress distribution and relative stress gradient [1]

The authors noticed that in the elasto-plastic calculation, the highest value of stress occurs at a certain distance behind the notch surface. It is usually observed for axial stress, maximum principal stress, but not for Huber-Mises-Hencky (HMH) stress. For maximum principal stress, the minimum of the relative stress gradient is calculated from the equation

$$\chi(r) = \frac{1}{\sigma_y(r)} \cdot \frac{d\sigma_y(r)}{dr}, \quad (3)$$

where:

σ_{yy} – maximum principal stress,
 r – radius in the calculation plane.

In order to obtain the proper relative stress gradient, the calculations should be done for the continuous function of stress, which allows to establish the inflexion point, the effective distance and, finally, the fracture process zone.

An additional aspect of making distinction between the mentioned non-local methods can be the method of stress calculation. Some authors perform stress calculations using

the FEM method and elasto-plastic material properties [6, 8, 10, 16]. This procedure requires the knowledge of the Ramberg-Osgood equation parameters. The stress in the vicinity of the notch is known to be usually above the cyclic yield stress. Hence, determining the stress tensor is an important task, as it decides about the obtained effective lengths. The effective stress values can be calculated using the FEM method and the multi-linear hardening model. It provides good stress (effective stress) results, which can be in proper way compared with the values read from smooth specimen fatigue curves. Some non-local fatigue criteria base on the weight function, which makes it possible to take into account the meaning of different material layers during fatigue processes. In the literature, two interesting weight functions can be found [6, 8]. They are used in the area method, nevertheless they can be adopted to the line methods. In the method presented in [6], the weight function is equal to 1 for surface layers and for layers on which the maximum stress point occurs (Fig. 2). The weight function should include values within the interval $\langle 0;1 \rangle$ and should satisfy the following conditions:

$$\begin{cases} 0 \leq \varphi(r, \chi) \leq 1 \\ Q(r=0, \chi(0)) = 1 \\ Q(r_{max}, \chi(r_{max})) = 1 \end{cases} \quad (4)$$

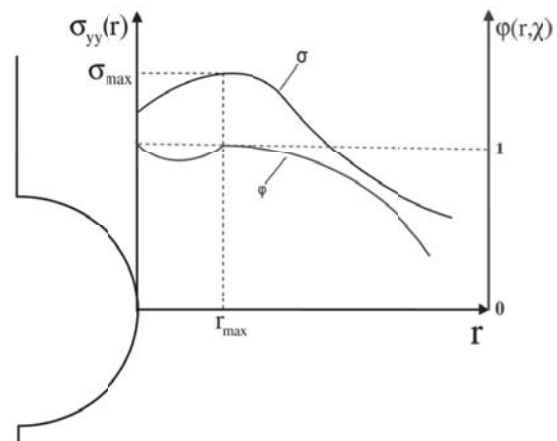


Fig. 2. Distribution of stress and weight function [1]

In [26], the authors describe the weight function as

$$\varphi(r) = 1 - \left(1 - \frac{\sigma_{eq}}{\sigma} \right) \cdot r(1 - \sin(\theta)), \quad (5)$$

where:

σ_{eq} – equivalent stress,
 σ_{max} – maximum value of equivalent stress,
 θ – angle of vector r .

According to this equation, the distance between the surface and the maximum effort point can be considered as the maximum effort area. Nevertheless, for the case of elastic condition, when the stress value is close to the cyclic yield

stress, or when the plastic strain is very small, the weight function is equal to 1 only on the surface.

The weight function proposed in [8] (Fig. 3) is described as

$$w(r) = e^{-\left(\frac{2r}{l_c}\right)^2}, \quad (6)$$

where:

r – vector applied at the maximum effort point,

l_c – critical length which determines the calculation area.

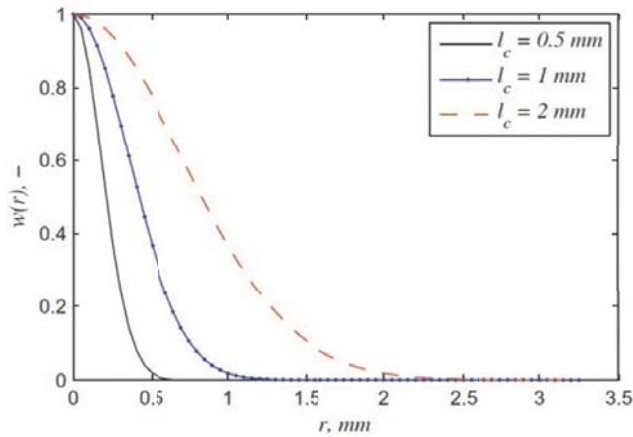


Fig 3. Weight function and different values of critical length [8]

Graphical representation of this weight function is the half plot of the normal Probability Density Function (PDF), where the critical length l_c plays the main role.

According to the previously mentioned issues, the essence of the method presented in the article consists in finding the value of effective length. The presented model is a modification of three models [6, 8, 16]. It allows the calculation to be performed in the elastic or elasto-plastic state of strain.

EXPERIMENTAL TESTS OF SMOOTH AND NOTCHED ELEMENTS

In order to meet the requirements of the proposed model, a series of experimental tests had to be done. The available literature publications on the subject do not contain complete data necessary to perform the planned calculations. The performed experimental tests were expected to provide the data for smooth and notched specimens. For smooth specimens (Fig. 4), the experimental tests of the tension-compression loading mode were performed. It allowed to determine the Wöhler fatigue curve and cyclic material properties. Mechanical properties of 40 HM-T (42CrMo4+QT) steel are presented in Table 1, while its chemical composition is given in Table 2. The cyclic hardening coefficient K' and the cyclic hardening exponent n' are material constants, which were used to describe the cyclic hardening curve in the FEM analysis. Strains were measured with the aid of an extensometer, which allowed to record a hysteresis loop. The fatigue tests were done with force control. The obtained fatigue curve is presented in Fig. 5. The specimens were

made according to the Polish Standard PN-84/H-04308, and the tests were performed according to the standards ASTM 739-80.

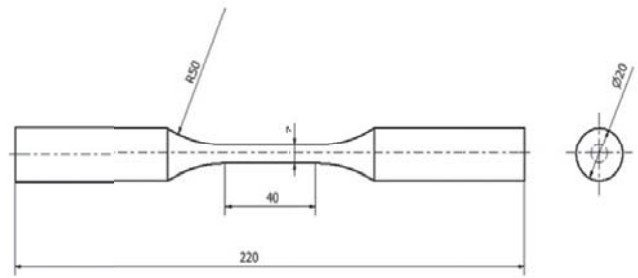


Fig. 4. Geometry of smooth specimen

Tab. 1. Mechanical properties of 40 HM-T (42CrMo4+QT) steel

Young's modulus E, GPa	Poisson's coefficient ν , -	Static yield strength σ_y , MPa	Ultimate tensile strength σ_{UTS} , MPa
210	0.31	1074	1170
Cyclic yield strength σ_y' , MPa	Cyclic hardening coefficient K', MPa	Cyclic hardening exponent n' , -	
600	1750.5	0.095	

Tab. 2. Chemical composition of 40 HM-T (42CrMo4+QT) steel (Fe the rest)

C	Mn	Si	P	S
0.44	0.77	0.27	0.011	0.008
Cr	Ni	Cu	Mo	Al
1.18	0.12	0.19	0.18	0.022

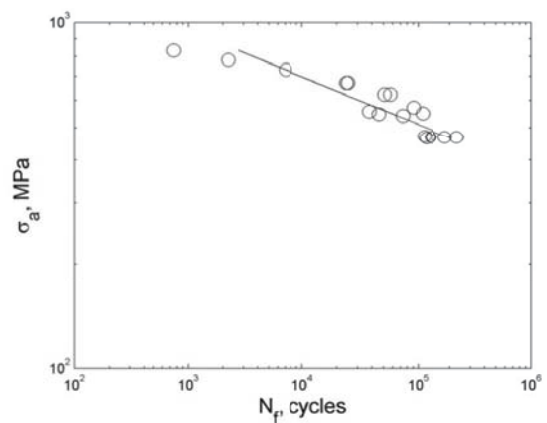


Fig. 5. Smooth specimen fatigue curve

The next series of experimental tests were performed with notched specimens subjected to cyclic bending. In order to compare different stress values at notch tip and the influence of the stress gradient on the number of cycles before crack initiation, two types of notch radius in the tested specimens were applied (Fig. 6). The values of the notch radius R in the

specimen were respectively equal to 0.2 mm, 0.5 mm, 0.8 mm, and 1 mm.



Fig. 6. Geometry of notched specimen

The crack length of 0.1 mm was assumed as the criterion of crack initiation. This value was accepted bearing in mind the camera capacity which enabled cracks of this length to be observed first. To create the Wöhlers fatigue curves, the number of cycles before crack initiation and the stress values calculated by the FEM code were used. Due to a complex state of stress at notch tip, the stress values were calculated according to the HMM hypothesis. Details of calculations are presented in the next chapter. Figure 7 shows the Basquin characteristics determined for smooth and notched specimens, for R = 0.5 mm and 1.0 mm and for the cycle number between 10⁴ and 10⁶. The calculated linear regression coefficients of the equation are presented in Table 3.

$$\log N_f = A - m \cdot \log \sigma_a, \quad (7)$$

where:

A and m - constants of the regression model.

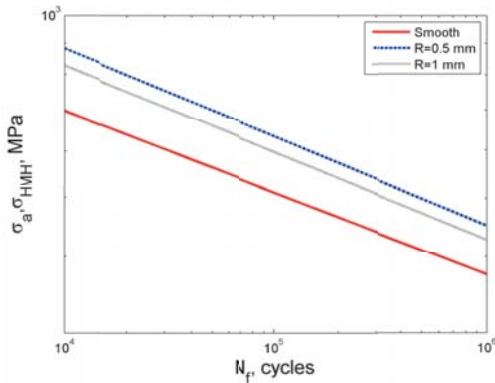


Fig. 7. Basquin fatigue curves for smooth and notched specimens

Tab. 3. Linear regression coefficients for smooth and notched specimens

Type of specimen	A, -	m, -
Smooth	25.02	7.39
Notched, R = 0.2 mm	22.56	6.11
Notched, R = 0.5 mm	24.201	6.85
Notched, R = 0.8 mm	22.70	6.40
Notched, R = 1 mm	24.37	6.98

FINITE ELEMENT METHOD CALCULATIONS

The performed calculations have the form of static non-linear analysis making use of the multi-linear hardening model. This type of calculations requires a powerful computer, due to a large number of elements in the solid model. Since the width of the specimen was relatively large, compared to its height, the plane strain state was used in the FEM analysis. Nevertheless, the calculations were also performed for the plane stress state. The obtained relation between effective length and nominal stress, and the comparison between the experimental and calculated fatigue life, are similar to those obtained in the plane strain state. Cyclic material properties and the multi-linear hardening model for 40 HM-T (42CrMo4+QT) steel are presented in Figure 8. The analyses were conducted in the ANSYS software environment, making use of the second order 8-nodes 2D element PLANE183. The influence of the order of element on the accuracy of FEM analysis of notched specimens was checked in [3]. The accuracy of FEM notch models depends not only on the characteristic mesh size [5], but also on mesh morphology [4]. To ensure control of the notch root element shape, mapped meshes with circular sub-areas [4] were used (Fig. 9). The characteristic mesh size near the notch root was 0.033 mm, while that for the remaining part of the specimen was 0.1 mm.

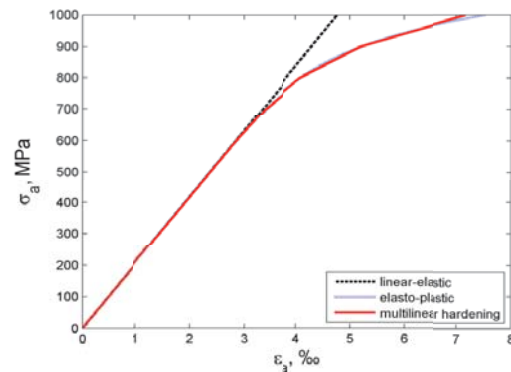


Fig. 8. $\sigma_a - \epsilon_a$ relations for 40 HM-T steel

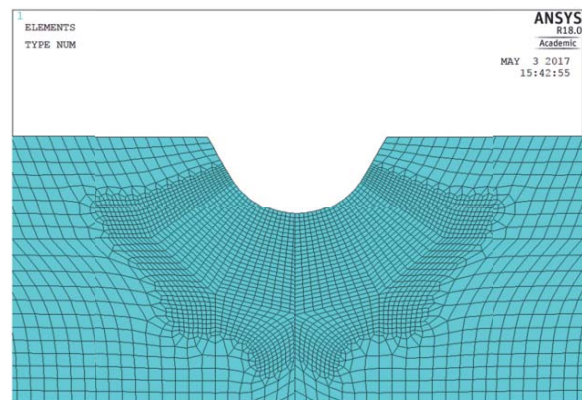
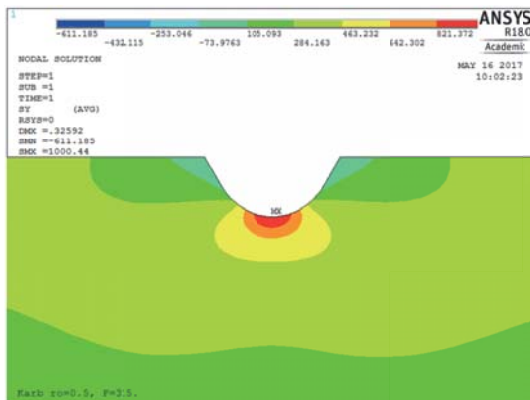


Fig. 9. Mesh structure near notch root for specimen R=0.5 mm

Selected sample results of the notched specimen analysis for $R=0.5$ mm and 1mm, and for the same loading level (nominal stress equal to 402.5 MPa, are shown in Fig. 10.

a)



b)

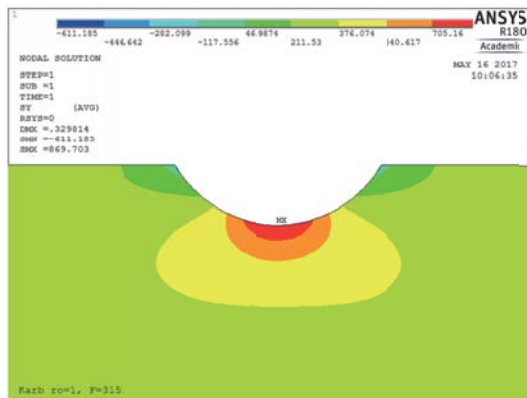


Fig. 10. Results of FEM analysis for notched specimens with a) $R=0.5$ mm (σ_{yy} stress, MPa) and b) $R=1$ mm (σ_{yy} stress, MPa)

Changes of stresses σ_{yy} and σ_{HMH} along the plane perpendicular to the specimen axis (predicted critical plane) are shown in Fig. 11.

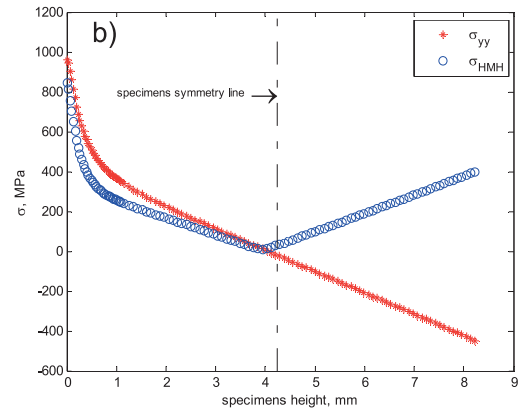
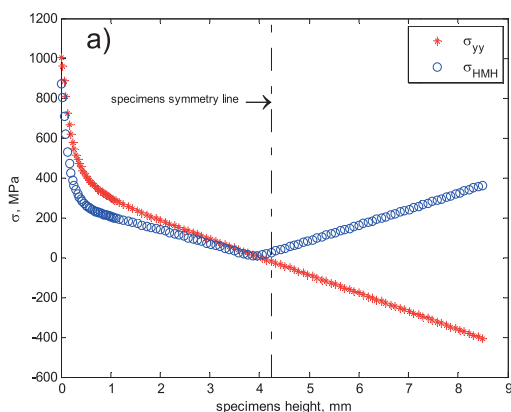


Fig. 11. Values of stresses σ_{yy} and σ_{HMH} along the plane perpendicular to the specimen symmetry axis, for a) $R=0.5$ mm and b) $R=1$ mm

CONCEPT OF NON-LOCAL LINE METHOD

As mentioned in Introduction, non-local line methods base on determining the fracture process zone, which is represented by some length. The main rule is that this zone should contain the highest stress region. The first task in this method is to determine the critical plane in which the calculation should be done. The critical plane is determined under an assumption that the crack initiation starts on the notch tip surface and then propagates in a plane where the normal stress is the highest. It has been proved experimentally that the crack initiation point is very close to the point at which the maximum value of HMH stress is recorded. Due to this fact, the position of the critical plane is determined by the point on the surface where HMH stress has the maximum value. This is well justified, as at this point the multi-axial state of stress is the highest and crack initiation most likely. Hence, at this point the critical plane is determined according to the equation

$$\sigma_{\eta} = \sigma_{ij} \cdot n_j, \quad (8)$$

where:

- σ – stress,
- η – position of the plane,
- n – vector normal to the surface,

The position of the critical plane is determined in the established coordinate system in which the x-axis is parallel to the roll axis of the specimen and the angle is measured in the yz-plane (Fig. 12).

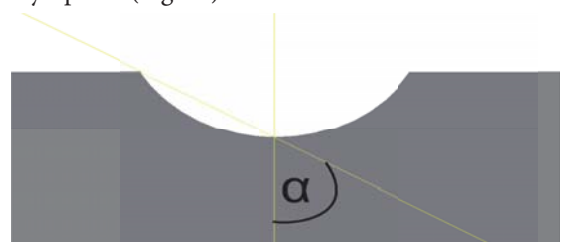


Fig. 12. Principle of critical plane position measurement

ANALYSIS OF RESULTS

The next step was to interpolate stress values in the defined plane and calculate stresses according to Eq. (8). It was done using the interpolation method available in the Matlab software. The interpolated gradient of stress σ_η was then averaged according to the equation

$$\sigma_{eq} = \frac{1}{\int_0^{l_{ef}} Q dl} \cdot \int_0^{l_{ef}} \sigma_\eta \cdot Q dl, \quad (9)$$

where:

- σ_{eq} – equivalent failure stress,
- Q – weight function,
- l_{ef} – effective length.

The effective length l_{ef} is the scope at which averaging is performed. The used weight function Q bases on the assumption proposed in [8]. Physical meaning of the weight function is that it takes into account weights of particular layers in the fracture process. It represents a half of the normal PDF and it has values between 0÷1. However, in cases of greater plastic strain, the stress has the maximum at a certain distance below the surface. It means that the highest stress point has the weight smaller than 1. Hence, some modification of the weight function was proposed, in which the layers between the element surface and the plane of highest stress point σ_η have also the weights equal to 1. It is described by the following formula

$$Q = 1 \text{ for } 0 \leq l < l_{\sigma_\eta, \max}$$

$$Q = e^{-\left(\frac{2 \cdot (l - l_{\sigma_\eta, \max})}{l_{ef}}\right)^2} \text{ for } l \geq l_{\sigma_\eta, \max}, \quad (10)$$

where:

- $l_{\sigma_\eta, \max}$ – length for which maximum value of σ_η occurs.

For smooth specimens without stress gradient, l_{ef} is equal to 0 and the weight of each layers is equal to 1. The weight function and the stress distributions are shown in Fig. 13. The length l_{ef} is determined using the numerical iteration process done by a special programmed script. The iteration point for which σ_{ef} has greater value than the stress in the smooth specimen for the same number of cycles is the inflexion point, which determines the value of l_{ef} . It is important to notice that the obtained values of l_{ef} can differ depending on the loading level.

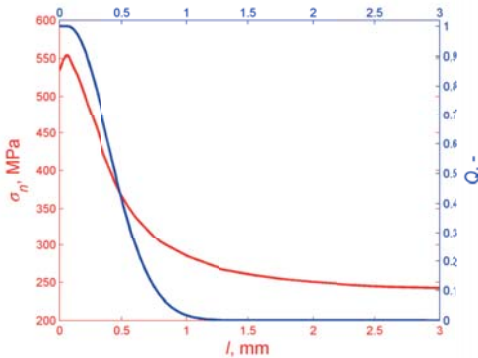


Fig. 13. Sample stress and weight function distributions along length

A set of final values of l_{ef} can be presented as a function of bending nominal stress σ_{nom} . It clearly shows the relation between the loading level and l_{ef} . The results for two notch radius values are presented in Fig. 14 and Fig. 15. Additionally, linear regression was done based on the obtained points. It can be seen that the relation between l_{ef} and σ_{nom} is linear.

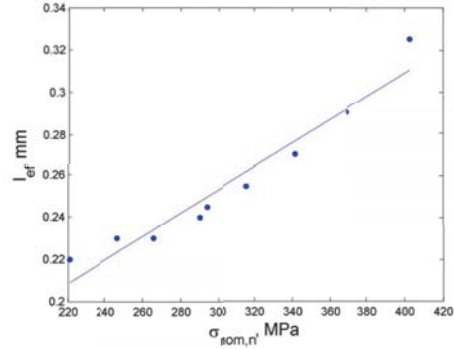


Fig. 14. Relation between effective length and nominal stress for notched specimen with $R=0.5$ mm. Correlation coefficient $r = 0.989$

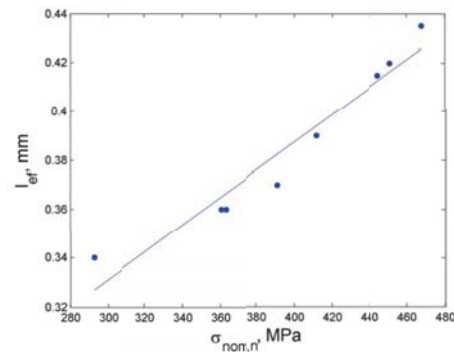


Fig. 15. Relation between effective length and nominal stress for notched specimen with $R=1$ mm. Correlation coefficient $r = 0.982$

The effective length dependence on both nominal stress and stress concentration factors can be represented by a plane (Fig. 16). The values of stress concentration factor k_t for different specimen geometries are presented in Table 4. Based on the results of calculations for 40 HM-T (42CrMo4+QT) steel, the plane equation can be established using multiple regression and 95% confidence bounds (the design curve based on 95% lower confidence limits).

Tab. 4. Values of stress concentration factor k_t for notched specimens

Type of specimen	R = 0.2 mm	R = 0.5 mm	R = 0.8 mm	R = 1.0 mm
k_t	3.7	2.6	1.8	1.4

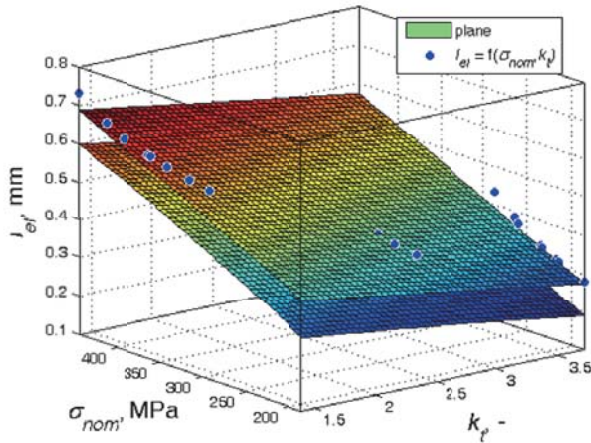


Fig. 16. Relation of effective length with stress concentration factor and nominal stress for 40 HM-T (42CrMo4+QT) steel notched specimen

Based on the calculated values of effective lengths, the plane equation for 95% lower confidence limit has the form:

$$l_{ef} = -0.496 \cdot k_t + 0.0011 \cdot \sigma_{nom} + 0.16. \quad (11)$$

A comparison between the calculated and experimental fatigue life for the cycle number ranging between 10^4 and 10^6 is given in Fig. 17 and 18. It can be noticed that in each case the scatter is smaller than 3. This scatter results from the use of linear regression in the fatigue curves and in the function $l_{ef} = f(\sigma_{nom}, k_t)$.

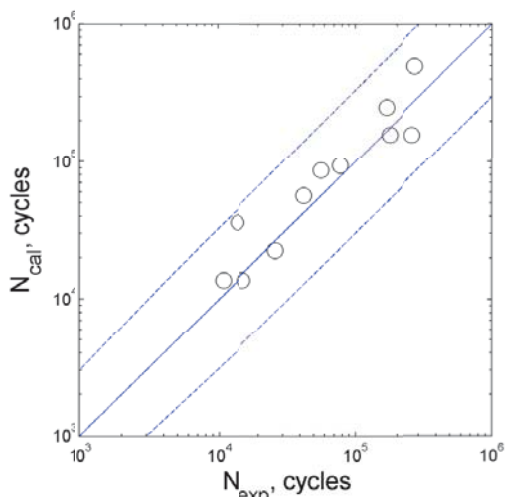


Fig. 17. Comparison between experimental and calculated fatigue life for notched specimens with $R=0.5$ mm

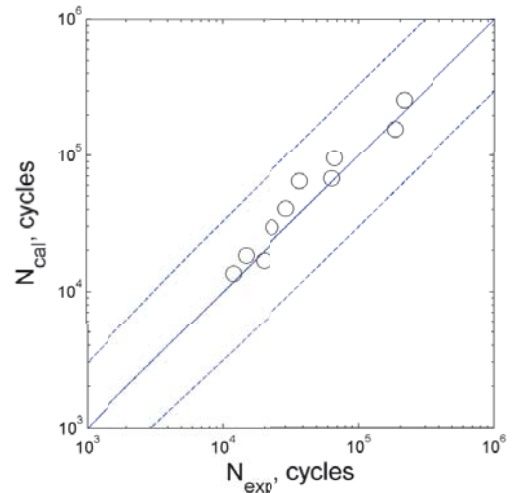


Fig. 18. Comparison between experimental and calculated fatigue life for notched specimens with $R=1$ mm

It is clear that from an engineering point of view, one constant value of l_{ef} is desirable. Analysing the calculated values of l_{ef} , the smallest value can be considered conservative. However, the range of stress calculated by the FEM code should also be mentioned. For the performed research, l_{ef} can be equal to 0.21 mm for the local effective stress ranging between 200÷450 MPa.

CONCLUSIONS

In non-local methods, the most important issues refer to proper determination of the fracture process zone and the equivalent stress. The stress distribution calculated in the elasto-plastic range differs from that calculated in the elastic range, which leads to different values of effective length. The other important issue is determining the plane in which the calculations are to be done. This plane should comply with the experiment. Based on the performed experimental tests and numerical simulations, the following main conclusions can be listed:

1. The position of the critical plane has been determined at the point where the multiaxial state of stress is the greatest.
2. The calculated position of the critical plane complies with that observed during fatigue tests.
3. The normal stress calculated in the defined plane has been established to be responsible for fracture.
4. In the notched element, a sub-area has been indicated between the outer surface of the element and the place at which the normal stresses reach the maximum. The normal stress values in this sub-area have the greatest impact on the effective length value.
5. The calculated effective length is not a constant value. The effective length increases as the load increases, but decreases when the stress concentration factor increases.

REFERENCES

1. Adib-Ramezani H., Jeong J., *Advanced volumetric method for fatigue life prediction using stress gradient effects at notch roots*, Computational Materials Science, 39 (2007) 649–663.
2. Carpinteri A., Spagnoli A., Vantadori S., Viappiani D., *A multi-axial criterion for notch high-cycle fatigue using a critical-point method*, Engineering Fracture Mechanics 75 (2008) 1864-1874.
3. Cichański A., *Influence of finite element order on SCF precision for U-shaped notches in flat bars under tension*, Proceedings of 17th International Conference on Engineering Mechanics 2011, Svratka-Czech Republic, (2011) 79-82.
4. Cichański A., *The influence of mesh morphology on the SCF in 2D FEM analysis of flat bars with opposite V-notch under tension*, Proceedings of 22nd International Conference on Engineering Mechanics 2016, Svratka-Czech Republic, (2016) 110-113.
5. Cichański A., *Mesh size dependency on notch radius for FEM analysis of notched round bars under tension*, AIP Conference Proceedings 1822, 020004 (2017).
6. De-Guang Shang, Da-Kang Wang, Ming Li, Wei-Xing Yao, *Local stress-strain field intensity approach to fatigue life prediction under random cyclic loading*, International Journal of Fatigue, 23 (2001) 903-910.
7. Irwin G., *Analysis of stresses and strains near the end of a crack traversing a plate*, Journal of Applied Mechanics, 24 (1957) 361–364.
8. Karolczuk A., Blacha Ł., *Fatigue life estimation under variable amplitude bending using the non-local damage parameter and multisurface plasticity model*, International Journal of Fatigue 33 (2011) 1376–1383.
9. Kluger K., Łagoda T., *Fatigue life estimation for selected materials in multi-axial stress states with mean stress*, Journal of theoretical and applied mechanics, 54 (2016) 385-396.
10. Krzyżak D., Łagoda T., *Fatigue life estimation of notched elements with use of non-local volumetric method*, International Journal of Fatigue, Vol. 61 (2014) 59-66.
11. Krzyżak D., Robak G., Łagoda T., *Determining fatigue life of bent and tensioned elements with a notch, with use of fictitious radius*, Fatigue and Fracture of Engineering Materials and Structures, 38 (2015) 693-699.
12. Krzyżak D., Robak G., Łagoda T., *Non-local line method with weight function and critical plane approaches used for fatigue life calculation of notched elements*, Fatigue and Fracture of Engineering Materials and Structures Vol. 40, 2017.
13. Łagoda T., Robak G. and Słowik, J., *Fatigue life of steel notched elements including the complex stress state*. Materials and Design, 51 (2013) 935–942.
14. Neuber H., *Über die Berücksichtigung der Spannungskonzentration bei Festigkeitsberechnungen*, Konstruktion im Maschinen-Apparate und Gerätebau, Heft 7 (1968) 245-251.
15. Pawliczek R., Kluger K., *Influence of irregularity coefficient of loading on calculated fatigue life*, Journal of Theoretical and Applied mechanics, 51 No. 4 (2013).
16. Pluvinage G., *Fracture and fatigue emanating from stress concentrators*, Kluwer, Dordrecht (2003).
17. Radaj D., Vormwand M., *Advanced methods of fatigue assessment*. Springer Verlag Berlin Heidelberg (2013).
18. Radaj D., Lazzarin P., Berto F., *Generalised Neuber concept of fictitious notch rounding*, International Journal of Fatigue, Vol. 51 (2013) 105-115.
19. Ritchie RO., Knott JF., Rice JR., *On the relationship between critical tensile stress and fracture toughness in mild steel*, Journal of the Mechanics and Physics of Solids, 21 (1973) 359–410.
20. Robak G., Szymaniec M., Łagoda T., *The fictitious radius as a tool for fatigue life estimation of notched elements*, Materials Science Forum, 726 (2012) 27-32.
21. Rozumek D., Marciniak Z., *Fatigue properties of notched specimens made of FeP04 steel*. Materials Science, 47(4) (2012) 462-469.
22. Seweryn A., *Brittle fracture criterion for structures with sharp notches*, Engineering Fracture Mechanics, 47 (4) (1994) 673-681.
23. Sonsino C.M., Łagoda T., *Assessment of multi-axial fatigue behaviour of welded joints under combined bending and torsion by application of a fictitious notch radius*, International Journal of Fatigue, 26 (2004) 265-279.
24. Szala G. *Comments on linear summation hypothesis of fatigue failures*, Polish Maritime Research 3(83) Vol. 21, (2014)
25. Taylor D., *Predicting the fracture strength of ceramic materials using the theory of critical distances*, Engineering

Fracture Mechanics, 71 (2004) 2407-2416.

26. Yao W., Ye B., Zheng L. A verification of the assumption of anti-fatigue design, International Journal of Fatigue, 23 (2001) 271-277

CONTACT WITH THE AUTHOR

Grzegorz Robak

e - mail: g.robak@po.opole.pl

Opole University of Technology
Mikołajczyka St. 5
45-270 Opole
POLAND

Daniel Krzyżak

e - mail: d.krzyzak@doktorant.po.edu.pl

Opole University of Technology
Mikołajczyka St. 5
45-270 Opole
POLAND

Artur Cichański

e - mail: artur.cichanski@utp.edu.pl

UTP University of Science and Technology
Al. prof. S. Kaliskiego 7
85-796 Bydgoszcz
POLAND